UNIVERSITY OF RIJEKA
FACULTY OF CIVIL ENGINEERING

Tea Sulovsky

NUMERICAL INVERSE MODELLING OF FIBRE-REINFORCED CONCRETE BEAMS UNDER THREE-POINT BENDING

DOCTORAL THESIS

Rijeka, 2025

UNIVERSITY OF RIJEKA
FACULTY OF CIVIL ENGINEERING

Tea Sulovsky

NUMERICAL INVERSE MODELLING OF FIBRE-REINFORCED CONCRETE BEAMS UNDER THREE-POINT BENDING

DOCTORAL THESIS

Supervisor: izv. prof. dr. sc. Neira Torić Malić, dipl.ing.građ.

Rijeka, 2025

Abstract

Computational modeling and analysis of Fiber-Reinforced Concrete (FRC), an advanced composite known for its enhanced flexural strength and resistance to crack propagation, form the focus of this research. The primary objective was to develop a stable deterministic computational model capable of accurately replicating the behavior of FRC beams under three-point bending. This model integrates fundamental material parameters observed at the micro-scale (fiber bond-slip and fiber geometry) and links them to the resulting bending mechanism across the meso- and macro-scales. A significant contribution of this work lies in the formulation of an efficient inverse model which utilizes the Levenberg-Marquardt algorithm. This method aims to extract explicitly defined material parameters (such as effective modulus and bundle scaling factor) by basing the objective function on the simplified forward model's expressions. The methodology includes comprehensive laboratory testing to validate the computational results and ensure their practical applicability. The fundamental novelty of this research is establishing a deterministic forward model with formulations that are simplified enough for efficient inverse analysis, yet precise enough to accurately predict FRC beam behavior, which thereby resolves the traditional challenge of high computational cost in multi-scale inverse modeling.

Acknowledgements

This research was funded by Croatian Science Foundation's project HRZZ 7926 "Separation of parameter influence in engineering modeling and parameter identification", and DOK-2020-01 "Young Researchers' Career Development Project – Training of New Doctoral Students".

Contents

Glossary of Terms

axial stiffness The combined resistance of the fiber bundle to axial deformation, calculated as the product of the effective elasticity modulus (E) and the total cross-sectional area (A) of the fibers.

crack inclination A parameter in the layered sectional model that represents the angle of the crack opening.

crack-bridging The mechanism by which fibers cross a crack to maintain residual strength and ductility.

deterministic model A computational model that always produces the same output for a given set of inputs under fixed conditions.

displacement-controlled loading A testing method where the rate of deformation (displacement) is held constant.

fiber bundle model A multiscale framework used to describe and analyze the mechanical behavior of fiber-reinforced materials by linking the microstructural properties of individual fibers to the overall strength, stiffness, and damage resistance of the composite.

flexural strength The maximum stress a material can withstand under bending.

forward model A computational model that predicts results (output) based on a specified set of known input parameters and governing physical laws.

global minimum The absolute smallest value of an objective function within the entire solution space.

inverse analysis A technique that uses measured output data and a predictive forward model to estimate or identify unknown input parameters of a system or material.

inverse model A computational method used to estimate unknown physical parameters (input data) of a system based on measured responses (output data).

Jacobian Matrix A matrix composed of the first partial derivatives of a vector-valued function.

load transfer The stress distribution mechanism across the cracked section from the concrete matrix to the fibers via the bond.

local minima A solution found by an optimization algorithm that is smaller than its neighbors but not the global minimum.

Monte Carlo Simulation A broad class of computational algorithms that rely on repeated random sampling to obtain numerical results, often used in stochastic modeling to simulate parameter variability.

multiscale modeling A computational framework that links phenomena occurring at different length scales (e.g., micro, meso, and macro) to accurately predict the overall structural response of a composite material.

parametric analysis A mathod of systematically mapping specific input parameters of a model to the corresponding predicted output or overall system behaviour.

post-cracked state The state of concrete after the formation of the first crack, where load is primarily sustained by the fibers.

post-peak softening The phase in the load-displacement test where the load-carrying capacity gradually decreases as the crack opens.

pseudo time A generalized time variable that represents the sequence of recorded data points relative to the total testing duration.

scale effects The observed discrepancies in physical phenomena when comparing a small specimen or model and its full-scale structural element.

self-compacting concrete A highly flowable concrete mixture designed to self-compact under its own weight without the need for mechanical vibration.

stochastic model A computational model incorporating randomness and uncertainty as an inherent part of its structure, often relying on statistical parameters.

Tikhonov regularization A technique for estimating model parameters in scenarios where the independent variables are highly correlated.

validation The process of determining the degree to which a computational model accurately represents the real-world phenomenon.

verification The process of confirming that a numerical algorithm correctly solves the underlying mathematical equations of the computational model.

List of Abbreviations

d_v Vertical Displacement.

EA Axial Stiffness.

BoA Basin of Attraction.

CMOD Crack Mouth Opening Displacement.

CT Computed Tomography Scan.

CV Coefficient of Variation.

DEM Discrete Element Method.

FBM Fiber Bundle Model.

FEM Finite Element Method.

FRC Fiber-Reinforced Concrete.

ITZ Interfacial Transition Zone.

LM Levenberg-Marquardt Algorithm.

LMA Levenberg-Marquardt Algorithm.

LVDT Linear Variable Differential Transformer.

NRMSE Normalized Root Mean Square Error.

PDF Probability Density Function.

RC Regular Concrete.

RMSE Root Mean Square Error.

RSR Relative Squared Residual.

RSS Residual Sum of Squares.

SCC Self-Compacting Concrete.

SS Sum of Squares.

TPBT Three-Point Bending Test.

V&V Verification and Validation.

VMA Viscosity Modifying Agent.

Chapter 1

Introduction

Fiber-reinforced concrete (FRC) is a composite material consisting of regular concrete (RC) with the addition of short-length, high-strength fibers which are added during the mixing process to enhance the material's overall behavior under static and dynamic loading [1]. The presence of fibers in the concrete matrix gives the structure the ability to improve the resistance to failure in the post-cracked state. Fibers bridge the micro-cracks and limit their propagation, preventing them from merging into even larger cracks that ultimately lead to a complete brittle collapse of the structure [2].

Various types of fibers are used in cement-based materials to improve their mechanical properties, such as, polyvinyl alcohol fibers, and polypropylene fibers, and the most common ones - steel fibers. Steel fibers are known for significantly enhancing the flexural and uniaxial tensile strengths of concrete due to their bridging effect, which increases the material's fracture energy [3]. Steel fibers have a high modulus of elasticity (typically between 200 and 210 Gpa) and a tensile strength between 500 and 3000 MPa, which when added to the concrete mixture influences the composite's own elasticity modulus and tensile strength [4]. However, steel fibers are prone to corrosion, particularly when exposed to chloride environments, which can compromise their durability [5, 6].

Despite its frequent use in construction, the procedures and regulations for designing FRC structures that would meet all the necessary criteria for practical application remain under-refined due to inherent uncertainties surrounding the material's response under various loadings and the complex, micro-scale interactions that govern its post-cracking behavior [7]. The insight into FRC behavior is primarily obtained through laboratory testing, where the material is examined under controlled conditions. Among these tests, the three-point bending test (TPBT) stands as the standard procedure for the determination of flexural fracture properties of beams. However, this experimental approach is both financially demanding and time-consuming. Therefore, computational modeling, with its ability to simulate

laboratory tests and predict material behavior, poses a convenient alternative. In recent years, models for systematic analysis of parameters have been developed for a range of materials, including concrete [8], steel [9], modern metamaterials [10], and others.

The development of computational models that accurately capture the heterogeneous and stochastic nature of FRC by connecting local and global parameters with constitutive laws, is of great interest to both researchers and engineers. Moreover, an inverse model based on a reliable computational framework holds the potential to provide additional insights into physically unmeasurable FRC material parameters.

Previous researchers in the field of multiscale modeling of FRC have developed stochastic models that were successfully implemented in an inverse analysis algorithm [11], [12]. These stochastic models incorporate the material's randomness and uncertainty as an inherent part of its structure. Techniques such as Monte Carlo simulations, probabilistic methods, and random field theory are commonly used to introduce randomness, particularly to model the fiber distribution and bond-slip law within the concrete matrix. For instance, Kožar et al. employed a stochastic approach to homogenize the FRC composite, utilizing the fiber bundle model to describe the fiber distribution [11, 13, 14].

However, these models heavily rely on statistical parameters, which often don't directly correlate with any specific physical properties of the material. The scattering in measurement data from stochastic models, although valuable for simulating and representing errors in real experiments, presents a significant challenge for interpreting through an inverse analysis [14]. As a result, the use of stochastic models for parametric estimation and precise analysis of material values on a multi-scale is limited.

In contrast, deterministic models always produce the same output given the same input under fixed conditions. These models are essential for scenarios where predictability and reproducibility are crucial, such as in FRC, where reliable and precise parameters are necessary. Although deterministic models can handle complex geometries, material properties, and boundary conditions, their comprehensive formulations make implementation in an inverse analysis and parameter identification an overly complicated, time-consuming, and resource-demanding task [15].

The research gap addressed in this work is the absence of a computationally efficient deterministic forward models for FRC that are suitable for subsequent integration into a stable inverse parameter identification framework. This study focuses on developing a novel deterministic numerical model of FRC beams under Three-point bending test (TPBT). This was accomplished by integrating analytical solutions and explicit parameters that define a fiber bundle model, which mitigates the mentioned challenges. The proposed model aims to provide a systematic and consistent

approach to simulating FRC behavior under TPBT, enabling more accurate and practical applications in engineering design, particularly through inverse analysis.

1.1 Thesis Outline

This dissertation is structured to address the research objectives systematically. Chapter 2 presents a relevant literature review that mainly focuses on multiscale modeling, fracture mechanics, and various forward and inverse modeling techniques for FRC. Chapter 3 outlines the research goals and hypothesis that motivate this work. Chapter 4 presents the detailed development and validation of the simplified deterministic forward model, including the analytical formulations used for the fiber-matrix bond and the equilibrium equations. Chapter 5 focuses on the formulation and validation of the inverse model using the Levenberg-Marquardt algorithm (LMA). Chapter 6 presents the results of the parametric analysis and the inverse analysis process on experimental data. Finally, Chapter 7 summarizes the key findings, conclusions, and provides recommendations for future research.

Chapter 2

Literature Review

2.1 General Characteristics of Fiber Reinforced Concrete

Fiber-reinforced concrete (FRC) integrates short, high-strength, and discontinuous fibers into the conventional concrete matrix of aggregates and cement, and represents a significant advancement in composite materials and construction. These fibers are added during the mixing process which fundamentally changes the material's mechanical properties. The primary function of these embedded fibers is to increase the concrete's inherent weak points, particularly its low tensile strength and brittle failure mechanisms. By doing so, FRC structure's tensile and compressive strength, ductility, and resistance to fatigue are significantly enhanced, while the performance of the structure under both static and dynamic loading conditions gets collectively improved [1]. A critical characteristic of FRC is its ability to improve resistance to failure in the post-cracked state, as the fibers act as crack-bridging elements that slow down the micro-propagation of cracks and prevent their union into larger fractures that could potentially lead to a sudden, brittle collapse of the structure [16]. This bridging action fundamentally changes the failure mode from brittle to a more ductile and controlled response, which is a highly desirable structural property in modern structural design.

The choice of fiber type greatly influences the mechanical properties and overall performance of FRC structures. Common types of fibers used in practice include steel, synthetic, glass, and other specialized fibers, where each possesses distinct material properties, shapes, and aspect ratios [17]. Steel fibers pose as the most common form of micro-reinforcement. They typically come in plain, hooked, crimped, and enlarged end shapes, as presented in Figure 2.1. Steel fibers have a high tensile strength in the range of 800–2,000 MPa, and elastic moduli of approximately 200 GPa. Their failure strains typically range from 3% to 5%, and the aspect ratio,

defined as the fiber length divided by its average cross-section diameter, commonly lies between 30 and 80. Typically added dose rates from 0.3% to 1% of the concrete volume, although higher dosages may negatively affect workability.[17].

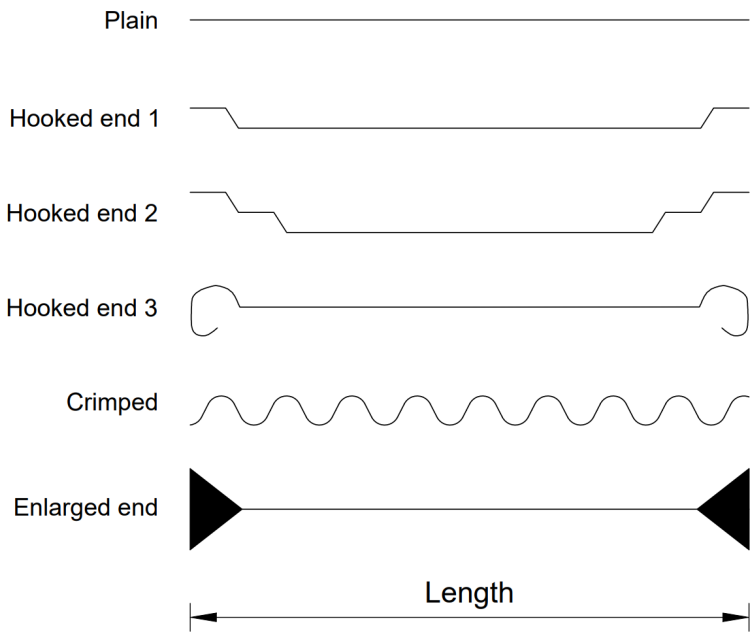

Figure 2.1: Common types of steel fiber reinforcement [17]

Central to the effectiveness of FRC is a microscopic region between the fibers and the surrounding cement matrix, known as the interfacial transition zone (ITZ). The ITZ is a weak link due to its porous nature which makes it is critical to the composite's overall performance. Around the predominantly heterogeneous ITZ, fiber-matrix debonding can occur as cohesive failure, while at the fiber-cement contact surface the fiber-matrix debonding appears as adhesive failure [18].

An appropriate bond is essential for high energy absorption through debonding and the subsequent frictional phase of fibers during pullout. A poor fiber-matrix bond obstructs efficient load and energy transfer, while an excessively strong one can lead to premature fiber breakage and minimize the fracture energy.Therefore, as the efficiency of force transfer within the ITZ plays a critical role in the overall performance of FRC structures, it is of high interest to evaluate its properties and parameters that govern it in order to improve the material performance.Previous studies used nano-indentation and fiber pullout tests to analyze this, even though a significant gap still remained in investigating its mechanical properties at a micro-scale and meso-scale [18].

Concrete reinforced with fibers operates through multiple interconnected mechanisms that enhance its structural integrity beyond simple crack bridging [19]. Some of the mechanisms include: crack arrest, load transfer and energy absorption. Crack

arrest mitigates micro-crack propagation by diverting their paths and redistributes strain. Studies that utilized digital image correlation and acoustic emission tests have showed that a higher volume of fibers leads to improved crack control and strain redistribution [19]. Load transfer is a mechanism that directly influences both pre-peak and post-peak stress-displacement relations [20]. Research has shown that the effectiveness of this mechanism is greatly governed by the robustness of interfacial fiber-matrix bond, as well as fiber position and orientation [19]. In terms of energy absorption, it primarily refers to the absorption done through the fiber pull-out and fracture mechanisms that directly affect structural toughness. Mechanical testing and computed tomography studies shown that some FRC structures had up to a 49% increase in toughness due to clever energy absorption solutions [21]. Approximately half of the internal energy dissipation is a result of concrete matrix cracking, which includes crack propagation and multiple other cracking systems governed by the fibers' influence, while the remainder is due to fiber pullout.

Fiber-reinforced concrete structures' enhanced mechanical properties have led to FRC being widely adopted for various applications where conventionally reinforced concrete falls short. The most common applications include sprayed concrete for tunnel linings and slope stabilization, industrial and airport runway flooring subjected to heavy dynamic loads, and other critical infrastructure elements like wind turbines and nuclear plant wall linings exposed to extreme stresses and fatigue. Furthermore, FRC offers significant economic benefits that extend beyond the improved structural performance [22]. It also allows for the design of thinner elements, which leads to reduced material usage and lighter structures, and a potential decrease in overall material costs and improved sustainability [22, 23]. The incorporation of fibers can also partially or completely replace traditional rebar reinforcement, and significantly lower labor and material costs associated with rebar installation [22, 24, 25]. Moreover, FRC's properties quicken the construction processes by reducing the complexity of reinforcement necessary for geometrically complex elements, which overall translates into lower overhead costs and shortened project timelines [24, 26]. While the initial investment in fiber materials can be a obstacle, the long-term savings in maintenance and labor often outweigh these initial expenses. All of this makes FRC a compelling choice for modern construction practices and further research [25].

Despite the increase in FRC usage in modern construction practices, it still remains an insufficiently described material from a computational modeling point of view. A significant gap exists in the establishment of standardized procedures and regulations for designing FRC structures that would comprehensively encompass all necessary criteria for practical application [27].Existing standards for FRC have several limitations, particularly in their ability to adequately address post-peak behavior and ductility, as well as inconsistencies in testing methodologies [28, 29]. This leads to engineers still choosing conservative design solutions even in cases where it's

structurally not the most optimal choice, simply due to current standards lacking sufficient parameters for evaluating post-peak stresses in FRC elements [28], and an agreed upon testing setups (e.g., four-point versus three-point bending), which creates discrepancies in for performance evaluations when choosing FRC over traditional RC [28]. This absence of a unified approach to testing and evaluation across different standards not only prolongs the reliance on traditional design methods, but also slows down the integration of innovative materials [29]. This shows that there is a clear need for studying of advanced modeling techniques to bridge the gap between costly experimental observations and vigorous design guidelines [30].

Traditionally, the knowledge about any engineering material, including FRC, is primarily gathered through laboratory testing. Experimental approaches allow for an accurate examination of various material properties and structural behaviors under highly controlled conditions. However, experimental testing of FRC has several significant limitations that obstruct reproducibility and accurate performance analysis. As fibers are inherently randomly distributed and the number of fibers bridging cracks can widely vary even within supposedly identical specimens, it causes a substantial variability in the post-cracking phase of tested performance. Such variability further complicates the establishment of standardized testing protocols, as existing methods often fail to take into account parameters such fiber count at crack surfaces and obscures their actual impact on the final element's behavior [31]. Furthermore, directly measuring localized strains and crack bridging forces is often impossible due to the interactions between individual fibers and the concrete matrix being either overly complex, microscopic or both [32]. Traditional testing methods frequently fail to capture the nuanced behaviors of fibers during crack formation which limits the ability to comprehensively understanding their contributions to structural integrity [33]. Lastly, scale effects pose a considerable challenge, because laboratory samples may not accurately represent full-scale structural behavior, as larger specimens can exhibit different mechanical properties than smaller ones [34, 35]. This further complicates the direct conversion of laboratory obtained data to real-world applications, but highlights how such limitations, coupled with the financial expense and time-consumption of experimental campaigns allude to a need for alternative and complementary approaches [35].

For all these reasons, computational modeling emerges as a key tool, for its capability to efficiently simulate and predict material behavior. It serves as a vital complement to, and in certain scenarios, a complete replacement for, traditional experimental methods. Therefore, the development of accurate and reliable computational models that effectively capture the complex interactions within FRC is of high interest to both engineers and researchers. By establishing clear connections between local and global parameters, such models provide a cost-effective and time-conserving means to explore diverse design scenarios and loading conditions.

Furthermore, the integration of an inverse model offers potential for a transformative method of gathering insight into FRC material properties. Such models provide a look into physically unmeasurable material parameters, as well as parameters that are difficult or impossible to obtain through direct experimental means. This includes, but is not limited to, the actual in-situ fiber distribution within a cast element, the characteristics of the fiber-matrix bond for individual fibers, or the localized post-cracking tensile constitutive law of the FRC beyond what can be derived from global load-displacement curves. This capability could be critical for improving FRC design optimization methods, as it allows engineers and other potential users to fine-tune material compositions and structural geometries for optimal performance. Moreover, inverse models can significantly contribute to the monitoring and evaluation of existing FRC structures, which allows for an eased inspection of current material states or even detection of any internal damages from observable structural responses. The research and development of such computational tools is essential for improving potential of fiber-reinforced concrete and establishing it as a comprehensively understood and confidently applied material in civil engineering practices.

2.2 Challenges and Approaches in Computational Modeling of Fiber Reinforced Concrete

In order to adequately model fiber-reinforced concrete, it is necessary to examine the characteristics that distinguish it from conventional concrete. As was pointed out in the work of Jansson[36], the primary benefit of fiber reinforcement lies in its ability to control cracking, which is largely governed by the bond mechanism between the fibers and the concrete matrix, as well as the pull-out behavior during crack propagation. Both of these mechanisms are directly related to two fiber-reinforced concrete material characteristics that can be observed on various scales: the bond-slip law and the fiber distribution within the concrete matrix [37].

2.2.1 The Multiscale Nature of Fiber-Reinforced Concrete

The behavior of FRC is inherently multiscale, as it spans from the micro-scale to the meso-scale and the macro-scale. At the micro-level, fibers interact with the concrete matrix through interfacial slip and pullout mechanisms, which influences the crack bridging and arresting [38], [39]. The meso-scale behavior is characterized by fiber distribution and orientation within the matrix, which affects the overall performance of the composite [40]. At the macro-scale, what is observed are the mechanical properties of FRC elements, which includes improved compressive, flexural, and

tensile behavior [41], [40].

Capturing this multiscale nature of FRC is critical for accurately predicting the overall response of finished FRC structures. Multiscale modeling approaches are essential for bridging these scales and capturing the complex interactions between them. For instance, Zhan and Meschke [42] developed a multiscale framework that links micro-scale fiber pullout behavior to macro-scale structural performance, demonstrating the importance of integrating fiber-matrix interactions into larger-scale models. Similarly, Huang et al. [43] used a meso-macro model to analyze the flexural behavior of FRC, showing how fiber orientation and distribution at the meso-scale influence the load-displacement response at the macro-scale. Without a multiscale approach, models risk oversimplifying the material behavior, which leads to inaccurate predictions of structural performance and ultimately being useless for any structural design.

However, multiscale models of fiber-reinforced concrete confront quite significant challenges, especially when applied for inverse analysis of material parameters. According to literature, these challenges can be categorized into three main areas: computational burden, parameter identification limitations, and cross-scale validation issues. First, integrating micro-, meso-, and macro-scale phenomena into a computational model is extremely computationally taxing. For example, studies have showed that the resource intensity of simulating problems containing large numbers of fibers and heterogeneous materials within the finite elements workframe could take up to hundreds of millions degrees of freedom in order to be solved [44]. To mitigate these issues, a common approach is applying order statistics to reduce simulation times [45, 46]. Second, inverse analysis for parameter identification faces significant limitations, such as sensitivity to experimental data quality, risks of converging to local minima instead of a global one, and the overestimation of post-cracking tensile capacity [32]. And third, validating models across different scales is a challenge on its own. Errors at the micro-level can propagate upward and lead to significant discrepancies at the structural level [47, 48]. This is also furthered by experimental limitations, such as data availability, precision and noise, which all affect the stability reliability of validation [44, 45].

Bridging the gap between length scales presents one of the primary challenges in multiscale modeling of FRC. Often times sophisticated coupling techniques are required to ensure consistency and accurate information transfer between scales, which are often computationally demanding. This can also be seen in the work of Zhan and Meschke [42] who highlighted the difficulty of accurately transferring localized micro-scale effects to the macro-scale without oversimplification, as a mismatch in scale-dependent phenomena can lead to inaccuracies in predicting structural behavior. Marfia and Sacco also developed a micromechanical model for FRC that makes use of the homogenization theory to predict macroscopic behavior from a periodic

microstructure [49]. This method uses a "cell model" to represent the composite's microstructure and defines the overall properties of the composite through homogenization. While homogenization techniques can be computationally efficient, they often rely on simplifying assumptions, such as a periodic or regular distribution of fibers, which contrasts with the real-life randomness of real FRC.

Another big challenge is how computationally intensive multiscale models are due to the need to simulate various phenomena at multiple scales simultaneously. Of course, this also greatly depends on the method used to build the model and will be further elaborated while categorizing models in chapter 2.2.

2.2.2 Modeling Mechanisms of Fiber-Matrix Interactions

In order to understand the specific challenges of modeling fiber-reinforced concrete as opposed to regular concrete, it is essential to identify the material and behavioral characteristics that set it apart. The primary difference lies in the addition of fibers within the concrete matrix and their influence on the cracking behavior of the element. This increased heterogeneity makes modeling this composite even more challenging, especially since the heterogeneity of fiber-reinforced concrete is closely connected to the failure mechanisms of regular concrete [**?**]. Modeling these mechanisms is key to successfully simulating FRC behavior. Key factors include fiber orientation, distribution, and the bond-slip relationship. Therefore, these parameters and their effects will be discussed in detail in the following chapters.

2.2.2.1 Modeling of Fiber Orientation and Distribution

Fiber orientation and distribution are FRC characteristics that represent the spatial arrangement and angular alignment of fibers within the concrete matrix, which directly influence the anisotropic mechanical properties, crack resistance, and overall performance of FRC structures. Modeling fiber orientation and distribution means mathematically defining these characteristics within a computational model of a composite matrix, in this case - concrete. This is critical for predicting the fiber-reinforced concrete's anisotropic mechanical properties, such as tensile strength, crack resistance, and overall structural behavior. However, this is highly challenging as mechanisms that define fiber orientation and distribution are influenced by a variety of factors, such as the fiber geometry, the rheological properties of the matrix, the bar embedding and concrete mixing methods, element shape, etc. [50]. Obtainment of detailed fiber orientation data within a cured concrete specimen is one of the main challenges when researching FRC. Some of the methods of measuring fiber orientation include electromagnetic induction, image analysis, and computed tomography scanning [51]. It is also important to note that the causes for anisotropic

fiber alignment cannot be evaluated independently due to their coupled nature. For instance, the effect of casting direction cannot be quantified by disregarding the type of casting element, and an isotropic fiber orientation cannot be assumed when anisotropy from fresh-state properties, casting, and compaction is likely to occur [52]. Even though fiber orientation and distribution are distinct concepts, they are frequently conflated and discussed under the same notion. This is due to their interconnected influence on the behavior of the structure, shared modeling challenges, and shared practical difficulties of isolating their effects in experimental studies.

Fiber orientation refers to the angular alignment of individual fibers within a composite matrix relative to loading directions or principal stresses. It is typically defined using spherical coordinates (azimuth angle ϕ, polar angle θ) or represented as a unit vector $\mathbf{p}$ along the fiber's longitudinal axis. A simplified representation of fiber orientation defined with fiber's angle of orientation, embedment length and embedment position relative to the loading axis is shown on Figure 2.2.

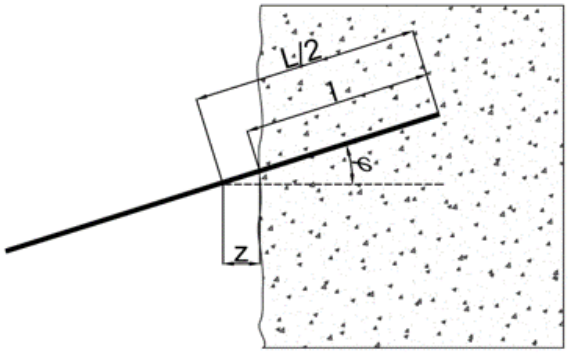

Figure 2.2: Half embedded fiber with angle orientation properties

On the other hand, the fiber distribution refers to the spatial arrangement of fibers within the composite, which includes their density, clustering, and interactions, and is seen in Figure 2.3. It is influenced by material rheology, parameters that influence the casting process, and fiber-matrix interactions. Unlike fiber orientation, distribution addresses both local heterogeneity (e.g., fiber clumping) and global uniformity.

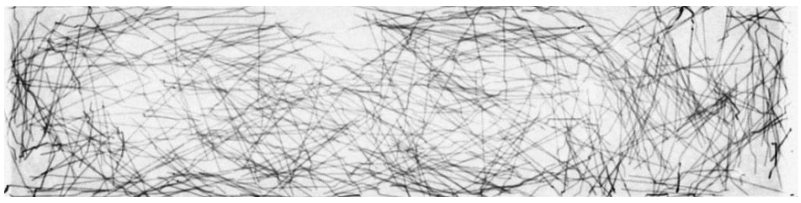

Figure 2.3: X-ray image of a FRC beam [53].

In the context of incorporating fiber orientation into computational models, second-order orientation tensors are frequently used to describe the average align-

ment of the fibers [54]. This approach, often used to describe the average 3D fiber configuration inside a concrete volume, provides a simplified yet effective way to account for fiber orientation, which is critical for predicting the anisotropic mechanical properties of fiber-reinforced concrete [51, 55].The main diagonal components of the tensor can be expressed as a percentage of fiber orientation in each of the three main directions [51]. For example, Reinold, Gudžulić, and Meschke [56] developed a finite element method framework based on the probabilistic representation of fiber distribution proposed by Advani & Tucker [54]. Their work builds on the Folgar–Tucker model, which incorporates the dynamic evolution of fiber orientation during processing, and takes into account effects such as flow-induced alignment and fiber to fiber interactions [57]. Despite its widespread use, the Folgar–Tucker model has a notable limitation as it tends to overpredict fiber orientation in certain scenarios [58]. Given the inherent complexity and stochastic nature of such models, and the significant challenge of validating them with experimental data, a more deliberate and simplified approach was chosen for this thesis.

In addition to orientation tensors, several other formulations have been proposed to quantify fiber orientation. Krenchel's orientation factor (α) is a 2D approach that relates the number of fibers in a cross section with the theoretically possible maximum number if all fibers were eligned perfectly equal relative to each other and homogeneously distributed [51]. Another broadly used formulation is Schönlin's orientation coefficient (η), which is based on the measured average out-of-plane angle (θ) among all visible fibers on a cross section [51]. The effective steel fiber reinforcement ratio ($\rho_{f,eff}$) combines these concepts and takes into account both the number of fibers and their measured out-of-plane angle. These parameters are used because the residual bending tensile strength can be directly related to both the orientation factor and the orientation angle [51].

In FRC elements, fibers are uniformly distributed and oriented in various directions, which means not all fibers align with the direction of the applied load. This variability in orientation affects the mechanical behavior of the composite material. Pullout response and bond-slip relations are sensitive to the fiber orientation [52]. Therefore, the pullout responses of fibers aligned with the load direction can be misleading for modeling the composite's tensile behavior [52]. Even so, it has been documented that fibers inclined at an angle between 0° and 20° show greater pull-out resistance compared to fully aligned fibers, while those at an angle greater than 30° have a great likelihood to be subjected to rupture and crumbling of the surrounding concrete matrix [59, 60]. The influence of fiber alignment on the bearing capacity of a singular fiber subjected to pullout is shown in Figure 2.4. The document states that the peak pullout load of an inclined fiber was found to be almost as high as that of an aligned one [52]. Moreover, the work required to completely remove an inclined fiber was higher than that of an aligned one [52]. Many modeling approaches also

focus on a unidirectional fiber alignment with an orientation angle of 0°, examples given in [37, 61], as it simplifies the problem and allows for a direct focus the pullout failure mechanism.

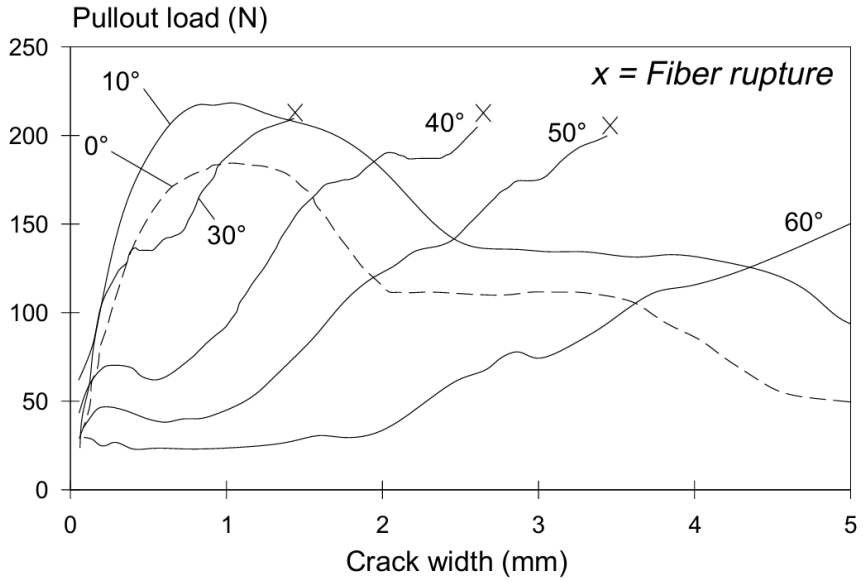

Figure 2.4: Pull-out load for different orientation angles of fibers [62].

For this research, a controlled, deterministic fiber arrangement with all fibers aligned parallel to the pullout axis (0° orientation) was adopted. This deliberate choice allowed the research to isolate the bond-slip law and the pull-out failure mechanism more directly, which is the primary focus of this work. Even though such simplification does not capture the full anisotropy of FRC, it provides a well-posed problem that is more suitable for the development and validation of an inverse analysis algorithm. The model's core structure and algorithm are designed to be extensible, and leave room for future implementation of more complex fiber orientation models. However, this would require significant experimental validation consisting of three-point bending of beams with fibers at known angular positions which also would be a challenge in itself, and developing the full procedure would be beyond the scope and budget of this research. Therefore, this is considered a key step for future work and model improvements.

Considering the complexity of an exact mathematical description of the fiber orientation and distribution, a different approach has been applied when taking into account that only the fibers that are directly crossing the crack path have an effect on adding to the crack initiation and crack propagation resistance, which significantly reduces the necessary complexity of the computer model of the fiber-reinforced concrete. With such an approach, the only position of the beam to have the fibers implemented is the position where the crack will be located during the simulation [63].

2.2.2.2 Modeling of the Bond-Slip Law

The bond-slip law represents the relation between the interfacial shear bond (the bonding stress) and the relative displacement (slip τ) at the interface between fibers and the surrounding concrete matrix. More simply put, The bond-slip law refers to the shear bond responsible for the load transfer parallel to the longitudinal axis of the reinforcement [64]. This relation is crucial for understanding how forces are transferred between reinforcement and concrete, as they impact the structural behavior of reinforced concrete elements [65]. Therefore, accurate modeling of the bond-slip law is essential for predicting the performance of reinforced concrete structures under various loading conditions [66].

The bond-slip law is typically modeled using constitutive laws that incorporate parameters such as fiber geometry, surface characteristics, concrete matrix properties, and interfacial friction. The impact of the bond-slip law on the mechanical properties of Fiber Reinforced Concrete (FRC) has been extensively investigated by Smolčić and Ožbolt [67], who used a meso-scale approach based on the microplane model to replicate experimental tests. A stochastic approach to model the bond-slip law and an adequate description of the force-displacement relation are applied by Kožar et al. [37]. Whereas more exact methods were used by Rukavina [15], whose model is developed using the finite elements method.

In terms of incorporating parameters into the model, it is important to note that the modulus of elasticity for individual fibers in FRC, particularly steel fibers, is not a standardized value in the same sense as the nominal $E \approx 200$ GPa commonly used for bulk steel. In a lot of the literature, what is reported is the effective modulus of the FRC composite rather than that of a single isolated fiber. For example, Kim et al. [68] reported that the effective modulus of steel-fiber-reinforced composites ranged between 45 and 55 GPa, which reflects the combined contributions of the fibers and the surrounding matrix. This effective modulus is a function of multiple parameters, including fiber material properties, aspect ratio, volume fraction, orientation, and interfacial bonding characteristics. Wang et al. [69] showed that complex micromechanical models can predict this composite modulus by accounting for these parameters in combination, instead of relying on a single inherent material property. Furthermore, empirical studies have shown that increases in fiber volume fraction and aspect ratio tend to modestly increase the composite's elastic modulus, which may also provide a partial explanation for observed size-effect correlations in FRC experimental results.

A notable approach of analytical modeling of FRC with solely deterministic parameters was developed by Parise, who created a comprehensive analytical model for full fiber pull-out [70]. This model was chosen as representative for its relatively simple formulation, completeness of its analytical solution, and good fit with experi-

mental data. What makes this model comprehensive in a deterministic context is its use of a functional relationship that captures the different phases of pull-out rather than a single value. The model is based on several simplifying hypotheses, such as a planar crack and negligible matrix deformation, and assumes a linear slip-hardening frictional bond where the interfacial shear stress at the tip of debonding zone (τ) is a function of fiber slip (S) and a non-dimensional hardening parameter (β) [70]. This allows the model to analytically describe the pull-out force-displacement relationship for both pre-debonding and post-debonding stages [70]. This approach was further extended to describe the behavior of hooked-end fibers, where the model integrates an energy approach to simulate the progressive straightening of the hook through the development of *plastic hinges* [70]. This deterministic model for hooked-end fibers produces a characteristic stepped force-displacement curve that successfully captures the main phases observed in experiments. This level of parameterization and breakdown of key complex phenomenon into a series of analytically solvable stages all within a deterministic framework, is a direct inspiration for the model developed in this thesis.

The influence of fiber geometry, such as half-hooked or hooked fibers, on pull-out behavior is significant and depends heavily on the embedment length [71]. For half-hooked fibers, the pullout performance can be superior to that of straight fibers at short embedment lengths. However, this effectiveness decreases with increasing length, and at very long embedment lengths, half-hooked fibers can rupture prematurely, which can result in lower pullout energy and equivalent bond strength compared to straight fibers. This shows that for mechanically anchored fibers, there is an optimal embedment length beyond which their effectiveness can diminish due to premature straightening or stress concentrations. This understanding of how embedment length and fiber geometry interact is important for developing FRC models, especially as the plastic deformation of the fibers is reflected on their pull-out behavior seen in relations such as load-displacement or load-slip. This elastic-plastic response can be simplified withing within a so-called *frictional pulley model*, where the input parameters are the mechanical and geometrical properties of the fibers and the concrete's ultimate strength, and which represent the pull-out force due to plastic deformation contribution of one, two, three or more plastic hinges [72].

By integrating the bond-slip law, and fiber orientation and distribution into a load-displacement curve approach, researchers can more accurately simulate the structural response of FRC elements under bending loads. This method involves developing constitutive models that account for the interfacial bond-slip behavior and the spatial distribution of fibers within the concrete matrix. For instance, Meng et al. [73] investigated the bond-slip constitutive relationship between basalt fiber-reinforced polymer bars and basalt fiber recycled-aggregate concrete. Through pullout tests, they derived bond stress-slip curves and established constitutive laws

that can be utilized in finite element modeling to predict load-displacement behavior. The load-displacement curve approach, which takes into consideration both the bond-slip mechanism and fiber orientation in 2D, provides a comprehensive framework for modeling the complex behavior of FRC elements. This methodology improves the accuracy of structural analyses and supports the optimization of FRC design for improved performance under various loading scenarios.

2.2.3 Comparison of Modeling Paradigms

When creating a numerical model that simulates the behavior of any structural element that is defined by its material parameters, it's important to properly define the scale on which the mechanism will be observed. Therefore, in engineering applications, macro-scale models are commonly employed for numerical modeling. Nevertheless, the use of meso-scale models offers a more detailed and insightful representation of concrete behavior, while micro-scale models provide detailed material parameter analysis. However, the immense heterogeneity of concrete presents a significant challenge to qualitatively describe with a numerical model on a micro-scale. This, in terms of FRC, is further compounded by the addition of fibers to the mixture. This increased heterogeneity makes modeling a composite even more challenging.

In previous research, two primary approaches have been taken to address this problem: applying an appropriate finite element model where the fibers are discretized and located along the edges of the finite elements [67], and using the fiber bundle model (FBM) for composite materials [74]. Both approaches assume that the material sample consists of extremely small elements, such as the concrete mixture and fibers, described by local properties, whose behavior during experiments can be described by the global response behavior of the concrete element.

As with these approaches, most computational models of fiber-reinforced cementitious composites, such as fiber-reinforced concrete, are based on:

1. formulation of the stress-strain behavior within the framework of homogenized continuum mechanics;
2. bridging stress-crack opening displacement of fibers (and the concrete matrix);
3. bond-slip behavior of fibers, where the concrete matrix and each fiber are modeled separately [75].

These three challenges can be seen as checklists when modeling FRC. A variety of modeling paradigms have been developed to tackle these challenges, each with distinct advantages and disadvantages, and applied approaches mostly depend on the researchers' goals and available tools.

2.2.3.1 Discrete and Semi-Discrete Models

Methods that take into account each individual fiber's interaction with the concrete matrix can be categorized as discrete modeling. This is most often seen in the Discrete Element Method (DEM) and Finite Element Method (FEM), where fibers are modeled as embedded elements or discrete entities with bond-slip relationships at the fiber-matrix interface. Caggiano et al. [76] developed a meso-scale model using DEM to simulate hybrid steel fiber-reinforced concrete, while Smolčić & Ožbolt [77] proposed a similar microplane-based meso-scale model to capture fiber-matrix bond-slip behavior. Finite element-based models, such as those by Soetens et al. [78] and Zhang et al. [79], also use embedded fiber elements to study flexural and fracture performance. This discrete approach was advanced by Huang et al. [43] who integrated meso and macro-scale models to analyze hooked-end steel fibers. Pros et al. [80] proposed a numerical strategy to account for individual fibers in their actual location and orientation within the concrete bulk. Congro et al. [81] developed a mesoscale approach with a novel finite element formulation, embedding fibers in cementitious matrix elements and considering fiber orientation, stiffness, and strength. This method allows for random fiber distribution without mesh dependency. Marcalikova & Sucharda [56] utilized a 3D computational model with a fracture-plastic material model, emphasizing the importance of determining input parameters and mechanical properties for accurate FRC modeling. Despite their accuracy in simulating crack bridging and stress transfer, these models face challenges in the form of computational costs, scalability limitations for large structures, and the need for precise calibration of bond-slip and fiber orientation parameters [82, 83].

Semi-discrete approaches can offer a relief to these issues by combining the ability to capture fiber-level parameters to a certain extent with methods borrowed from continuum models that are much more efficient. Here, fibers are represented as semi-discrete bodies within a continuum matrix, which allows for the simulation of fiber-concrete interactions without explicitly modeling every individual fiber. Cunha et al. [84] developed a semi-discrete model where steel fibers are represented as line elements embedded in a finite element mesh, which enables the simulation of crack bridging and stress transfer in FRC beams. This model was validated using experimental results, which proved its ability to accurately predict flexural behavior. Kang and Kim [85] proposed a semi-discrete framework that combines orientation tensors with discrete fiber representations to model the anisotropic behavior of FRC under bending loads. Their approach reduced computational costs while maintaining accuracy in predicting crack patterns and load-deflection responses. However, semi-discrete models face limitations in capturing localized effects, such as fiber clustering or complex crack patterns, due to the simplified representation of fiber-

matrix interactions [55]. Moreover, the calibration of semi-discrete models often requires extensive experimental data to accurately define fiber orientation and distribution parameters, which can be a significant drawback for practical applications [56]. Capturing the stochastic nature of fiber distribution and orientation remains a significant challenge, particularly for multiscale applications.

2.2.3.2 Continuum and Stochastic Models

In contrast to these methods, continuum modeling approaches treat fiber-reinforced concrete as a homogeneous material with effective properties that represent the average behavior of the composite, which also includes the fibers. These methods do not explicitly model individual fibers but instead use homogenized material properties to describe the overall response of the material. One common continuum approach is homogenization, where effective material properties are derived by averaging the contributions of fibers and the matrix at a macroscopic scale. For example, Zhan and Meschke [42] developed a multiscale homogenization framework to predict the mechanical behavior of FRC structures, starting from micro-scale fiber pullout and scaling up to macro-scale structural response. While continuum models are computationally efficient and suitable for large-scale structural analyses, they rely on simplifying assumptions about fiber orientation and distribution, which limits their capability in capturing localized parameters or complex failure mechanisms [55]. Despite these limitations, continuum modeling and homogenization of the material remains a widely used approach in FRC modeling practice.

Most widespread approach to mathematically include the fiber orientation and distribution effect into an FRC model is by introducing probability density function (PDF), like the von Mises-Fisher distribution for 3D orientations [86], the Watson distribution [87] etc. An example can be found in the work of Cunha et al. (2021) who employed a PDF to generate stochastic fiber orientations in meso-scale models, calibrated using X-ray computed tomography scan (CT)s. When it comes to modeling of fibers' spatial homogeneity/heterogeneity within the concrete matrix, a common method is by applying spatial statistics. In the work of Huang et al. [88], the authors proposed a statistics-based algorithm that combines orientation probability to angle the fibers at a certain angle, and spacing distance to distribute fibers within a given space. Stochastic models often generate fiber positions using various probability distribution functions. Soroushian and Lee [89] developed a stochastic model for fiber orientation that uses probability density functions to describe the random distribution of fibers in FRC in isotropic conditions. Stroeven [90] developed and experimentally validated a streological model for rigid fiber distribution that considers lengths of fibers in different directions. In various publications by Kožar et al. [46, 91, 92] the stochastic approach was applied to homogenize the

fiber-reinforced concrete composite, and utilized the fiber bundle model to describe the fiber distribution in the fiber-reinforced concrete using various statistical distributions. They also expended their models to include the dispersion of fibers in the matrix based on X-ray scans of FRC beams [37]. In contrast to methods of modeling fiber distribution in stochastic models, deterministic approaches include modeling virtual layers of the concrete flow during pouring and assuming fibers' alignment in those layers [93]. Many models, such as the one developed by Alberti et al. [94], combine probability methods in an inherently deterministic model to predict fiber orientation and distribution.

In empirical models, a so-called *orientation efficiency factor* is often used to model fiber orientation while simultaneously simplifying its effects using scalar factors. The orientation factor, denoted as λ, scales the contribution of fibers based on their alignment relative to principal stresses:

$$\lambda = \frac{1}{L} \sum_{i=1}^{N} l_i \cos^2 \theta_i, \tag{2.1}$$

where l_i is fibers' embedment length, θ_i is the angle between the fiber and the plane in which the cracking occurs, and L is fiber length.

Design codes incorporate orientation factors [95], as the post-cracking behavior of fiber-reinforced concrete (FRC) elements is highly dependent on fiber orientation [96], making these factors essential for structural design. These orientation factors are typically defined as the ratio between the performance of the designed structural element and that of a standard beam, since the actual material properties of the designed beam often differ from those of the standard specimens. However, current orientation factors used in design codes are often based on a limited number of research studies, which provide only partial insights into this complex phenomenon [64]. Furthermore, orientation prediction models based on orientation factors have so far not been established to connect orientation with mechanical properties of FRC due to complexity [97].

Alhassan et al. [63] pointed out how this presence of added fibers induces a bridging action across the crack in the fracture process zone at the front of the crack tip and complicates the fracture mechanics. However, in the domain of fracture mechanics and cases where applicable, modeling only the fibers that effectively contributing to carrying the load pose as a notable solution to the extreme heterogeneity and computational extensiveness issues [63].

Chapter 3

Motivation

Deterministic and analytical formulations of materials, such as the fiber-reinforced concrete, provide a clear and predictable understanding of the material's response under various conditions which is why they are preferred in engineering practices. The straightforwardness of deterministic models makes them simpler and easier to implement in engineering design and analysis practices without compromising precision and accuracy. On the other hand, this precisely defined relationship between input and output data when analyzing material behavior is something stochastic models lack by introducing randomness that may compromise and complicate prediction accuracy.

The motivation to develop and work with deterministic models also lies in their ease of validation and calibration by using experimental data in a lesser quantity than stochastic models require. As these models allow engineers to analyze how changes in input parameters directly impact the performance of concrete which is why many design codes and standards are based on deterministic principles.

Furthermore, a complement to deterministic forward analysis is inverse modeling, which offers a distinct advantage in understanding and optimizing the behavior of FRC through direct parameter identification. This is particularly relevant for FRC, where direct measurement of certain properties can be challenging or outright impossible. Through the use of inverse models based on deterministic formulations, essential parameters such as the ones defining the fiber-matrix bond and fiber orientation can be extracted, which is crucial for understanding and optimizing FRC behavior under various conditions.

This characteristic has historically limited their usage for inverse analysis for complex materials like FRC, as real-world experimental results invariably exhibit scatter and variability. Due to the complex and time-consuming nature of deterministic forward models for fiber-reinforced concrete, coupled with this perceived inability to handle experimental variability, their application in inverse analysis has

not yet been fully realized. This need for a deterministic predictive model that is both simplified enough for an efficient inverse analysis and robust enough to produce accurate parameter extraction results despite experimental data variability presents a gap in literature and serves as the direct motivation for this research.

3.1 Hypothesis

The hypothesis for this thesis is as follows:

1. A simplified and analytical computational model of fiber-reinforced concrete, where both the concrete and the fibers are formulated with optimized deterministic expressions, devoid of any random variables and processes, as developed by Parise [70], and brought into relation within equilibrium equations as was established by Kožar in multiple works, should be able to successfully replicate three-point bending test results.

2. Such a forward model, featuring precise yet simplified expressions, can serve as the foundation for an inverse model. These optimized formulations, already validated by numerous researchers for their accuracy in predicting FRC behavior, are expected to quicken the iterative computation process in the inverse analysis. This approach could effectively address the issue of excessive time consumption that poses as one of the main issues why such models are not yet established.

3. While deterministic models don't account for experimental data's inherent variations, a well-posed, robust, and simplified deterministic model can effectively compensate for this during the inverse analysis. This means that such a model will be capable of adequately extracting necessary material parameters even when dealing with the inherent variability present in measured experimental results. This compensation will be further achieved by comprehensively analyzing parameter sensitivity and interdependencies, which will assist in interpreting and validating the extracted parameters against real-world, variable data.

3.2 Research Goals

Considering this, the research goals for this thesis are the following:

1. Develop and validate a computational model that replicates three-point bending tests of fiber-reinforced concrete beams. This model will as input values

have precisely defined both load-displacement laws of fibers and the concrete matrix. Once validated, the model will be used as a basis for developing the inverse model.

2. Develop and validate the inverse model using the Levenberg-Marquardt algorithm, the previously established forward model and crack mouth opening displacement data obtained from laboratory testing.

3. Utilize the inverse analysis process to perform a parametric analysis of the fiber reinforced concrete beams subjected to three-point bending.

Chapter 4

Methodology

Determination of the pull-out behavior of fibers and failure mechanism of FRC in bending was done by subjecting beams to three-point bending as well as single fibers to pull-out tests. Initial findings of these results were already presented in previous works, more recently published in [98], and this thesis extends that work by applying the experimental results more comprehensively in the later chapters focused on the inverse analysis.

The computational framework in this thesis primarily relies on Wolfram Mathematica, which was used to implement the new deterministic forward model algorithm, solve the non-linear system of equilibrium equations, and execute the iterative Levenberg-Marquardt inverse analysis. Data processing, calculation of statistical metrics, and visual representation of results were performed using a combination of MS Excel and integrated functions within the Mathematica environment.

4.1 Material properties

All testing samples were made using the same type of self-compacting concrete (SCC) to eliminate the need for mechanical vibration, which in practice disrupts fiber orientation and distribution. The SCC mixture was specifically designed to achieve optimal flowability while maintaining adequate segregation resistance, which allows the concrete to thoroughly coat the positioned fibers without the need for mechanical vibration. This eliminated the risk of unintentionally altering the fibers' predetermined location and orientation.

The recipe of the SCC mixture is detailed in Table 4.1 that also outlines the quantity and density of each constituent material required for one cubic meter (1 m^3) of fresh concrete. The mixture was formulated to comply with the EN 206-9:2010 standard for self-compacting concrete [99].

Table 4.1: Recipe for Self-Compacting Concrete Mixture for a 1.0 m^3 Reference Volume

Component	**Mass (kg)**	**Density (g/cm^3)**
Cement 42,5 R	500.0	2.96
Sand 0 - 4 mm	1091.9	2.74
Aggregate 4 - 8 mm	468.0	2.74
Water at room temperature	225.0	1
Superplasticizer 2.5% mc	10.0	1.04
viscosity modifying agent (VMA) (0.44%)	2.2	1.01

The fresh state characteristics of the SCC mixture were evaluated through standardized testing ([100],[101],[102], [103]). This was crucial to make sure the SCC possessed the necessary properties for proper embedment and consistent distribution of the precisely placed fibers, which is fundamental to controlling the experimental variables in this study. The results of these tests, presented in Tables 4.2, 4.3, and 4.4, confirmed the desired workability and density of the fresh concrete.

Specifically, the mean density of the fresh SCC was measured as 2.305 kg/dm^3 (Table 4.2). The slump flow test resulted with a flow time (T_{500}) of 4.0 s and a maximum spread diameter (D_{max}) of 685 mm (Table 4.3), which indicated high flowability. This high flowability was necessary for the concrete to effortlessly flow around and encapsulate the fibers within the molds, preventing voids and ensuring optimal bond development between the fibers and concrete mixture. Furthermore, the V-funnel flow time (t_v) was recorded as 4.4 s (Table 4.3), which indicated adequate viscosity for self-compaction without segregation. This ensures the stability of the mixture and prevents the fibers from floating freely and not maintaining their pre-determined positions. The L-box test, done in accordance with the testing standard [104], resulted in an average height ratio (H_2/H_1) that demonstrated good passing ability through obstacles, with average heights of 9.50 mm after the first set of bars and 8.97 mm after the second, which resulted in blocking ratio of 0.94 (Table 4.4). The results of the fresh state tests confirmed the stability and flowability required to maintain the precisely placed fibers and ensure a uniform mix without segregation.

Table 4.2: Fresh concrete density measurement results

Volume (dm^3)	**Mass (kg)**	**Density (kg/dm^3)**	**Mean Density (kg/dm^3)**
5.000	11.290	2.258	
5.299	12.440	2.348	2.305
5.299	12.240	2.310	

Table 4.3: Slump flow test results (EN 12350-5)

Parameter	**Symbol**	**Value**
Flow time	T500	4.0 s
Maximum spread diameter	D_{max}	685 mm
Measurement 1	d_1	700 mm
Measurement 2	d_2	670 mm
V-funnel time	t_v	4.4 s

Table 4.4: L-box test results (EN 12350-10)

Measurement	**Height (mm)**	**Average height (mm)**
H11	9.0	
H12	9.4	0.95
H13	10.1	
H21	8.8	
H22	9.0	0.90
H23	9.1	

The characteristics of the steel fibers used in all tests are summarized in Table 4.5 [105]. These were DE 30/0,55 N steel fibers specifically chosen for their dimensions and mechanical anchorage. A visual representation of a single fiber is provided in Figure 4.1.

Table 4.5: Properties of DE 30/0,55 N steel fibers used in testing

Property	**Value/Description**
Type	DE 30/0,55 N steel fibers
Shape of ends	Hooked
Cross-section	Round
Diameter (d)	0.55 mm ($\pm$ 10%)
Length (l)	30 mm ($\pm$ 10%)

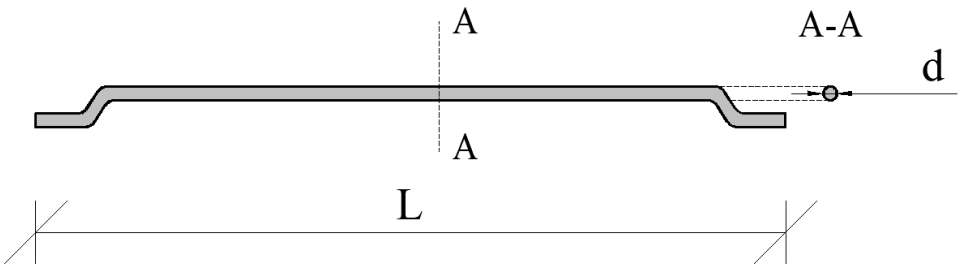

Figure 4.1: Fiber type used in laboratory testing [105]

Fibers with two distinct surface conditions were used - coarse and smooth. While a comprehensive comparative analysis of the influence of this on bond behavior is beyond the primary scope of this study, their inclusion in the testing program allows for the characterization of a broader range of bond-slip responses and provides data for potential future investigations into fiber surface engineering.

4.1.1 Specimen Naming Convention

In order to maintain clarity, consistency and transparency of identification of experimentally obtained data throughout this thesis, a systematic naming convention was done for all test specimens.

Every specimen was assigned a unique identifier based on the testing type, dimensions (for beam specimens), fiber type, and the consecutive sample number. This labeling system helped easy referencing and comparison of results between different experimental conditions, and is used throughout this whole thesis.

The convention for specimens subjected to three-point bending tests follows the format `[Size Code]-[Fiber Type Code]-[Sample Number]`.

- Size Codes:
  - S: Small-sized beams ($40 \times 40 \times 160$ mm)
  - M: Medium-sized beams ($70 \times 70 \times 280$ mm)
  - L: Large-sized beams ($100 \times 100 \times 400$ mm)
- Fiber Type Codes:
  - P: Plain concrete (without fibers)
  - CF: Fiber-reinforced concrete with coarse surface steel fibers
  - SF: Fiber-reinforced concrete with smooth surface steel fibers

- Sample Number: The unique numerical identifier assigned to each individual specimen (e.g., L-SF-1, L-SF-2, L-SF-3, L-SF-4).

For example, a large-sized beam specimen with smooth surface fibers would be identified as L-SF-X (e.g., L-SF-1), while a small plain concrete beam would be S-P-X (e.g., S-P-1).

For specimens subjected to single fiber pull-out tests, the identifier follows the format `SFP-[Fiber Typ Code]-[Sample Number]`.

- SFP: Single fiber pull-out test indicator.
- Fiber Type Codes:
  - CF: Coarse surface fibers
  - SF: Smooth surface fibers
- Sample Number: The number corresponding to the order of testing (e.g., SFP-CF-1, SFP-SF-1).

With this labeling system, it was ensured that all presented experimental data can be linked to its specific test conditions and individual specimen.

4.2 Compressive Strength Tests

In order to get an insight into the mechanical properties of the self-compacting concrete (SCC) used in this study, compressive strength tests were performed. These tests are important for understanding the concrete matrix's load bearing capacity because it's baseline data on both material's stiffness and strength. This characterization is taken into account when modeling the concrete's contribution to the overall behavior of the composite. Prior to testing all machines were carefully calibrated and tests were performed in accordance with the EN ISO 7500-1:2018 norm [106].

A total of one 130 × 300mm cylindrical and four 150 × 150 × 150mm cubic specimens were prepared using the same SCC mixture described in Section 4.1. All specimens were cast and cured in accordance with the EN 12390-2:2019 norm [107]. The four cubic specimens were designated as the primary data source for concrete characterization due to laboratory standardization, while the single cylindrical specimen was prepared for a simple comparative analysis purpose to provide a direct conversion reference ($\mathbf{f}_{c,cyl} = 0.8 \cdot \mathbf{f}_{c,cube}$) in accordance with the testing norm. The tests were conducted on a universal testing machine, specifically configured for uniaxial compression. All specimens were loaded continuously at a constant loading rate of 0.6 MPa/s until failure. The maximum load attained by each specimen was recorded.

Obtained results for the cubic specimens are summarized in Table 4.6.

Table 4.6: Compressive strength and density results for 150×150×150 mm cubic specimens at 28 days

Cube ID	**Area (mm^2)**	**Force (kN)**	**Compressive Strength (MPa)**	**Density (kg/m^3)**
1	22290.10	1180.40	52.96	2338.9
2	22514.90	1313.80	58.35	2334.7
3	22604.90	1315.00	58.17	2312.3
4	22665.10	1186.80	52.36	2336.8
Mean Value	–	–	**55.46**	**2330.7**

The average compressive strength for the cubic specimens at 28 days was determined to be 55.46 MPa, while the cylindrical specimen showed a compressive strength of 49.91 MPa. These values were determined to be expected values of compressive strength for the SCC mixture, and served as a baseline for characterization of the concrete matrix, as well as essential for the subsequent numerical modeling of FRC.

Once the foundational material properties established, the focus shifted to evaluating the mechanical behavior of the concrete, through three-point bending tests and single fiber pull-out tests.

4.3 Three-Point Bending Tests

TPBT on notched beams were conducted as the primary experimental method to evaluate the flexural and fracture behavior of FRC beams. These tests directly assess the material's ability to resist crack propagation and carry load in the post-cracked phase, and provide the force-displacement and CMOD data for developing and validating the proposed numerical model.

All beams were subjected to displacement-controlled loading at a rate of 0.06 mm/min until failure. The displacement controlled method was chosen to capture any post-peak softening behavior. This procedure followed the standard for determining the flexural strength of hardened concrete specimens [108]. The recorded values during the testing included vertical displacement, crack mouth opening displacement (CMOD), and the applied force. Vertical displacement was measured by a LVDT integrated into the testing machine's crosshead, while the CMOD was measured using a manually affixed LVDT alongside the notch edge with an auxiliary plate, as seen in Figure 4.2. Results obtained from TPBT of beams are presented in Section 4.5.1.

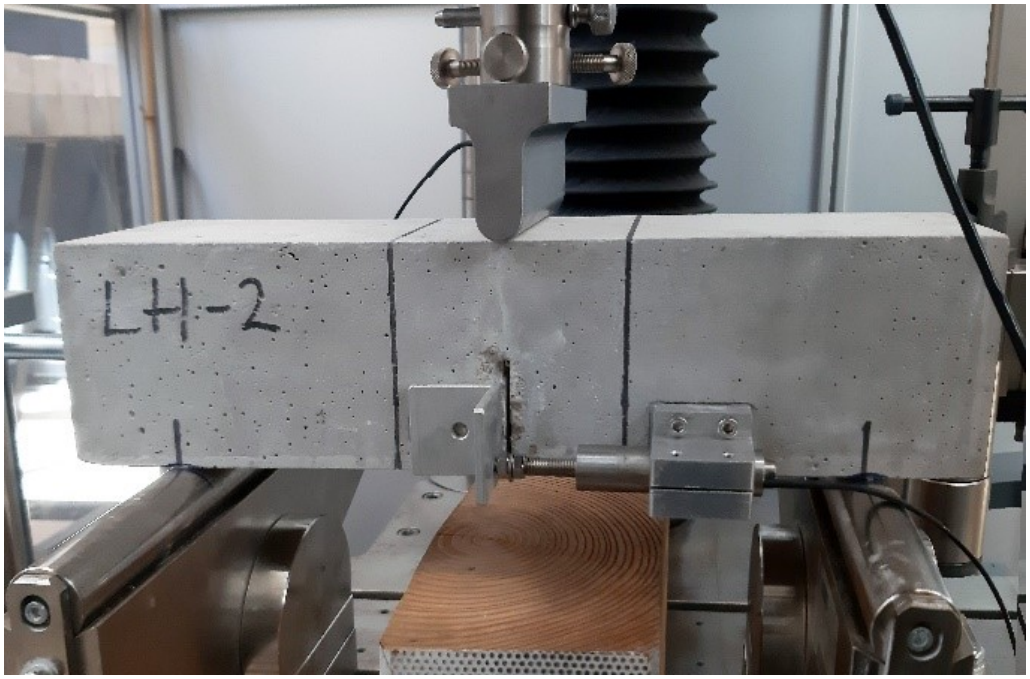

Figure 4.2: TPBT setup on an L-sized beam

4.3.1 Specimen Preparation

Specimens of three different sizes were prepared: $40 \times 40 \times 160$mm (referred to as small-sized beams), $70 \times 70 \times 280$mm (medium-sized beams), and $100 \times 100 \times 400$mm (large-sized beams). This range was chosen to enable the investigation of potential size effects. For each size, four plain concrete beams (without fibers), four beams with coarse surface fibers, and four beams with smooth surface fibers were initially prepared. This amounted to a total of 12 plain concrete beams and 35 fiber-reinforced beams. However, one small-sized beam was damaged during the demolding process, which resulted in a final total of 47 beams subjected to three-point bending tests.

Typically, in the preparation of FRC mixtures, fibers are added during the mixing of wet ingredients, which leads to their homogeneous yet random distribution within the matrix. To eliminate the inherent uncertainty associated with random fiber location and orientation, which is a significant challenge in understanding and modeling FRC fracture behavior, all fibers in this study were embedded at predetermined positions within the beam. This was achieved by fixing the fibers to a narrow, ruler-like element, which was then placed in the molds prior to pouring the concrete, a technique previously established in research such as that by Grbac [109].

Figure 4.3: Fibers positioned in the mold before concrete pouring

The ruler-like element consisted of two parts that clamped the fibers in place. Shallow indexing dents on both clamping edges ensured the precise in-plane spacing and angular alignment of each fiber, while a small amount of water-soluble adhesive prevented fibers from slipping during casting. The element was positioned perpendicularly to the mold, as shown in Figure 4.3, and held by simple supports. The number of fibers crossing the midspan was scaled based on the beam size: large beams contained 9 fibers, medium beams contained 6 fibers, and small beams contained 3 fibers. Fibers were placed at the midspan of the beam, crossing the expected crack plane, and vertically located at approximately 2/10 of the cross-section height from the tension face (20 mm for large beams, 10 mm for medium beams, and 5 mm for small beams). This placement ensured that after cracking, the embedded length of each fiber in either half of the concrete beam was equal to half of its total length, as illustrated conceptually in Figure 4.4.

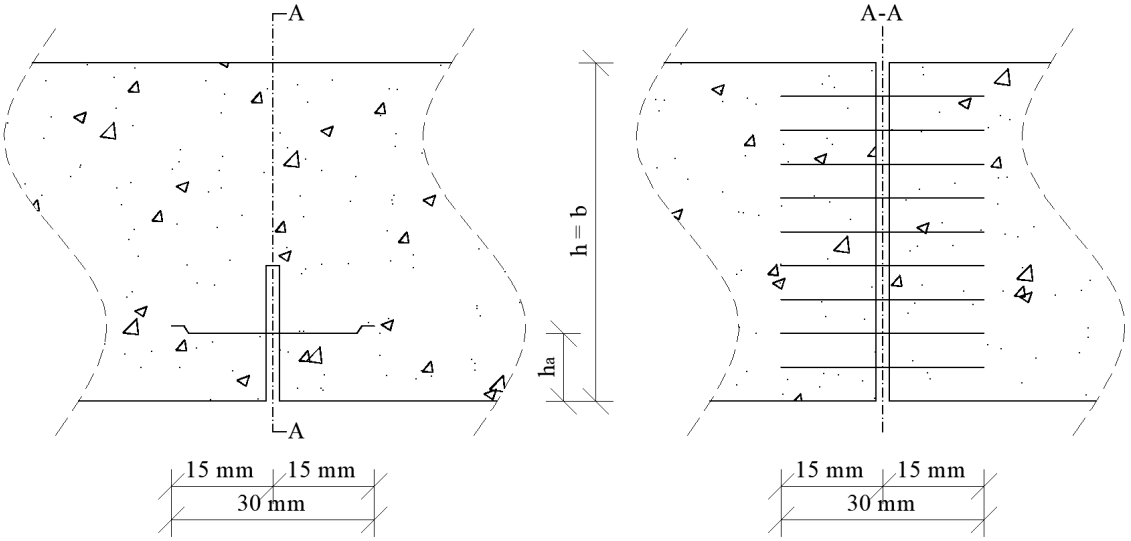

Figure 4.4: Fiber embedment scheme on L-sized beams: (Left) Cross-section showing the vertical fiber position (h_a) and notch depth. (Right) Plan view illustrating the uniform spacing and embedment length across the crack plane.

Once the concrete hardened (after a minimum of 28 days),the auxiliary element securing the fiber position was removed. As the element was made of an easily destructible soft plastic and thoroughly greased before immersion in the concrete mixture, its removal was done by controlled breaking and pulling which produced a rectangular notch with fibers arranged in a straight line at known positions. The notch dictated the crack location and orientation, which provided a deterministic crack path and a controlled number of load-bearing fibers crossing the fracture plane. This choice is central to the thesis hypothesis so that by fixing the fiber count, orientation (0° relative to the pull-out axis), spacing, and embedment lengths, the post-cracking response becomes a direct function of explicitly modeled parameters (matrix law and fiber pull-out law), which is a necessary precondition for the intended inverse analysis. The exampled outcomes of this controlled placement for all three specimen sizes is visually shown in Figure 4.5.

(a) Large beam after failure (9 fibers)

(b) Medium beam after failure (6 fibers)

(c) Small beam after failure (3 fibers)

Figure 4.5: Visual confirmation of deterministic fiber placement in the notch after three-point bending testing of beams.

The TPBT configuration with a notch and deliberately embedded, aligned fibers removes two dominant sources of stochasticity in FRC: the randomly positioned crack plane, and the random fiber orientation at the crack. Because of this, the recorded force–CMOD and force–displacement curves can be interpreted as the response of a system where the concrete matrix law and the fiber pull-out law are the only governing mechanisms.

4.4 Single fiber pullout tests

Single fiber pull-out tests were conducted as a fundamental micro-scale investigation method for quantifying the bond-slip relation between the steel fibers and the concrete matrix. Understanding this relationship is important because it directly governs the crack-bridging efficiency of the fibers and the post-cracking behavior and overall toughness of the beams, observed in three-point bending tests [37]. Determining this interface property is crucial input for developing a deterministic numerical model that realistically represents fiber action.

Eight specimens made of the same self-compacting concrete used for three-point bending tests, with dimensions $40 \times 40 \times 40$mm were tested. The steel fibers tested in this study were the same type of fibers described earlier in section 4.1. The fibers were manually embedded to half their length of 15mm in the geometric center of each concrete specimen using a custom alignment jig, as seen in Figure 4.6. Five specimens were prepared with coarse surface fibers and four with smooth surface fibers. The concrete was poured in one layer, without vibrating and the specimens were cured and treated as instructed by the EN 12390-2:2019 norm [110].

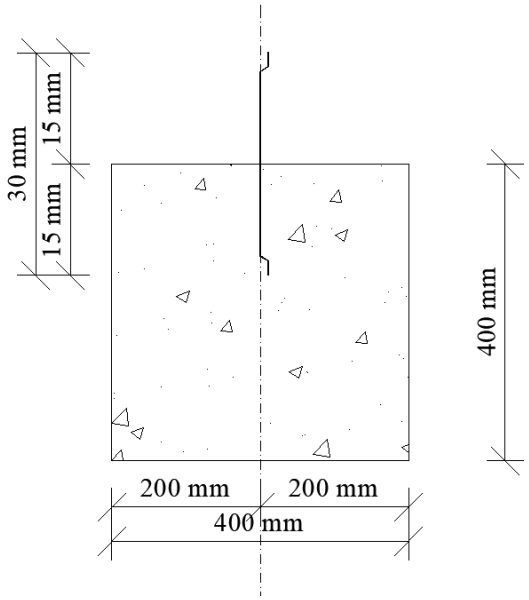

(a) Schematic cross-section showing fiber embedment geometry.

(b) Example specimen with the fiber exposed for testing.

Figure 4.6: Preparation of single fiber pull-out test specimens. (a) Systematic representation of the fiber embedded to half its length in the geometric center. (b) Example of a prepared specimen prior to testing.

The pullout tests were conducted using an electromechanical fiber pull-out machine compliant with the testing standard EN ISO 7500-1:2018 for static uniaxial testing machines. The machine was equipped with a custom gripping mechanism designed to clamp the exposed fiber end without inducing premature slippage or damage. To ensure axial alignment between the fiber and the loading axis, the concrete prism was secured in a steel fixture bolted to the machine's base, shown in Figure 4.7.

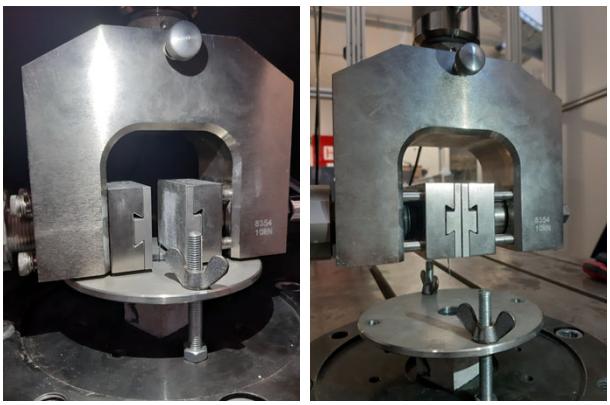

Figure 4.7: Single fiber pullout setup. Left) Prior to fiber pull-out; Right) After the fiber pull-out

All pull-out tests were performed in a displacement controlled environment, with the displacement rate was set to 0.5 mm/min, as prescribed by the standard for fiber pullout testing [111]. Data recorded during the tests were the pullout force (via the load cell) and displacement (via the linear variable differential transformer) at a sampling frequency of 50 Hz. Each test was performed until the fiber was fully extracted from the prism. After each test, the prism and extracted fiber were visually inspected to classify the failure mode, which showed that all testing samples exhibited complete fiber pullout. Results obtained from single fiber pull-out tests are presented in Section 4.5.2.

These tests provided a direct, micro-scale characterization of the bond–slip law under a strictly controlled geometry with fixed fiber type, controlled embedment length, axial alignment, and identical SCC matrix as in TPBT. Because the tests were displacement-controlled and all specimens exhibited full pull-out, the resulting force–slip curves can be used either to parameterize an analytical pull-out law with hardening stage) or to validate the inverse identification performed from TPBT data.

4.5 Results

The dispersion and differences in results are due to imperfections in the specimen production and accuracy of the testing machines.

Table 4.7: Summary of Laboratory Test Samples

Test Type	**Prism Size**	**Fibers/ Sample**	**Fiber Type**	**Samples**
Three-point bending	L (100×100 ×400)	9	No fiber	4
		9	Coarse	4
		9	Smooth	4
	M (70×70 ×280)	6	No fiber	4
		6	Coarse	4
		6	Smooth	4
	S (40×40 ×160)	3	No fiber	4
		3	Coarse	4
		3	Smooth	4
Fiber pullout	40×40 ×40	–	Smooth	4
		–	Coarse	4

4.5.1 Three-point bending test results

4.5.1.1 Large sized beams

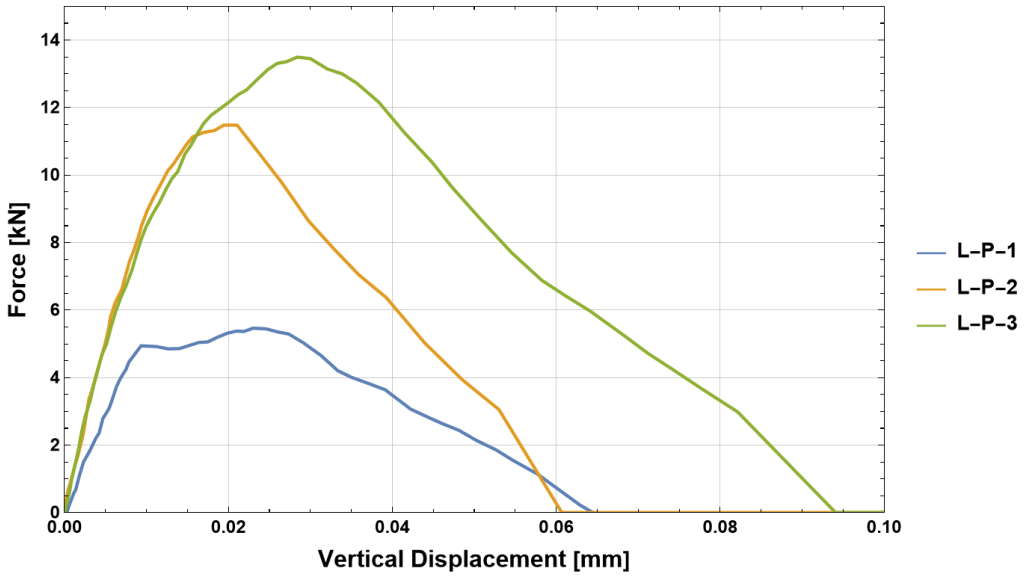

Figure 4.8: Force-Vertical Displacement curves obtained from three-point bending tests on large-sized plain concrete beams

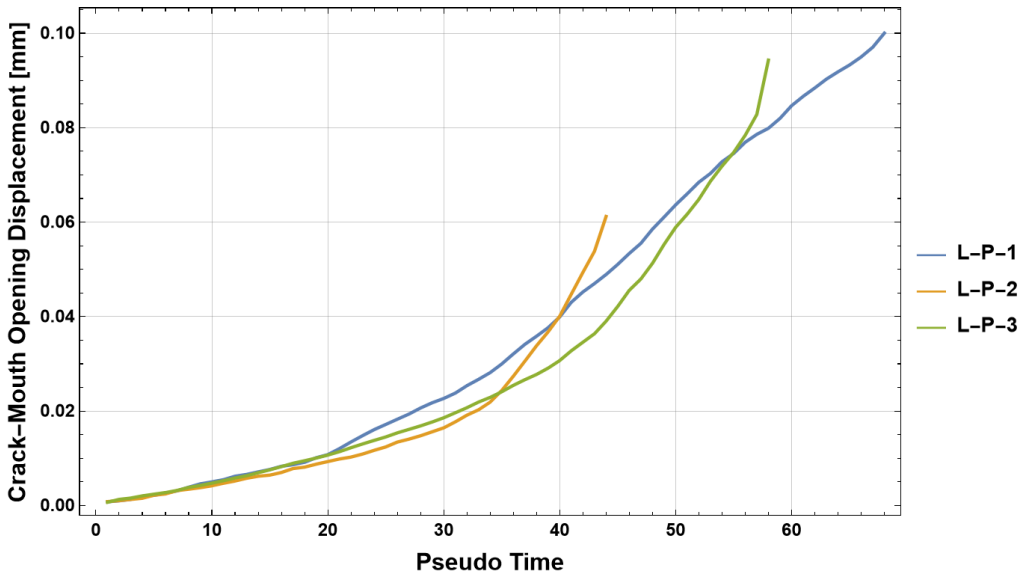

Figure 4.9: Crack Mouth Opening Displacement-Pseudo Time curves obtained from three-point bending tests on large-sized plain concrete beams

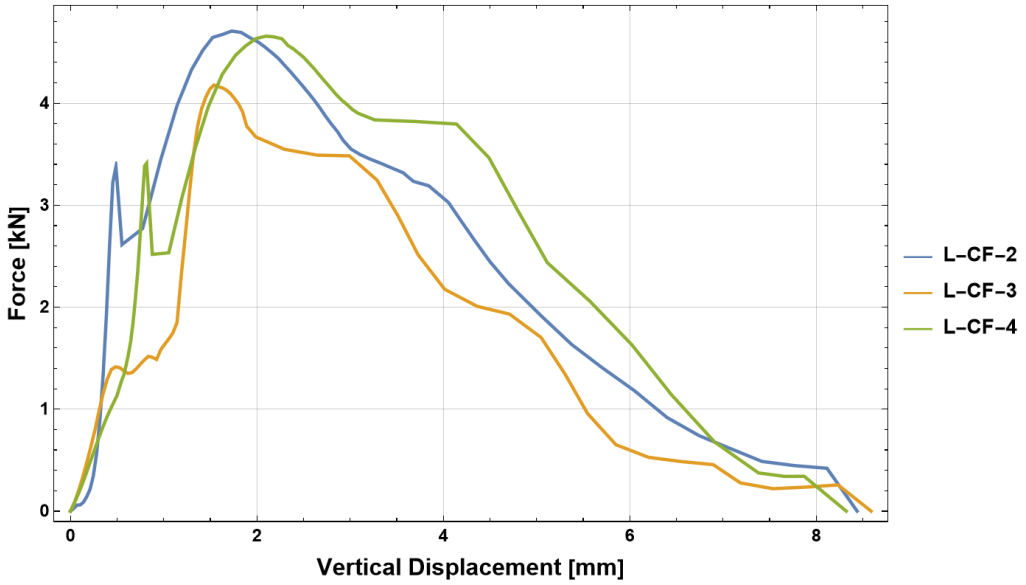

Figure 4.10: Force-Vertical Displacement curves obtained from three-point bending tests on large-sized concrete beams with coarse fibers

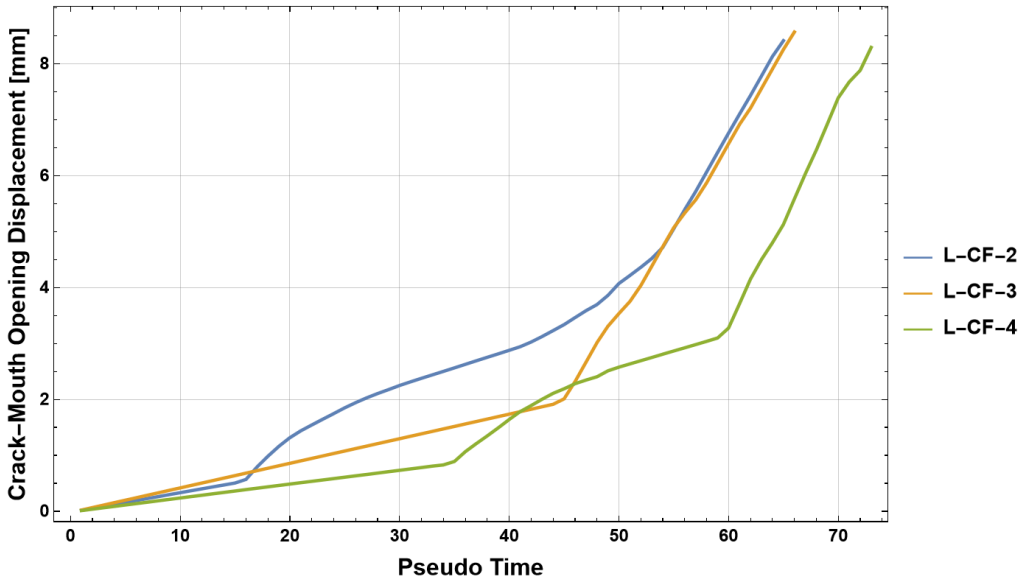

Figure 4.11: Crack Mouth Opening Displacement-Pseudo Time curves obtained from three-point bending tests on large-sized concrete beams with coarse fibers

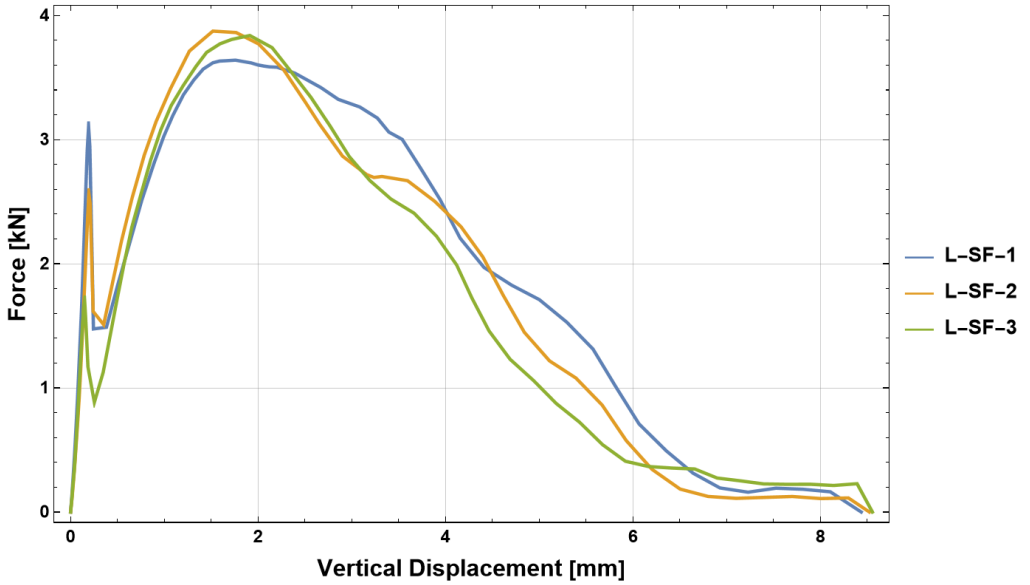

Figure 4.12: Force-Vertical Displacement curves obtained from three-point bending tests on large-sized concrete beams with smooth fibers

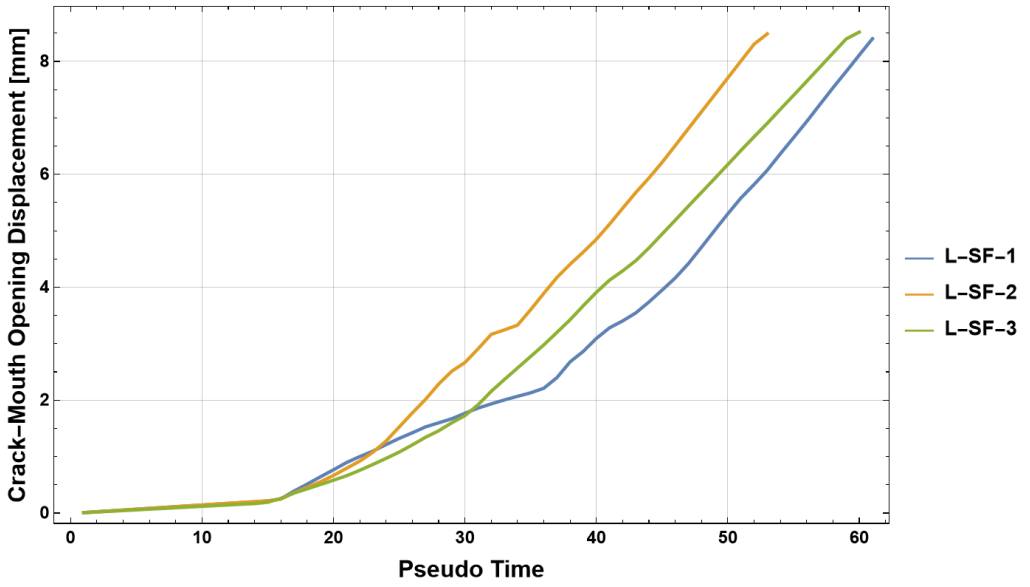

Figure 4.13: Crack Mouth Opening Displacement-Pseudo Time curves obtained from three-point bending tests on large-sized concrete beams with smooth fibers

4.5.1.2 Medium sized beams

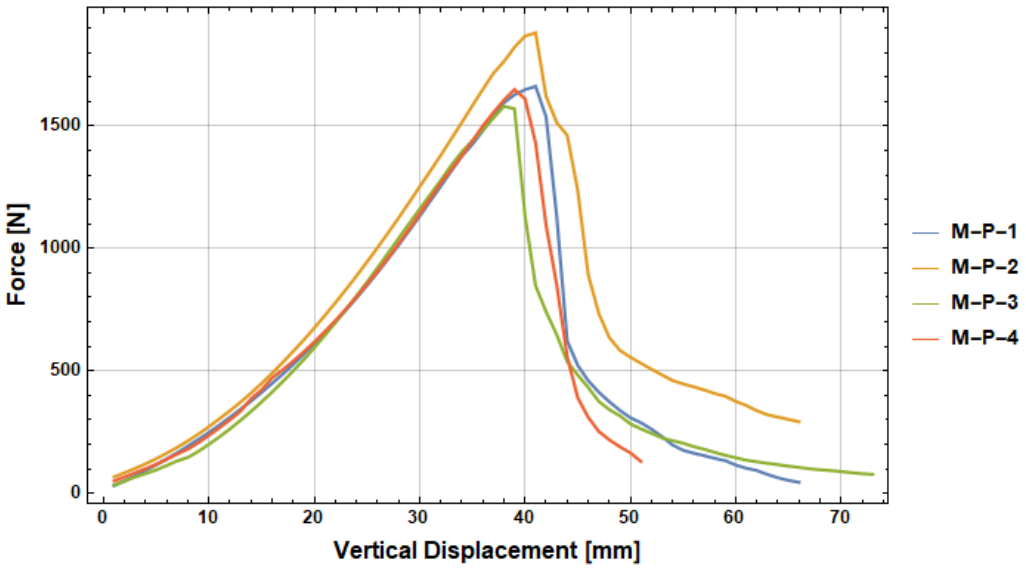

Figure 4.14: Force-Vertical Displacement curves obtained from three-point bending tests on medium-sized plain concrete beams

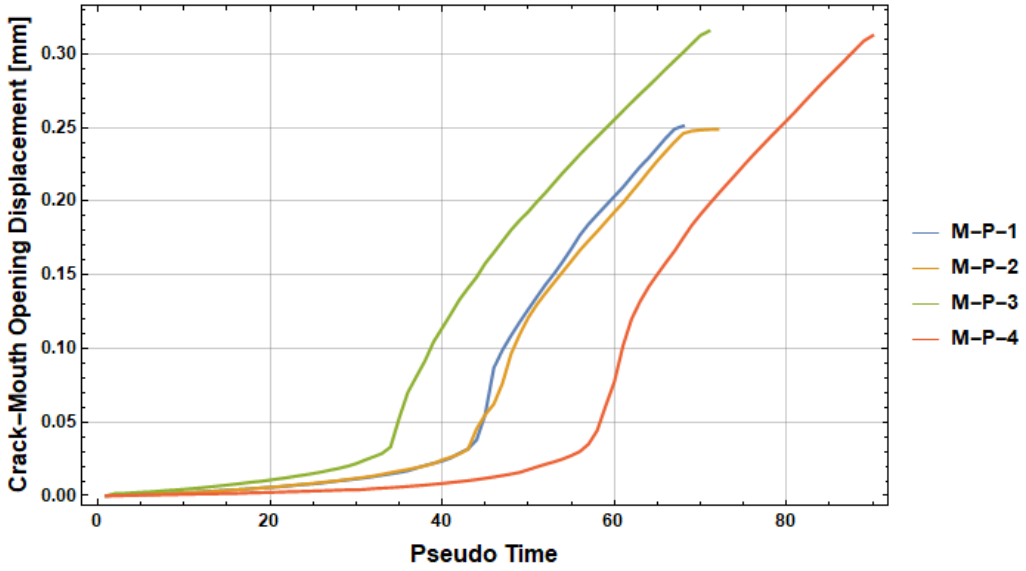

Figure 4.15: Crack Mouth Opening Displacement-Pseudo Time curves obtained from three-point bending tests on medium-sized plain concrete beams

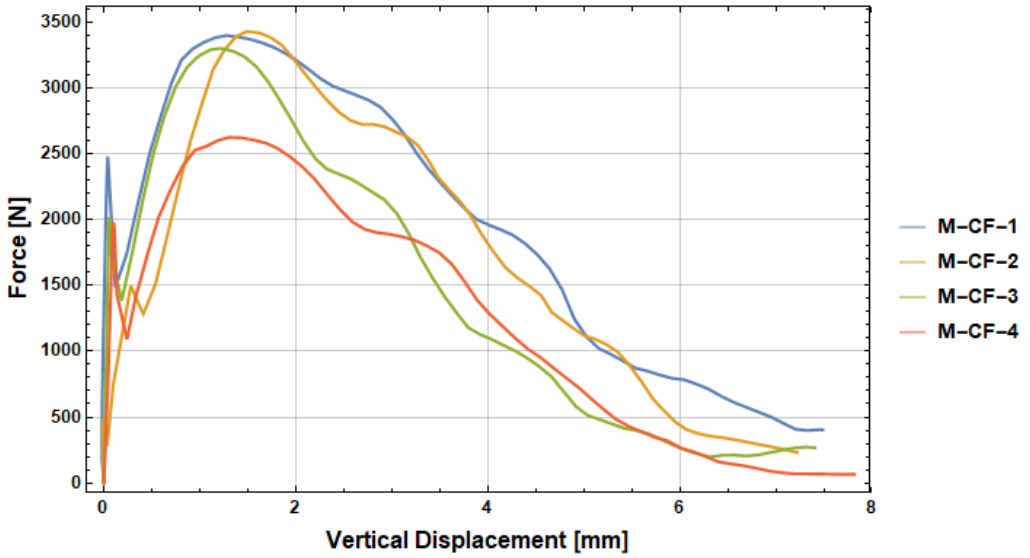

Figure 4.16: Force-Vertical Displacement curves obtained from three-point bending tests on medium-sized beams with coarse fibers

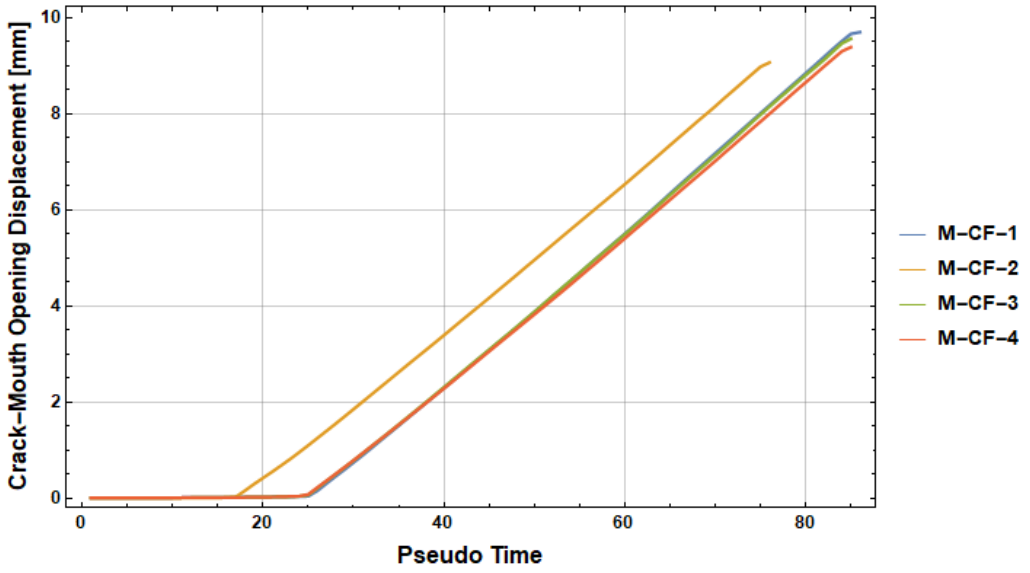

Figure 4.17: Crack Mouth Opening Displacement-Pseudo Time curves obtained from three-point bending tests on medium-sized beams with coarse fibers

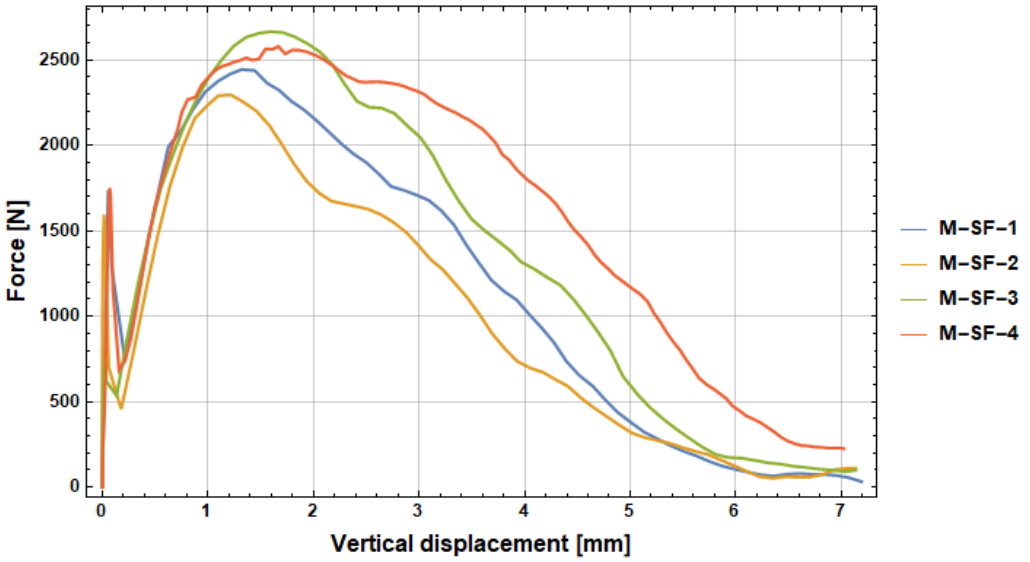

Figure 4.18: Force-Vertical Displacement curves obtained from three-point bending tests on medium-sized beams with smooth fibers

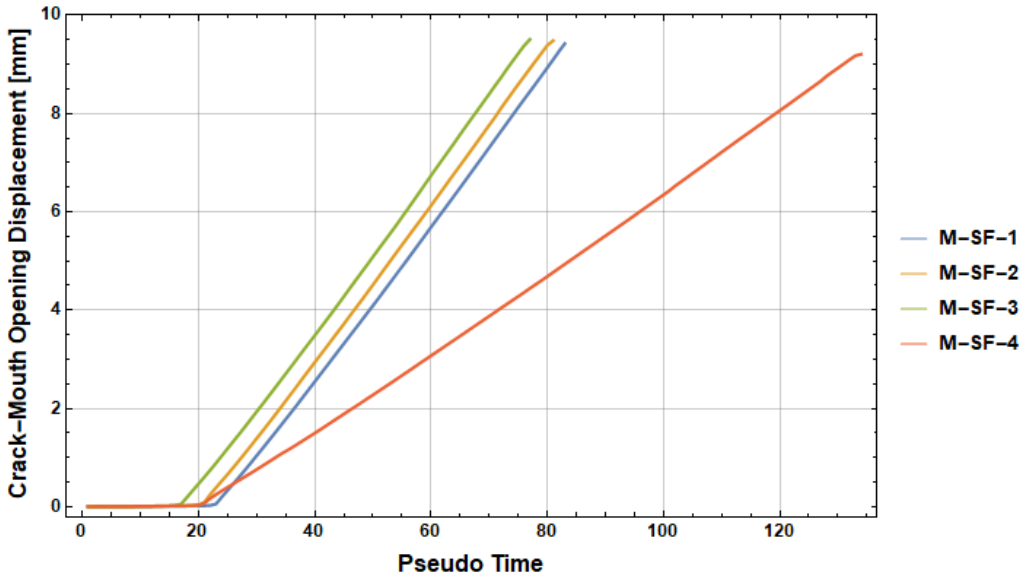

Figure 4.19: Crack Mouth Opening Displacement-Pseudo Time curves obtained from three-point bending tests on medium-sized beams with smooth fibers

4.5.1.3 Small sized beams

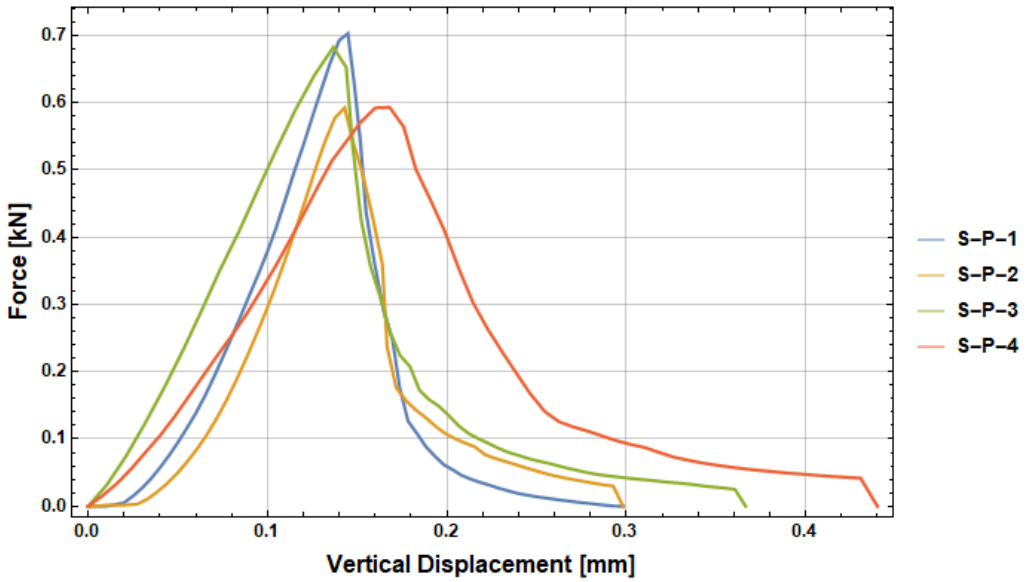

Figure 4.20: Force-Vertical Displacement curves obtained from three-point bending tests on small-sized plain concrete beams

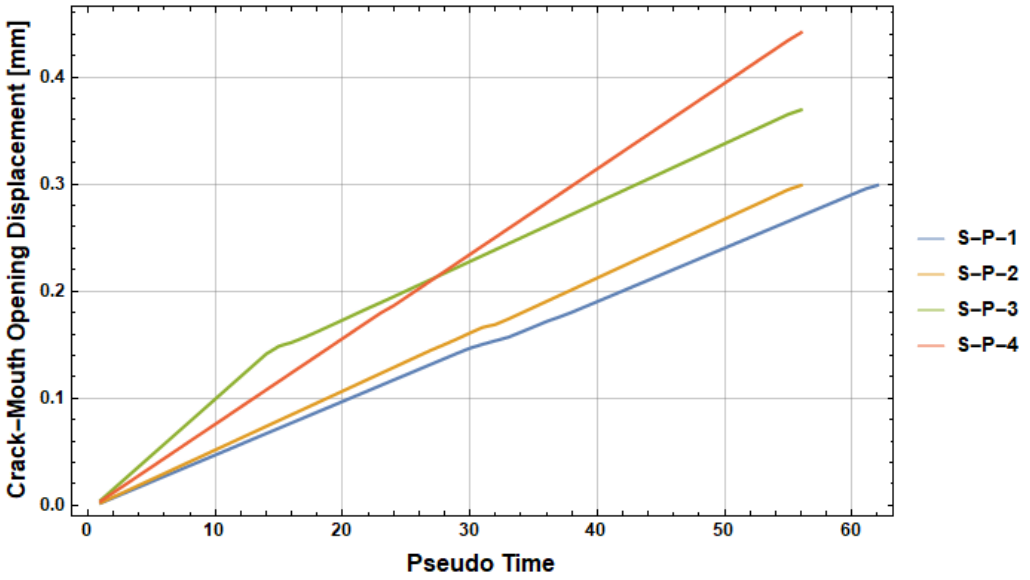

Figure 4.21: Crack Mouth Opening Displacement-Pseudo Time curves obtained from three-point bending tests on small-sized plain concrete beams

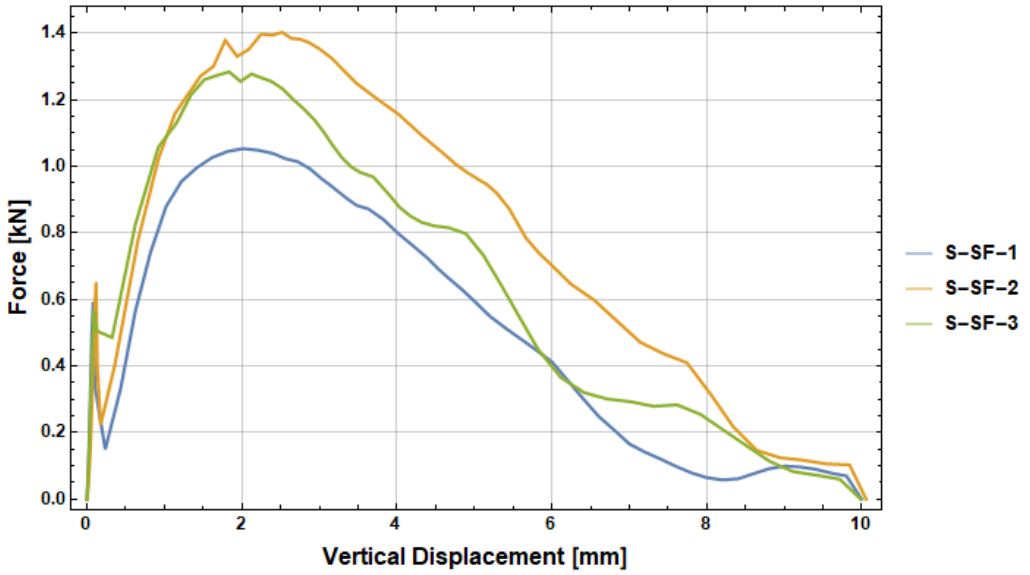

Figure 4.22: Force-Vertical Displacement curves obtained from three-point bending tests on small-sized beams with smooth fibers

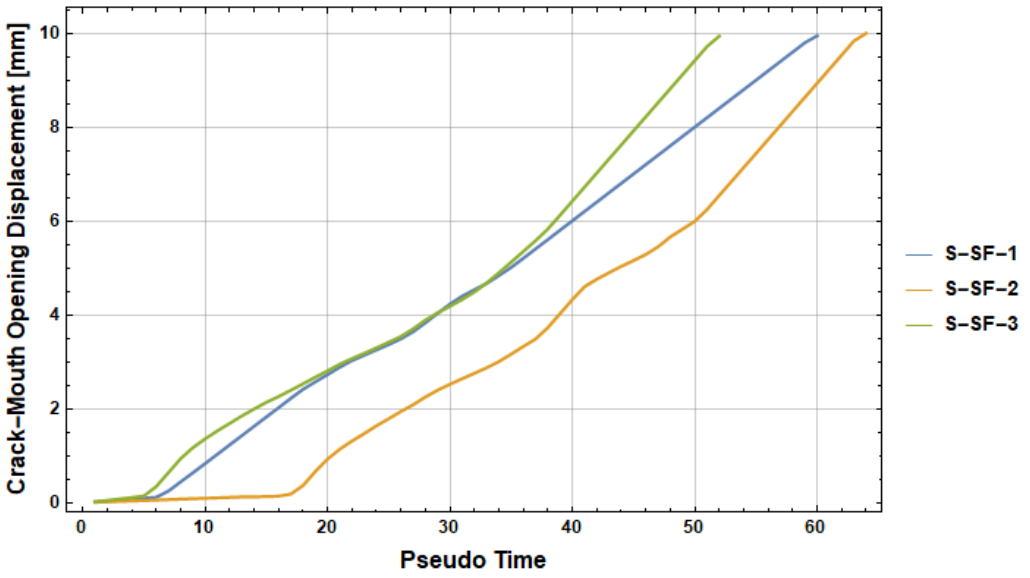

Figure 4.23: Crack Mouth Opening Displacement-Pseudo Time curves obtained from three-point bending tests on small-sized beams with smooth fibers

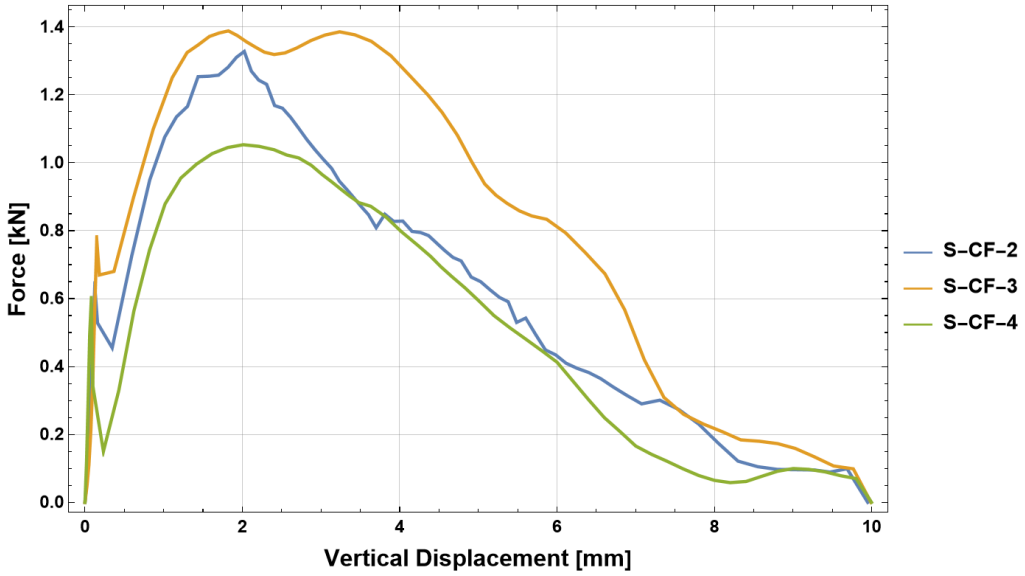

Figure 4.24: Force-Vertical Displacement curves obtained from three-point bending tests on small-sized beams with coarse fibers

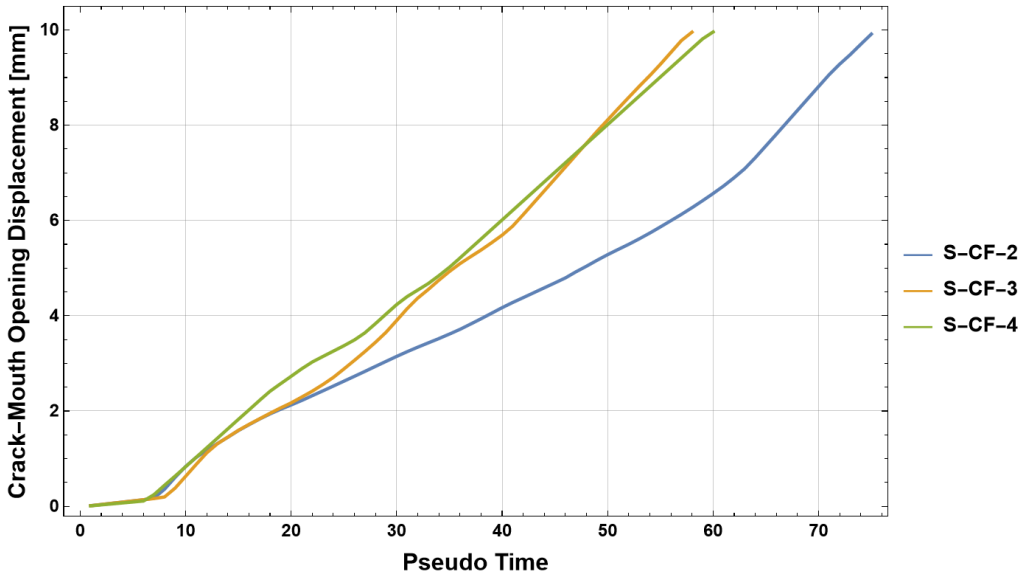

Figure 4.25: Crack Mouth Opening Displacement-Pseudo Time curves obtained from three-point bending tests on small-sized beams with coarse fibers

4.5.1.4 Interpretation of Three-Point Bending Test Results

Figure 4.26 shows the Force-CMOD curves obtained from testing on L-CF-1 and L-SF-4, large-sized beams with integrated fibers, that were disregarded from further analysis. These particular tests had anomalous behavior that was characterized by severe, high-frequency oscillations in the force signal that started approximately midway through the loading process, which was due to a badly positioned LINEAR VARIABLE DIFFERENTIAL TRANSFORMER (LVDT). This extreme noise

completely masked the post-peak softening behavior of the specimens, and made it impossible to interpret the true mechanical response of the material. Due to the inability of the recorded data to reliably represent the specimens' behavior under loading, these test results were consequently excluded from all quantitative analyses.

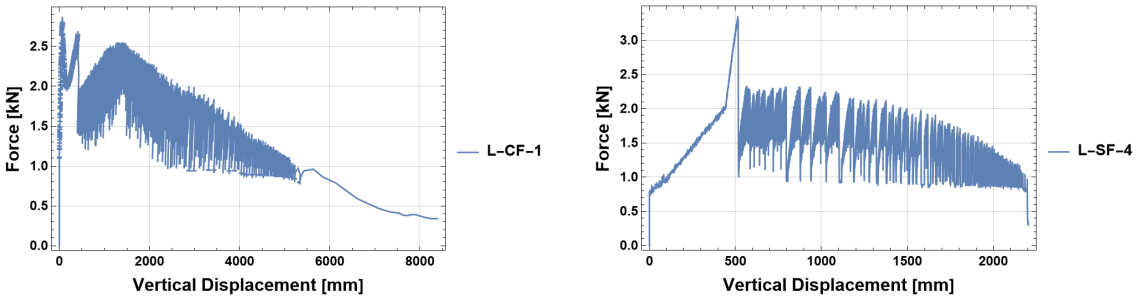

(a) L-CF-1: Coarse Fibers (b) L-SF-4: Smooth Fibers

Figure 4.26: Force-Crack Mouth Opening Displacement curves obtained from beams L-CF-1 and L-SF-4

The three-point bending tests on plain and fiber-reinforced concrete beams of all three sizes exhibit several behavioral trends. The recorded force-displacement and CMOD curves give insights into the flexural behavior of the materials and the influence of fiber reinforcement.

- CMOD vs. Pseudo Time
  The CMOD curves for plain concrete beams (Figures 4.9,4.15 and 4.21) consistently show a sharp, linear increase until a the point where a first crack is initiated, after which the curve becomes more vertical. This vertical slope signifies rapid crack propagation and failure of a higher magnitude, as there are no fibers to bridge the crack and carry the load in the post-cracking phase. This behavior is expected as plain concrete is categorized as brittle material. On the other hand, the CMOD curves for FRC beams (Figures 4.11, 4.13, 4.17, 4.19, 4.23 and 4.25) show a more gradual change in behavior after the initial elastic phase. After the initial cracking, the slope of the curve becomes significantly more gradual, which indicates that the fibers are effectively bridging the crack and are providing a resistance to the crack propagation.

- Force-Displacement
  The force-displacement curves show a similar trend. Plain concrete beams (Figures 4.8, 4.14 and 4.20) exhibit a sharp peak that corresponds to the ultimate flexural strength, followed by a sudden and steep drop to zero load upon cracking. FRC beams (Figures 4.10, 4.12, 4.16, 4.18, 4.22 and 4.24), however, demonstrate a more ductile response. After the initial cracking peak, the force decreases but does not drop to zero, instead it enters a post-peak

softening phase where the load is sustained and carried by the fibers. This behavior confirms the existence of the transfer of tensile load from the concrete matrix to the fibers, which is the fundamental mechanism of FRC.

The results show that the scale of the specimens has a direct impact on the observed behavior. In general, CMOD curves for the large beams (Figures 4.9, 4.11 and 4.13) appear to be more detailed and gradual than those for the medium and small beams (Figures 4.15, 4.17, 4.19, 4.21, 4.25, 4.23). This is due to the larger number of fibers bridging the notch, so the post-crack response is the sum of more individual pull-out events than in the medium and small beams. Higher absolute forces and displacements found in large-sized specimens also improve the signal-to-noise ratio recorded by the LVDT.

Discrepancies in the force-displacement curves due to minor variations in specimen production and testing machine accuracy are seen throughout the results, but they are most notable in large-sized beams (Figures 4.8, 4.10 and 4.12). Not only does the larger scale of the specimen amplify any imperfections, but any variations in fiber positioning and alignment are also more prominent due to the larger fiber count.

While the majority of the recorded data follows these general trends, a few specific specimens exhibited unique characteristics that require attention. In the force-displacement diagram for large beams with coarse fibers (Figure 4.10), beam L-CF-3 does not exhibit the sharp initial peak followed by a drop that is characteristic of concrete cracking, as seen in other FRC beams. This initial peak typically represents the flexural strength of the plain concrete matrix. Once it's reached, a crack forms, and the load is transferred from the matrix to the fibers, which causes the force to drop before rising again as the fibers begin to carry the load. The absence of this distinct peak in L-CF-3 suggests that the concrete's tensile strength was compromised from the get-go, possibly due to a flaw in the casting or curing process, or a localized air void in the concrete matrix.

The CMOD curve obtained for M-SF-4, seen in Figure 4.19, stands out with a unique slope within its testing group, and for which it is marked as an outlier. This result will be considered in the later inverse analysis, as it may reflect a slight testing error or an anomaly in the specimen's properties that could skew the results of the parameter extraction.

Within the small-beam group (Figure 4.25), specimen S-CF-2 exhibits a slightly distinct force–displacement and CMOD profile compared to S-CF-3 and S-CF-4, as both the pre- and post-peak evolution differ in shape and magnitude. This is assumed to be due to either a test set-up or specimen preparation mishap. Due to the small magnitude of difference, this dataset was not disregarded for any future analysis. However, its application in the inverse analysis will be carefully handled

to avoid propagating any assumed testing error into the obtained results.

4.5.2 Single Fiber Pullout Test Results

Figure 4.27 and 4.28 show obtained force–displacement diagrams from four tested specimens. From these, a clear development of plastic hinges as the fiber undergoes pull-out is evident. The observed shape corresponds to that of the final phase in the three-point bending of fiber reinforced beams.

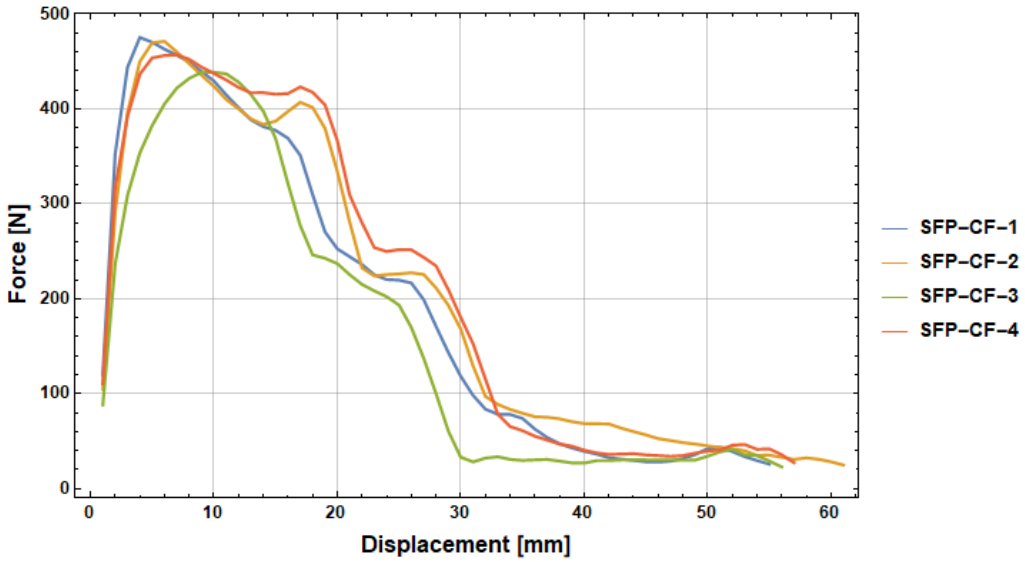

Figure 4.27: Force-displacement curves obtained from single fiber pull-out tests for coarse surface steel fibers

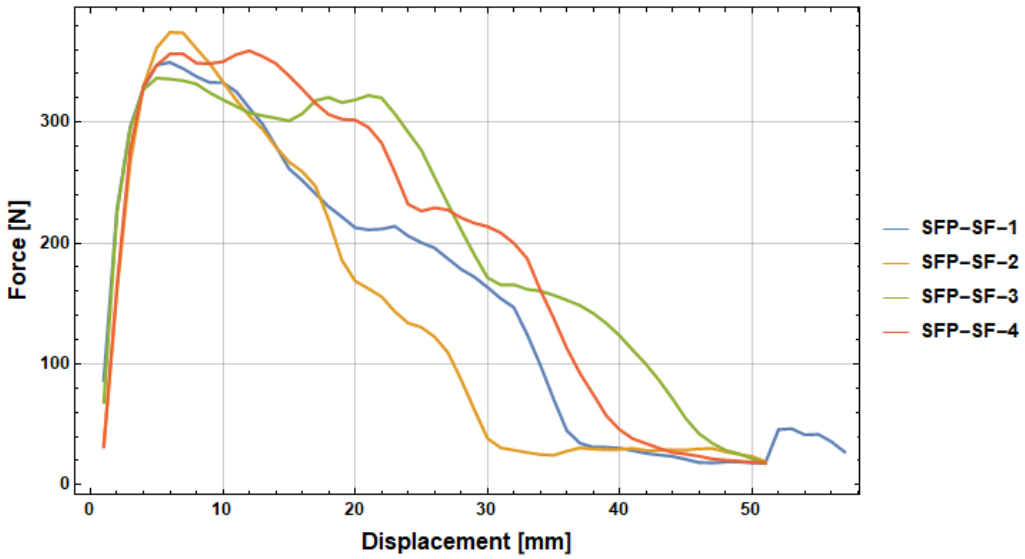

Figure 4.28: Force-displacement curves obtained from single fiber pull-out tests for smooth surface steel fibers

4.5.2.1 Interpretation of Single Fiber Pullout Test

Figures 4.27 and 4.28 show the measured force–displacement histories of single fibers under displacement control, with full pullout observed in all specimens. The pull-out response observed across all performed tests follows a clear sequence: an initial increase in force as the interfacial bond is mobilized (pre-debonding phase), which is followed by a maximum or threshold force that marks the beginning debonding. In the post-peak stage, the force is governed by frictional sliding, and for hooked-end fibers, an additional hardening appears due to the rotation and straightening of the hook and the formation of a plastic hinges near the anchorage. The force then gradually descends to zero as the fiber is fully pulled out. The development of plastic hinges during pull-out is evident in the experimental results and is consistent with the final post-cracking phase observed in the three-point bending tests on FRC beams.

The observed shape of the force-displacement curves from the single fiber pullout tests corresponds to the final, post-cracking phase of the three-point bending tests on FRC beams. In both tests, the ductile behavior and load-carrying capacity after initial cracking are governed by the same fiber bridging and pullout mechanisms. This correlation shows that the fiber pullout behavior at the micro-scale dictates the post-cracking toughness of the FRC beams at the macro-scale. This essentially means that the force-displacement curve of a TPBT specimen is a cumulative response that is roughly equivalent to the sum of the individual pullout responses of all the fibers bridging the crack.

The two different fiber surface finishes sampled here were included to expand the range of bond–slip responses. Coarse-surface fibers exhibit higher peak resistance and a more pronounced post-peak steeps between plastic hinges, while smooth fibers tend toward a lower peak and a flatter frictional plateau.

The data from the single fiber pullout tests exhibit good consistency within each group, with the curves generally following a similar trend. This consistency is important for the subsequent numerical modeling and inverse analysis, as it provides a reliable and deterministic pullout law that can be used to accurately simulate the behavior of the fiber-reinforced concrete. The results confirm that all tested samples experienced a complete fiber pullout failure mode, which makes the force-displacement curves a reliable representation of the bond-slip law.

Chapter 5

Multiphase Deterministic Model for Inverse TPBT Analysis

5.1 Novel Forward Model

The forward material model developed here is a deterministic, predictive model that relates strains and stresses in the beam's cross section through constitutive laws, and in turn simulates the internal and global response of the FRC beam under three-point bending.

To represent the heterogeneous nature of FRC without introducing randomness, the classical fiber bundle model (FBM), that is typically stochastic [61], was reformulated with strictly deterministic empirical parameters. Fibers and concrete were modeled as two interacting phases (as e.g.,in [37]), each with its own force–displacement law. This simplifies the model's concept while allowing it to capture both pre-peak and post-peak behavior in bending. This deterministic foundation is key because it guarantees the extracted parameters are physically interpretable, as wečč as offers direct, practical advantages for engineering design and optimization.

The concrete's force-displacement law is discretized as a three-phased piecewise function representing loading until failure and is graphically presented in Figure 5.1 in red. The mathematical formulation of this tri-linear softening law is as follows:

$$f_c(x) = \begin{cases} kc_1 \cdot x & \text{if } kc_1 \cdot x \leq f_c^{\max} \\ f_c^{\max} - E_b \cdot x - kc_2 \cdot f_c^{\max} & \text{if } f_c^{\max} \geq f_c^{\max} - E_b \cdot x - kc_2 \cdot f_c^{\max} > 0 \\ 0 & \text{if } f_c^{\max} - E_b \cdot x - kc_2 \cdot f_c^{\max} < 0 \end{cases} \tag{5.1}$$

where $f_c^{\max}$ is the maximum loading force, k_{c1} and k_{c2} are the stiffnesses of the beam during the loading and softening phases, respectively. These stiffness terms

are calculated as $k_{cn} = \frac{E_b I}{L_b L_{sn}}$, where E_b is the elasticity modulus of concrete, I is the moment cross section's moment of inertia, L_b is the beam's length, and L_{sn} is a scaling length factor that, in practice, acts as a calibration coefficient that ensures the slope of the simulated force-displacement curve matches the magnitude derived from experimental data.

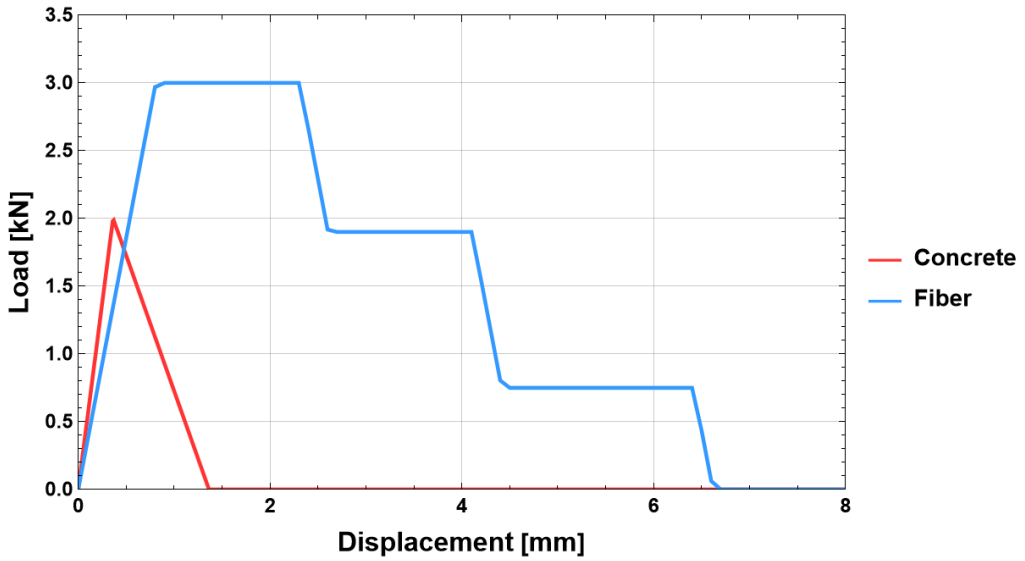

Figure 5.1: Modeled load-displacement law for concrete (red) fibers (blue)

The force-displacement law for the fibers, as given in Equation 5.2, is a piecewise function modified from the equation for the force-displacement law established in previous stochastic models ([37], [13], [61]), but with probabilistic parameters replaced with deterministic ones. This modification was done by directly adapting the mathematical formulation for the fiber force-displacement law based on the approach developed by Parise [70], where the crack propagation phase manifests as multiple plastic hinges on the force-displacement diagram. Additionally, this modification expands the existing formulation by integrating further fiber behavior parameters, as listed after the equation, which directly influence the shape of the piecewise function. The shape of the hinges is modeled to match those obtained from single fiber pull-out tests while ensuring that the values align with those obtained from three-point bending tests, one example of which is shown in Figure 6.2.

The full mathematical description of the fiber force-displacement law in tension

is formulated as follows:

$$f_a^{\mathrm{t}}(x) = \begin{cases} EA \cdot (x - d_0) & \text{if } x \leq d_{elastic} \\ F_a^{max} & \text{if } d_{elastic} < x \leq d_{p1} \\ F_a^{max} - EA \cdot \frac{x - d_{p1}}{L_{s2}} & \text{if } d_{p1} < x \leq d_{s1} \\ F_a^2 & \text{if } d_{s1} < x \leq d_{p2} \\ F_a^2 - EA \cdot \frac{x - d_{p2}}{L_{s2}} & \text{if } d_{p2} < x \leq d_{s2} \\ F_a^3 & \text{if } d_{s2} < x \leq d_{p3} \\ F_a^3 - EA \cdot \frac{x - d_{p3}}{L_{s2}} & \text{if } d_{p3} < x \leq d_{s3} \\ 0 & \text{if } x > d_{s3} \end{cases} \tag{5.2}$$

where the key displacements defining the phases of bending and subsequent fiber pullout are given by:

$$\begin{aligned} d_{elastic} &= d_0 + \frac{F_a^{max} \cdot L_{s2}}{EA} \\ d_{p1} &= d_{elastic} + d_{t1} \\ d_{s1} &= d_{p1} + \frac{(F_a^{max} - F_a^2) \cdot L_{s2}}{EA} \\ d_{p2} &= d_{s1} + d_{t2} \\ d_{s2} &= d_{p2} + \frac{(F_a^2 - F_a^3) \cdot L_{s2}}{EA} \\ d_{p3} &= d_{s2} + d_{t3} \\ d_{s3} &= d_{p3} + \frac{F_a^3 \cdot L_{s2}}{EA} \end{aligned}$$

The defined parameters: $d_{elastic}$ is the yield displacement point until which the beam bending is purely elastic, d_0 is the displacement offset or the magnitude at which the fibers start contributing to load carrying, axial stiffness (EA) is the combined axial stiffness of the fiber bundle, and L_{s2} is the embedment length of the fibers. F_a^{max}, F_a^2, and F_a^3 are the force thresholds defining the vertical components of the pullout phases, while d_{t1}, d_{t2}, and d_{t3} are the corresponding displacement increments for the plateau regions during which the fibers are being pulled out. d_{s1}, d_{s2}, and d_{s3} are cumulative total displacements that mark the end of each force-softening phase.

F_a^{max} is defined as a summation of the contribution of all the individual fibers intersecting the observed crack, as:

$$F_a^{\max} = \sum_{i_f=1}^{n_f} f_a^{\max} \tag{5.3}$$

which can be simplified with explicit parameters:

$$F_a^{\max} = n_{fiber} \cdot \bar{f}_a^{\max} \tag{5.4}$$

where n_{fiber} is the total number of fibers in the cross-section and $\bar{f}_a^{\max}$ the average force threshold for a single fiber pull-out. An example force-displacement diagram for a modeled fiber is represented on the right in Figure 5.1 in blue. $\bar{f}_a^{\max}$ can also be expressed as a function of the embedment length of a single fiber, l_e, as an expansion of the model. A common simplification for this relationship assumes that the force threshold is a product of the average interfacial bond strength, τ, and the fiber's surface area calculated from the diameter and and embedment length [112], as follows:

$$\bar{f}_a^{\max} = \tau \cdot \pi \cdot \Delta a \cdot l_e \tag{5.5}$$

In this formulation, the average force threshold increases linearly with the embedment length while assuming a constant average bond strength and fiber diameter.

The parameter E in Equation (5.2) is not the bulk steel modulus of an isolated fiber, rather it is treated as an effective elasticity modulus of the fiber–matrix system that captures the combined contribution of the fiber material, bond, partial debonding, and local slip. While the model can accommodate a more thorough description of stiffness degradation phenomenon, not only through plastic hinges, but by integrating different E parameters during tension or loading, and during unloading. However, for simplicity purposes, a singular parameter in tension, $E_{f,T}$, was used throughout this research. The effective stiffness EA is then formulated as:

$$EA = f_{bundle} \cdot E_{f,T} \cdot (\Delta a)^2 \cdot \frac{\pi}{4} \cdot n_{fiber} \tag{5.6}$$

Here, Δa is the individual fiber diameter, and the term f_{bundle} is an empirical scaling factor introduced to connect properties of a single fiber with the collective behavior of the fiber bundle. While the overall maximum force threshold, $F_a^{\max}$, is simplified as a summation of individual fiber contributions, in reality, the influence of the fibers is not a simple linear relationship. The f_{bundle} parameter accounts for this non-linear, collective behavior and it serves an essential empirical parameter to be evaluated during the later inverse analysis. Unlike models that would fix $E_{f,T}$ to the nominal steel modulus, this formulation makes room for both $E_{f,T}$ and f_{bundle} to be exactly determined through the inverse analysis process.

Given that the equations and the associated material parameters describing the two material phases are independent, concrete and fiber forces are coupled through

sectional equilibrium of a layered cross-section [14]:

$$F(\epsilon,\kappa) = \Delta h \sum_{i=1}^{\text{layer}} f_c\left[(h_i - \epsilon h)\tan(\kappa)\right] + \Delta a f_a^{\text{t}}(h_a - \epsilon h) = 0 \tag{5.7}$$

$$M(\epsilon,\kappa) = \Delta h \sum_{i=1}^{\text{layer}} (h_i - \epsilon h) f_c\left[(h_i - \epsilon h)\tan(\kappa)\right] + \Delta a (h_a - \epsilon h) f_a^{\text{t}}(h_a - \epsilon h) = 0 \tag{5.8}$$

Here, ϵ represents the neutral axis position, κ is the inclination of the crack opening, h is the height of the beam's cross-section, h_i is the height of each layer, h_a represents the position of fibers, and f_c and f_a are given in equations 5.1 and 5.2, respectively. The layered model is based on previously established principles presented in [113], with an example of cross-section geometry for a beam discretized into eight layers given in Figure 5.2.

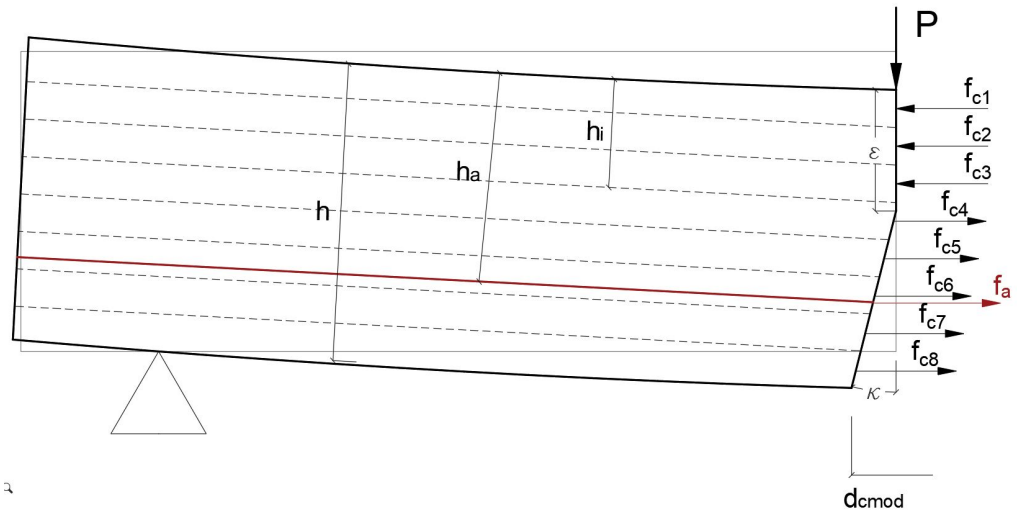

Figure 5.2: Diagram for the three-point bending of a layered FRC beam

Given the non-linear material constitutive laws defined in Equations 5.1 and 5.2, the equilibrium Equations 5.7 and 5.8 form a non-linear system that cannot be solved analytically. To simulate the beam's response throughout the loading process, mimicking the displacement-controlled experiments, a numerical path-following approach was adapted using the vertical displacement d_v (Eq. 5.9) as the control parameter:

$$d_v = -\epsilon \cdot h \cdot \tan(\kappa) \tag{5.9}$$

At each step of the simulation, a target vertical displacement, $d_{v,target}$, is prescribed. A system of three equations is then solved numerically for three unknowns:

the neutral axis position, ϵ, the crack inclination, κ, and the external bending moment, M_{ext} required to maintain equilibrium at that displacement level. Therefore, the system that needs solving comprises of the following:

1. Force equilibrium equation 5.7: $F(\epsilon, \kappa) = 0$
2. Moment equilibrium equation 5.8: $M_{\text{int}}(\epsilon, \kappa) = M_{\text{ext}}$
3. Prescribed displacement equation 5.9: $d_{v,\text{target}} = -\epsilon h \tan(\kappa)$

This non-linear system is solved iteratively using a numerical root-finding algorithm similar to the Newton-Raphson method integrated in Wolfram Mathematica's `FindRoot` function. The solution from the previous displacement step is used as the initial guess in the current step for preserving continuity and supporting convergence along the solution path.

Successfully solving this system at successive increments of $d_{v,target}$ results with the evolution of the state variables ϵ and κ, along with the corresponding equilibrium moment M_{ext}. From the obtained ϵ and κ, the Crack Mouth Opening Displacement d_{cmod} is calculated as:

$$d_{\text{cmod}} = (1 - \epsilon) \cdot h \cdot \tan(\kappa) \tag{5.10}$$

The calculated external moment, M_{ext}, can be related to the load P applied on the mid span of the beam $L/2$, from which the load-CMOD and load-displacement relationships can be obtained and compared to experimental data.

To simulate the beam's global behavior under three-point bending, the computed M_{ext} is related to the externally applied load P at mid-span through standard beam theory:

$$P = \frac{4 \cdot M_{ext}}{L} \tag{5.11}$$

where L is the span of the supported beam. This relationship enables the connection between the obtained moment–curvature response with the force–displacement response representative of the actual structural test. Although the vertical displacement (d_v), and crack mouth opening displacement, d_{cmod}, are computed as sectional quantities based on geometry their pairing with the global load, P, allows for the construction of synthetic load-displacement and load–CMOD diagrams, which are comparable to experimental data.

5.2 Novel Inverse Model

5.2.1 Model Updating Framework

The inverse analysis in this research serves as a model updating procedure, where parameters are iteratively adjusted to minimize the residual between simulated and experimental CMOD data. This follows the general model updating expression:

$$m_n = m_{n-1} + \Delta m_n \tag{5.12}$$

where m_{n-1} represents the parameter vector at iteration $n-1$, and Δm_n is the update computed via the Levenberg-Marquardt algorithm.

5.2.2 Levenberg-Marquardt Implementation

Taking into consideration that the newly formulated predictive model (detailed in Chapter 5.1) is non-linear in nature and a direct inversion method could not be successfully applied, the LEVENBERG-MARQUARDT (LM) algorithm was applied for the inverse parameter analysis. This method iteratively adjusts a function's parameter to minimize the error between predicted and actual data by alternating between the Gauss-Newton algorithm and the method of gradient descent [114].

The method is formulated as a minimization problem of weighted residual. In this research, the measured data consists of n crack mouth opening displacement values, y_i (where $i = 1, ..., n$), each corresponding to a specific state of the beam. The forward model predicts a CMOD value, $d_{\text{cmod}i}(m)$, for each of these states using a vector of model parameters $\mathbf{m}$. The objective is to minimize the SUM OF SQUARES (SS) of the differences between the measured and modeled CMOD values as:

$$SS(\mathbf{m}) = \sum_{i=1}^{n} (y_i - d_{\text{cmod }i}(\mathbf{m}))^2 \tag{5.13}$$

The minimum of $SS(\mathbf{m})$ occurs when its gradient with respect to each parameter m_j is zero. For the j-th parameter, this condition is:

$$\frac{\partial SS}{\partial m_j} = -2 \sum_{i=1}^{n} (y_i - d_{\text{cmod}i}(\mathbf{m})) \left(\frac{\partial d_{\text{cmod }i}(\mathbf{m})}{\partial m_j} \right) = 0 \tag{5.14}$$

The partial derivatives $\left(\frac{\partial d_{\text{cmod}i}}{\partial m_j} \right)$ form the elements of the Jacobian Matrix $\mathbf{J}$ that has $n \times m_p$ dimensions, where n is the number of measured data points (indexed with i), and m_p is the number of model parameters being estimated (indexed with j). Every $\mathbf{J}_{i,j} = \left(\frac{\partial d_{\text{cmod}i}}{\partial m_j} \right)$ represents the sensitivity of the i-th model output to a

change in the j-th parameter. The Levenberg-Marquardt algorithm solves this for the parameter update vector Δm through a damped least-squares approach:

$$\left(\mathbf{J}^T\mathbf{J} + \lambda\mathbf{I}\right)\Delta\mathbf{m} = \mathbf{J}^T\left(\mathbf{y} - \mathbf{d}_{\text{cmod}}(\mathbf{m})\right) \tag{5.15}$$

where y is the vector of measured CMOD values y_i, $\mathbf{d}$cmod($\mathbf{m}$) is the vector of simulated CMOD using the current parameter vector m, and $\mathbf{I}$ is the identity matrix. Solving this system gives Δm used to update the parameters in each iteration in Equation (5.12).

For the case of estimating a single parameter m (scalar), the update Δm can be calculated using a simplified form derived from the Gauss-Newton method adapted by the Levenberg-Marquardt algorithm:

$$\Delta m = \frac{\sum_{i=1}^{n}(y_i - d_{\text{cmod }i}(m))\chi_{m,i}}{\sum_{i=1}^{n}\chi_{m,i}^2} \tag{5.16}$$

In this formulation, $\chi_{m,i} = \frac{\partial d_{\text{cmod}i}}{\partial m}$ is the sensitivity coefficient of the i-th model output with respect to the single parameter m. This equation is the basis for the user-controlled iterative updates procedure for adjusting the parameter based on the weighted error and its sensitivity.

The value for the model parameters in step n is calculated using equation 5.12. Considering the calculation is iterative, the algorithm terminates when either:

- Convergence is reached and parameter changes between iterations become negligible ($\|\Delta\mathbf{m}\| < 10^{-4}$). This specific threshold value is chosen to both ensure numerical stability and maintain sufficient precision without unnecessary increasing computational costs from marginal improvements;
- The residual SS falls below a tolerance threshold ($\epsilon = 10^{-6}$);
- A fixed maximum iteration count is reached.

The relationship between the forward and inverse model, and any parameter n_A and n_B, is graphically presented in the flow chart in Figure 5.3.

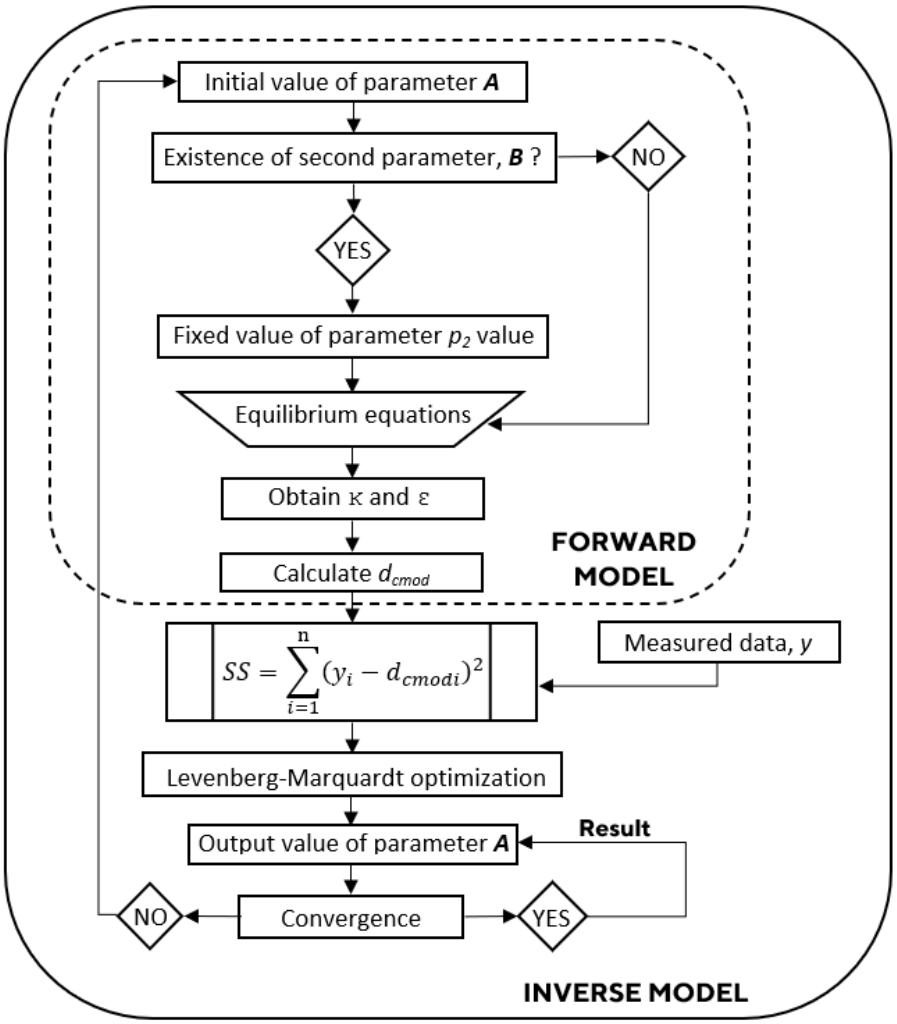

Figure 5.3: Flow chart of forward and inverse model algorithms

5.2.3 Dual-Parameter Extraction Strategy

This inverse analysis framework becomes more complex when estimating multiple parameters simultaneously, when vector m contains more than one element. In the case of nonlinear behavior, as seen in FRC, different combinations of parameters could result in the optimization function achieving the same minimum error when fitting the measured data, which is a phenomenon known as solution non-uniqueness. This ambiguity can make it challenging for reliable inverse parametric characterization of FRC.

When possible, this issue can mitigated through the implementation of the Tikhonov regularization through which unrealistic parameter combinations are disregarded by adding a penalty term to the objective function:

$$SS_{\text{reg}}(m) = SS(m) + \alpha||\mathbf{m}||^2 \tag{5.17}$$

where $SS(\mathbf{m})$ is the original sum of squares of residuals from Equation 5.13), α is a user-defined regularization coefficient that controls the strength of the penalty, and $||\mathbf{m}||_2^2$ is the squared L2-norm of the parameter vector. This regularization term discourages unrealistically large or physically improbable parameter values, and through this guiding the optimization towards a more stable and physically possible solution, even in the presence of noisy data or parameter correlations.

However, in situations where this is not applicable, or more fundamentally, for gaining a more comprehensive understanding of the parameter landscape and their interdependencies, a dual-parameter extraction strategy can be used. This is particularly useful for identifying parameters that might be correlated, where the influence of one parameter can be compensated by another, which can lead to potential solution non-uniqueness issues.

For this research, a systematic grid search method was used as the main dual-parameter extraction strategy. This method exhaustively evaluates the objective function's behavior across a predefined multi-dimensional solution space.

Through this method, the objective function's behavior is mapped across the solution space by evaluating a predefined range of parameter combinations, which thereby identifies the optimal parameter set and showcases potential parameter correlations. By systematically mapping the error associated with each parameter combination, this approach identifies the globally optimal parameter set within the defined search bounds as well as provides a visual representation of potential parameter correlations and the overall sensitivity of the model to these parameters. This direct mapping contrasts the Levenberg-Marquardt iterative optimization algorithms, which, while efficient, sometimes converges to local minima or struggles to characterize the full extent of solution non-uniqueness without multiple starting points.

The systematic grid search was implemented in following steps:

1. Definition of parameter ranges based on prior knowledge, material characteristics, and initial sensitivity analysis. Plausible minimum and maximum values are established for the two parameters ($\boldsymbol{A}$ and $\boldsymbol{B}$) that are under investigation.

2. Discretization of both preset ranges by dividing them into a fixed number of discrete steps, which creates a $n_A \times n_B$ grid of unique parameter pairs.

3. Predictive model evaluation for each ($\boldsymbol{A}$ - $\boldsymbol{B}$) pair within the defined grid, across a set of κ values.

4. Error calculation (objective function evaluation) for each ($\boldsymbol{A}$ - $\boldsymbol{B}$) combination by quantifying the discrepancy between the predicted CMOD data and target CMOD data, following previously defined Equation 5.13, where for

dual-parameter extraction, $\mathbf{m} = \{A, B\}$, y_i are the target CMOD values. High error is assigned to cases where the predictive model fails to converge for specific parameter combinations, which effectively penalizes such regions in the solution space.

The output of this process is a dense dataset that represents the error surface in the parameter space. Such datasets subsequently form the basis for creating contour maps, which are used for the interpretation and discussion of the inverse analysis results in the later sections. Such visualizations directly highlight the global minimum of the objective function, the sensitivity of the resulting CMOD curves to changes in $\boldsymbol{A}$ and $\boldsymbol{B}$, and the presence and nature of any interdependencies or correlations between the two parameters, which is key in non-linear material characterization.

5.3 Model Assumptions and Limitations

The integrity and computational efficiency of this novel inverse framework are based on several explicit assumptions and necessary analytical simplifications. Therefore, this section outlines these limitations to clearly define the boundary conditions under which the model is to remain accurate and applicable.

The model is subject to several essential limitations that stem directly from its formulation, and primarily concern the simplification of inherently complex physics in order to achieve computational speed (as per hypothesis 2). Concerning the material constitutive laws, the approach applies a tri-linear softening law for the concrete matrix and a piecewise function with discrete plastic hinges for the fiber pull-out. This represents an abstract version of the physical reality (which involves a continuous, non-linear function and micro-scale cracking) in favor of a more efficient, deterministic form that sacrifices these accuracies for computational speed. Second, the fundamental assumption of the model dictates a zero-degree fiber orientation that is parallel to the pull-out axis and operates exclusively on a specific cross-sectional basis. This simplification was necessary in order to eliminate the major source of stochastic variability in the experimental data but restricts the model's direct applicability to FRC beams that have random fiber alignment ($\neq 0°$). Furthermore, the model is limited to tracking only the kinematics at the crack plane (CMOD and d_v at midspan), which means it does not simulate the full moment-curvature distribution along the entirety of the beam's span.

In addition to these formulation constraints, the inverse analysis is subject to several limitations regarding data accuracy and algorithmic application. The numerical stability verified in this study depends directly on having tested only a single material family (steel fibers in an SCC matrix).

This means applying the extracted coefficients to vastly different materials (like polymer fibers or conventional vibrated concrete) requires re-calibration and re-validation. Crucially, the optimization algorithm is mathematically designed to converge even from physically impossible starting points (e.g. negative parameter values). Therefore, the final parameter estimate requires the user to discard non-physical numerical solutions, with confidence depending on the bounds defined by the Basin of Attraction values and the maintenance of physical plausibility to ensure the results are meaningful.

Chapter 6

Verification and Validation Framework

A systematic process of verification and validation process (V&V) was conducted in order to ensure that the newly formulated models meet all requirements for reliability, accuracy, and conceptual validity.

The verification processes addressed whether the numerical algorithm correctly solves the underlying mathematical model, with a focus on the accuracy of the code's implementation. On the other hand, validation of the model was done to evaluate its ability to simulate and estimate parameters from real data, through a comparative analysis of simulated versus experimentally obtained data.

6.1 Validation of the Predictive Model

The validation of the predictive numerical model was done to confirm its ability to accurately represent the real behavior of fiber-reinforced concrete beams under three-point bending. This involved simulating the experimental results obtained from all three beam sizes and configurations tested in the laboratory, as detailed in Chapter 4.3.

The input parameters for the predictive model were first defined based on the geometric configurations and material properties of the specific beams selected for simulation. These configurations (all sizes and fiber types) correspond directly to those tested in the laboratory, as described in Chapter 4. The values for the concrete and fiber constitutive laws within the numerical model were derived from a combination of laboratory material testing (compressive strength, single fiber pull-out tests) and specifications provided by the manufacturer [105]. Specifically, the force-displacement curves representing the constitutive behavior of the concrete matrix (controlled by Equation 5.1) and steel fibers (Equation 5.2) were implemented

within the predictive model. The parameters controlling these constitutive laws were calibrated by aligning the shapes of the simulated force-displacement curves with the corresponding experimental curves obtained from the respective three-point bending tests, as seen on the left hand side in Figures 6.1, 6.3 and 6.6.

The input parameters for the predictive model were first defined based on the geometric configurations and material properties of the specific beams selected for simulation. These configurations (all sizes and fiber types) correspond directly to those tested in the laboratory, as described in Chapter 4. The values for the concrete and fiber constitutive laws within the numerical model were derived from a combination of laboratory material testing (compressive strength, single fiber pull-out tests) and specifications provided by the manufacturer [105]. The combined stiffness parameter during loading, $E_{f,T}$, was initially assumed to be $210000 N/mm^2$ for convenience, equating it with the provided elasticity modulus of the fiber. Specifically, the force-displacement curves representing the constitutive behavior of the concrete matrix (controlled by Equation 5.1) and steel fibers (Equation 5.2) were implemented within the predictive model. The parameters controlling these constitutive laws were calibrated by aligning the shapes of the simulated force-displacement curves with the corresponding experimental curves obtained from the respective three-point bending tests, as seen on the left hand side in Figures 6.1, 6.3 and 6.6.

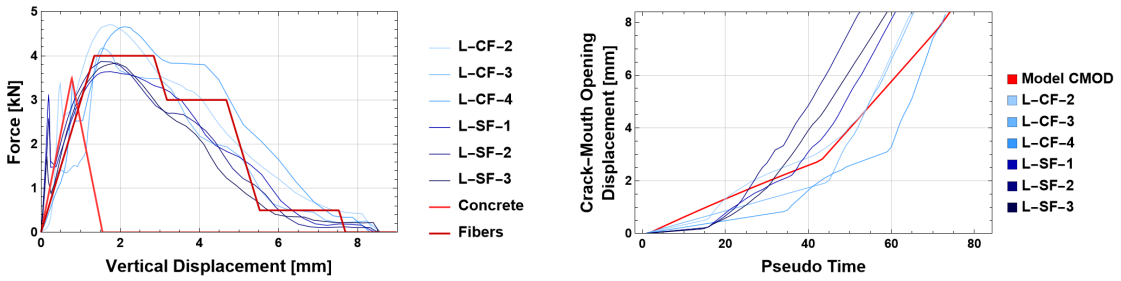

Figure 6.1: Predictive Model data overlayed with experimentally obtained data for large-sized FRC beams: (left) Modeled vs. Experimental Load-Displacement Curves (Input) and (right) Modeled vs. Experimental CMOD-Pseudo Time Curves (Output).

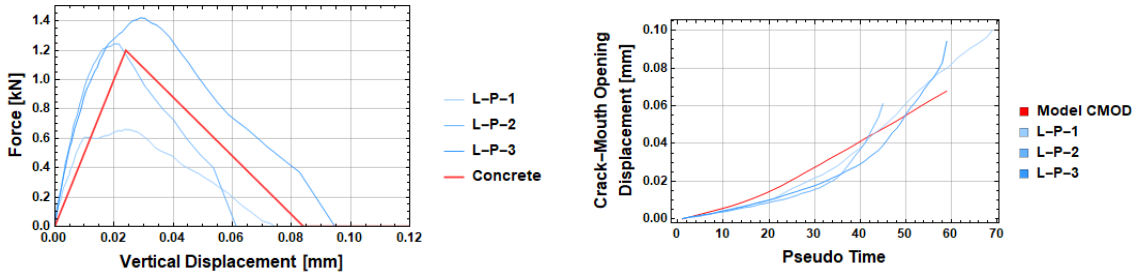

Figure 6.2: Predictive Model data overlayed with experimentally obtained data for large-sized plain beams: (left) Modeled vs. Experimental Load-Displacement Curves (Input) and (right) Modeled vs. Experimental CMOD-Pseudo Time Curves (Output).

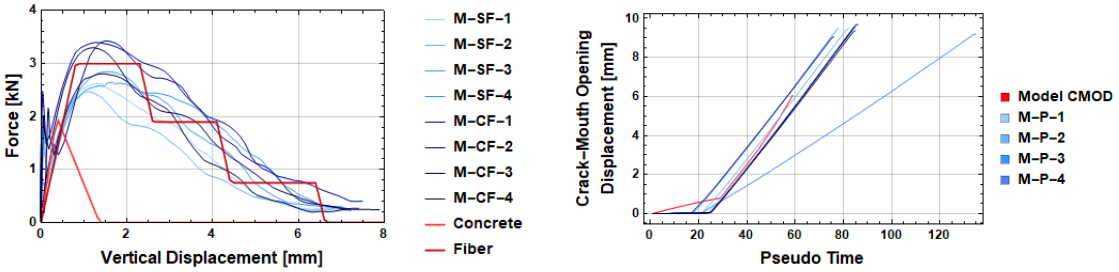

Figure 6.3: Predictive Model data overlayed with experimentally obtained data for medium-sized FRC beams: (left) Modeled vs. Experimental Load-Displacement Curves (Input) and (right) Modeled vs. Experimental CMOD-Pseudo Time Curves (Output).

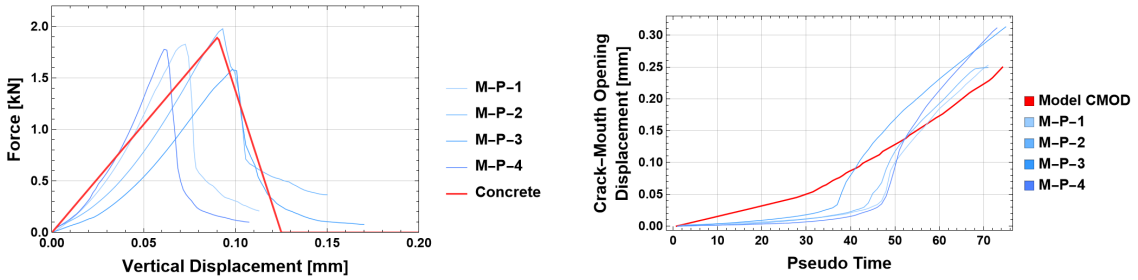

Figure 6.4: Predictive Model data overlayed with experimentally obtained data for medium-sized plain beams: (left) Modeled vs. Experimental Load-Displacement Curves (Input) and (right) Modeled vs. Experimental CMOD-Pseudo Time Curves (Output).

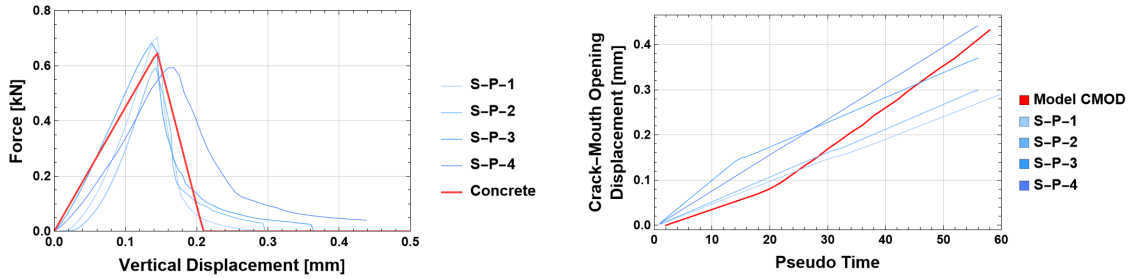

Figure 6.5: Predictive Model data overlayed with experimentally obtained data for small-sized plain beams: (left) Modeled vs. Experimental Load-Displacement Curves (Input) and (right) Modeled vs. Experimental CMOD-Pseudo Time Curves (Output).

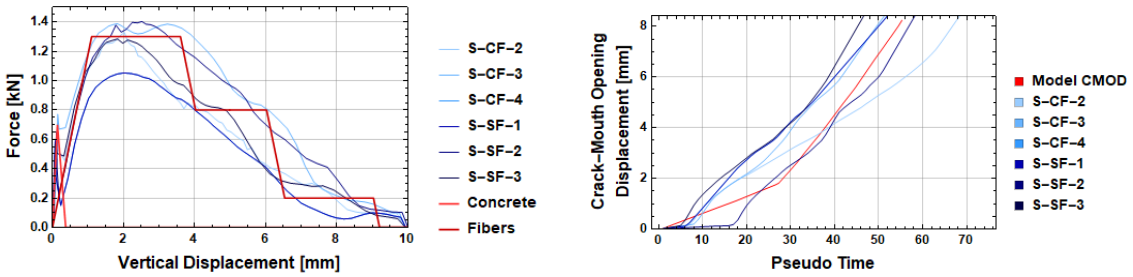

Figure 6.6: Predictive Model data overlayed with experimentally obtained data for small-sized FRC beams: (left) Modeled vs. Experimental Load-Displacement Curves (Input) and (right) Modeled vs. Experimental CMOD-Pseudo Time Curves (Output).

The resultant CMOD curves (right hand side in the Figures 6.1, 6.3 and 6.6) were analyzed for the purpose of validating the predictive model. An overall visual qualitative assessment of the overall profile of the resulting CMOD curves was done. This included the inspection of initial stiffness, peak load (if presenting in the CMOD curve), and post-peak softening behavior, as well as comparison of the simulated curves to the experimentally obtained ones. The quantitative accuracy evaluation was done by calculating the root mean square error (RMSE) between the simulated and average experimental CMOD values, which provides a measure of the average magnitude of the errors by quantifying the difference between the predicted and observed CMOD values across the entire curve. It is calculated as:

$$\text{RMSE} = \sqrt{\frac{1}{n}\sum_{i=1}^{n}(y_{\text{exp},i} - y_{\text{sim},i})^2} \tag{6.1}$$

where $y_{\text{exp},i}$ is the i-th experimental CMOD value, $y_{\text{sim},i}$ is the i-th simulated CMOD value, and n is the total number of data points. As a right hand rule, the lower the RMSE score the better the accuracy.

A RMSE score of zero would indicate a perfect fit, as it would mean the predicted values align perfectly with actual values [115]. However, such fit is rarely achieved in practice due to data variability and model limitations.

Since RMSE is scale dependent, the normalized root mean square error (NRMSE) was also calculated to enable a more objective comparison of obtained results across different beam sizes, as NRMSE provides a relative measure of error, independent of the raw data's magnitude. This specific normalization was calculated by dividing previously obtained RMSE with the range of the observed CMOD data:

$$\text{NRMSE} = \frac{\text{RMSE}}{\max(y_{\text{exp}}) - \min(y_{\text{exp}})} \times 100\% \tag{6.2}$$

NRMSE was expressed as a percentage in order to directly indicate the model's error relative to the total variability of experimentally obtained data. For the context of this study, an NRMSE value below 10% is generally evaluated as excellent, while values between 10% and 20% are considered a good fit. This assessment criteria is consistent with findings in literature for similar materials, where NRMSE values up to 18% are often valued as satisfactory [116, 117].

To provide a more widely accepted measure of the model's predictive capability, the Coefficient of Determination (R^2) was calculated. R^2 quantifies the proportion of the variance in the experimental data that is predictable from the numerical model. R^2 ranges from 0 to 1, where a value closer to 1.0 indicates a near-perfect fit between the simulated and observed data. It is calculated as:

$$R^2 = 1 - \frac{\sum_{i=1}^{n}(y_{\text{exp},i} - y_{\text{sim},i})^2}{\sum_{i=1}^{n}(y_{\text{exp},i} - \bar{y}_{\text{exp}})^2} \tag{6.3}$$

Additionally, the relative squared residual (RSR) was calculated as a goodness-of-fit indicator to provide a standardized measure of the average magnitude of the errors, normalized by the standard deviation (SD) of the observed data. RSR is calculated as the ratio of the RMSE to the standard deviation of the observed data (σ_{exp}):

$$\text{RSR} = \frac{\text{RMSE}}{\sigma_{\text{exp}}} = \frac{\sqrt{\frac{1}{n}\sum_{i=1}^{n}(y_{\text{exp},i} - y_{\text{sim},i})^2}}{\sqrt{\frac{1}{n}\sum_{i=1}^{n}(y_{\text{exp},i} - \bar{y}_{\text{exp}})^2}} \tag{6.4}$$

An RSR value of 0 indicates a perfect model fit. According to common criteria in literature, RSR values less than 0.50 are typically considered to indicate a "very good" model fit, while values between 0.50 and 0.60 represent a "good" fit ([118]).

The calculated RMSE, NRMSE, RSR and R^2) for all simulated beam configurations are summarized in Table 6.1. These metrics provide a precise evaluation of the predictive model's accuracy against the average experimental CMOD curves.

Table 6.1: Summary of Predictive Model Validation Results (RMSE, NRMSE, RSR, and R^2) for Various Beam Configurations

Beam Size	**Type**	**RMSE [mm]**	**NRMSE [%]**	**RSR**	**R^2**	**Performance rating**
Large	FRC	1.053	9.94	0.324	0.895	Very good fit
Large	Plain	0.014	12.35	0.431	0.814	Very good fit
Medium	FRC	0.302	5.65	0.169	0.971	Very good fit
Medium	Plain	0.030	10.97	0.312	0.903	Very good fit
Small	FRC	0.840	10.45	0.341	0.884	Very good fit
Small	Plain	0.028	15.10	0.384	0.852	Very good fit

By observing the simulated CMOD curve for large-sized beams with and without fibers in Figures 6.8 and 6.7, respectively, it consistently falls well within the ±2 standard deviation band, and largely within the ±1 standard deviation band.

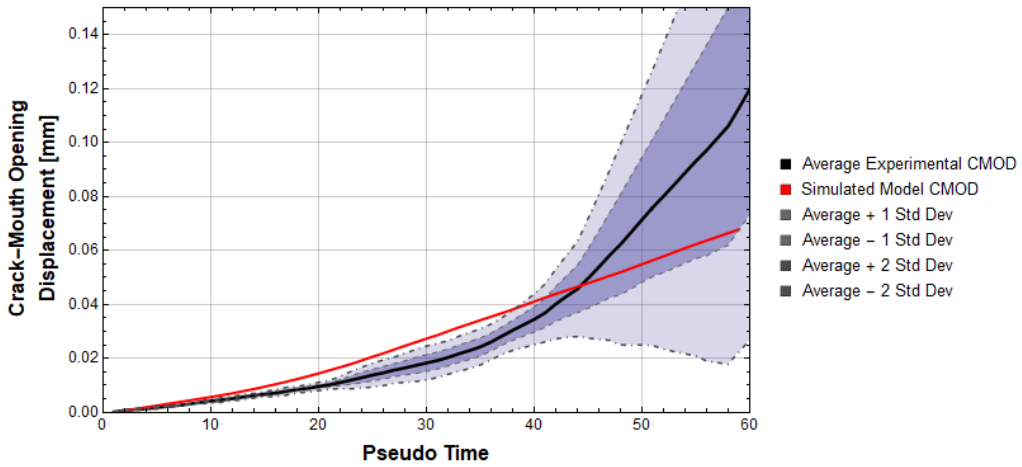

Figure 6.7: Crack Mouth Opening Displacement versus Pseudo Time plot for the numerical model simulation and average experimental results with their standard deviation bands for large-sized plain concrete beams

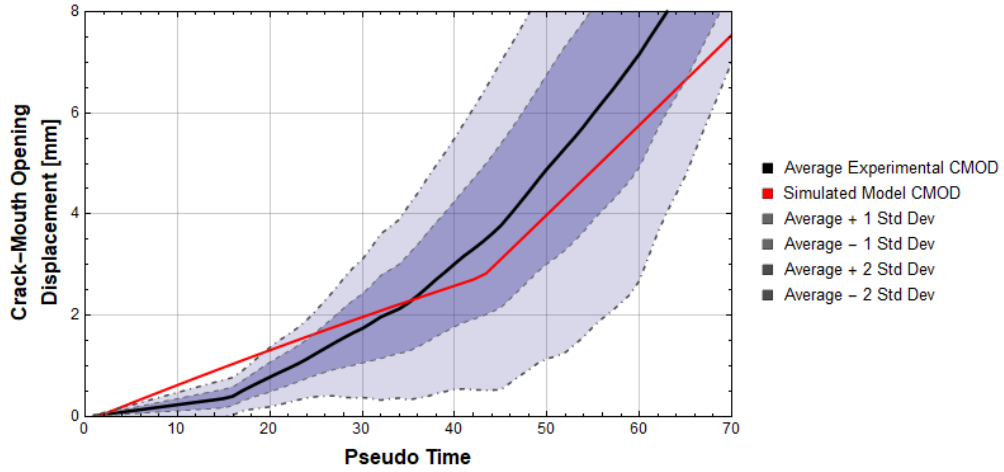

Figure 6.8: Crack Mouth Opening Displacement versus Pseudo Time plot for the numerical model simulation and average experimental results with their standard deviation bands for large-sized FRC beams

Figures 6.9 shows that the simulated CMOD curve for a plain medium-sized beam exhibits the characteristic non-linear, accelerating increase, which is consistent with the experimental data. However, a discrepancy in the steepness of the CMOD progression is present between the simulated and experimental results, particularly around the crack initiation phase. Nevertheless, despite these local deviations, the simulated curve largely remains within the ± 2 standard deviation band. Considering the overall small magnitude of these deviations (e.g., an NRMSE of 10.97% and absolute deviations typically below 0.05 mm), the model is considered to provide a good fit to the experimental data. The CMOD result (Figure 6.10) for the same model with activated fiber parameters almost entirely falls within the ± 1 standard deviation band of the experimentally obtained data.

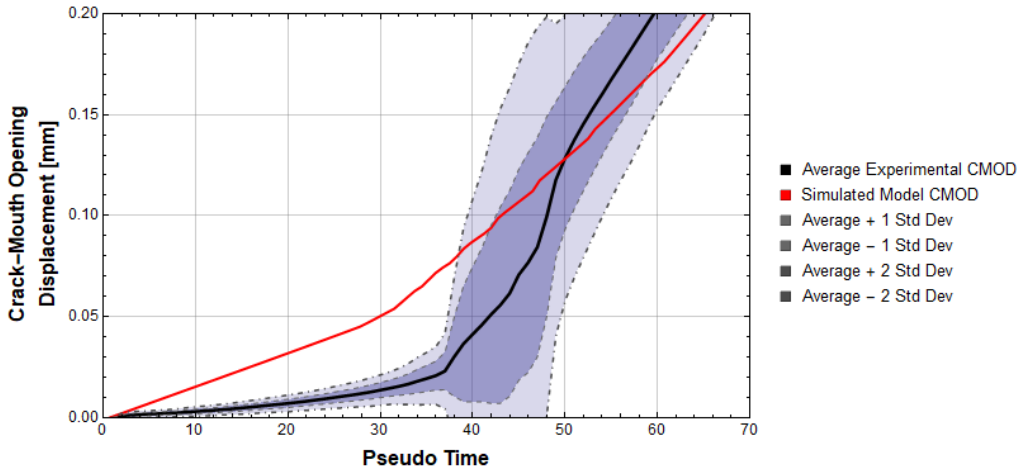

Figure 6.9: Crack Mouth Opening Displacement versus Pseudo Time plot for the numerical model simulation and average experimental results with their standard deviation bands for medium-sized plain concrete beams

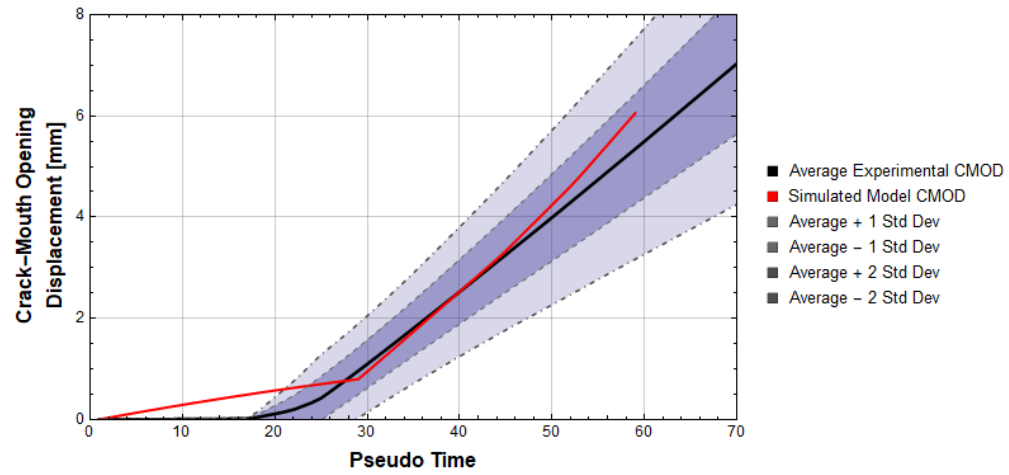

Figure 6.10: Crack Mouth Opening Displacement versus Pseudo Time plot for the numerical model simulation and average experimental results with their standard deviation bands for medium-sized FRC beams

Similarily, resulting CMOD curves for plain and FRC beams, shown respectively in Figures 6.11 and 6.12, exhibit the same consistent behavior. Both results fall within the ±2 standard deviation band of their respective experimental data.

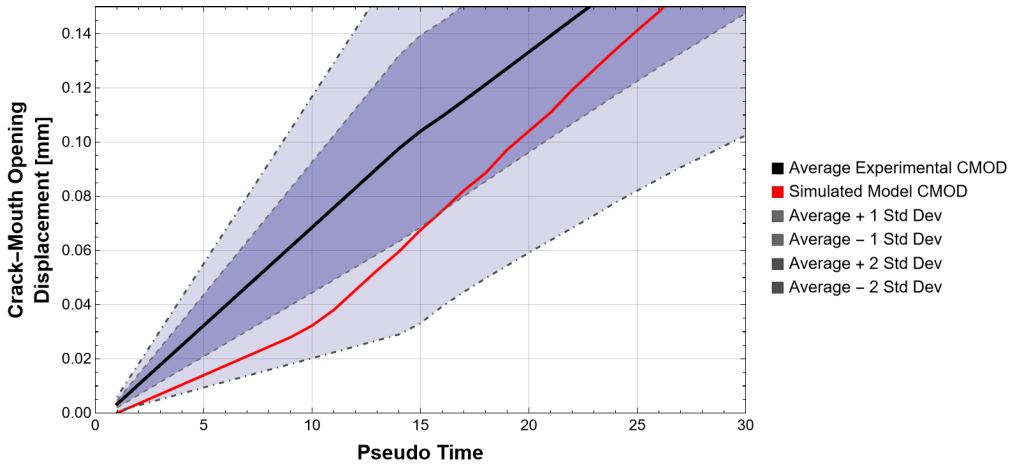

Figure 6.11: Crack Mouth Opening Displacement versus Pseudo Time plot for the numerical model simulation and average experimental results with their standard deviation bands for small-sized plain concrete beams

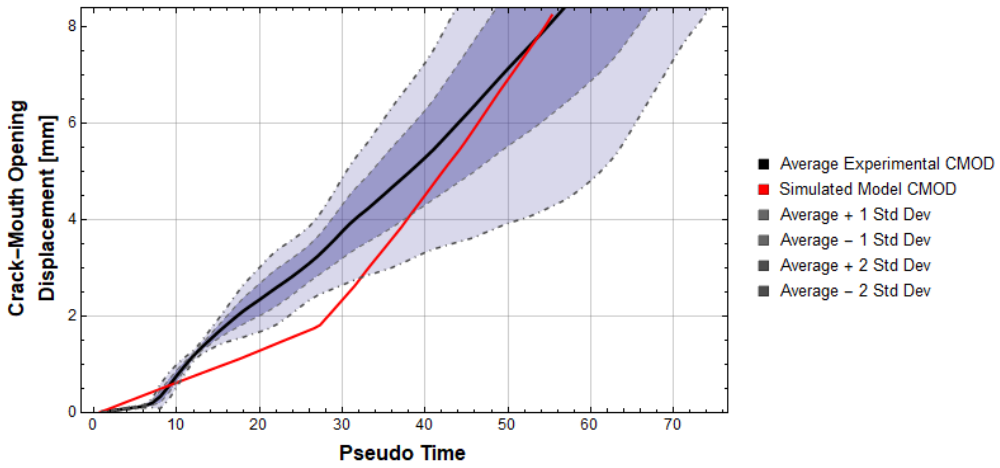

Figure 6.12: Crack Mouth Opening Displacement versus Pseudo Time plot for the numerical model simulation and average experimental results with their standard deviation bands for small-sized FRC beams

All simulated CMOD curves effectively capture the overall behavior of experimental ones, and is a good representative of the scattered experimentally obtained data.

Through this validation process of the predictive model against experimental three-point bending data for all three beam sizes and configurations, the model consistently demonstrated its capability to simulate the crack mouth opening displacement progression. The consistently low RMSE values, NRMSE values mostly falling within the "excellent" (below 10%) and "very good" (10-20%) ranges, and RSR and R^2 values consistently showed "very good" fits (all below 0.50 and above 0.81, respectively), confirmed the model's predictive accuracy. Visual inspection of the simulated curves further confirmed this, as it showed a strong agreement with the average experimental responses and consistently falling within the observed experimental variability bands.

6.2 Comparison with Stochastic Model's Results

This chapter focuses on the verification of the presented novel deterministic computational model through direct comparison with data generated using an established stochastic model for the three-point bending of fiber-reinforced concrete beams. The stochastic model used for this comparison was developed by Kožar et al. [13, 14, 61]. It was specifically chosen due to its fundamental similarities with the model developed in this thesis, particularly in its adoption of a layered beam discretization and Newton's procedure for solving the system of nonlinear equilibrium equations [61]. This commonality allows for a direct comparison of how the handling of material

variability effects the simulated behavior, rather than comparing the differences in fundamental modeling approaches. Furthermore, this specific stochastic model was chosen as it serves as an ideal benchmark because it is a well-established and well-documented model, and was developed independently by my research collaborators.

The primary goal of this comparison was to verify the predictive capabilities of the deterministic model and to inspect its suitability as a foundation for inverse analysis, which directly addresses the core of the thesis hypothesis. While Kožar et al. (2021) rightfully state that deterministic models inherently *"don't explain variations in experimental data"* [61], a key aspect of this thesis's hypothesis is that a well-posed, robust, and simplified deterministic model can effectively compensate for this during the inverse analysis. This means that such a model should be capable of adequately extracting necessary material parameters even when dealing with randomness present in measured experimental results. Therefore, establishing the deterministic model's predictive accuracy against a validated stochastic counterpart, known for its ability to represent experimental variability, is an important preliminary step before proceeding with the deterministic model's own inverse extraction capabilities in subsequent chapters.

The stochastic model by Kožar et al. (2021) is based on the Fiber Bundle Model (FBM) concept, where stochastic parameters such as the fiber peak tension load and the fiber area are described by a Gaussian probability distribution. While individual fibers possess slightly different material or geometric properties, the collective behavior of the fiber bundle, is simplified and represented by a non-linear stochastic function. For the purpose of forward modeling in three-point bending, Kožar et al. (2021) generalized this FBM into a simpler, microplane-like material model described by a two-parameter exponential equation ($f(x, A, B) = A \cdot x \cdot \mathrm{Exp}(-B \cdot x)$) that represents the global force-displacement relationship. This exponential material model is applied to describe both the concrete matrix and the fibers within the layered beam model [61].

The comparison process involved generating mechanical responses from both models under simulated three-point bending tests. For the novel deterministic model, the simulations done in Chapter 6.1 were directly adapted here as well. For the stochastic model, key material parameters ('A' and 'B' of the exponential load-displacement law for both the concrete matrix and the fibers) were treated as random variables [61]. These parameters were set to follow a Gaussian probability distribution, with their mean values matching the corresponding parameters established in the deterministic model, where direct equivalents existed. It has to be noted that due to differing model formulations between the deterministic model developed herein and the stochastic model, not all parameters have their direct, one-to-one equivalents. In order to effectively visualize the model's behavior and the impact of randomness, small standard deviations were assigned to these random

parameters to ensure a controlled spread of results.

A Monte Carlo Simulation approach, involving 50 independent iterations, was adopted. In each iteration, a unique set of random material parameters was sampled from their previously defined probability distributions. The equilibrium equations were solved across the full range of curvatures for each sampled set, which resulted with a random CMOD sample.

This collection of stochastic CMOD responses provided a comprehensive comparison with the predicted CMOD curve generated by the deterministic model. The choice of 50 simulations was a pragmatic decision done in order to balance the computational intensity required to solve the equilibrium equations for each iteration and the requirement for a sufficiently solid number of samples that would capture the statistical distribution of the stochastic model's output.

The main aim of this comparison is to determine if the simplified deterministic model, despite its lack of randomness, can accurately capture the average behavioral trends and the overall responses predicted by an established model with a different approach. Based on the results, the validation of the model's suitability as basis for the subsequent inverse analysis was assessed.

The results of the comparative analysis for different beam sizes is presented in Figures 6.13, 6.14, and 6.15, respectively.

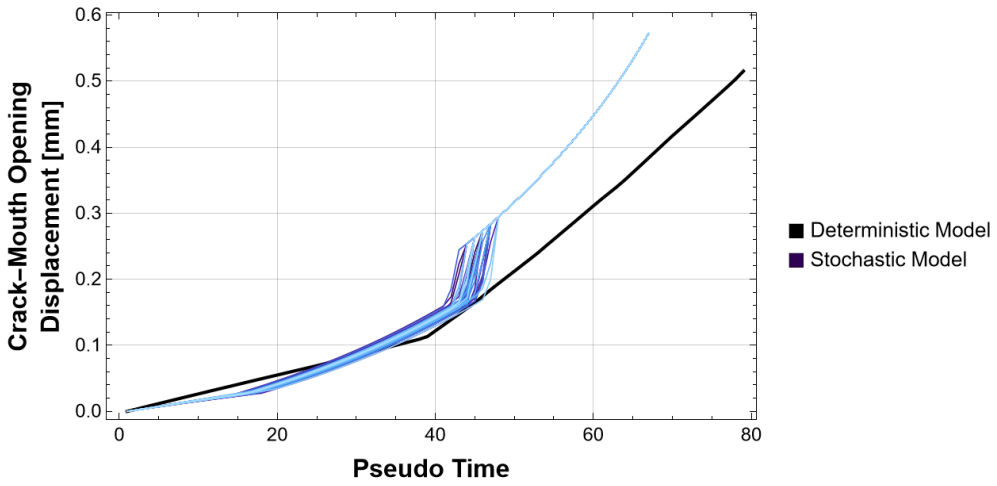

Figure 6.13: Comparison of deterministic and stochastic model CMOD responses for small beams

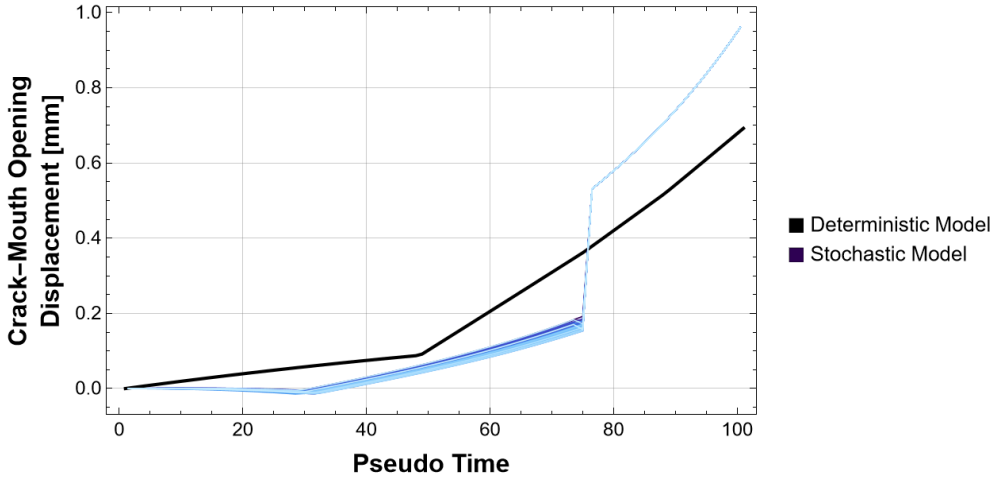

Figure 6.14: Comparison of deterministic and stochastic model CMOD responses for medium beams

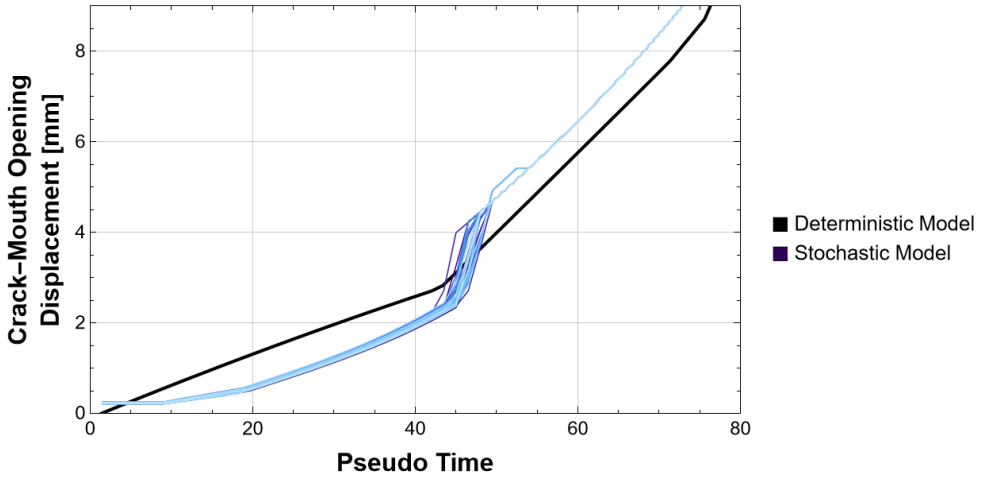

Figure 6.15: Comparison of deterministic and stochastic model CMOD responses for large beams

For all three beam sizes, the deterministic model's resulting CMOD curve generally aligns with the mean trend of the stochastic simulations, particularly in pre-cracking and early post-cracking phases. This alignment can mostly be observed in Figure 6.13 (small beam), where the deterministic model gives a good average representation of the stochastic outcomes. As the crack opening increases and fibers get pulled out the spread of the stochastic model's results becomes more pronounced, which reflects the variability in fiber distribution.

An observation made for all results is the distinct inflection point in both the deterministic and stochastic curves, which corresponds with the the onset of significant cracking and the activation of fiber bridging mechanisms. The timing and

magnitude of this in deterministic model's results is in line with stochastic results. The slope of the deterministic CMOD curve in the post-cracking phase generally follows the average slope of the stochastic ones. While the relative behavior of two result types remains consistent, the absolute values of both displacement and pseudo time posses a certain level of expected discrepancy, which is due to differences in fundamental mathematical backgrounds of the two models.

The correspondence between the deterministic model and the mean behavior of the stochastic simulations indicates that, in terms of this verification criteria, the simplified and optimized deterministic formulations can successfully replicate the average three-point bending test results. The observation that the novel model's results consistently fall within the range of variability predicted by the stochastic model indicate it to be a suitable contender for a successful inverse model implementation and analysis. Which means that while the deterministic model doesn't explicitly take into account the random variations in parameter values, its predictive accuracy for the mean response makes it a reliable tool for extracting material parameters.

6.3 Sensitivity analysis

In order to systematically quantify the influence of parameters that govern the behavior of fiber-reinforced concrete beams in bending, a sensitivity analysis was conducted. This analysis evaluates the hierarchical importance of parameters on crack mouth opening displacement in both pre-fractured and post-fractured state. It is meant to identify which parameters have the strongest impact on the bending behavior of the beam, as well as quantify parameter inter-dependencies that may affect damage evolution.

Key application of sensitivity analysis is for guiding the search process in inverse modeling, especially in cases where the initial guess for the parameters is lacking. Furthermore, if certain parameters are found to have only a negligible influence on the model's predictions, they will fixed to a reasonable value or excluded from the inverse optimization process altogether. This effectively reduces the dimensionality of the parameter space that needs to be explored and makes the optimization problem more tractable. Contrarily, parameters that show high sensitivity are those that need to be estimated with greater accuracy, and the search for their optimal values is to be prioritized and focused on their most plausible ranges.

The sensitivity analysis for any MODEL parameter $\mathbf{P}$ is done by running the forward model with $P = P_{\text{true}}$ and a slightly perturbed value, $P = P_{\text{true}} + dP$, where dP is a relatively small increment. For this research, the analysis was performed on medium-sized beams, but the general results are applicable for all beam sizes. The

behavioral patterns would follow a similar trend across other beam sizes since they're directly tied to the model's formulation, regardless of the specimen's scale. The following parameters were systematically varied within a defined range to generate CMOD output, while all other parameters were kept at constant values:

- The fibers' threshold force, F_a^{max}
- Fiber diameter, Δa
- Maximum load capacity of concrete, F_c^{max}
- Fiber position in the cross-section, h_a
- Combined fiber-matrix system's effective elasticity modulus during loading, $E_{f,T}$
- Fiber bundle influence, f_{bundle}
- Number of fibers, n_{fiber}

The resulting CMOD versus Pseudo Time curves were then plotted to visually evaluate the sensitivity of the beam's response to changes in each parameter.

The sensitivity analysis, as presented in Figures 6.16 through 6.22, show distinct influences of each parameter on the CMOD-Pseudo Time response of the FRC beam. It is generally that parameters that model the pre-peak, post-peak, or both phases of the materials' input force-displacement diagram have a corresponding influence on those same phases of the resulting crack mouth opening displacement.

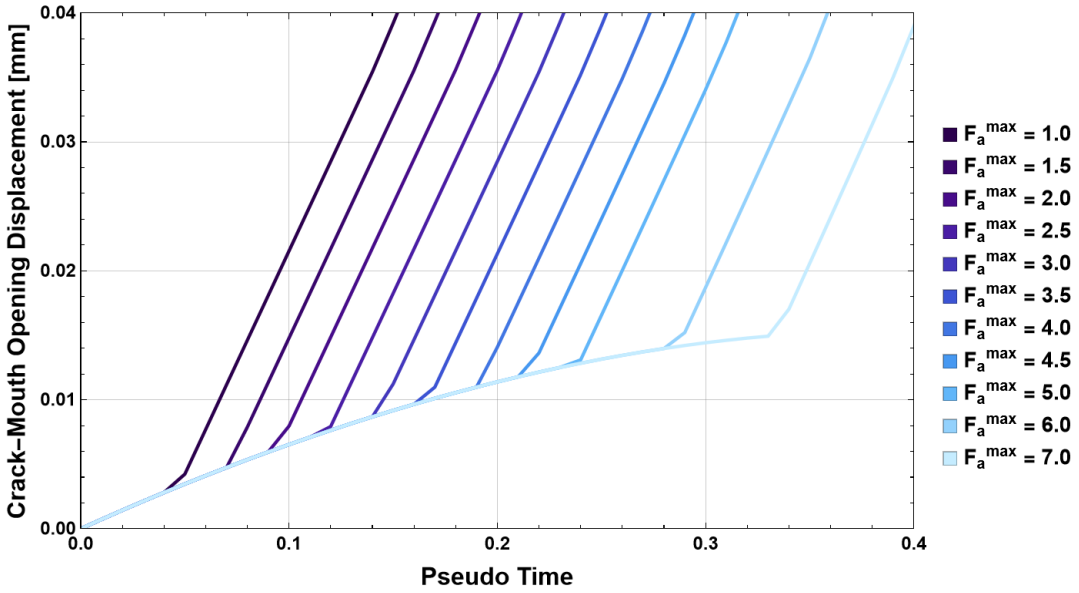

Figure 6.16: Influence of parameter F_a^{max} on CMOD-Pseudo Time response

Figure 6.16 demonstrates the significant influence of F_a^{max} on the post-fracture behavior of the beam. A higher F_a^{max} leads to a steeper CMOD curve in the post-peak region, which suggest an improved crack bridging capacity and greater resistance to crack propagation and opening after the initial fracture. This parameter mostly dictates the maximum force that individual fibers can bear before pull-out, which directly affects the ductility and residual strength of the FRC beam overall. This parameter's impact on the post-peak behavior indicates that F_a^{max} is a critical for characterizing the toughening effect of fibers and will require precise estimation in inverse analysis.

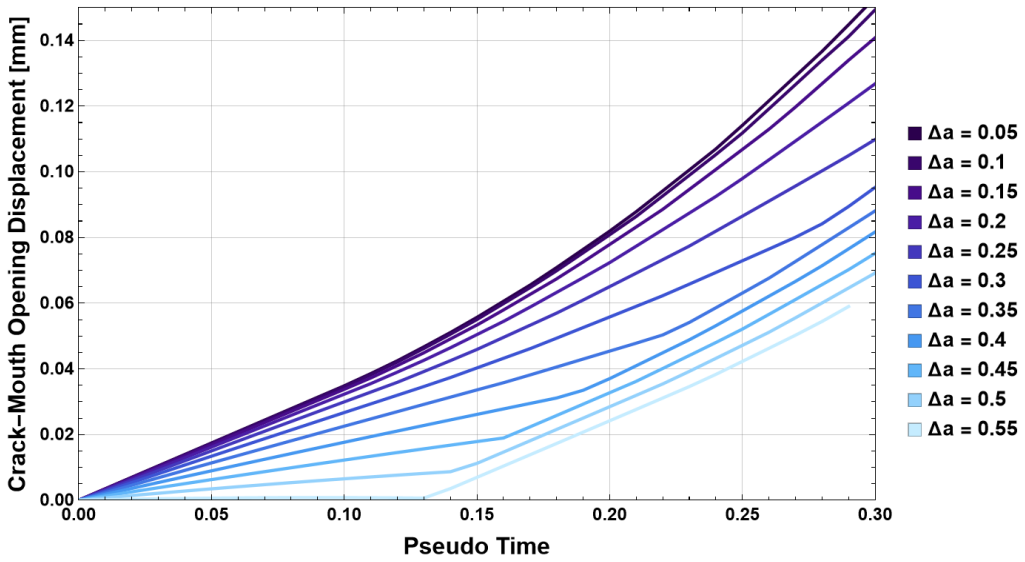

Figure 6.17: Influence of parameter Δa on CMOD-Pseudo Time response

As seen in Figure 6.17, the individual fiber diameter, Δa has influence on the entire CMOD-Pseudo Time curve, and it affects both pre and post-preak phases. Larger fiber diameters generally lead to a stiffer response and higher displacement for a same observed pseudo time step. This can be attributed to the larger cross-sectional area of individual fibers contributing to a greater load transfer capacity of the entire fiber. This parameter scales the contribution of individual fibers to the overall collective behavior which makes it valuable for an accurate parameter identification.

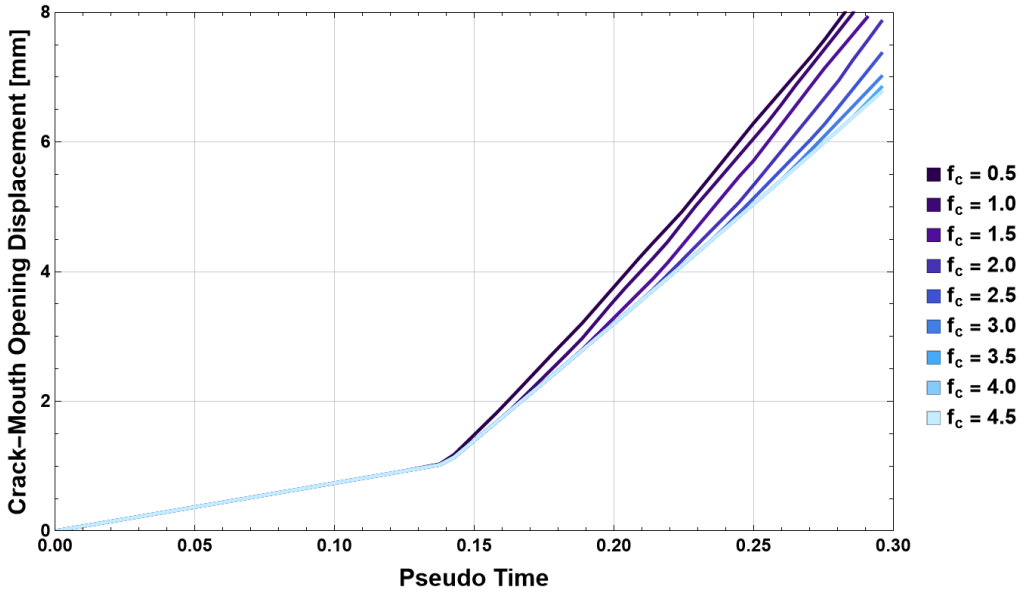

Figure 6.18: Influence of parameter f_c^{max} on CMOD-Pseudo Time response

The influence of f_c^{max} is shown in 6.18, where it's demonstrated that the maximum load capacity of the concrete matrix alone, has minimal effect during the initial loading phase as all curves follow a nearly identical path until the onset of cracking. However, in the post-peak phase, once the micro-cracking occurs, fiber bridging is activated and becomes the dominant load bearing mechanism, and f_c^{max}'s influence on the displacement becomes more noticeable. This is due to concrete, even though secondary, still plays a role in load bearing alongside the fibers. The contribution of concrete in this phase of loading is mainly governed by the value of this parameter.

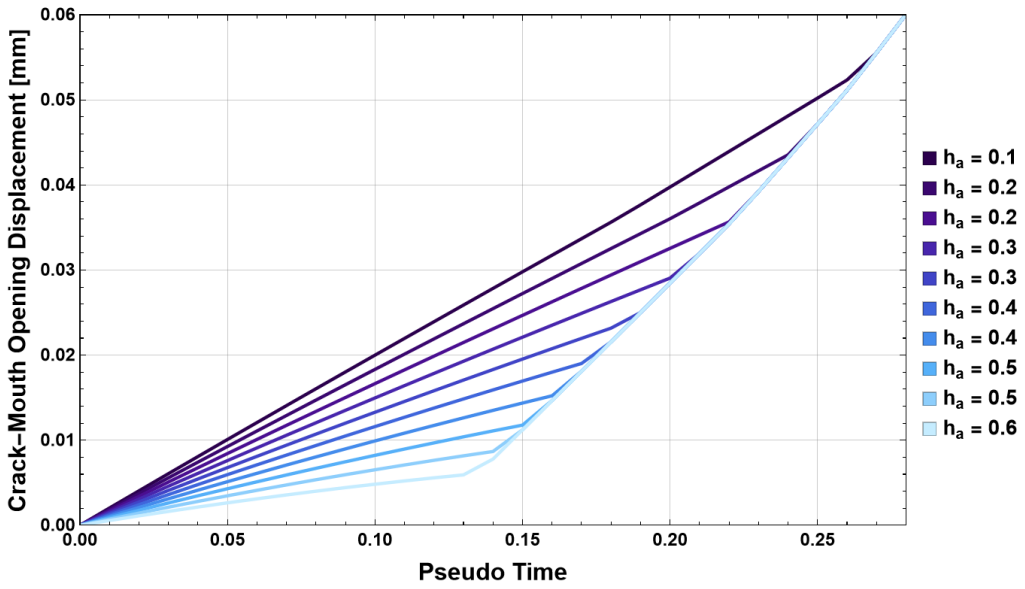

Figure 6.19: Influence of parameter h_a on CMOD-Pseudo Time response

The role of role of fiber position in the cross-section, h_a, during beam bending is shown on Figure 6.19. The vertical placement of fibers significantly impacts all phases of bending and impacts the overall evolution of CMOD. Varying the h_a values noticeable impacts the beam's flexural response. Fibers closer to the tension face (higher h_a values) cause the fiber bridging mechanism to be activated earlier and an overall les brittle response from the beam. This parameter is fundamental to the structural efficiency of the fiber reinforcement and its accurate determination is vital in optimization procedures.

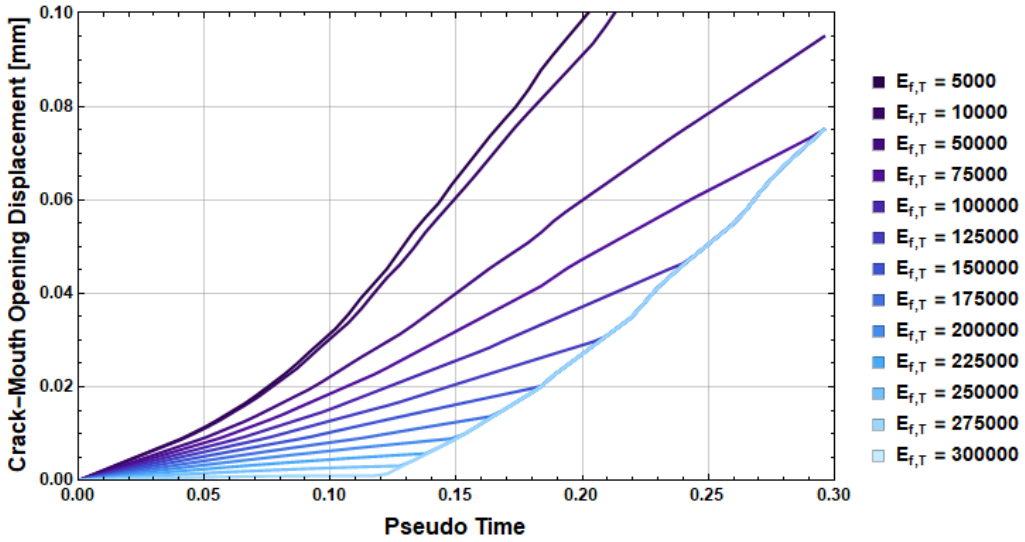

Figure 6.20: Influence of parameter $E_{f,T}$ on CMOD-Pseudo Time response

Figure 6.20 presents the results of the sensitivity analysis performed for the fiber-matrix combined effective modulus during loading, $E_{f,T}$. It's observed how this parameter particularly affects the stiffness of the beam, as higher values correspond with a more stiffer response from the beam, especially in the pre-peak phase, while beams with fiber with significantly low $E_{f,T}$ basically behave like regular concrete beams with no added reinforcement. This reiterates that the elastic properties of the individual fibers play a role in the overall deformation behavior of the FRC beam. This parameter directly governs how much load the fibers carry elastically before breaking or getting pull-out.

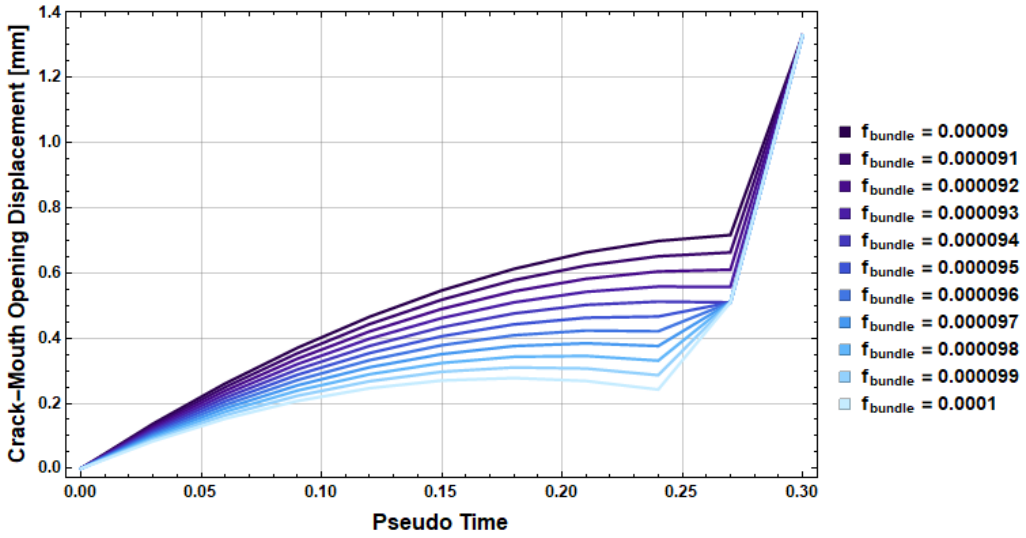

Figure 6.21: Influence of parameter f_{bundle} on CMOD-Pseudo Time response

Figure 6.21 shows the influence of parameter f_{bundle} that links the properties of a singular fiber with the observed bundle in the cross section. This parameter appears to explicitly influence the pre-peak stage and has little to no influence after fiber pull-out. A higher f_{bundle} value results in a stiffer response and a greater load-carrying capacity. The main takeaway is how this parameter is affecting the transitional phase from concrete-dominated to fiber-dominated behaviour, and its impact suggests it playing a role in calibrating the overall effectiveness of the fiber reinforcement.

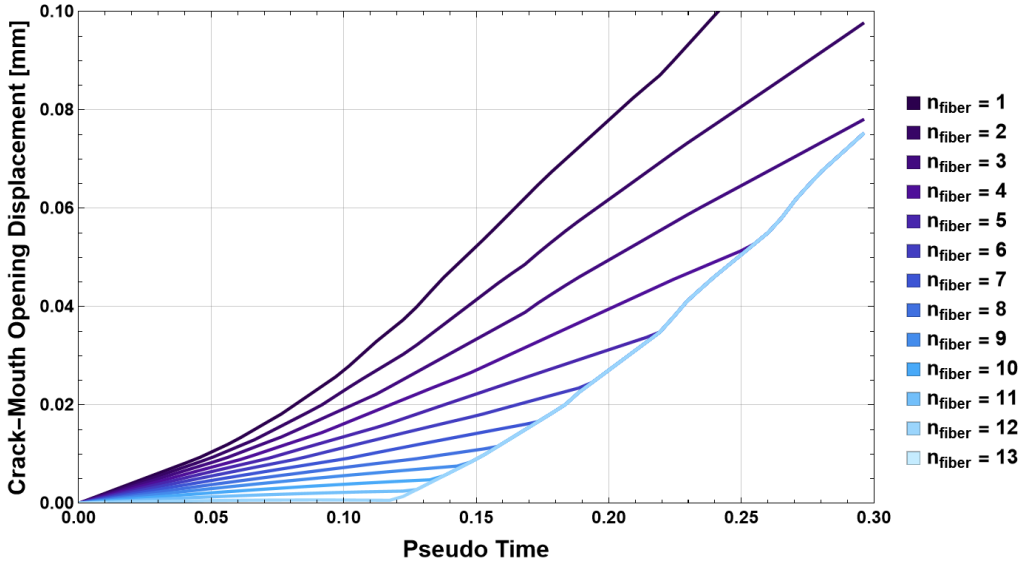

Figure 6.22: Influence of parameter n_{fiber} on CMOD-Pseudo Time response

The sensitivity analysis of n_{fiber}, in Figure 6.22, shows that the number of fibers has an pronounced effect on the stiffness of the beam and compeltel pullout time. A

greater number of fibers generally leads to a much stiffer and more ductile response in the post-peak regime, which lets the beam to sustain higher CMOD values with increased resistance. This is expected, as more fibers in the beam means more to more crack bridging elements, which directly the composite's ability to resist crack propagation and maintain load transfer. The beam's response shows a great sensitivity to this particular parameter.

The conducted sensitivity analysis provides an insights into the importance and interdependencies of the governing parameters of the FRC beam's bending behavior. It systematically quantifies how changes in material and geometric properties influence the CMOD response, and confirmed that parameters that affect the pre-peak properties primarily govern the initial response, while those related to fiber contribution are ones having a critical role in the post-peak phase where the ductile behavior is present. Parameters such as F_a^{max}, Δa, $E_{f,T}$, h_a, f_{bundle}, and n_{fiber} show significant sensitivity,which highlighting their importance for accurately describing the characteristics of FRC, while F_c^{max} manly affects the pre-cracking regime.

This analysis will serve as a tool for the subsequent and any future inverse analysis. Parameters showing high sensitivity will be prioritized for estimation, and their search space will be based on their observed influence. On the other hand, parameters with little to no influence will be extracted with the purpose of validating the inverse model, but in any future parametric analysis they may be treated as fixed. This systematic understanding of parameter sensitivity is crucial for planning an efficient inverse optimization strategy, especially in cases where a global minimum might not be clearly presenting.

6.4 Verification using Synthetic Data

This section presents the process and the results of the verification of the developed inverse analysis procedure through the use of "synthetic" experimental data. The inverse model's accuracy and robustness was tested using data crack mouth opening displacement data generated by the predictive model where all model parameters are defined as deterministic and are known beforehand. This helps ensuring that the model implementation is without errors and works as intended from a technical standpoint, before its it is applied to more noisy and uncertain laboratory experimental data.

The analysis involves several preparatory steps necessary establish a controlled environment for testing the model's capability of parameter extraction. A "true" numerical model is first defined by selecting a specific, physically realistic value for the chosen parameter P_{true} that is intended to be extracted via the inverse procedure. All other material and geometric parameters in the predictive model are assiged to

fixed, known values, which remain as such throughout the analysis. This defined, "true" model, is then used to generate synthetic target data for the crack mouth opening displacement, which serves as an idealistic experimental reference.

The use of synthetic data is crucial at this stage, because it allows for an unambiguous validation of the inverse procedure's algorithmic integrity. Since the synthetic data is generated using the exact same predictive model formulations as in inverse model, the implemented inverse algorithm is correct only if the extracted P_{true} exhibits zero error, thereby confirming that the equations, algorithms, and code for the inverse process are accurately implemented according to the conceptual and mathematical model before its application to noisy and uncertain actual laboratory experimental data.

After the generation of target data, a visual sensitivity of the model's CMOD output to variations in the parameter P is performed. The inverse analysis for each parameter begins with defining a plausible range of initial guesses (P_0). This range is not arbitrary, but is established by referencing the known physical constraints of the materials. For instance, the nominal diameter of the steel fibers is 0.55 mm, which is a value that provides a realistic center point. Similarly, the elasticity modulus is bounded by known values for typical fibers (e.g., $E_{\text{f,T}}$ ranging from low-stiffness polypropylene to high-stiffness carbon). This reliance on physically sound initialization is key to solving the inverse problem efficiently and ensuring that the final convergence is physically meaningful, even when starting far from the true value. The results are presented as lists that include values below, above, close to, and further from P_{true}, while also considering the physically plausible range for tested P. The specific range chosen for each parameter is aimed to understand the algorithm's behavior with both good and relatively poor starting estimates.

After this, the perturbation value dP used for the numerical calculation of sensitivity coefficients, is defined. Its value is set to a small $(1 - 3\%)$ fraction of the assumed magnitude of P_{true}. Furthermore, a maximum number of iterations is set to prevent indefinite execution if convergence is not achieved, and a tolerance criterion for the change in the parameter estimate $|\Delta P|$ is defined to signal convergence.

The iterative inverse analysis procedure is performed for each selected initial guess of the parameter P, as detailed in the subsequent sections for each specific parameter investigated. In addition to the final converged values, the performance of the inverse algorithm was further assessed and quantified by determining the basin of attraction (BoA). The BoA represents the range of initial guesses from which the algorithm will successfully converge to the true parameter value, where a wider BoA indicates a more robust and a less guess-dependent model.

6.4.1 Inverse Extraction of Synthetic Δa

This subsection showcases results of the inverse analysis of the parameter Δa, representing a single fiber's cross section diameter. The inverse procedure was tested across all three beam sizes and a wide range of initial guesses, and the results are summarized in Tables 6.2, 6.3 and 6.4.

Table 6.2: Summary of Inverse Iteration Results for Estimating Δa on Large-Sized Samples

True Δa Value (Δa)	Initial Guess (Δa_0)	Iterations (k)	Final Result (Δa_{k+1})	BoA Range (% of true value)
0.1	0.03	8	0.1	2470
	0.2	4	0.1	
	0.35	3	0.1	
	0.5	6	0.1	
	2.5	8	0.1	
0.2	0.06	9	0.2	1220
	0.1	5	0.2	
	0.35	4	0.2	
	0.5	4	0.2	
	2.5	8	0.2	
0.35	0.11	7	0.35	683
	0.2	4	0.35	
	0.5	3	0.35	
	2.5	6	0.35	
0.5	0.15	6	0.5	470
	0.2	5	0.5	
	0.35	3	0.5	
	2.5	5	0.5	

Table 6.3: Summary of Inverse Iteration Results for Estimating Δa on Medium-Sized Samples

True Δa Value (Δa)	Initial Guess (Δa_0)	Iterations (k)	Final Result (Δa_{k+1})	BoA Range (% of true value)
0.1	0.03	9	0.1	2070
	0.05	7	0.1	
	0.2	5	0.1	
	0.5	7	0.1	
	2.1	9	0.1	
0.2	0.06	8	0.2	720
	0.07	8	0.2	
	0.1	6	0.2	
	0.15	4	0.2	
	0.25	4	0.2	
	0.5	5	0.2	
	0.7	6	0.2	
	1.5	7	0.2	
0.35	0.13	6	0.35	985
	0.15	6	0.35	
	0.25	4	0.35	
	0.4	3	0.35	
	2.1	5	0.35	
0.5	0.17	5	0.5	551
	0.2	6	0.5	
	0.3	4	0.5	
	0.4	3	0.5	
	0.5	3	0.5	
	0.6	3	0.5	
	0.7	4	0.5	
	0.8	4	0.5	
	0.9	5	0.5	
	1.1	4	0.5	
	1.2	5	0.5	
	1.3	5	0.5	
	2.1	5	0.5	

Table 6.4: Summary of Inverse Iteration Results for Estimating Δa on Small-Sized Samples

True Δa Value (Δa)	Initial Guess (Δa_0)	Iterations (k)	Final Result (Δa_{k+1})	BoA Range (% of true value)
0.1	0.04	6	0.1	890
	0.09	2	0.1	
	0.11	2	0.1	
	0.2	5	0.1	
	0.35	6	0.1	
	0.5	6	0.1	
	0.93	7	0.1	
0.2	0.08	6	0.2	850
	0.1	5	0.2	
	0.35	4	0.2	
	0.5	5	0.2	
	0.93	6	0.2	
0.35	0.11	6	0.35	410
	0.2	3	0.35	
	0.5	4	0.35	
	0.93	5	0.35	
0.5	0.14	5	0.5	226
	0.2	4	0.5	
	0.35	3	0.5	
	0.93	4	0.5	

The results show that the method is generally capable of converging to the true Δa value for a wide range of initial guesses, with convergence achieved on average within 5 iterations. Initial guesses closer to the true value converged most rapidly, while those further away required more steps for the algorithm to correct the initial deviation. The convergence accuracy is 100% when a solution is reached, which fulfills the primary objective of this verification stage and confirms the technical integrity of the inverse algorithm for Δa.

A limitation was observed for guesses too lower from the true one, as those produced an extremely large update step in the first iteration, which calculated the next guess to be extremely high. With such overly inflated value, entirely outside any physically plausible ranges for realistic fiber dimensions, the predictive part of the inverse model failed to compute a CMOD curve in any subsequent iteration. This failure seen only in values lower than the true one can be attributed to the non-linear relationship between Δa and the CMOD, and the behavior of the sensitivity term $\chi_{\Delta a,i} = \frac{\partial d_{\mathrm{CMOD}\,i}}{\partial \Delta a}$.

These relatively too low guesses leads to a low sensitivity $\chi_{\Delta a,i}$, and therefore a very small sum of squared sensitivities, $\sum_{i=1}^{n} \chi_{\Delta a,i}^2$. When a potentially large error term, $\sum_{i=1}^{n}(y_i - d_{\text{CMOD }i}(\Delta a)) \cdot \chi_{\Delta a,i}$, is divided by this very small denominator in the update equation:

$$\Delta(\Delta a) = \frac{\sum_{i=1}^{n}(y_i - d_{\text{CMOD }i}(\Delta a)) \cdot \chi_{\Delta a,i}}{\sum_{i=1}^{n} \chi_{\Delta a,i}^2} \tag{6.5}$$

a disproportionately large update step can occur. This "overshoot" pushes the parameter estimate into a region where the forward model becomes numerically unstable or the parameter value physically unrealistic. In contrast, for an initial guess like $\Delta a = 1.3$ in case of true $\Delta a = 0.5$, while the initial error $(y_i - d_{\text{CMOD }i}(\Delta a))$ is also large, the model's sensitivity to changes in Δa in that higher range appears to be more substantial. This results in a more appropriately scaled update step, and allows a more stable convergence towards the true value.

A distinct relationship between the BoA range and the magnitude of the true Δa value was observed. For all beam sizes, as the true value of Δa increases, the BoA range as a percentage of the true value decreases. This is only relative to the true Δa, as the absolute range of guesses within which a successful convergence occur is pretty much stable across all true Δa.

However, a trend in the BoA range appears to be correlated with the beam size. For a given true Δa value, the BoA range is largest for the large beams and smallest for the small beams. This suggests that the model's sensitivity and the complexity of the error surface are functions of the beam's geometry. In smaller beams, where geometric effects are more pronounced, the inverse algorithm seems to have a more constrained and complex search space, which limitis the model's robustness to a wide range of initial guesses. This observation also provides a partial explanation for why inverse analysis might be more challenging to perform on smaller specimens with real experimental data.

6.4.2 Inverse Extraction of Synthetic h_a

The inverse analysis for the synthetically generated fiber position parameter, h_a, was done for all three beam sizes. The results are summarized in Tables 6.5, 6.6, and 6.7, and show consistent and rapid convergence to the true values for a wide range of initial guesses. The iterative procedure consistently converged to the true value for h_a with 100% accuracy and fulfilled the primary objective of this verification stage.

Table 6.5: Summary of Inverse Iteration Results for Estimating h_a on Large-Sized Samples

True h_a Value (h_a)	Initial Guess (h_{a_0})	Iterations (k)	Final Result ($h_{a_{k+1}}$)	BoA Range (% of true value)
0.05	-1.7	4	0.05	8200
	0.01	2	0.05	
	0.2	2	0.05	
	0.5	3	0.05	
	0.8	3	0.05	
	0.95	3	0.05	
	1.5	3	0.05	
	2.4	5	0.05	
0.5	-1.7	4	0.5	820
	0.05	2	0.5	
	0.8	2	0.5	
	0.95	3	0.5	
	1.5	4	0.5	
	2.4	4	0.5	
0.8	-1.7	4	0.8	512
	0.05	3	0.8	
	0.5	3	0.8	
	0.95	2	0.8	
	2	3	0.8	
	2.4	4	0.8	
0.95	-1.7	4	0.95	432
	0.05	3	0.95	
	0.5	4	0.95	
	0.8	3	0.95	
	1.5	3	0.95	
	2	3	0.95	
	2.4	4	0.95	

Table 6.6: Summary of Inverse Iteration Results for Estimating h_a on Medium-Sized Samples

True h_a Value (h_a)	Initial Guess (h_{a_0})	Iterations (k)	Final Result ($h_{a_{k+1}}$)	BoA Range (% of true value)
0.1	-2.5	5	0.1	5000
	0.05	2	0.1	
	0.35	3	0.1	
	0.5	3	0.1	
	0.8	3	0.1	
	2.5	4	0.1	
0.35	-2.5	5	0.35	1686
	-2	4	0.35	
	0.05	3	0.35	
	0.65	3	0.35	
	0.8	3	0.35	
	3.4	4	0.35	
0.5	-2.5	5	0.5	1180
	0.05	3	0.5	
	0.1	3	0.5	
	0.65	2	0.5	
	0.8	2	0.5	
	3.4	4	0.5	
0.65	-2.5	5	0.65	908
	0.05	3	0.65	
	0.1	3	0.65	
	0.35	3	0.65	
	0.5	2	0.65	
	0.8	2	0.65	
	3.4	4	0.65	

Table 6.7: Summary of Inverse Iteration Results for Estimating h_a on Small-Sized Samples

True h_a Value (h_a)	Initial Guess (h_{a_0})	Iterations (k)	Final Result ($h_{a_{k+1}}$)	BoA Range (% of true value)
0.01	-3.7	5	0.01	87000
	0.15	2	0.01	
	0.3	3	0.01	
	0.39	3	0.01	
	0.8	3	0.01	
	5	4	0.01	
0.15	-3.7	5	0.15	5800
	0.01	2	0.15	
	0.3	2	0.15	
	0.39	3	0.15	
	0.8	3	0.15	
	5	4	0.15	
0.3	-3.7	5	0.3	2900
	0.01	3	0.3	
	0.15	2	0.3	
	0.39	2	0.3	
	0.8	3	0.3	
	5	4	0.3	
0.39	-3.7	4	0.39	2231
	0.01	3	0.39	
	0.15	2	0.39	
	0.3	2	0.39	
	0.8	3	0.39	
	5	4	0.39	

The most striking observation from the analysis is the relatively large range of values for which the model converged successfully. This is quantitatively seen by the BoA ranges, which were 4.1 cm, 5.0 cm and 8.7 cm for large, medium, and small beams, respectively. When expressed as a percentage of the true value, this resulted in a BoA range as high as 87,000% for small-sized beams with a true h_a of 0.01 cm. It is found that the BoA range is largest for smaller beam sizes, which suggests that the model's sensitivity and the complexity of the search space are functions of the specimen's geometry.

As seen in the presented tables, the iterative procedure successfully converged to the true value for h_a even when initial guesses were outside the physical boundaries of the beam ($h\_a < 0$ or $h_a > h$). This is due to the mathematical formulation of the predictive model and the nature of gradient-based optimization. The equations

defining the fiber's contribution to force and moment are mathematically defined for any numerical value of h_a. The inverse algorithm does not inherently "know" nor is written to take in account values only within the physical bounds of the beam, and therefore does not disregard initial guesses that are physically unrealistic. As long as the fiber constitutive law is defined such that it still produces a calculable force and a non-zero sensitivity ($\chi_{ha} = \frac{\partial \mathrm{CMOD}}{\partial h_a}$) in that region, the algorithm can still determine the direction in which to adjust h_a. If the target CMOD data (measured data) indicates a fiber contribution, the error term will be sizable even when the guessed h_a places fibers ineffectively. The optimizer iteratively adjusts the initially guessed value, which is guided by the sensitivity, to bring the fiber position to a location that gets it to contribute to the beam's behavior and thus minimizes the error, even when starting from a non-physical location.

The algorithm's ability to converge from such physically unrealistic starting points shows that the error surface in the parameter space contains gradients that effectively navigate the solution towards a physically correct minimum.

6.4.3 Inverse Extraction of Synthetic $E_{\mathrm{f,T}}$

This section details the verification of the inverse model for the fiber-matrix combined effective elasticity modulus during loading, $E_{\mathrm{f,T}}$. The procedure was tested across all three beam sizes (Tables 6.8, 6.9, and 6.10) and a wide range of values to represent different fiber types, from less stiff glass and polypropylene (PP) fibers (as low as 5000 N/mm^2) to stiff basalt and carbon fibers (up to 300000 N/mm^2)

In this chapter, the inverse model's verification was conducted by extracting the fiber-matrix combined effective elasticity modulus during loading„ $E_{\mathrm{f,T}}$), on medium-sized samples. The testing covered a range from minimum to maximum converged values, along with plausible values representing commercially available steel fibers. Furthermore, its performance was assessed for less stiff fibers, including glass and polypropylene (PP) fibers, by extracting preset $E_{\mathrm{f,T}}$ values within the range of 5 to 75 GPa (or approximately 500 to 7500 kp/mm^2). In the same manner, $E_{\mathrm{f,T}}$ was set to 100000 and 300000 kp/mm^2 to generate synthetic data, which was then used to extract these same values for cases involving basalt and carbon fibers, respectively.

Table 6.8: Summary of Inverse Iteration Results for Estimating $E_{f,T}$ on Large-Sized Samples

True $E_{f,T}$ Value (N/mm^2)	Initial Guess (N/mm^2)	Iterations (k)	Final Result (N/mm^2)	BoA Range (% of true value)
5000	1	3	5000	960
	2500	3	5000	
	10000	3	5000	
	25000	3	5000	
	48000	5	5000	
75000	1	4	75000	807
	5000	4	75000	
	100000	3	75000	
	210000	4	75000	
	300000	4	75000	
	605000	6	75000	
100000	1	4	100000	645
	5000	4	100000	
	75000	3	100000	
	210000	3	100000	
	300000	4	100000	
	645000	5	100000	
210000	1	4	210000	730
	5000	4	210000	
	75000	5	210000	
	100000	5	210000	
	300000	4	210000	
	730000	7	210000	
300000	1	4	100000	438
	5000	5	300000	
	210000	4	300000	
	500000	3	300000	
	920000	8	300000	

Table 6.9: Summary of Inverse Iteration Results for Estimating $E_{f,T}$ on Medium-Sized Samples

True $E_{f,T}$ Value (N/mm^2)	Initial Guess (N/mm^2)	Iterations (k)	Final Result (N/mm^2)	BoA Range (% of true value)
5000	1	3	5000	3200
	2500	3	5000	
	75000	4	5000	
	160000	4	5000	
75000	1	4	75000	593
	70000	3	75000	
	210000	4	75000	
	445000	5	75000	
100000	1	4	100000	500
	5000	4	100000	
	75000	3	100000	
	210000	4	100000	
	500000	5	100010	
210000	1	5	210000	405
	150000	4	210000	
	200000	3	210000	
	250000	3	210000	
	400000	4	210000	
	850000	6	210000	
300000	1	5	100000	492
	75000	4	100000	
	100000	4	100000	
	210000	4	300000	
	400000	4	300000	
	1475000	5	300000	

Table 6.10: Summary of Inverse Iteration Results for Estimating $E_{f,T}$ on Small-Sized Samples

True $E_{f,T}$ Value (N/mm^2)	Initial Guess (N/mm^2)	Iterations (k)	Final Result (N/mm^2)	BoA Range (% of true value)
5000	1	2	500	4600
	75000	3	5000	
	210000	3	5000	
	230000	3	5000	
75000	1	3	75000	400
	5000	3	75000	
	210000	3	75000	
	300000	4	75000	
100000	1	4	100000	750
	75000	3	100000	
	210000	3	100000	
	300000	4	100000	
	810000	5	100000	
210000	1	4	210000	1002
	75000	3	210000	
	100000	3	210000	
	300000	4	210000	
	2105000	4	210000	
300000	1	5	300000	702
	5000	4	300000	
	75000	4	300000	
	210000	4	300000	
	350000	3	300000	
	2105000	5	300000	

The results demonstrated that the inverse model consistently and accurately converged to the true $E_{f,T}$ value for a vast range of initial guesses, with a 100% accuracy in all successful convergence cases. This confirms that the model's stability and ability to handle parameters is applicable to a broad spectrum of physical magnitudes. The convergence was also consistently fast, with the algorithm typically requiring only 3 to 5 iterations to reach the solution.

A trend was observed in the tables is the inverse relationship between the magnitude of the true $E_{f,T}$ and the value of the BoA range. For all beam sizes, the BoA range, both at its absolute value and as a percentage of the true value, is largest for a low modulus and decreases as the modulus increases. For instance, in medium-sized beams, a true $E_{f,T}$ of 5000 N/mm^2 has a BoA of 160000 or 3200%, while a true $E_{f,T}$ of 210000 N/mm^2 has a BoA of 850000 or 405%. This means that for less stiff

beams, the inverse algorithm has a much broader and more forgiving search space, which likely comes from the model's sensitivity to this parameter in different regions of the CMOD curve.

Furthermore, a distinct size effect is also evident in the BoA ranges. For the same true $E_{\text{f,T}}$, the BoA range is largest for smaller beams and decreases as the beam size increases. This suggests that the complexity of the error surface for this parameter is more constrained in larger specimens, which leads to a narrower range of initial guesses that can successfully guide the algorithm to the correct solution. However, an exception to the convergence pattern occurred with a true value o f5000 N/mm^2 when an initial guess of 75000 N/mm^2 failed to converge for large beams, as seen in A.46. Despite the initial guess being well within the BoA of other cases, this failure confirms how non-linear optimization is not only dependent on the distance of the initial guess from the true value, but also on the specific shape of the error surface. In this instance, a much higher initial guess predicts an overall much stiffer beam than the target, and the algorithm had to optimize with overly aggressive update steps that lead to computational failure.

6.4.4 Inverse Extraction of Synthetic f_{bundle}

This subsection presents the results of the verification of the inverse model for the empirical scaling parameter, for all three beam sizes and a wide range of initial guesses. The results are summarized in Tables 6.11, 6.12, and 6.13.

Table 6.11: Summary of Inverse Iteration Results for Estimating f_{bundle} on Large-Sized Samples

True f_{bundle} Value —	Initial Guess —	Iteration (k)	Final Result —	BoA Range (% of true value)
0.000001	0.0000001	4	0.000001	990
	0.000001	4	0.000001	
	0.000005	5	0.000001	
	0.00001	8	0.000001	
0.00005	0.000001	6	0.00005	198
	0.00004	4	0.00005	
	0.0001	4	0.00005	
0.000095	0.000001	7	0.000095	99
	0.000005	7	0.000095	
	0.0001	2	0.000095	
0.0001	0.0000001	8	0.0001	100.9
	0.000001	8	0.0001	
	0.00001	8	0.0001	
	0.00005	5	0.0001	
	0.000095	3	0.0001	
	0.000101	2	0.0001	

Table 6.12: Summary of Inverse Iteration Results for Estimating f_{bundle} on Medium-Sized Samples

True f_{bundle} Value —	Initial Guess —	Iteration (k)	Final Result —	BoA Range (% of true value)
0.00001	0.000001	4	0.00001	390
	0.000005	4	0.00001	
	0.000015	4	0.00001	
	0.00004	5	0.00001	
0.00005	0.000001	5	0.00005	198
	0.00004	3	0.00005	
	0.0001	3	0.00005	
0.000095	0.000001	5	0.000095	103
	0.000085	3	0.000095	
	0.0001	3	0.000095	
	0.000104	3	0.000095	
0.0001	0.00000001	5	0.000095	90
	0.000001	5	0.0001	
	0.000005	5	0.0001	
	0.00005	4	0.0001	
	0.00009	3	0.0001	

Table 6.13: Summary of Inverse Iteration Results for Estimating f_{bundle} on Small-Sized Samples

True f_{bundle} Value —	Initial Guess —	Iteration (k)	Final Result —	BoA Range (% of true value)
0.000001	0.0000001	2	0.000001	9990
	0.000005	3	0.000001	
	0.00005	4	0.000001	
	0.0001	4	0.000001	
0.00001	0.0000001	4	0.000001	999
	0.000001	3	0.00001	
	0.00005	3	0.00001	
	0.0001	3	0.00001	
0.00005	0.0000001	4	0.00005	200
	0.000001	4	0.00005	
	0.00001	3	0.00005	
	0.0001	3	0.00005	
0.0001	0.0000001	4	0.0001	50
	0.000001	3	0.0001	
	0.00001	3	0.0001	
	0.00005	3	0.0001	

The results show that the inverse model consistently and accurately converged to the true f_{bundle} value for a wide range of initial guesses, with 100% accuracy in all successful convergence cases. The convergence was also consistently fast, with the algorithm typically requiring only 2 to 8 iterations to reach the final solution.

The BoA range, when expressed as a percentage of the true value appears as variable, but its absolute value remains consistently between 0.00005 and 0.0001 across all beam sizes, without any apparent trend. This suggests that the stability of the model is tied to a specific magnitude of this empirical parameter. The analysis of the BoA range shows that the model is numerically stable as long as the search space for f_{bundle} does not exceed a certain absolute boundary, regardless of the specimen's size. Furthermore, for a given absolute BoA, the relative percentage range is significantly larger for a smaller beam (e.g., BoA range of 9990% for a true value of 1×10^{-6} in small beams) and decreases as the beam size increases. This is a direct consequence of dividing a constant absolute BoA by a smaller true value, and it provides insight into how the parameter's magnitude affects the perception of the algorithm's search space.

It was determined that inverse analysis for extracting f_{bundle} does not work for negative values of initial guesses, as well as an initial guess that equals zero. However, the model was tested for initial guesses as low as $f_{\text{bundle}} = 1 \times 10^{-6}$, and it was

concluded that no matter how small the initial guess for f_{bundle} is the inverse model will be able to preform the iteration as long as the initial guess is a non-zero, non-negative value. This shows the numerical stability of the algorithm even for values that approach a singularity in the optimization space.

It is observed that crack mouth opening displacement generated with values higher than $f_{bundle} \approx 0.000105$ would contain non-physical negative values, which leads to the model not being able to properly capture the post-cracking behavior. This is an important boundary of the model's applicability on inverse identification of f_{bundle}, as there is a clear range of values where it can be applied that are defined by the model's numerical stability limits and physical realism boundaries. Knowing this limitation will come in handy for interpreting results when the model is applied to real experimental data.

6.4.5 Inverse Extraction of Synthetic f_c^{max}

This subsection verification of the inverse model for the concrete threshold force, f_c^{max}, which governs the pre-cracking behavior of the beam is shown. The analysis was done across three beam sizes (Tables 6.14, 6.15, and 6.16) and a wide range of initial guesses.

Table 6.14: Summary of Inverse Iteration Results for Estimating f_c^{max} on Large-Sized Samples

True f_c^{max} Value (kN/mm^2)	Initial Guess (kN/mm^2)	Iterations (k)	Final Result (kN/mm^2)	BoA Range (% of true value)
1	0.01	4	1.0	809
	0.5	3	1.0	
	2.0	4	1.0	
	3.0	4	1.0	
	4.5	4	1.0	
	8.1	5	1.0	
2	0.01	4	2.0	420
	1.0	3	2.0	
	1.5	2	2.0	
	3.0	3	2.0	
	4.5	4	2.0	
	8.4	4	2.0	
3	0.01	5	3	450
	1.0	3	3.0	
	2.0	3	3.0	
	2.5	3	3.0	
	4.5	3	3.0	
	9.0	5	3.0	
4.5	0.01	5	4.5	356
	1.0	3	4.5	
	2.0	3	4.5	
	3.0	2	4.5	
	5.0	3	4.5	
	10.7	5	4.5	

Table 6.15: Summary of Inverse Iteration Results for Estimating f_c^{max} on Medium-Sized Samples

True f_c^{max} Value (kN/mm²)	Initial Guess (kN/mm²)	Iterations (k)	Final Result (kN/mm²)	BoA Range (% of true value)
1.5	0.0	4	1.5	380
	2.0	3	1.5	
	3.0	3	1.5	
	4.5	4	1.5	
	5.7	5	1.5	
2	0.0	3	2	300
	1.5	2	2	
	2.25	2	2	
	3.0	3	2	
	4.0	3	2	
	6.0	5	2	
3	0.0	4	3	250
	1.5	3	3	
	2.0	3	3	
	3.25	2	3	
	4.5	3	3	
	7.5	6	3	
4	0.0	5	4.5	323
	1.5	4	4.5	
	2.0	4	4.5	
	3.0	3	4.5	
	5.0	3	4.5	
	9.7	6	4.5	

Table 6.16: Summary of Inverse Iteration Results for Estimating f_c^{max} on Small-Sized Samples

True f_c^{max} Value (N/mm^2)	Initial Guess (N/mm^2)	Iterations (k)	Final Result (N/mm^2)	BoA Range (% of true value)
0.4	0	4	0.4	750
	0.3	2	0.4	
	0.6	3	0.4	
	0.8	3	0.4	
	1.5	4	0.4	
	3.0	4	0.4	
0.6	0.01	4	0.6	815
	0.4	2	0.6	
	0.8	4	0.6	
	1.5	4	0.6	
	4.9	4	0.6	
0.8	0.01	3	0.8	624
	0.4	3	0.8	
	0.6	3	0.8	
	1.5	3	0.8	
	5.0	4	0.8	
1.5	0	4	1.5	488
	0.4	3	1.5	
	0.6	3	1.5	
	1.25	2	1.5	
	2.0	2	1.5	
	3.9	5	1.5	
2	0	4	2	267
	0.4	3	2	
	0.6	3	2	
	0.8	3	2	
	1.5	3	2	
	4.0	4	2	

The results show that the inverse model consistently and accurately converged to the true f_c^{max} value for a vast range of initial guesses, with 100% accuracy in all successful convergence cases. This confirms the model's ability to handle parameters that define the concrete matrix itself. The algorithm typically requiring only 2 to 5 iterations to reach the final solution.

It was observed that the BoA range values and the magnitude of the true f_c^{max} have an inverse relationship in all beam sizes.

The BoA range as a percentage of the true value is largest for a low f_c^{max} and

decreases as the true value increases. This implies that when the concrete's contribution to the overall stiffness is less dominant, the inverse algorithm has a much broader and more forgiving search space.

Furthermore, as in previous cases, a size effect is evident in the BoA ranges. The percentage BoA range is consistently largest for the smallest beams and smallest for the largest beams. Since this is a recurring trend, it can be concluded that the model's behavior and the complexity of the error surface are influenced by the specimen's scale. The algorithm's search space is more constrained in smaller specimens where a parameter's influence is more localized.

6.4.6 Inverse Extraction of Synthetic n_{fiber}

This subsection presents the results of the verification of the inverse model for the fiber count parameter, n_{fiber}. The procedure was tested across all three beam sizes and a wide range of initial guesses, with the results summarized in Tables 6.17, 6.18, and 6.19.

Table 6.17: Summary of Inverse Iteration Results for Estimating n_{fiber} on Large-Sized Samples

True n_{fiber} Value —	Initial Guess —	Iterations (k)	Final Result —	BoA Range (% of true value)
1	2	3	1	400
	4	4	1	
	6	4	1	
9	1	4	9	344
	5	4	9	
	12	3	9	
	20	4	9	
	32	5	9	
12	1	7	12	367
	9	4	12	
	15	3	12	
	20	4	12	
	45	7	12	
20	1	5	20	390
	9	4	20	
	15	4	20	
	30	4	20	
	79	6	20	

Table 6.18: Summary of Inverse Iteration Results for Estimating n_{fiber} on Medium-Sized Samples

True n_{fiber} Value —	Initial Guess —	Iterations (k)	Final Result —	BoA Range (% of true value)
1	2	3	1	400
	5	5	1	
	6	1	1	
5	1	5	5	280
	3	4	5	
	6	4	5	
	9	4	5	
	15	5	5	
9	1	5	9	156
	4	3	9	
	6	3	9	
	15	4	9	
15	1	6	15	87
	5	5	15	
	9	5	15	
	14	4	15	

Table 6.19: Summary of Inverse Iteration Results for Estimating n_{fiber} on Small-Sized Samples

True n_{fiber} Value —	Initial Guess —	Iterations (k)	Final Result —	BoA Range (% of true value)
1	2	3	1	700
	5	3	1	
	9	4	1	
5	1	3	5	980
	4	3	5	
	6	3	5	
	10	3	5	
	50	4	5	
15	1	4	15	327
	5	4	15	
	12	3	15	
	20	3	15	
	50	4	15	
30	1	4	30	163
	5	3	30	
	20	3	30	
	50	3	30	
50	1	4	50	58
	5	5	50	
	20	3	50	
	30	3	50	

The results show that the inverse model is generally successful in converging to the true n_{fiber} value, with convergence achieved on average within 3 to 7 iterations.

An inverse relationship trend can be observed between the magnitude of the true n_{fiber} value and the BoA range expressed in percentage of the true value, even though in absolute values the BoA range is proportional with the number of fibers. This means that when the fiber contribution to the overall stiffness is less dominant, the inverse algorithm has a much broader and more forgiving search space.

The distinct size effect is evident in the BoA ranges for this parameter, as well, as te percentage BoA range is consistently largest for the smallest beams for small true values. This confirms that the algorithm's search space is more constrained in smaller specimens where a parameter's influence is more localized.

6.4.7 Main Findings from Synthetic Data Verification

The inverse analysis procedure was successfully verified using synthetic data, and demonstrated a 100% accuracy in recovering the true parameter values for a wide Band of Attraction (BoA) for all tested parameters (Δa, h_a, $E_{\mathrm{f,T}}$, f_{bundle}, f_c^{max}, and n_{fiber}). Convergence was consistently rapid, and it typically requiring less than 8 iterations. An inverse relationship trend was observed between parameter magnitude and the BoA (as a percentage of the true value), and a clear trend where the BoA was generally larger for smaller beam sizes, which suggests a more complex error surface in larger specimens. This verification confirms the algorithmic integrity and stability of the inverse procedure before its application to real data that include noise.

6.5 Validation using Real Data

In this chapter the final stage of model verification was done by performing the inverse analysis of real experimental data obtained from three-point bending tests on various FRC beams. The objective was to validate the predictive capabilities of the new computational model by through (successfully) extracting physically meaningful parameters and to demonstrate the stability of the inverse identification process in a real-world scenario with experimental data that has inherent variability.

6.5.1 Inverse Parameter Identification Methodology

As described in section 5.2, the core of the inverse analysis relies on the Levenberg-Marquardt optimization algorithm to minimize the difference between the model's predicted CMOD response and the measured experimental data. The method was initially implemented for this task due to its recognized efficiency in handling nonlinear least-squares problems, which posed true for problems dealing with real synthetic obtained. However, during the implementation on experimental data some practical challenges were observed.

It was observed that when the initial guess for the parameters was far from the true values, the residual sum of squares (RSS) changed very slowly with respect to the parameter estimation. This led to a very flat residual landscape with extremely small gradients, which in turn resulted in negligible parameter updates in each step and caused the inverse algorithm to stagnate. This meant that without a reasonable starting point near the global minimum the algorithm frequently converged to a local minima.

It is important to note that these convergence pathologies do not originate in uncontrolled material randomness. Because the beams were cast with self-compacting

concrete to avoid vibration-induced variability, and because fibers were embedded at known number, location, and orientation along a pre-defined crack path, the experimental setup was deliberately deterministic, as seen in Chapter 4. Consequently, the observed flat residual landscapes arise primarily from algorithmic sensitivity, rather than from stochastic scatter in fiber response.

To overcome these issues and ensure a reliable convergence, a preliminary grid search was introduced within the inverse process. This hybrid approach works so that it first performs a global search across the chosen range of initial guesses of the observed model parameter $\mathbf{m}$, $\mathbf{m} \in [0, 30]$, and evaluates the objective function, which produces a coarse landscape of RSS values.

$$\mathrm{RSS}(\mathbf{m}) = \sum_{i=1}^{N} \Big(y_i - \alpha(\mathbf{m})\, d_{cmod,i}(\mathbf{m}) \Big)^2, \tag{6.6}$$

where, similarily to Equation 5.13, y_i is the experimental CMOD data, $d_{cmod,i}(\mathbf{m})$ is the simulated CMOD for the assumed parameter $\mathbf{m}$ value, and $\alpha(\mathbf{m})$ is a scaling factor used to align the peak magnitude of the model response with the experimental data:

$$\alpha(\mathbf{m}) = \frac{\max\big(y_i\big)}{\max\big(d_{cmod,i}(\mathbf{m})\big)}. \tag{6.7}$$

This generates a vector of RSS values corresponding to each candidate for $\mathbf{m}$, which constructs a discrete residual landscape. By plotting and observing $\mathrm{RSS}(\mathbf{m})$ against $\mathbf{b}$, the global minimum can be identified without relying solely on local derivatives. The most stable range of values from this grid search is then used for assuming the initial guess for the LM algorithm, which significantly improves convergence reliability.

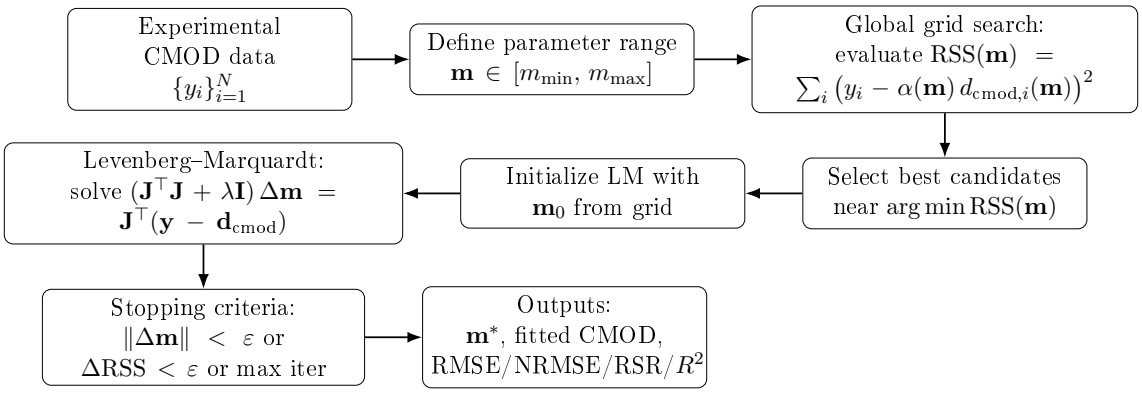

Figure 6.23: Hybrid inverse workflow for parameter identification

This hybrid approach (Figure 6.23) consisting of a global grid search followed by local Levenberg-Marquardt sifting ensures that the inverse analysis is both stable to poor initial guesses and efficient in achieving an accurate parameter estimation.

6.5.2 Results of Inverse Extraction

A total of 47 experimental CMOD curves that encompassed various beam sizes and fiber reinforcement types were analyzed. To manage this dataset and provide a structured validation, the data was grouped based on the experimental design. This grouping strategy allows for a meaningful comparison of model performance across different material types and geometries, as per the objectives of this thesis.

6.5.3 Parameter Values obtained from Large-Sized Samples

The inverse analysis results for large-sized beams are presented through a sequence of diagnostic figures and a summary table. Figures 6.24 through 6.26 showcase the inverse estimation process for the number of fibers (n_{fiber}), fiber position (h_a), and fiber diameter (Δa), respectively. In each figure, the left-hand plot illustrates the coarse grid search which guides the initial guess, while the right-hand plot shows the Levenberg-Marquardt iteration paths as they converge to the optimal solution from multiple starting points. The final converged values and their statistical characterization for large samples are summarized in Table 6.20.

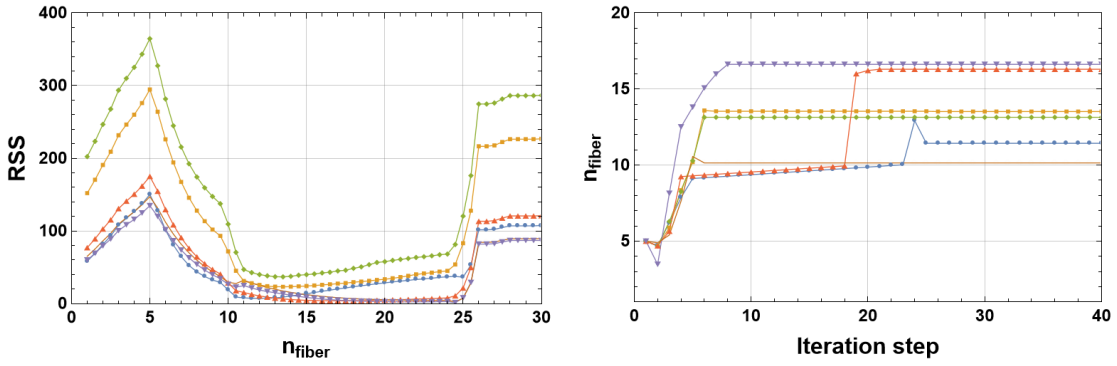

(a) Initial Guess Candidates (b) Iteration Paths

Figure 6.24: Final results of inverse analysis of parameter n_{fiber} from large-sized samples

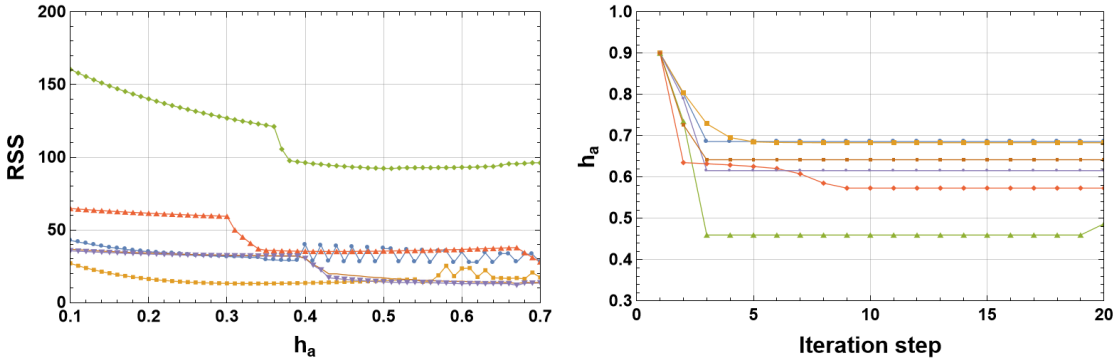

(a) Initial Guess Candidates (b) Iteration Paths

Figure 6.25: Final results of inverse analysis of parameter h_a from large-sized samples

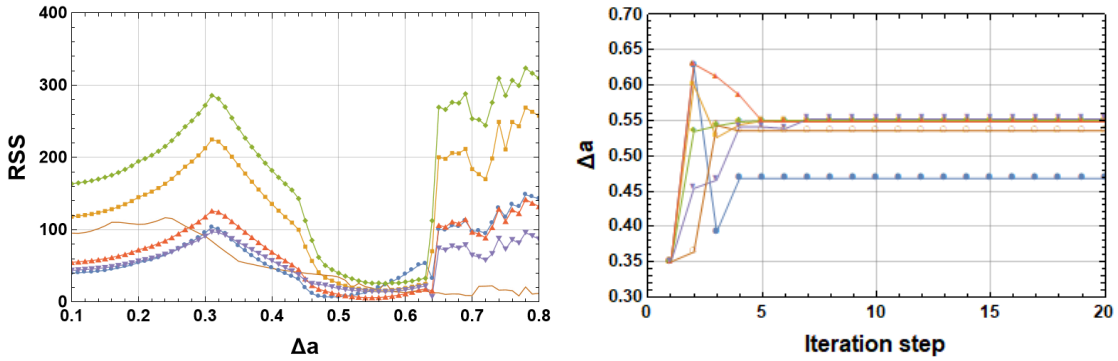

(a) Initial Guess Candidates (b) Iteration Paths

Figure 6.26: Final results of inverse analysis of parameter Δa from large-sized samples

Table 6.20: Final converged values of parameters with their statistical characteristics.

Parameter	**Converged Values**	**Mean (μ)**	**Standard Deviation (σ)**	**Coefficient of Variation (CV)**	**Difference (%)**
$n_{fiber} = 9$	11 14 13 16 17 10	13	2.65	19.72%	33.09
$h_a = 0.80$	0.69 0.68 0.49 0.57 0.62 0.64	0.62	0.08	12.20%	30.08
$\Delta a = 0.55$	0.47 0.55 0.55 0.55 0.56 0.53	0.54	0.03	6.36%	2.77

The inverse analysis of h_a was also performed on a randomly chosen single experimental dataset by adjusting the initial load-displacement curve so it would fit the chosen dataset better. Figure 6.27 presents the fitted model input data for sample L-SF-1, while Figure 6.28 displays the corresponding inverse extraction process.

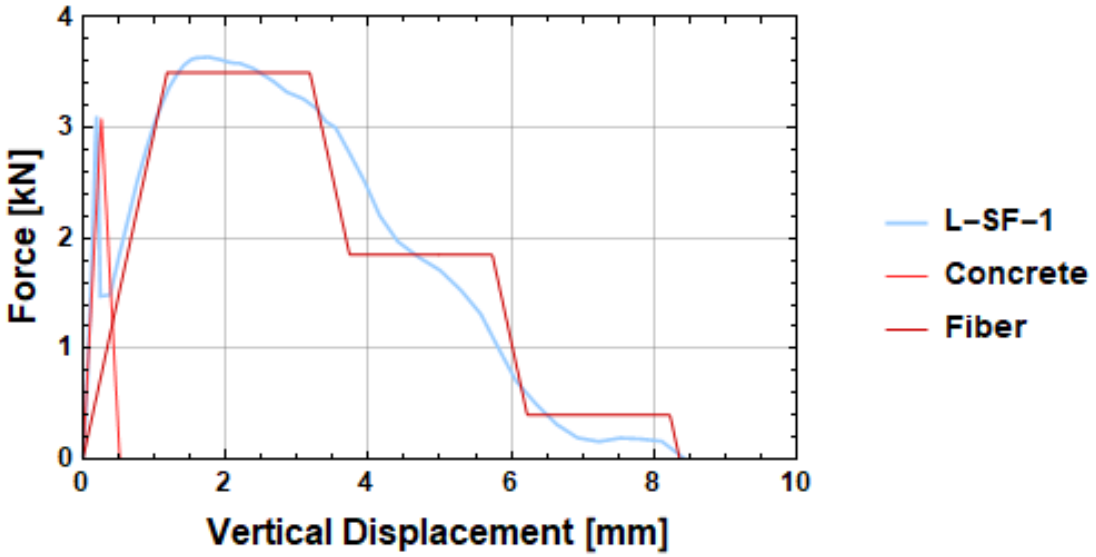

Figure 6.27: Input data for inverse extraction of h_a from sample L-SF-1

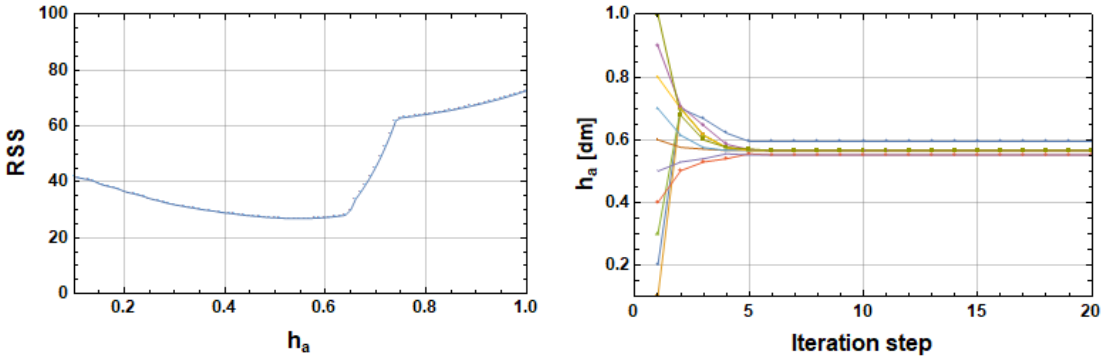

(a) Initial Guess Candidates

(b) Iteration Paths

Figure 6.28: Final results of inverse analysis of parameter h_a from sample L-SF-1

6.5.4 Parameter Values obtained from Medium-Sized Samples

The results of the inverse identification for medium-sized specimens follow the same structure as the large beams. Figures 6.29, 6.30, and 6.31 illustrate the inverse convergence paths for the parameters n_{fiber}, h_a, and Δa, respectively. The overall stability and converged values for this group are showcased in Table 6.21.

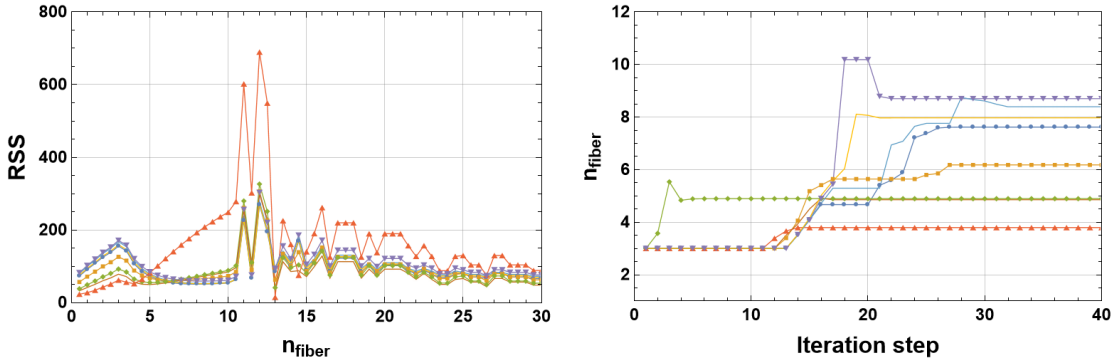

(a) Initial Guess Candidates (b) Iteration Paths

Figure 6.29: Final results of inverse analysis of parameter n_{fiber} from medium-sized samples

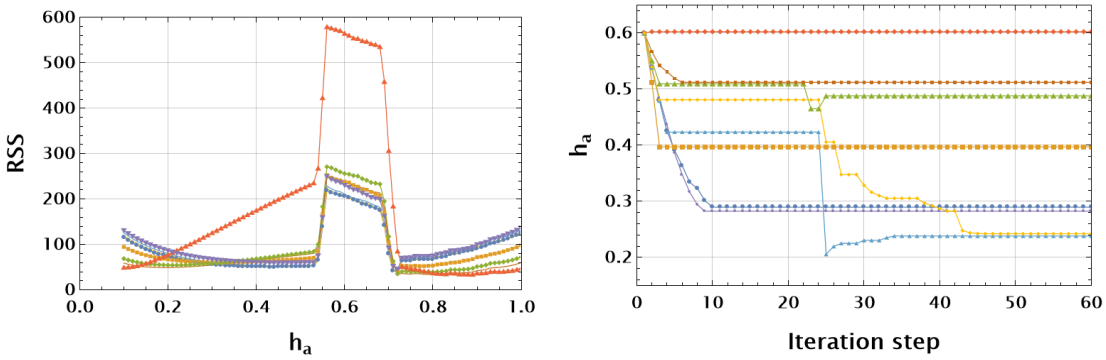

(a) Initial Guess Candidates (b) Iteration Paths

Figure 6.30: Final results ofit inverse analysis of parameter h_a from medium-sized samples

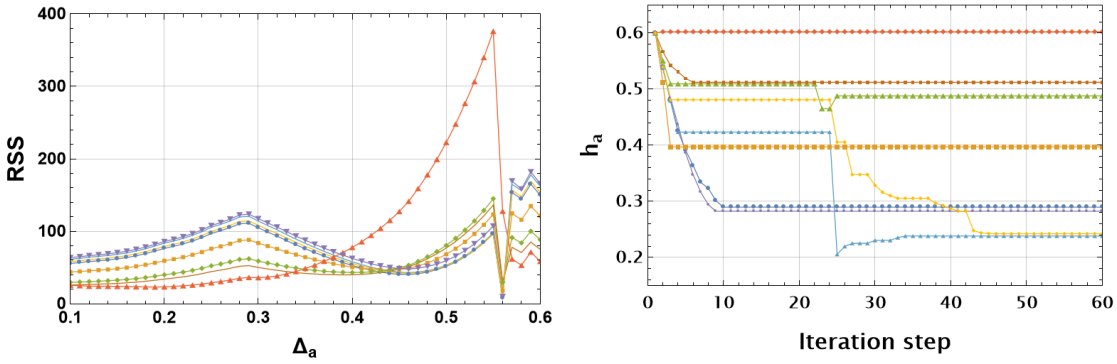

(a) Initial Guess Candidates (b) Iteration Paths

Figure 6.31: Final results of inverse analysis of parameter Δa from medium-sized samples

Table 6.21: Final converged values of parameters with their statistical characteristics.

Parameter	**Converged Values**	**Mean (μ)**	**Standard Deviation (σ)**	**Coefficient of Variation (CV)**	**Difference (%)**
$n_{fiber} = 6$	8 6 5 4 9 5 8 8	7	1.87	28.58%	8.38
$h_a = 0.6$	0.29 0.39 0.49 0.60 0.28 0.51 0.24 0.25	0.38	0.14	35.84%	57.17
$\Delta a = 0.55$	0.46 0.44 0.40 0.30 0.46 0.40 0.46 0.46	0.42	0.06	13.25%	30.18

The inverse analysis of h_a was also performed on a randomly chosen single experimental dataset by adjusting the initial load-displacement curve so it would fit the chosen dataset better. Figure 6.32 and Figure 6.33 illustrate the input data and the resulting inverse estimation for sample M-SF-3.

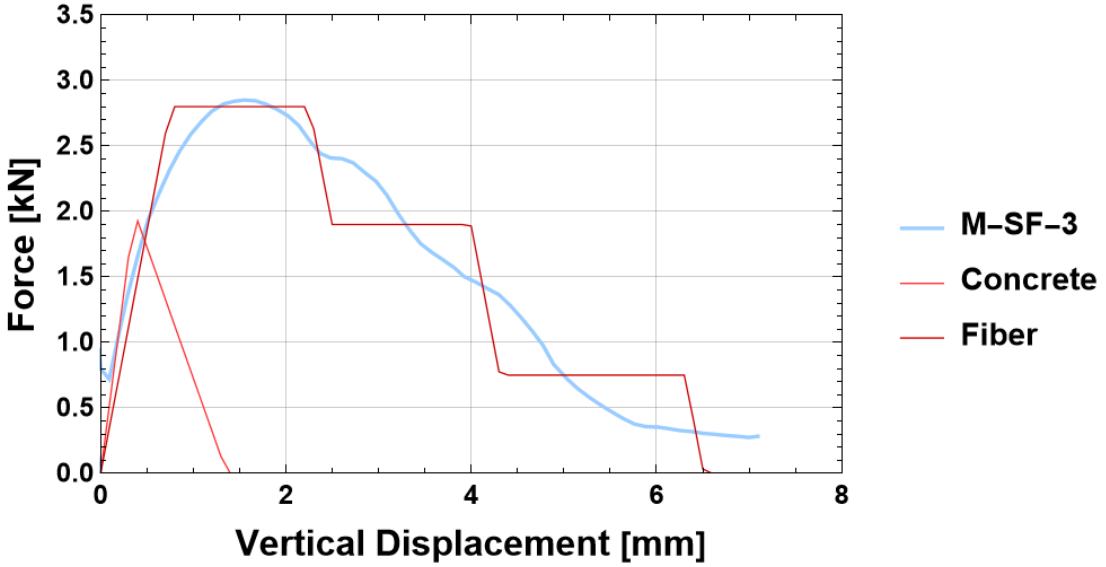

Figure 6.32: Input data for inverse extraction of h_a from sample M-SF-3

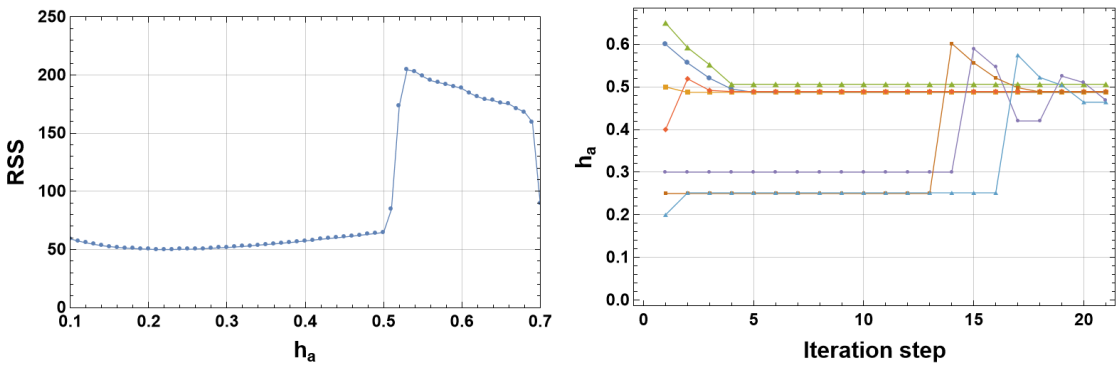

(a) Initial Guess Candidates

(b) Iteration Paths

Figure 6.33: Final results of inverse analysis of parameter h_a from sample M-SF-3

6.5.5 Parameter Values obtained from Small-Sized Samples

The inverse extraction process for the smallest beam size ($40 \times 40 \times 160\,\text{mm}$), which represents the most constrained geometry, is shown in Figures 6.34 through 6.36. These figures confirm the previously observed search pattern trends for n_{fiber}, h_a, and Δa. The final converged values that have higher variability due to size effects are summarized in Table 6.22.

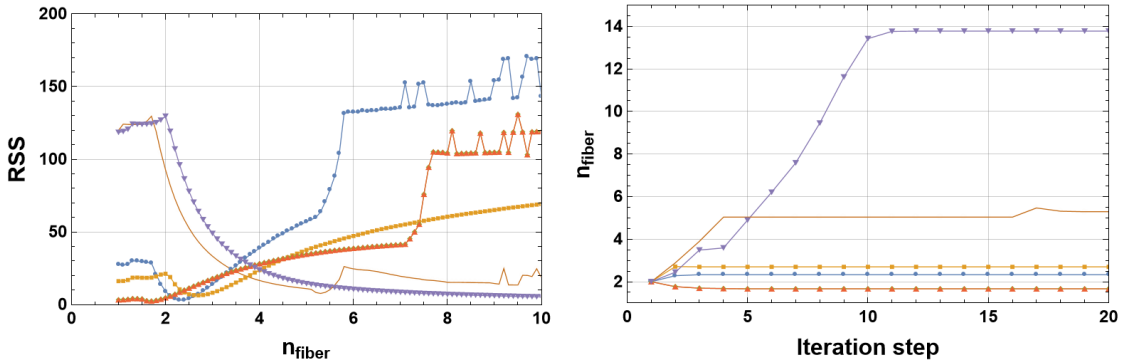

(a) Initial Guess Candidates (b) Iteration Paths

Figure 6.34: Final results of inverse analysis of parameter n_{fiber} from small-sized samples

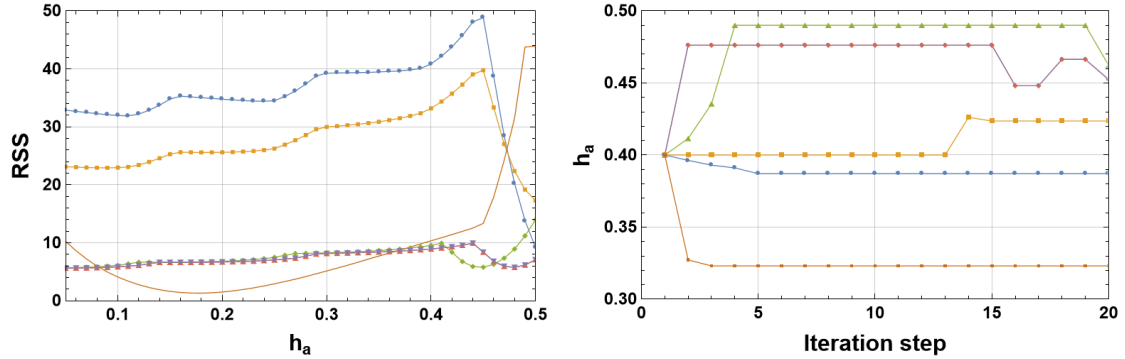

(a) Initial Guess Candidates (b) Iteration Paths

Figure 6.35: Final results ofit inverse analysis of parameter h_a from small-sized samples

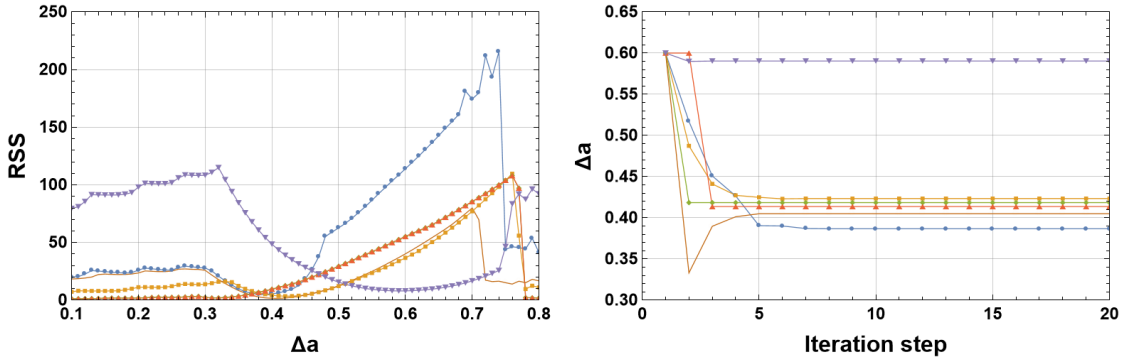

(a) Initial Guess Candidates (b) Iteration Paths

Figure 6.36: Final results of inverse analysis of parameter Δa from small-sized samples

Table 6.22: Final converged values of parameters with their statistical characteristics.

Parameter	**Converged Values**	**Mean (μ)**	**Standard Deviation (σ)**	**Coefficient of Variation (CV)**	**Difference (%)**
$n_{fiber} = 3$	2 3 2 2 2 14 5	4	4.42	103.23%	
$a_0 = 0.45$	0.39 0.41 0.46 0.46 0.32	0.41	0.06	13.89%	10.31
$\Delta a = 0.55$	0.39 0.42 0.42 0.41 0.59 0.40	0.44	0.07	17.06%	25.12

The inverse analysis of Δa was also performed on a randomly chosen single experimental dataset by adjusting the initial load-displacement curve so it would fit the chosen dataset better. Figure 6.37 presents the fitted model input data for sample S-SF-3, while Figure 6.38 displays the corresponding inverse extraction process.

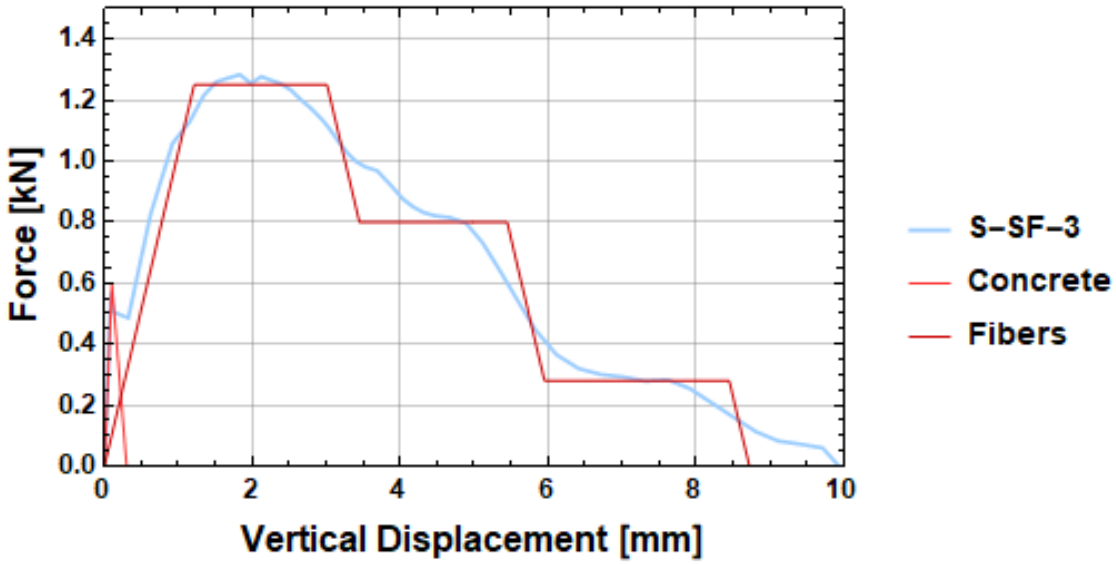

Figure 6.37: Input data for inverse extraction of Δa from sample S-SF-3

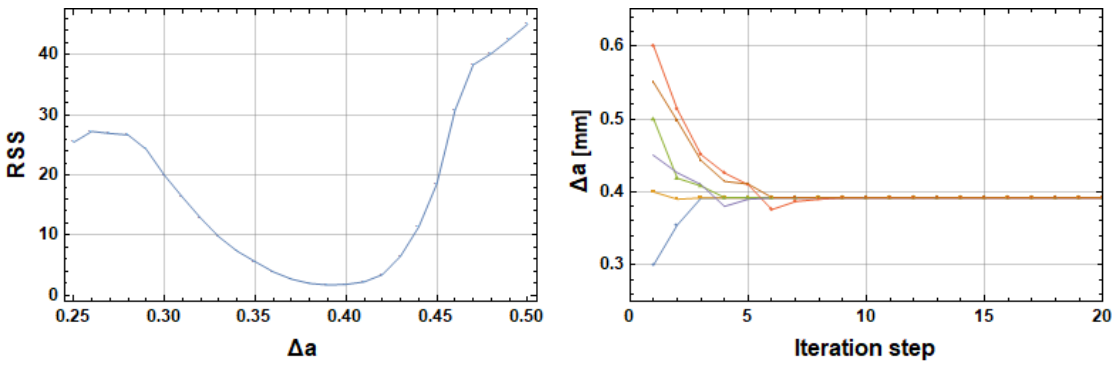

(a) Initial Guess Candidates

(b) Iteration Paths

Figure 6.38: Final results of inverse analysis of parameter Δa from sample S-SF-3

6.5.6 Cross–Size Synthesis of Inverse Estimates

The inverse analysis done with real experimental data as input provided a comprehensive validation of the model's capabilities and stability in a practical application. Unlike the verification using synthetic data that was designed to converge to a known value with 100% accuracy, the experimental data predictably converged to a range of results due to the inherent variability of the physical specimens. Therefore, the statistical characterization of these results, in form of the mean, standard deviation, and coefficient of variation (Tables 6.20 - 6.22), is a direct measure of the model's ability to handle scatter in real-world data.

For easier interpretation of results, a summary of the obtained coefficient of variation (CV %) across all three beam sizes is presented in Table 6.23. Lower CV indicates more stable/identifiable parameters.

Table 6.23: Coefficient of variation (CV %) from inverse identification

Parameter	**Large beams**	**Medium beams**	**Small beams**
n_{fiber}	19.72	28.58	103.23
h_a	12.20	35.84	13.89
Δa	6.36	13.25	17.06

The observations are the following:

1. Size clearly impacts parameter identifiability, as large beams consistently exhibit low scatter for all extracted parameters (CV $\approx$ 6–20%). In contrast, the small beams show a very high CV for n_{fiber} ($>$ 100%) that indicates that the effective fiber count is much harder to pin down on short span sections, where the CMOD signal carries less information about the full bridging fiber population, which can be seen when comparing iteration paths for large beams in Figure 6.24) versus those for small beams in Figure 6.34). This size effect is precisely what would be expected as with fewer engaged fibers the inverse problem becomes more sensitive to individual variations, which makes it harder to constrain to a single, stable solution.

2. Δa is comparatively robust as it stays within CV 6–17% across different beam sizes, which is visually supported by the tight clusters of convergence paths for both large beams in Figure 6.26 and small beams in Figure 6.36. This indicates that the post-peak softening behavior, which is directly influenced by the effective fiber diameter in the model, is reliably captured by the simulated CMOD data even when other parameters vary.

3. As the CV for h_a is lower for large and small beams (12–14%) and slightly higher for medium beams (36%), it is concluded how extracting the fiber position parameter is a less stable process in medium beams. This is consistently observed in the iteration path figures for medium beams in Figure 6.30b which show a wider band to which the convergence occurs, when compared to those for large and small beams in Figures 6.25b and 6.35b, respectively.

The initial guess candidates graphs visualize the coarse residual surface that is sampled by the grid search while the the iteration paths graphs show the subsequent Levenberg–Marquardt updates fr different seta of measured data from the same starting points. Observing the two together, they indicate the following:

- Large beams: For all analyzed parameters the iteration paths monotonically collapse to a single optimum regardless of the tested dataset, as seen in Figures 6.24b, 6.25b and 6.26b. This points to a broad basin of attraction and strong

parameter observability, which is also in line with the low CV values in Table 6.23.

- Medium beams: Convergence remains reliable after the hybrid optimization is initialized, but the paths for h_a in Figure 6.30b occasionally require more steps and show mild curvature that signifies local flatness in the residual surface. This explains the elevated CV for h_a in Table 6.23.

- Small beams: The iteration paths for all three parameters (Figures 6.34 to 6.36) are overall stable after candidates search is introduced, but exhibit sensitivity to the the different levels of scatter in different target data. This is especially seen for n_{fiber}, which matches its very high CV and underscores a genuine identifiability limit for this parameter on both small specimens and highly scattered laboratory data.

Because the laboratory tests used self-compacting concrete with no vibration and deterministic fiber embedding was enforced, variability due to random fiber placement was intentionally suppressed (see Chapter 4). Therefore, the cross-size CV trends above, in large, do not reflect uncontrolled physical randomness, but rather the identifiability of parameters from the information contained in measured CMOD curves and the shape of the optimization landscape. From here, two outcomes support the hypothesis: (i) for sufficiently informative tests (large beams) the deterministic forward model plus the hybrid inverse scheme recovers parameters with low scatter, and (ii) even where scatter of measured data increases (small beams) the hybrid grid $\Rightarrow$ LM procedure separates algorithmic sensitivity from material randomness.

6.6 Engineering Applicability and Chapter Conclusion

The validation and verification framework successfully validated the deterministic model, and extends it beyond mere numerical accuracy to establish its direct applicability for engineering practice.

The thesis establishes a dual-stage validation framework that stands as a stable foundation for the model's credibility. This approach first involves verification using synthetic data (Section 6.4), which confirms the algorithmic integrity and 100% accuracy of the inverse procedure against a known numerical data. This is followed by validation using real experimental data (Section 6.5), where the model's stability and coefficient of variation are evaluated against real-world scattered data. This two-step methodology isolates numerical errors from physical variability and provide a

basis for the model's overall trustworthiness and reliability for structural analysis.

The inverse analysis framework proves its capacity to distinguish the mechanical effects of different fiber types through the successful and stable extraction of the composite parameters $E_{\mathrm{f,T}}$ and f_{bundle}. As demonstrated in the synthetic verification sections, the model accurately recovers target $E_{\mathrm{f,T}}$ values that range from low-stiffness polymer fibers to high-stiffness metallic or carbon fibers. This functionality potentially allows engineers to use the inverse model on field data to quickly and reliably characterize the performance of different FRC mixtures and predict post-cracking toughness without extensive and costly laboratory studies for every new fiber product.

Furthermore, the established CV trends provide a quantitative basis for improving the reliability of parameter identification on different structural scales. The consistent finding that parameter scatter is lowest in larger beams confirms that this inverse model results with stable values when the testing specimen provides sufficient structural information. This confidence in parameter stability is essential for integrating the model's output into any structural optimization and design codes.

In conclusion, the validation process confirms that the model is not only mathematically correct but also a practical and stable tool for extracting physically meaningful parameters (like Δa and h_a), as well as material performance parameters ($E_{\mathrm{f,T}}$ and f_{bundle}) under real-world experimental variability.

Chapter 7

Inverse Analysis and Parameter Identification

This chapter represents the core experimental-numerical outcome of this thesis: the identification and extraction of real, physically meaningful FRC material parameters using the developed inverse analysis framework. After the validation of both forward and inverse models in the previous chapters, in this section the validated methodology is applied to experimentally obtained (real-world) data, which in turn provides solution to the challenges of FRC characterization.

7.1 Extraction of Parameter Pairs

This section explores how different pairs of parameters can be uniquely identified by mapping the CMOD error surface. It distinguishes between well-posed problems that are characterized by isolated minima, and deterministically non-unique problems, which can be identified by elongated minima or ridges in the parameter space.

A dual-parameter extraction was conducted to simultaneously obtain two parameter values with different influences identified through sensitivity studies, in order to address an inherent limitation of single-parameter extraction in fiber-reinforced concrete modeling. This approach directly deals with the issue of non-uniqueness in FRC simulations, where different combinations of parameters can produce identical crack mouth opening displacement responses, which comes from the physical interdependence of material properties. For instance, where an increase in one parameter can cause a decrease in the other while maintaining the same or similar structural response.

Certain cases of single-parameter extraction methods introduce significant bias by requiring a fixed assumption about values for secondary parameters. For example, assuming an incorrect effective loading modulus, $E_{\mathrm{f,T}}$, could force compensatory

adjustments to the fiber threshold pullout force, F_a^{max}, during the optimization process to match the experimental CMOD data. These compensatory errors then further propagate through the model and distort parameter values, all the while reducing the model's predictive accuracy.

Therefore, to resolve this, a dual-parameter inverse analysis methodology was developed to systematically map and analyze the interdependence between two chosen parameters. This parametric analysis was primarily conducted using data generated by the predictive numerical model itself. Reasons for using synthetic data over experimental were several. Such data provides a control environment with precisely known "true" input parameters, which allows for an unambiguous analysis as the extracted parameters can be directly compared against their known counterparts. Furthermore, to reiterate, certain parameters of high interest for this study (such as f_{bundle}) have no means of being physically measurable, which makes collected experimental data irrelevant to use in this case. What's more, by eliminating experimental noise and uncontrolled variability, using synthetic data enables a more isolated and focused study of inherent characteristics of the parameter space, in this case - interdependence and non-uniqueness. This ensures that any encountered challenges and/or successes are attributed solely to the algorithm's performance and the mathematical formulation of three-point bending.

The process included varying the values of two selected parameters over a chosen range, while keeping all other model parameters fixed. All tested parameter pair combinations are summarized in Table 7.1. For each combination of these two parameters, the predictive numerical model was used to generate a corresponding CMOD curve. The fit error between this simulated CMOD curve and a target synthetic CMOD curve was then quantitatively evaluated. This process generated a two-dimensional error surface across the parameter space, represented by contour plots. Each contour line represents a specific fit error (value expressed as a sum of square difference for easier interpretation and readability) that would be achieved by any corresponding parameter pair combination on the grid. The lower the contour value the better the fit. The optimal parameter pair, corresponding to the global minimum of this error surface, is identified by the inverse analysis algorithm. This approach provides an insight into multiple pairs of parameters' affect on the beam behavior that has potential for an improvement in design optimization but also a less biased approach in certain single parameter extraction cases.

Table 7.1: Analyzed dual-parameter pairs and their physical interdependence

Parameter pair	**Physical relation**
$E_{f,T}$ vs h_a	Effective elasticity modulus vs fiber vertical position
n_{fiber} vs f_{bundle}	Fiber count vs empirical bundle scaling factor
n_{fiber} vs F_a^{max}	Fiber count vs maximum pullout force per fiber
Δa vs f_c^{max}	Fiber cross section diameter vs concrete matrix strength
f_{bundle} vs f_c^{max}	Bundle scaling factor vs concrete matrix strength
F_a^{max} vs f_{bundle}	Maximum pullout force per fiber vs bundle scaling factor
n_{fiber} vs $E_{f,T}$	Fiber count vs effective elasticity modulus
Δa vs f_c^{max}	Fiber cross section diameter vs concrete matrix strength

7.1.1 Explanation of Contour Plots and Results

The results of the dual-parameter extraction inverse analysis are presented as error contour plots in Figures 7.1, to 7.3. Each plot maps the fit error in a two-dimensional parameter space, where contour lines connect combinations of the two varied parameters that resulted with an identical level of fit error (presented in μm^2).

To interpret these graphs effectively:

- **Contour Lines**
  Each line represents a different level of constant fit error. Contour values that are decreasing indicate a better match between the simulated CMOD curve and the target CMOD curve, while higher contour values indicate a higher discrepancy between target and simulated data.

- **Global Minimum**
  The red marker found in each plot shows the parameter pair that represents the best fit achieved by the inverse analysis algorithm for that specific parameter combination. Ideally it would indicate the "true" parameter values for the observed data.

- **Shape of Contours**

  - **Circular or isolated** - roughly circular contours that converge sharply to a single point indicate a well-defined, unique minimum. This means that the model has a higher sensitivity to the precise values of both parameters in combination, and there is less ambiguity in their correct extraction.

  - **Elongated or valleys-shaped** - elongated contours that form a narrow "valley" or "ridge" signify a degree of non-uniqueness or strong interdependence between the two observed parameters. In such cases, multiple

combinations of the parameters along the same ridge produce almost identical fit errors. This directly reflects the physical interdependencies where an increase in one parameter's value can be compensated by a change in the other to produce a comparable structural response. The orientation of a ridge indicates the nature of the compensatory relation between the parameters.

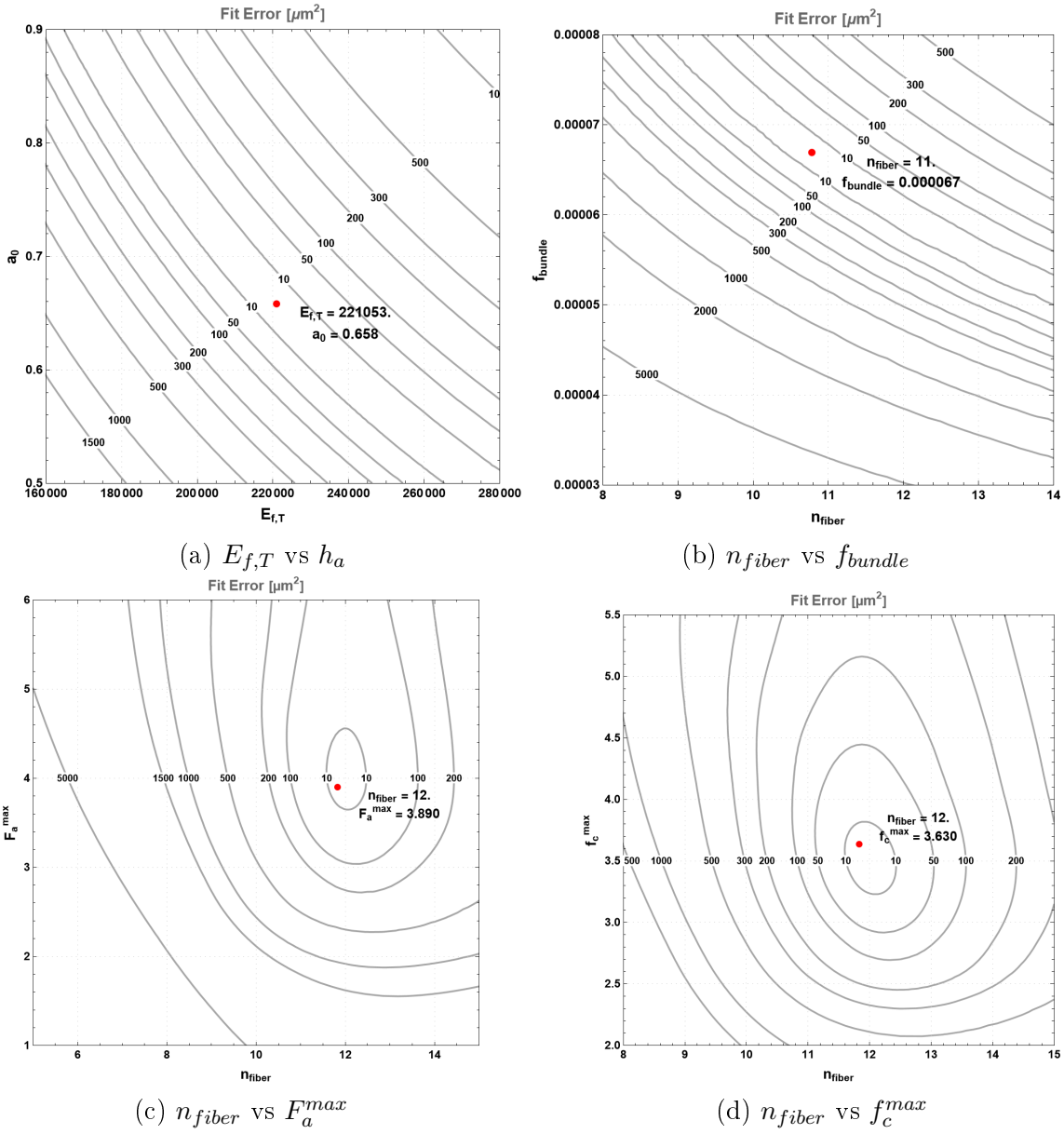

(a) $E_{f,T}$ vs h_a

(b) n_{fiber} vs f_{bundle}

(c) n_{fiber} vs F_a^{max}

(d) n_{fiber} vs f_c^{max}

Figure 7.1: Error Contour Plot for Dual-Parameter Extraction – Part 1 (L-size beams).

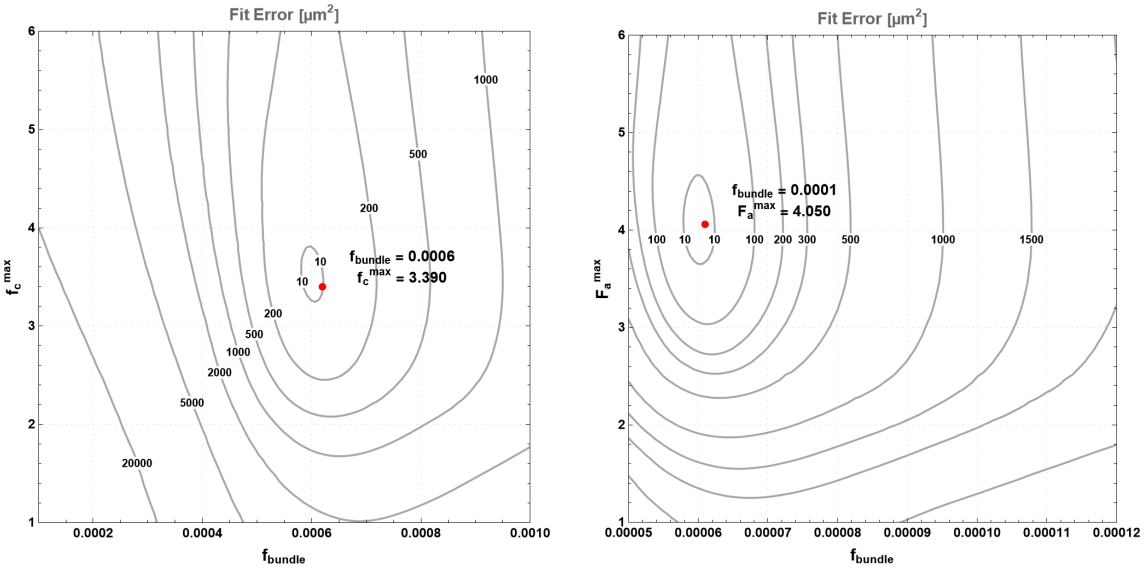

(e) f_{bundle} vs f_c^{max} (f) F_a^{max} vs f_{bundle}

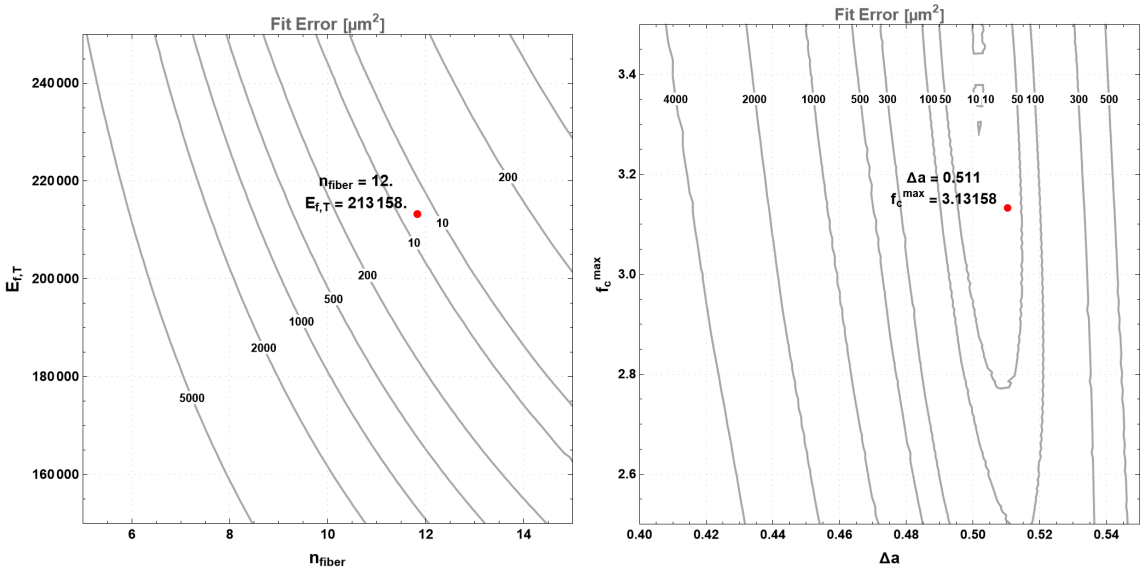

(g) n_{fiber} vs $E_{f,T}$ (h) Δa vs f_c^{max}

Figure 7.1: Error Contour Plot for Dual-Parameter Extraction – Part 2 (L-size beams).

From these results, parameter interdependence in large beams is easily interpretable, with clear elongated ridges that suggest high interdependence and well defined isolated minima for pairs with little to no interdependence. Even in less precisely defined minimas, for Δa and f_c^{max}, the dual plot serves as a valuable guidance for searching for the most optimal solution.

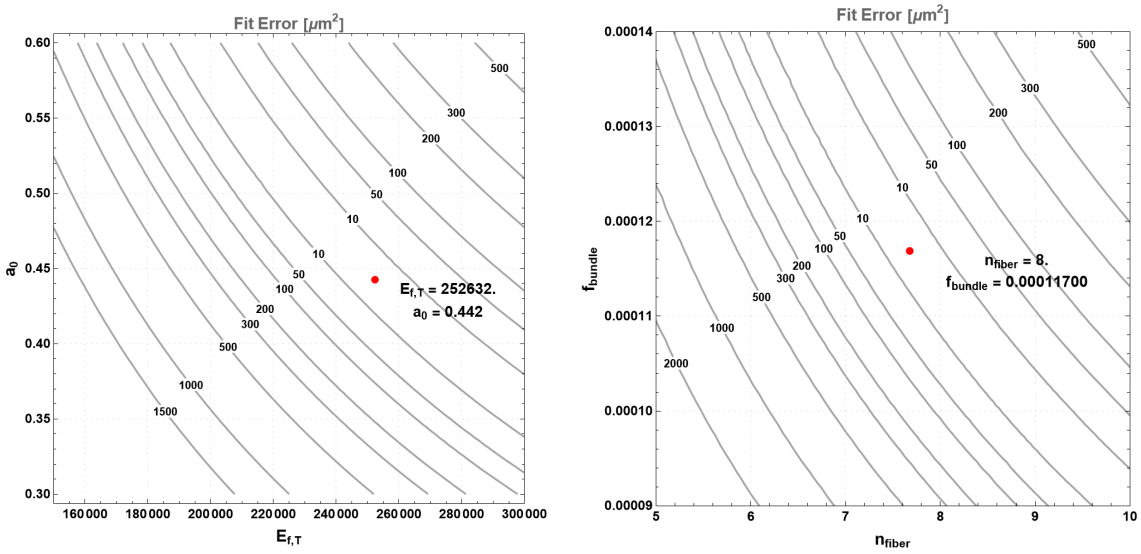

(a) $E_{f,T}$ vs h_a

(b) n_{fiber} vs f_{bundle}

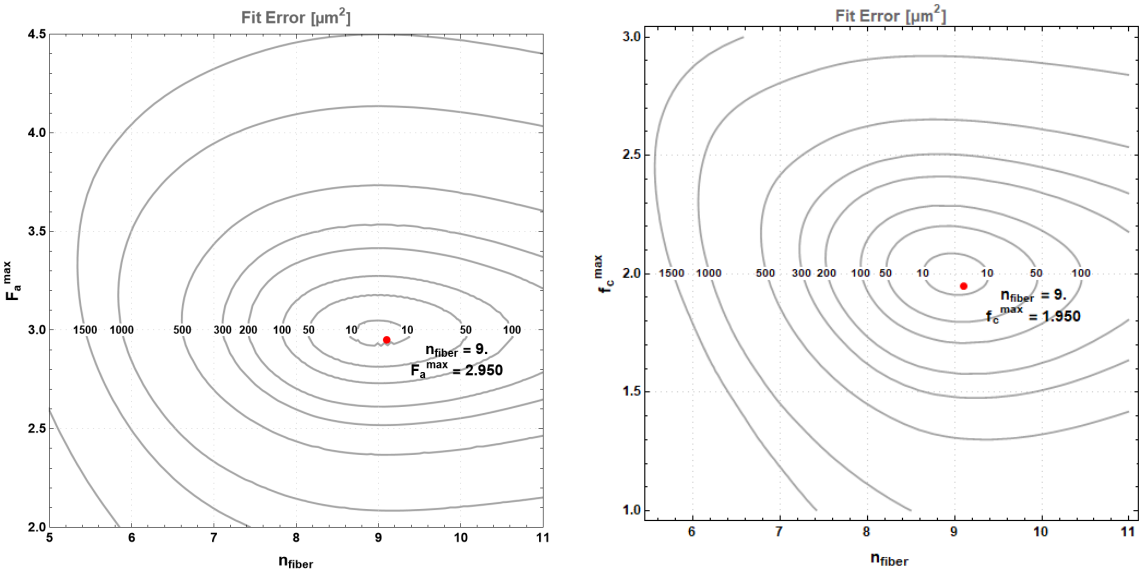

(c) n_{fiber} vs F_a^{max}

(d) n_{fiber} vs f_c^{max}

Figure 7.2: Error Contour Plot for Dual-Parameter Extraction – Part 1 (M-size beams).

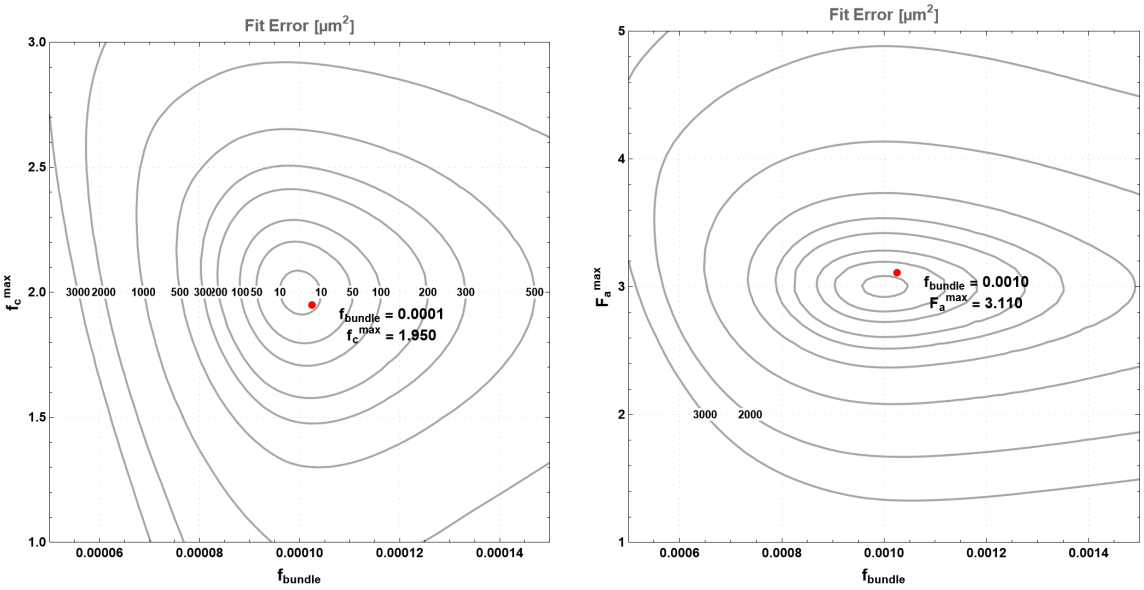

(e) f_{bundle} vs f_c^{max} (f) F_a^{max} vs f_{bundle}

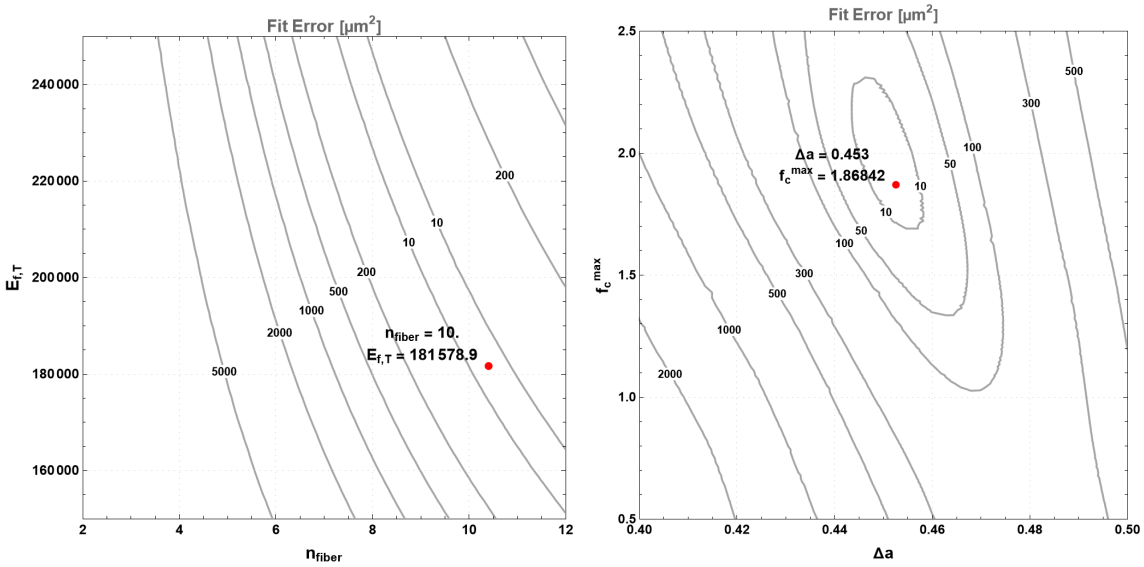

(g) n_{fiber} vs $E_{f,T}$ (h) Δa vs f_c^{max}

Figure 7.2: Error Contour Plot for Dual-Parameter Extraction – Part 2 (M-size beams).

These results show that medium-sized beams provide the sharpest, most pronounced global minima for the majority of parameter pairs with no interdependancies. This also indicates that the numerical model is optimally tuned for the geometric proportions of the medium beams, which means analysis done on these beams will result in the lowest ambiguity during parameter identification.

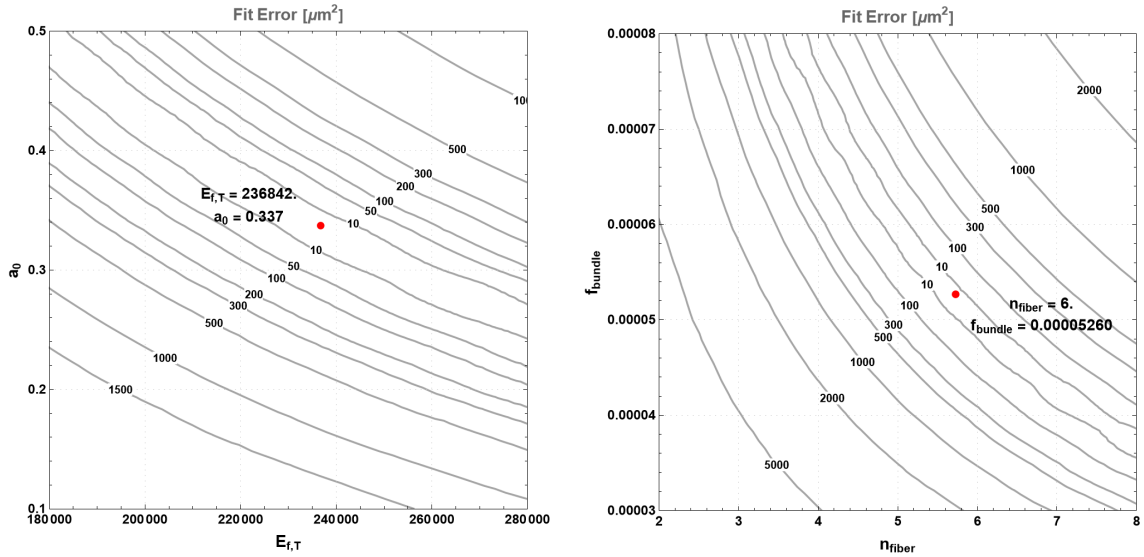

(a) $E_{f,T}$ vs h_a

(b) n_{fiber} vs f_{bundle}

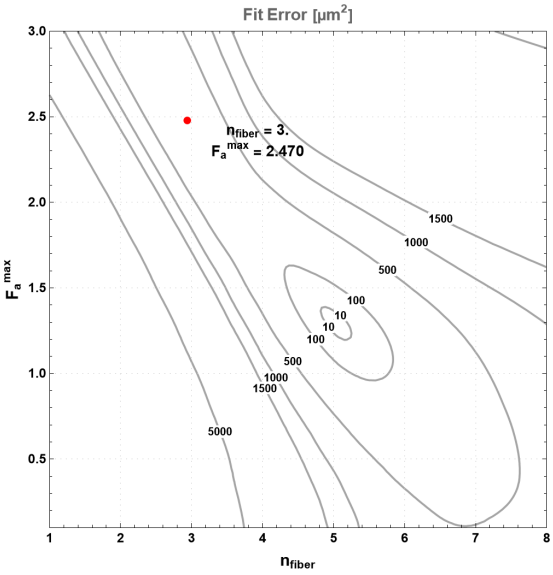

(c) n_{fiber} vs F_a^{max}

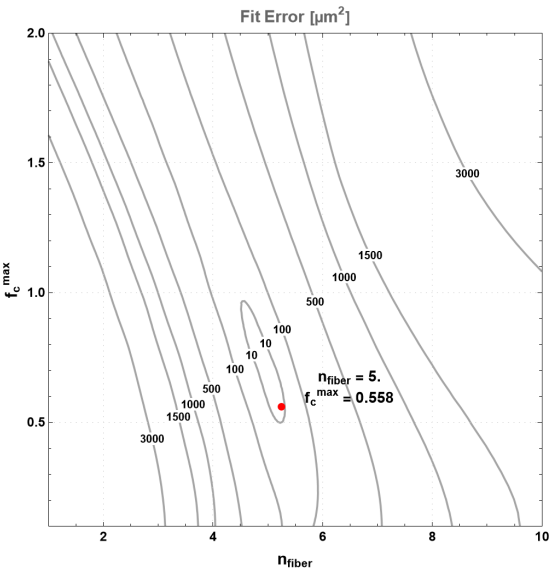

(d) Δa vs f_c^{max}

Figure 7.3: Error Contour Plot for Dual-Parameter Extraction – Part 1 (S-size beams).

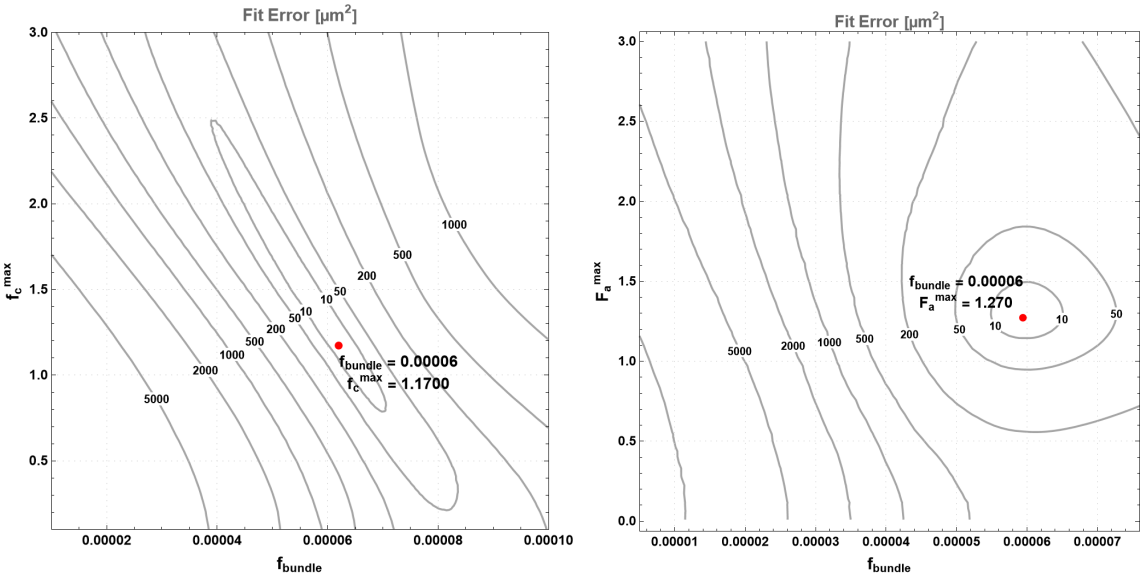

(e) f_{bundle} vs f_c^{max} (f) F_a^{max} vs f_{bundle}

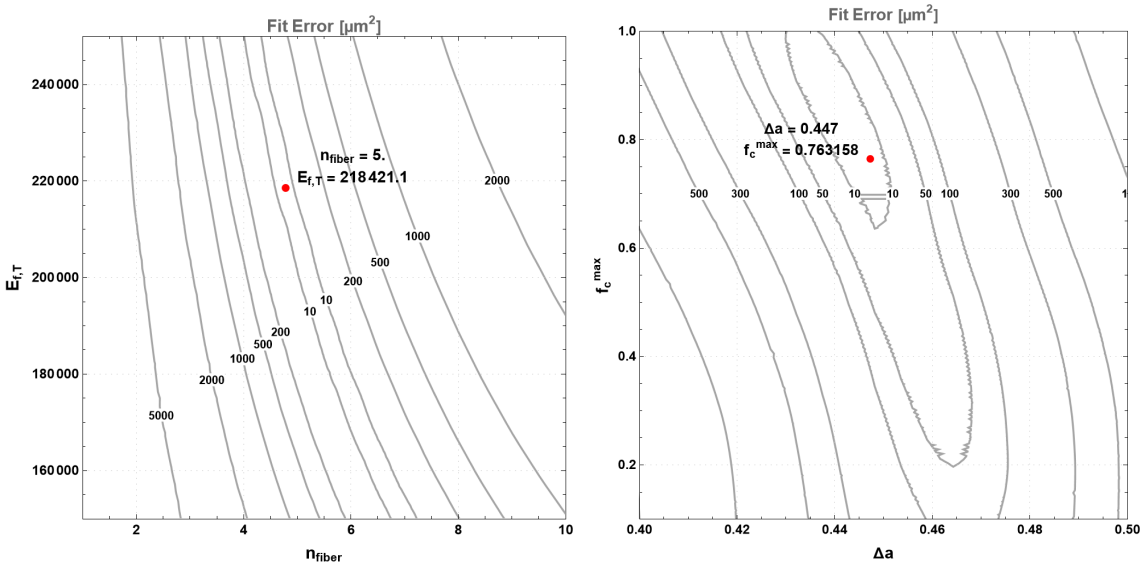

(g) n_{fiber} vs $E_{f,T}$ (h) Δa vs f_c^{max}

Figure 7.3: Error Contour Plot for Dual-Parameter Extraction – Part 2 (S-size beams).

From these results it can be determined how small specimens consistently exhibit the highest degree of non-uniqueness, which is characterized by a greater degree of elongated residual valleys when compared to results for medium and large beams. This means that the identifiability of certain parameters is significantly constrained by the limited geometrical information provided by smaller test volumes.

7.1.2 Interpretation of Results

The results of the dual-parameter extraction inverse analysis are presented as error contour plots in Figures 7.1 to 7.3. To reiterate section 7.1.1, each plot maps the fit error in a two-dimensional parameter space, where contour lines connect combinations of the two varied parameters that give an identical level of fit error (measured in μm^2). The red marker in each plot indicates the parameter pair that corresponds to the global minimum of the error surface, and represents the best fit achieved by this type of inverse analysis for the developed algorithm.

A general observation across all three beam sizes is the relative consistency of all parameter interdependence. However, a notable trend is present among the shape of the minima with respect to beam size. The clear and isolated minima showing in medium and larger sized beams tend to obtain a more elongated or form in smaller sized beams. This indicates a higher degree of parameter interdependence for the same parameter pairs when applied to smaller beam geometries. This phenomenon is a strong indicator of size effect on identifiability of parameter and suggest that the scale of the specimen influences the uniqueness of optimal parameter pair combinations. The relative influence of individual fibers in smaller beams and their precise location becomes more dominant and their complex to uniquely separate and identify.

The most pronounced sharp minima are found in the analyses for medium-sized beams (Figures 7.2). This is due to the numerical model being calibrated and fine-tuned primarily using experimental results from medium-sized beams during its development. Therefore the model's formulations are most optimized and provide the most distinct parameter identification for these dimensions. However, this does not imply a lack of reliability for larger or smaller beams but rather emphasizes that the model's in this stage of development achieves it peak precision within the experimental data range it was initially designed to fit.

The dual-parameter combinations that were consistently characterized by elongated contours, meaning they exhibited non-uniqueness, were $E_{f,T}$ and a_0 and n_{fiber} and f_{bundle}. This indicates that the fiber-matrix combined effective elasticity modulus during loading and the position od said fibers, as well as number of the fibers and scaling f_{bundle}, have a mutually high compensatory relationship, meaning each or both can be adjusted in order to achieve the same response of the beam during bending. For instance, in the case of $E_{f,T}$ and a_0, the undesirable influence of a decreased effective elasticity modulus can be compensated by positioning said fibers in a cross-section zone closer to the tension face of the beam. Likewise, it's a guideline for any future research on the existence and exact identification of f_{bundle} parameter, as its value is strongly tied to the number of fibers places in the beam.

Example Analysis of Figure 7.3 (c) - Specific Case of n_{fiber} and F_a^{max} for Small Beams As an illustrative example on Figure 7.3 (c), which plots the fit error for the number of fibers, n_{fiber}, and the fiber's maximum threshold force F_a^{max} for small beams, a discrepancy in the optimization process was observed. With true values set for the synthetic data $n_{fiber} = 5$ and $F_a^{max} = 1.6kN$, the algorithm converged at $n_{fiber} = 3$ and $F_a^{max} = 2.47kN$. However, a visual inspection of the contour plots shows that this extracted best-fit solution corresponds to a local minimum, not the visually apparent global minimum of the error surface, which appears to be significantly close to the true values. This difference is mainly due to the resolution of the parameter grid (20×20 in this case) used for calculating the error surface. The discrete sampling points failed to adequately capture the region of the true global minimum which led the grid search to identify the lowest error only within the sampled points rather than the absolute global optimum of the whole observed error space. This explicitly points out the effect of grid density in grid-based optimization approaches as well as it emphasizes the importance of visual inspection and of not accepting the obtained results uncritically.

7.1.2.1 Implications of the Dual Parameter Extraction Results for Inverse Modeling

The results the dual-parameter extraction analysis presented in the previous chapter has valuable guidelines for the subsequent inverse analysis.

Firstly, the observed interdependencies visually confirm the challenge of non-uniqueness that dual-parameter extraction aimed to evaluate and address. This verifies the initial hypothesis that single parameter extraction methods can be prone to bias and inaccuracies if the potential of the existence of parameter interdependacies is overlooked. The dual extraction approach maps these relationships and provides a more holistic understanding of the parameter space and a more refined strategy for exact extraction.

Secondly, the successful identification and quantification of optimal parameter pairs for the majority of the tested combinations validates the stability of the deterministic predictive model and its ability to generate CMOD responses that enable the successful recovery of input parameters, despite the complexity of FRC formulation and behavior. This indicates that the model's mathematical formulations are indeed *"simplified enough that it could be utilized in an inverse analysis, yet precise so it would accurately predict fiber-reinforced concrete beam behavior"*, as stated previously.

Furthermore, the review of the resulting sharpness of global minima and the presence of size effects directly aids the strategy for using the Levenberg-Marquardt algorithm in the later inverse analysis with experimental data as input.

In case of parameter pairs that have a very apparent minima, the algorithm is expected to converge efficiently and more accurately for both parameters. However, for parameters within more elongated ridges (especially found in smaller beams), additional strategies may be considered, such as:

- Constraining the search space for specific parameters to a more narrow one by using prior knowledge from observing both the dual parameters results and the sensitivity analysis;
- Multi-objective optimization by trying to achieve several optimal results at once, rather than just one. For instance, aiming for the smallest possible difference between the model's predictions and the actual test results while also prioritizing other possible goals such as a physically realistic parameter values withing the observed range;
- Utilizing the sensitivity analysis for the initial guess assumption by leveraging the sensitivity maps to estimate better initial guesses for the iterative algorithm.

The observation regarding the grid resolution's impact (Figure 7.3 (c)) also highlights the impact of choosing an appropriate optimization method. Simple grid searches simply can be proved to not be advanced enough for such complicated materials and algorithms, and gradient-based algorithms like Levenberg-Marquardt are a better option as they're designed to navigate such optimizations more effectively.

7.2 Extraction of Experimental Parameters

The hypothesis of this thesis is that a well-posed deterministic forward model, paired with a disciplined inverse routine, can recover physically meaningful FRC parameters from structural tests even when experimental data contain scatter. With that in mind, after successfully validating the forward and inverse model, both are used to extract the previously unknown bundle scaling factor f_{bundle} and the effective elastic modulus in tension $E_{f,T}$ from real three-point bending data.

In the force-displacement law of the fiber-matrix, defined by Equation 5.6, the pre-peak stiffness is determined by the product $EA = f_{\text{bundle}} \times E_{f,T} \times n_{\text{fiber}} \times (\Delta a)^2$. Since the empirical scaling factor f_{bundle} and the effective elasticity modulus $E_{f,T}$ both contribute to the bending stiffness, a change in one can be compensated for by a change in the other while maintaining a similar CMOD response. The dual-parameter maps in Figure 7.4 confirm this relationship by showing elongated valleys for the pair $(f_{\text{bundle}}, E_{f,T})$. This interdependence makes the simultaneous extraction of both parameters from a single CMOD curve deterministically non-unique, so the

hierarchical identification approach described below is designed to minimize this issue.One parameter is temporarily fixed to a physically plausible reference value, while the other is identified. Once the first parameter is reasonably stabilized, the fixed assumption is released and the second parameter is extracted. This staged procedure collapses the otherwise flat residual ridge into a well-posed direction at each step, which bypasses the issue of deterministic non-uniqueness. What is crucial is that the validity of the approach depends on the forward model being robust enough to withstand the temporary inaccuracy of the fixed parameter, so that on the second stage refit the released parameter converges to physically plausible values without compromising the overall fit quality.

The extraction of both parameters was conducted in the following steps:

1. Fixing known parameters by using familiar geometry and material characteristics as inputs.

2. Hierarchical identification

   (a) Useing the hybrid coarse grid search → Levenberg–Marquardt refinement described in Section 5.2 for f_{bundle} to impose limits where the forward model becomes non-physical.

   (b) Estimating $E_{f,T}$ primarily from the pre-crack slope and early CMOD evolution, which are most sensitive to the elastic bundle stiffness.

3. Validating the obtained LM minimum for each dataset by a constrained global search using Wolfram Mathematica's integrated function `NMinimize` (Simulated Annealing) over the same bounds, and recording the relative difference to confirm that LM reached a near-global minimum.

4. Due to computational cost of repeated equilibrium solves, the analysis was done on representative random subsets for each beam size. After that, the central tendency and scatter (mean, standard deviation, coefficient of variation, CV) was summarized across each subset.

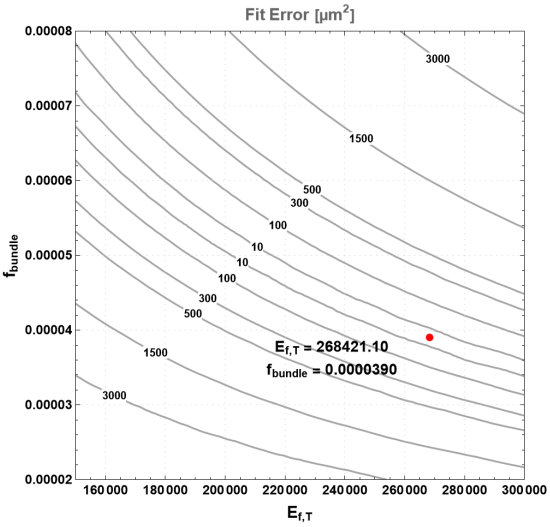

(a) Small-Sized Samples

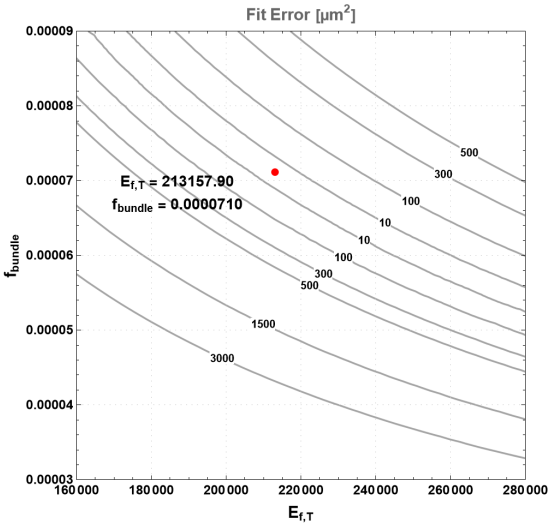

(b) Medium-Sized Samples

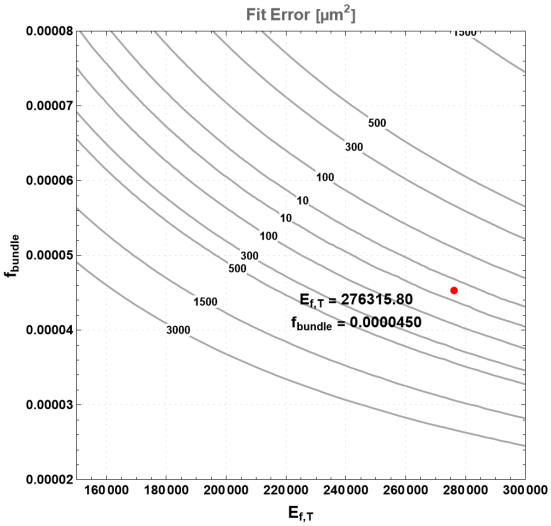

(c) Large-Sized Samples

Figure 7.4: Error Contour Plot for Dual-Parameter Extraction of $E_{f,T}$ vs f_{bundle}.

The dual-parameter extraction maps (shown in Figure 7.4) were generated and used to both decide the order of estimation, and to set physically plausible search windows that avoid numerically unstable zones, as well as to have a sense of when the optimization method might stagnate (flat residuals along a ridge) so that a coarse grid initialization should precede Levenberg–Marquardt. The sensitivity analysis from Section 6.3 served as a guide for where to place weight in the objective (early CMOD for $E_{f,T}$) and how tight the bounds for f_{bundle} must be to prevent non-physical forward responses.

Throughout the thesis and specifically in the first pass of f_{bundle} extraction, $E_{f,T}$ was fixed to $E_{f,T} = 210{,}000$ N/mm^2. This choice does not assert that the effective modulus of the fiber bundle is exactly equal to that of bulk steel, rather it serves as a neutral, physically plausible reference point to resolve the interdepen-

dence between f_{bundle} and $E_{f,T}$, while calibrating f_{bundle}. This two-stage approach was adopted to address the issue of non-uniqueness. By temporarily fixing $E_{f,T}$, the inverse problem collapses the search space of the interdependent $(f_{\text{bundle}}, E_{f,T})$ pair into a single direction for f_{bundle}, and therefore prevents the algorithm from drifting along the compensatory ridge. Importantly, this prior is explicitly removed in the second stage when $E_{f,T}$ itself is estimated. The results showed that releasing this prior and re-fitting $E_{f,T}$ did not compromise the goodness-of-fit. The final reported $E_{f,T}$ values were consistent with the effective bundle stiffness in real steel-fiber systems. Therefore, the initial $210,000$ N/mm^2 value is used strictly as a temporary regularization to stabilize the identification of f_{bundle}; the final reported $E_{f,T}$ value reflects the data, not the initial assumption.

The previous cross-size summary of the coefficient of variation shows that large beams consistently exhibit lower scatter in the extracted values for both f_{bundle} and $E_{f,T}$, while small beams show higher CVs. Given the deterministic nature of the experimental setup, these trends are best understood as differences in parameter identifiability. Larger sections provide richer and more stable information on the collective fiber behavior, which leads to better-conditioned inverse problems. In contrast, smaller sections, with their lower fiber count and smaller total area give flatter residual landscapes along the interdependent $(f_{\text{bundle}}, E_{f,T})$ ridge. This behavior was entirely anticipated from observing the dual-parameter maps and the initial sensitivity analysis.

7.2.1 Extraction of Experimental f_{bundle}

7.2.1.1 Extraction of Experimental f_{bundle} from Small-Sized Samples

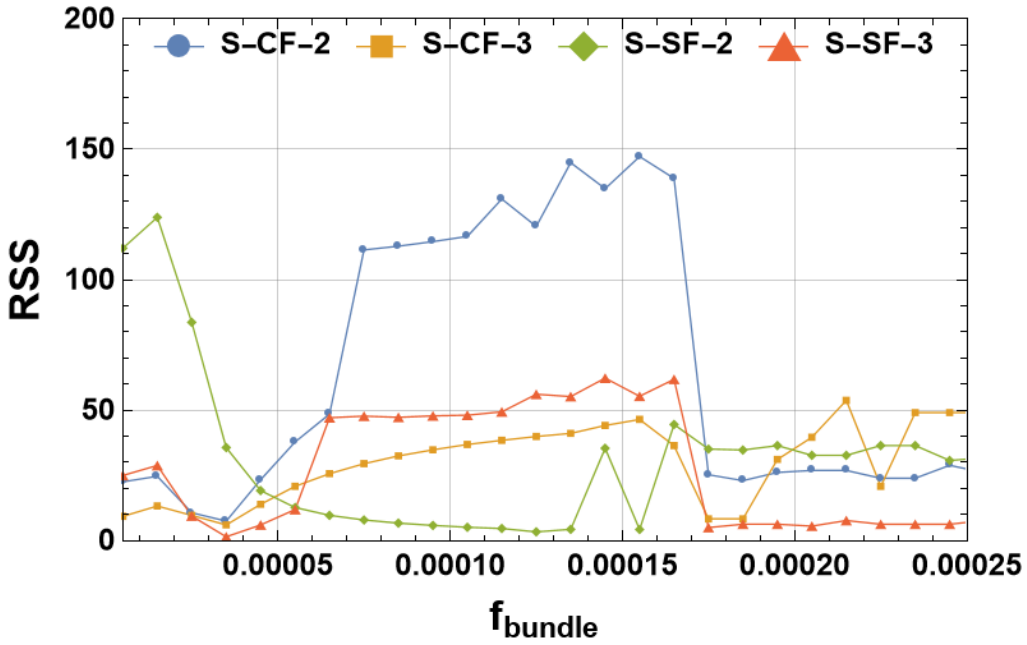

Figure 7.5: Initial Guess Candidates

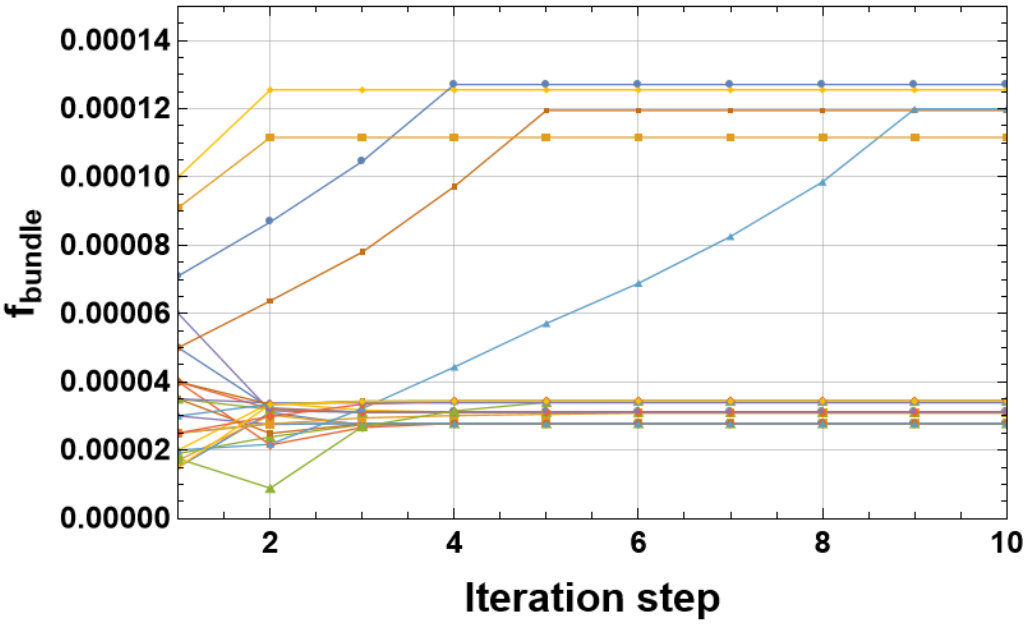

Figure 7.6: Results of Extraction of f_{bundle} from Small-Sized Samples

Table 7.2: Final Converged Values of f_{bundle} from Small-Sized Samples

Parameter	Final Values	Mean (μ)	Standard Deviation (σ)	Coefficient of Variation (CV)	Nminimize	Difference (%)
f_{bundle} S-CF-2	0.0002780 0.0000278 0.0000278 0.0000278 0.0000278 0.0000278 0.0000278	0.00002780	0.0000000	0.00%	0.0000278	0.00
f_{bundle} S-CF-3	0.00003113 0.00003113 0.00003084 0.00003113 0.00003113 0.00003113	0.00003108	0.0000012	0.38%	0.0000311	0.0558
f_{bundle} S-CF-2	0.0011947 0.0001199 0.0001255 0.0001271 0.0001116	0.00012070	0.0000610	5.06%	0.00013085	8.4121
f_{bundle} S-CF-3	0.00003434 0.00003434 0.00003385 0.00003434 0.00003435 0.00003435	0.0000343	0.0000020	0.59%	0.0000343	0.2466

Average obtained f_{bundle} from small-sized samples has a value of 0.0005346.

7.2.1.2 Extraction of Experimental f_{bundle} from Medium-Sized Samples

The results of f_{bundle} extraction shown as following: rang of candidates for the initial guess in 7.7, results of the extraction in Figure. 7.8.

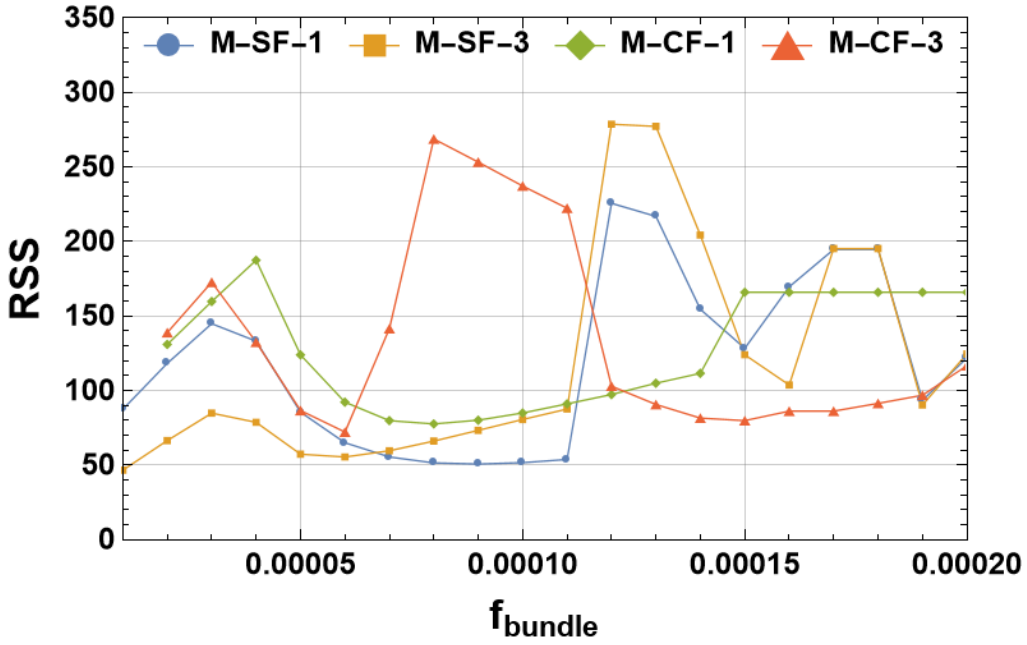

Figure 7.7: Initial Guess Candidates

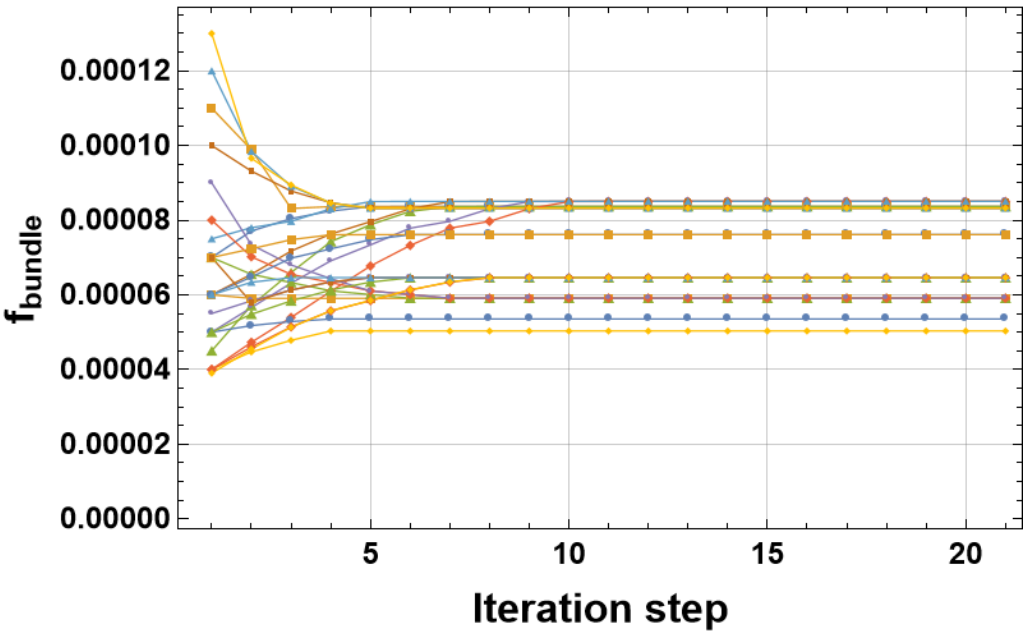

Figure 7.8: Results of Extraction of f_{bundle} from Medium-Sized Samples

Table 7.3: Final Converged Values of f_{bundle} from Medium-Sized Samples

Parameter	**Final Values**	**Mean (μ)**	**Standard Deviation (σ)**	**Coefficient of Variation (CV)**	**Nminimize**	**Difference (%)**
f_{bundle} M-SF-1	0.00008364 0.00008364 0.00008364 0.00008501 0.00008501 0.00008501	0.00008432	0.0000075	0.89%	0.00008894	5.49
f_{bundle} M-SF-3	0.00005031 0.00005352 0.00005905 0.00005909 0.00005909 0.00005909	0.00005669	0.0000384	6.77%	0.00005631	0.6831
f_{bundle} M-CF-1	0.00008315 0.00008322 0.00008322 0.00007611 0.00007611	0.00008036	0.0000388	4.83%	0.00006552	18.4650
f_{bundle} M-CF-3	0.00006455 0.00006455 0.00006455 0.00006460 0.00006460 0.00006460	0.00006458	0.0000002	0.04%	0.00006552	1.4681

7.2.1.3 Extraction of Experimental f_{bundle} from Large-Sized Samples

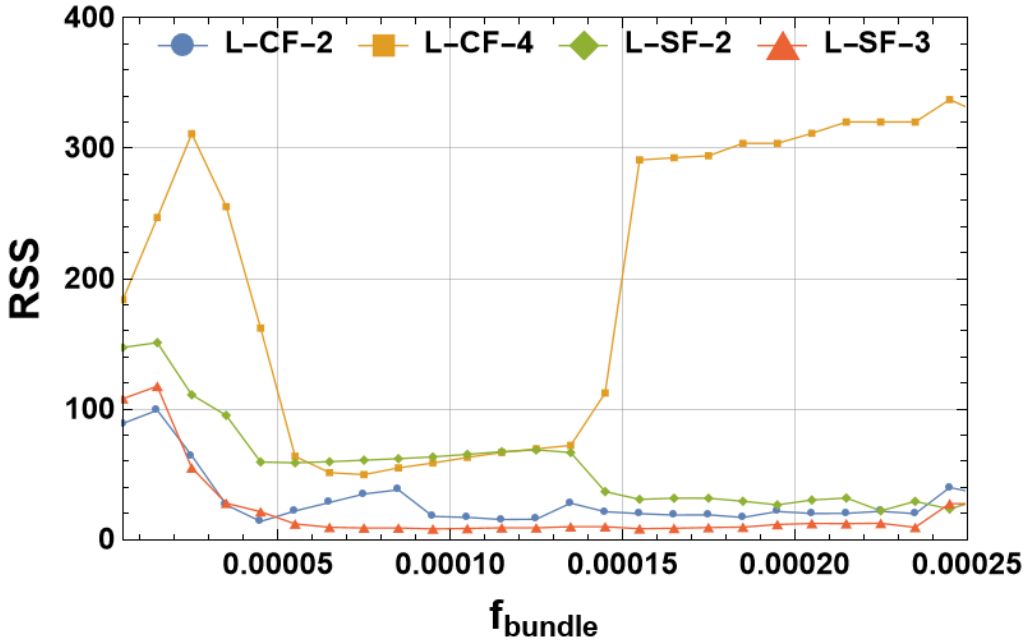

Figure 7.9: Initial Guess Candidates

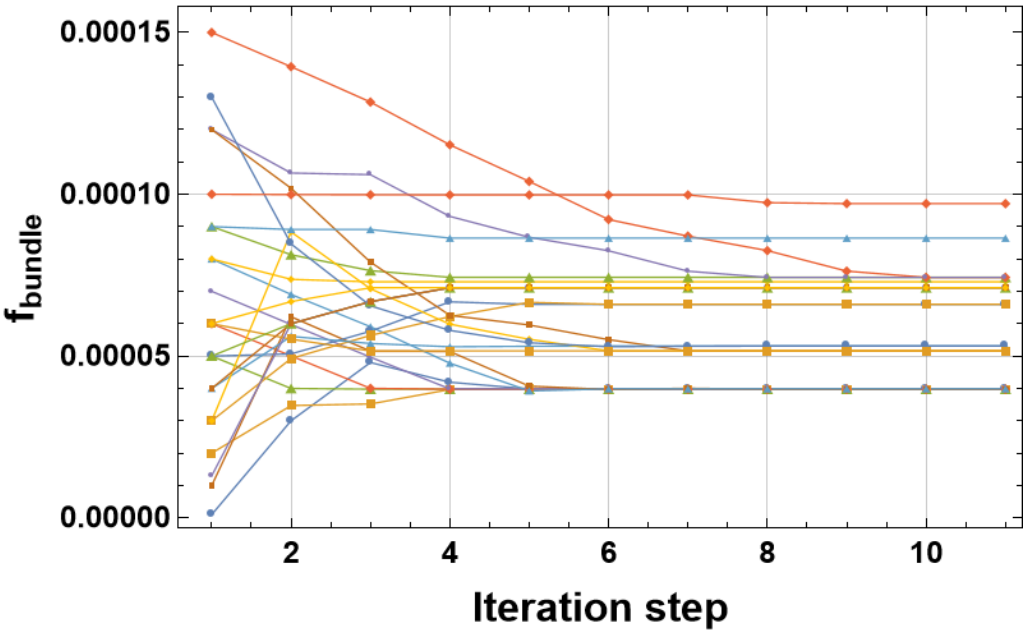

Figure 7.10: Results of Extraction of f_{bundle} from Large-Sized Samples

Table 7.4: Final Converged Values of f_{bundle} from Large-Sized Samples

Parameter	Final Values	Mean (μ)	Standard Deviation (σ)	Coefficient of Variation (CV)	Nminimize	Difference (%)
f_{bundle} L-CF-2	0.00003984 0.00003976 0.00003976 0.00003976 0.00003986 0.00003985 0.00003976	0.00003980	0.0000005	0.13%	0.0000398395	0.11
f_{bundle} L-CF-4	0.00007295 0.00006599 0.00007431 0.00007430 0.00007430 0.00006598	0.00007131	0.0000415	5.82%	0.000074805	4.9082
f_{bundle} L-SF-1	0.00005157 0.00005310 0.00005159 0.00005310 0.00005157 0.00005159	0.00005208	0.0000078	1.50%	0.000181725	248.904
f_{bundle} L-SF-3	0.00007110 0.00009710 0.00007110 0.00007110 0.00008643 0.00007110	0.00007799	0.00001119	14.35%	0.0013122	68.256

7.2.1.4 Interpretation of f_{bundle} Extraction Results

The Levenberg–Marquardt iteration paths demonstrated quick stabilization for all beam sizes, typically settlingby iteration 3–4. This fast convergence, coupled with the generally low within-dataset scatter of the converged f_{bundle} values, confirms good local identifiability when the parameter $E_{f,T}$ is held fixed. However, the agreement with `NMinimize` varies by size and fiber type, which indicates where the residual landscape stays flat due to any existing interdependence. The low scatter in these results also aligns with the expectation that larger beams provide more sta-

ble retrieval of information on the overall fiber behavior, which is a trend that is anticipated from the initial sensitivity and dual-parameter mapping (Figure 7.4).

For most small-beam datasets, the LM paths stabilized to a narrow band around 3–3.5 $\times$ 10^{-5} (Figure 7.6). This aligns with the very small scatter seen in Table 7.2 (CV $\leq$ 0.4% for S–CF–3 specimen) and the equality between the LM solution and the `NMinimize` global check. This confirms that f_{bundle} is well identified when the residual landscape is well conditioned. S–CF–2 dataset systematically returned a larger f_{bundle} and a slightly higher discrepancy (about 8%), which is a difference that coincides with the unique force–displacement shape of that particular specimen reported in 4.5. This demonstrates how the inverse algorithm compensates for individual any specimens deviations by shifting the f_{bundle} when $E_{f,T}$ is held fixed.

The extraction process for medium-sized beams consistently showed stable convergence, with iteration paths converging to a specific f_{bundle} values, as seen in Figure 7.8. The coefficients of variation for the group are mostly low, which points to high consistency in the extracted parameter values.

Despite having a greater scatter in the experimental force-displacement curves, large-sized beams had the most stable parameter extraction results for f_{bundle}. Figure 7.10 illustrates the convergence paths for these specimens. The coefficient of variation for the outlier L-CF-2 dataset was low at 0.13%, which confirms that the deterministic experimental setup on larger specimens leads to more easily identifiable parameters. The larger number of fibers and a greater total area in these specimens provide a stable collective response, which leads to a flatter residual landscape along the compensatory ridge.

Average obtained values for f_{bundle} across all specimen sizes are summarized in Table 7.5.

Table 7.5: Cross-size synthesis for bundle scaling factor (f_{bundle}) results

Metric	**Small beams**	**Medium beams**	**Large beams**
Mean (μ)	0.00004959	0.00007208	0.00005947
Average CV	2.71%	3.58%	5.20%
Average SD (σ)	0.0000161	0.0000212	0.0000405

7.2.2 Extraction of Experimental $E_{f,T}$

This parameter was extracted last due to it's high interedependancy on f_bundle. Without knowing a more precise f_bundle value, $E_{f,T}$ extraction was just a shot in the dark. Therefore, in this section, f_bundle from section 7.2.1 was used as a fixed input parameter while $E_{f,T}$ was extracted.

7.2.2.1 Extraction of Experimental $E_{f,T}$ from Small-Sized Samples

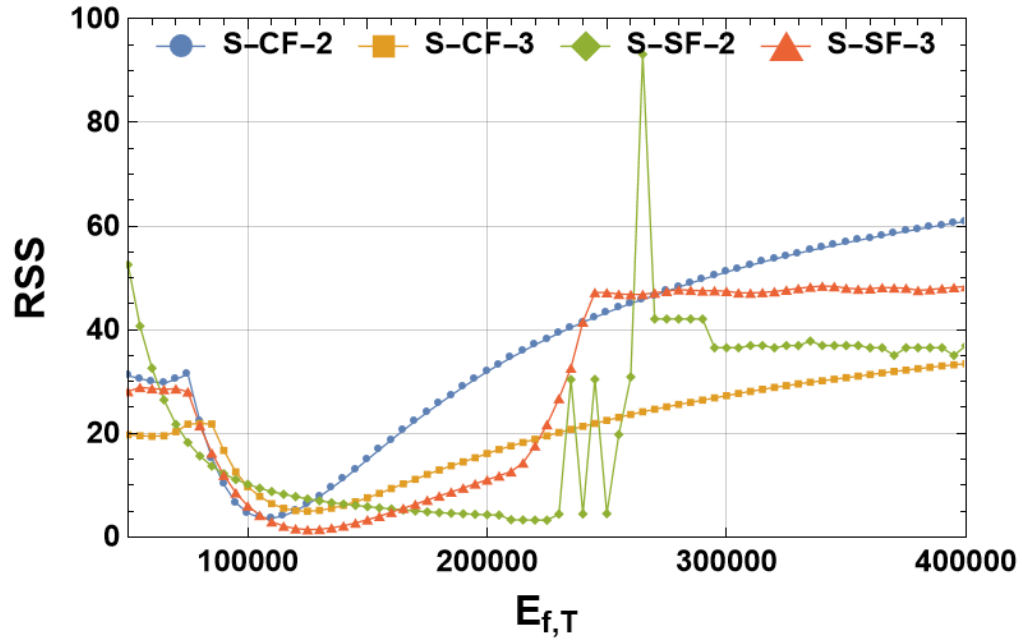

Figure 7.11: Initial Guess Candidates

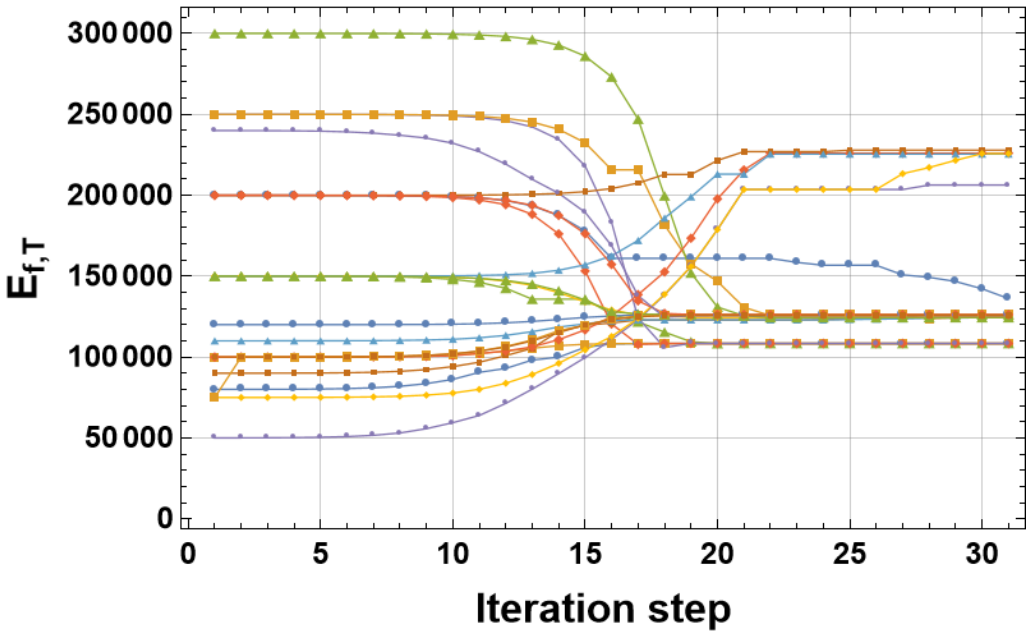

Figure 7.12: Results of Extraction of $E_{f,T}$ from Small-Sized Samples

These results show that the Levenberg-Marquardt algorithm demonstrates stable local convergence and rapidly settles to a solution from a wide range of initial guesses.

Table 7.6: Final Converged Values of $E_{f,T}$ from Small-Sized Samples

Parameter	**Final Converged Values**	**Mean (μ)**	**Standard Deviation (σ)**	**Coefficient of Variation**	**Nminimize**	**Difference (%)**
$E_{f,T}$ S-CF-2	108382.1 108382.1 108389.2 108382.1 108382.1 108383.8	108383.6	0.28	0.00%	108436.3	0.05
$E_{f,T}$ S-CF-3	124409.4 124403.1 124443.5 136149.5 124409.1 124409.4	126370.7	479.06	3.79%	124471.6	1.50
$E_{f,T}$ S-CF-2	226018.4 206291.7 227878.3 225421.3 225712.1 227994.7	223219.4	836.60	3.75%	225910.6	1.21
$E_{f,T}$ S-CF-3	126214.0 126214.0 126271.8 126265.0 125654.7 125649.4	126044.8	30.52	0.24%	126278.3	0.19

7.2.2.2 Extraction of Experimental $E_{f,T}$ from Medium-Sized Samples

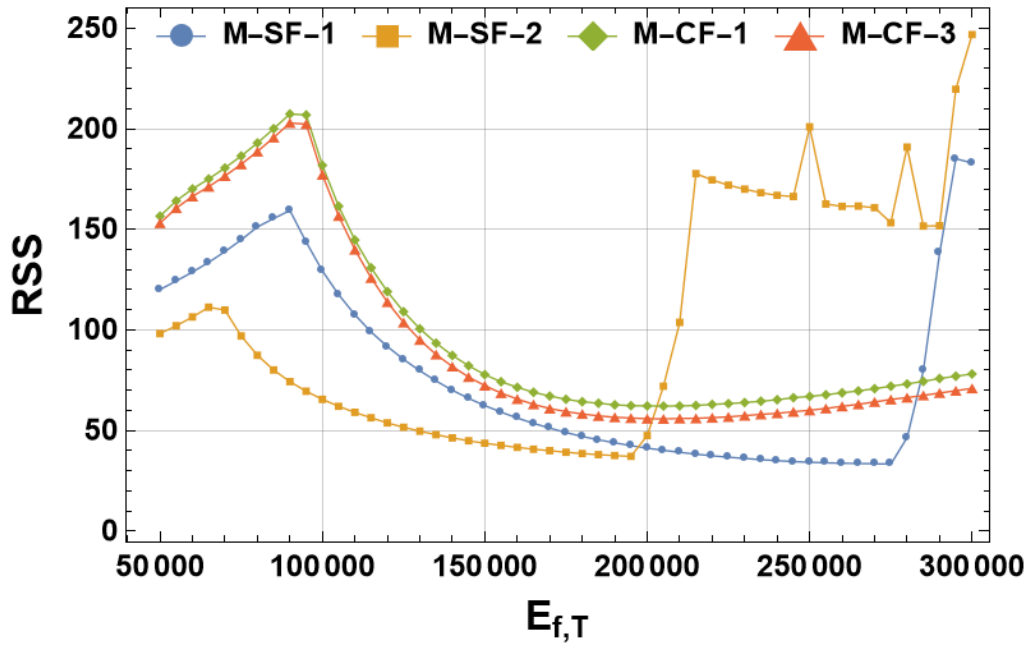

Figure 7.13: Initial Guess Candidates

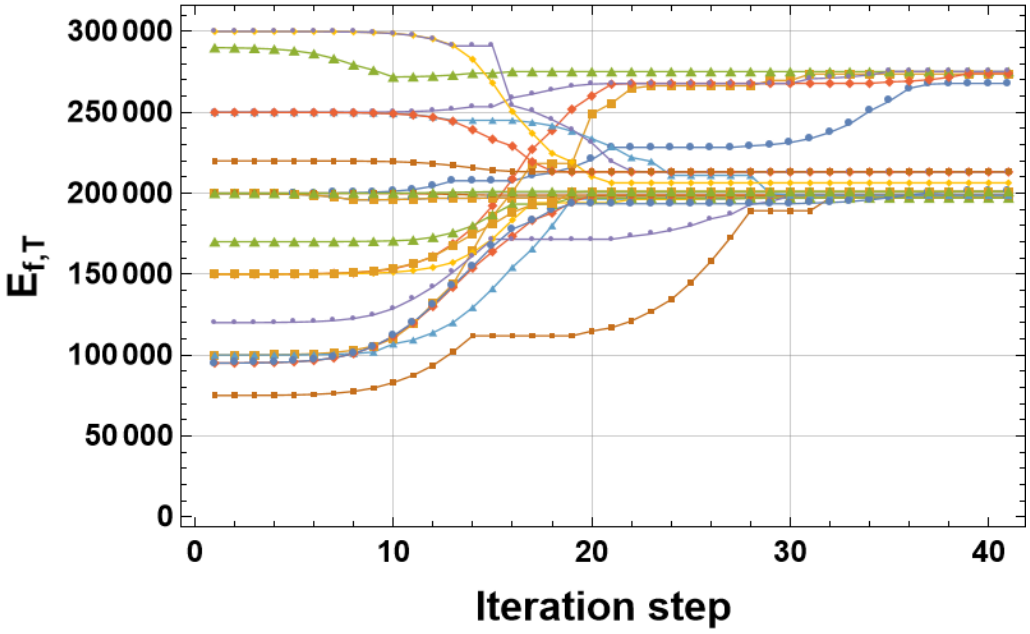

Figure 7.14: Results of Extraction of $E_{f,T}$ from Medium-Sized Samples

These results demonstrate that the extraction procedure maintains high stability across the medium-sized samples, and achieve consistent convergence paths for $E_{f,T}$. The candidate plots show a well-defined minima, which validates the strategy of sequential parameter fixing to resolve the initial interdependence issue.

Table 7.7: Final Converged Values of $E_{f,T}$ from Medium-Sized Beams

Parameter	**Final Converged Values**	**Mean (μ)**	**Standard Deviation (σ)**	**Coefficient of Variation**	**Nminimize**	**Difference (%)**
$E_{f,T}$ M-SF-1	267879.17 273687.00 275200.70 274003.55 275207.51	273195.58	3050.6925	1.12%	275411.74	0.81
$E_{f,T}$ M-SF-2	197028.01 197068.27 197076.57 197142.72 197142.72 197072.57	197088.48	45.48	0.02%	197157.45	0.04
$E_{f,T}$ M-CF-1	198695.91 198695.91 198727.52 198785.38 206407.92 198695.91	200001.42	3138.72	1.57%	206511.11	3.25
$E_{f,T}$ M-CF-3	201069.99 201070.08 201070.08 213168.58 213169.31 213205.89	207125.66	6633.60	3.20%	205048.45	1.00

7.2.2.3 Extraction of Experimental $E_{f,T}$ from Large-Sized Samples

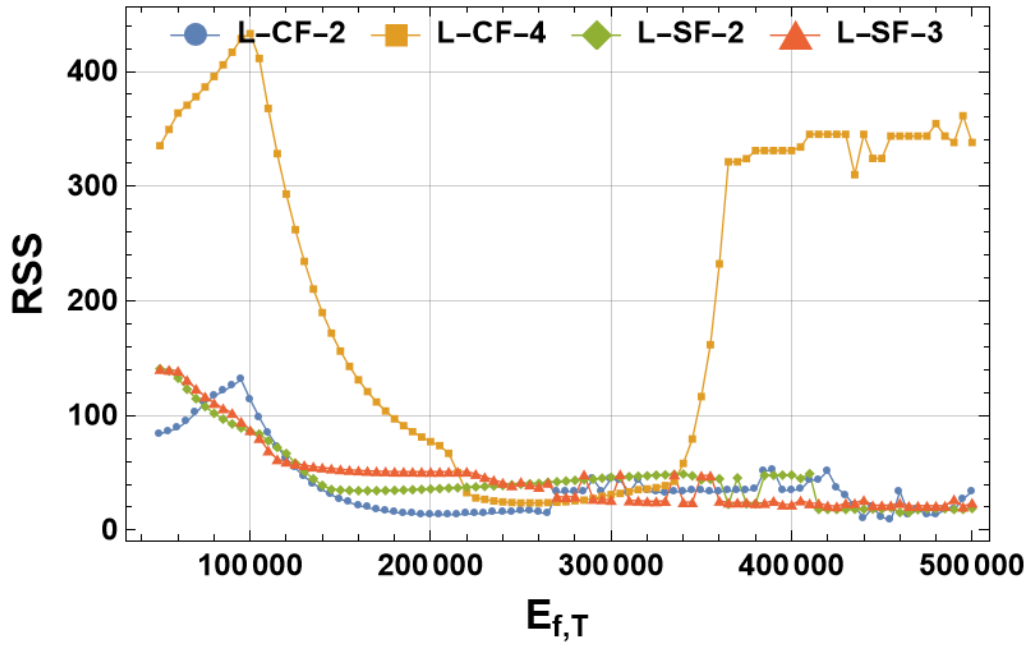

Figure 7.15: Initial Guess Candidates

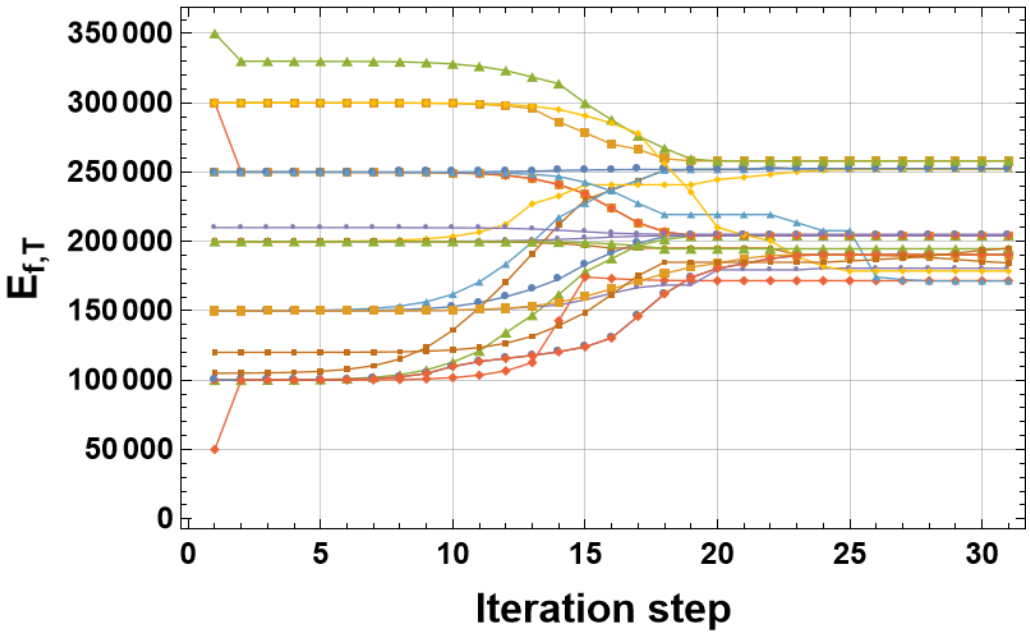

Figure 7.16: Results of Extraction of $E_{f,T}$ from Large-Sized Samples

These iteration results show that the inverse model remains stable for the largest specimens, and the process is characterized by rapid convergence to values consistent with the expected effective steel modulus. These results also underscores the

principle that increased size and fiber engagement provide richer, more constrained data, which leads to a more precise parameter identifiability.

Table 7.8: Final Converged Values of $E_{f,T}$ from Large-Sized Samples

Parameter	**Final Values**	**Mean (μ)**	**Standard Deviation (σ)**	**Coefficient of Variation**	**Nminimize**	**Difference (%)**
$E_{f,T}$ L-CF-2	204205.08 204311.35 204205.08 204311.32 204205.08	204247.58	58.20	0.03%	205220.0	0.48
$E_{f,T}$ L-CF-4	252537.69 252537.82 252015.70 252497.24 258110.46 258053.84	254292.13	2942.43	1.16%	258120.0	1.51
$E_{f,T}$ L-CF-1	171718.21 180621.06 184541.77 171534.67 178699.67 209749.23	182810.77	14146.15	7.74%	180660.0	1.18
$E_{f,T}$ L-CF-3	190480.62 190479.36 194743.94 190480.74 205097.93 195061.10	194390.61	5676.16	2.92%	291230.0	49.82

7.2.2.4 Interpretation of $E_{f,T}$ Extraction Results

The extraction of the effective elastic modulus in tension, $E_{f,T}$, was conducted as the second stage of the inverse analysis, after the bundle scaling factor, f_{bundle}, was determined. Overall, the analysis demonstrates a stable extraction process.

The initial guess candidates and convergence paths for the small-sized beams are shown in Figures 7.11 and 7.12. The results in Table 7.6 show that the extraction for most small-sized specimens was stable and converged with a very low coefficient of variation. Two clustered results are apparent: one around 1.25×10^5–1.26×10^5N/mm^2 and another near 2.23×10^5N/mm^2. These twin clusters likely and correctly reflects fiber-type or batch differences rather than size effects. Coefficient of variation for this testing group remains low, S-CF-2 shows a CV of 0.00% and a minimal difference of 0.05% from the `NMinimize` check, while some samples, like S-CF-3, show a slightly higher CV (3.79%), which suggests more variability but still in ranges.

The convergence paths for the medium-sized beams (Figure 7.14) show a stable and well-behaved extraction process, with rapid plateaus and low to moderate scatter. Iteration paths again converge in two distinct clusters: one around 2.13×10^5–1.26×10^5N/mm^2 and another one around 2.7×10^5N/mm^2. The results in Table 7.7 further confirm the stability of this optimization process, with most datasets showing a low CV. For instance, M-SF-2 has a CV of just 0.02% and a `NMinimize` difference of 0.04%, while the highest CV, seen in the specimen S-CF-3, is only 3.20%.

Most large-sized beam datasets confirm that more engaged fibers improve $E_{f,T}$ identifiability. The two cases that stand out have different signatures, as L–CF–1 shows a wide within-block spread, while L–CF–3 fits well locally but has a distant minimum for the same error surface under `NMinimize`. Notably, L–CF–3 is also the specimen whose TPBT force–displacement lacked a clear first peak, so the early CMOD window that anchors $E_{f,T}$ is less informative in this case, when that is precisely the condition that can create a flat landscape.

Across all beams, the identified $E_{f,T}$ spans roughly 1.08×10^5 to 2.75×10^5 MPa depending on fiber set and beam size, with within-type CVs typically $\leq 3\%$ and LM–global gaps $\leq 1.5\%$ in well-conditioned cases. Such magnitudes are consistent with steel fiber effective stiffness and with the bundle-scale picture established in Section 7.2.1.4. $E_{f,T}$ parameter is largely governed by the initial CMOD growth and is not size-dependent per se, since observed differences due to size reflect data informativeness rather than a physical size effect on the modulus.

Average obtained values for $E_{f,T}$ across all specimen sizes are summarized in Table 7.9.

Table 7.9: Cross-size synthesis for effective modulus ($E_{\mathrm{f,T}}$) results

Metric	**Small beams**	**Medium beams**	**Large beams**
Mean (μ) [N/mm^2]	146000	219600	208900
Average CV	1.95%	1.49%	3.06%
Average SD (σ)	336.61852	3217.12440	5705.73650

The most significant engineering implication of this analysis is the creation of a reliable and quantified dataset for FRC characterization. The final converged mean values (μ) for the effective modulus ($E_{\mathrm{f,T}}$) and the fiber bundle scaling factor (f_{bundle}) paired with their quantified scatter (CV), can be directly used as calibrated input parameters for various FRC engineering models, such as FEM simulations or standardized design code formulations. This allows structural engineers to predict the post-cracking behavior of FRC elements with parameters derived from a controlled experimental study, which can improve the accuracy of engineering models compared to relying only on manufacturer specifications.

Chapter 8

Discussion

This thesis was formed on the basis of asking a question whether a simple, well-posed deterministic forward model, coupled with a strategically chosen inverse algorithm, can recover physical and material parameters of fiber reinforced concrete beams from three-point bending tests. The collective results from verification and parameter extraction processes proved the viability of the developed inverse method for translating simplified modeling into real-world applications despite heterogeneity.

8.1 Recapitulation of Findings

The thesis was formed on the basis of asking a question whether a simple, well-posed deterministic forward model, coupled with a strategically chosen inverse algorithm, could recover physical and material parameters of fiber reinforced concrete beams from three-point bending tests. The collective results from verification and parameter extraction processes showed the potentiality of the developed inverse method for translating simplified modeling into real-world applications despite the inherent heterogeneity.

The forward model successfully reproduced crack mouth opening displacement for all beam sizes and various fiber configurations with low relative errors (NRMSE typically $\leq 20\%$, RSR < 0.5 and and $R^2 > 0.81$). These simulated curves consistently fell within the experimental variability bands of $\pm 1\sigma$ to $\pm 2\sigma$, which confirmed that the model's constitutive components and numerical solution are sufficiently accurate enough for deriving results from structural responses. For an inverse identification to be valid, the accuracy of the simplified forward model is essential because otherwise any parameter estimates would be compromised by model error.

A direct comparison with an established complex stochastic fiber bundle model showed that the deterministic approach successfully replicates the average behavior. Divergence only appeared in the regions where fiber variability is highest. This kind

of stability in the predictability of the relationship between parameters and the average structural response is a prerequisite for the inverse identification procedure. This being successful validates using the simplified deterministic representation as a tool for parameter estimation, as it .enables the extraction of material signals from structural data, even without providing an explanation for the measured data's inherent scatter.

The technical reliability of the inverse model can be categorized as established and technically sound. The Levenberg–Marquardt optimizer successfully recovered the true values of all seven parameters with 100% accuracy from synthetic data, while typically converging within 3 to 7 iterations. The bound-of-attraction (BoA) analysis further quantified the solution's stability and identified numerical limits and specific failure modes for different parameters. Through the process of validation it was confirmed that if real data fails to converge clearly, it can be confidently attributed to either the quality of the measured data, wrongly fixed input parameters, or the problem of non-uniqueness, rather than a malfunctioning algorithm.

The dual-parameter extraction analysis mapped error surfaces in two-dimensional parameter spaces in order to highlight both unique and non-unique cases of identifiability. This systematic mapping addressed the central challenge of the deterministic inverse analysis, which is the danger of a biased extractions when parameters are treated independently. As an example, the parameter pair ($E_{f,T}$, f_{bundle}) consistently produced maps with elongated valleys that reflect their compensatory relationship in governing the pre-peak bundle stiffness. By explicitly characterizing there interdependencies, the dual-parameter analysis establishes a guideline for a hierarchical identification strategy, as long as the formulated deterministic model is robust enough to compensate for the temporary assumption error.

Sensitivity scans and BoA analyses indicated that the size of the beam influences identifiability, but not in a monotonic fashion.

- Small beams are greatly affected by the localized placement of individual fibers, which makes the overall parameter extraction results jumpy and unpredictable. In practice, this led some datasets to near-perfect convergence (CV $\approx$ 0%), but in others, scatter increased significantly (CV up to 5% for f_{bundle}, and 3–4% for $E_{f,T}$).
- Medium beams proved the most consistently well-conditioned. Their coefficients of variation for inverse parameter estimation were generally lowest. This reflects both the balance between fiber count, material characteristics and the experimental measurement resolution, but also the fact that the model was originally calibrated using medium-sized specimens.

- Large beams give the most reliable and stable information about how the fibers are working because large beam sections have average out the randomness to a greater degree. However, these beams are also the most vulnerable to errors that propagate from experimental irregularities which are also greater in magnitude simply due to the scale of the beams being greater. For example, this is seen in the specimen lacking a clear first peak in the load–displacement response (L–CF–3), which ended up showing inflated scatter and larger discrepancies between LM and global optimization.

Therefore, size of beams affects how well parameters can be identified by influencing how much useful information the data signal contains, rather than by following a predictable pattern.

This has direct implications for experimental design. If the goal is parameter identification and not just flexural strength testing, beam geometry should be chosen so it best averages the mechanisms of interest. Medium beams are the most reliable geometry for FRC CMOD-based identification, while large beams are advantageous for that purpose but demand stable and clean experimental signals, and small beams should be used cautiously due to their sensitivity to local fiber effects.

The extraction procedure successfully recovered both f_{bundle} and $E_{f,T}$ from experimental data. The two-stage approach where, first, f_{bundle} was constrained under a fixed $E_{f,T}$, then released prior to extractiong $E_{f,T}$ proved to be effective in navigating the compensatory ridge observed in dual-parameter maps.

The obtained values of f_{bundle} ($\approx 5 \times 10^{-4}$ to 7×10^{-4}) align with physically plausible scaling of bundle stiffness, while the extracted $E_{f,T}$ values spanned $1.08 \times 10^5 \leq E_{f,T} \leq 2.75 \times 10^5\,\mathrm{N/mm^2}$, and showed recognition of two different fiber systems (coarse and smooth). Importantly, all these values were obtained with low within-group scatter and with good agreement between LM and global checks, except in cases where individual experimental irregularities produced flat error landscapes.

Overall, these findings support the hypothesis that a simplified deterministic model, despite its abstraction, is capable of extracting meaningful FRC parameters even when experimental data includes scatter.

8.2 Original Scientific Contributions

The findings of this thesis contribute to the field of FRC modeling and inverse analysis in several ways:

1. Novel deterministic model

This research developes a simplified yet physically consistent deterministic model that connects micro-level inputs (fiber bond–slip law) with macro-level outputs (beam's crack mouth opening displacement response), and achieves functional multiscale coupling without a need for computationally extensive explicit multiscale frameworks.

2. Inverse analysis strategy
   The study demonstrates how a multi-staged parameter identification strategy can resolve deterministic non-uniqueness,and offer a structured methodology for dealing with interdependent parameters.

3. Guidelines for experimental design
   By systematically comparing parameter identifiability for different specimen sizes, the study establishes how geometry influences and conditions the information content of CMOD tests. This can provide researchers with practical guidance when selecting specimen configurations for parameter extraction, unlike purely strength-based assessments.

4. Deterministic modeling under variability
   The research shows that deterministic formulations paired with sensitivity-informed inverse routines, can be effective simulation and extraction methods even when experimental data contain scatter. In doing so, it demonstrates how deterministic models can complement and, in some contexts, substitute stochastic approaches in material characterization.

8.3 Practical Implications and Future Work

From an engineering perspective, the ability to identify parameters that cannot be physically measured has direct relevance to structural design and material optimization. Models like this can be used to calibrate design parameters more efficiently and reduce reliance on expensive and time-consuming experimental programs. And in specific cases of maintenance and inspection of FRC structures, they also provide a systematic path for excluding unsuitable fiber types by ruling out parameter ranges inconsistent with observed behavior.

Future work may extend this research by:

- Extending the forward model beyond the CMOD based response by incorporating moment–curvature distributions along the beam span. This would make it possible to recover full load–deflection profiles and deformation shapes, and link local crack-opening behavior to the structural response along the whole beam, not just the observed cross-section.

- Establishing experimental procedures for producing and testing beams with controlled fiber orientations ($\neq 0°$) and distributions. With such protocols are in place, the current framework can be extended to quantify the effects of non-random or preferential fiber alignment on CMOD behavior and to overall better characterize FRC as an engineering material.

- Expanding the experimental database to include different fiber types, contents, and beam geometries. With such a richer dataset strengthen the validation of parameter ranges and broader spectrum of what the model can capture, beyond FRC behaviors.

- Coupling the current analytical framework with finite element modeling, to integrate different material heterogeneity zones, and more complex boundary conditions. This would significantly broaden the applicability of the model to real structural configurations.

- Investigating multi-objective optimization strategies. Beyond minimizing residual error, these approaches could balance additional goals such as ensuring the physical plausibility of analyzed parameters while maintaining stability under experimental noise, which would improve parameter identification.

8.4 Summary

In summary, this discussion establishes that the proposed deterministic framework, though simplified, is technically sound, physically meaningful, and practically useful. It extracts parameters that are not directly measurable, demonstrates robustness against experimental variability, and provides clear insights into how experimental design (notably specimen size) shapes identifiability. The thesis therefore makes both a methodological and a practical contribution as it advances scientific insights into deterministic modeling of heterogeneous composites, while also offering a foundation for developing future engineering guidelines for efficient and reliable FRC characterization.

Chapter 9

Conclusion

This dissertation successfully addressed the challenge of efficient and reliable inverse material parameter identification in Fiber-Reinforced Concrete using a novel deterministic modeling framework. The research validates a methodology that connects micro-scale material behavior (bond-slip law and fiber properties) with macro-scale structural response (CMOD) in order to extract physically meaningful, but unmeasurable parameters.

The central problem that was addressed was the historical difficulty in implementing complex deterministic FRC models for an inverse analysis due to computational cost and difficulty to handle experimental data scatter. This thesis proposed three primary hypotheses, all of which are confirmed by the results:

1. The simplified and analytical deterministic model, built on the layered beam approach and piecewise pullout formulation, successfully replicated three-point bending test results. The model achieved a high quantitative fit with experimental data, which is also demonstrated by a Coefficient of Determination (R^2) consistently above 0.81 for all beam sizes and material configurations.

2. The formulation of the forward model's algorithm provided a suitable foundation for the inverse procedure. Computational quantification showed that the Levenberg-Marquardt iterations, initialized by a grid search, consistently converged to the optimal solution within 7 iteration steps, which confirmed that the approach effectively resolves the issue of excessive computational time inherent in more complex models.

3. The deterministic model proved capable of compensating for experimental scatter during inverse analysis, which confirms it as well-posed and robust. The hybrid grid $\rightarrow LM$ procedure reliably extracted material parameters from noisy data, and demonstrated that the observed scatter primarily reflects parameter identifiability limits due to specimen geometry (size effects) rather

than any algorithmic issues.

These findings advance scientific insights into heterogeneous composites and computational modeling of FRC by demonstrating that deterministic formulations can reliably extract and quantify material performance parameters like $E_{\mathrm{f,T}}$ and f_{bundle}. The extracted (μ) and quantified scatter (CV) can be directly used as calibrated input data for structural engineering models and design codes. The thesis, therefore, provides a strong foundation for developing future engineering guidelines for efficient FRC characterization.

Future research extending this framework aims to focus on three primary directions. First, it is necessary to develop experimental procedures that allow for testing and extension of the current model to include the effects of controlled fiber orientations, that would extend beyond only unilateral fiber orientation. Second, the forward model is to be extended to incorporate moment–curvature distributions along the beam span, which is essential for recovering complete load–deflection profiles and validating the model against the structural response across the entire beam. Finally, the analytical framework should be integrated with more complex computational models (like FEM) to investigate stress distribution under more complex boundary conditions and load transfer in heterogeneous sections.

List of Figures

List of Tables

Appendices

Appendix A

Appendix A:Inverse Analysis Iteration Summaries for Synthetic Data

Small-Sized Samples h_a

Table A.1: Iteration Summary for Estimating Synthetic $h_a = 0.01$cm with Different Initial Guesses on Small-Sized Samples

Initial Guess (h_{a_0})	Iteration (k)	Guess (h_{a_k})	Update (Δh_a)	Result ($h_{a_{k+1}}$)	Comment
-3.70	1	-3.70	2.16	-1.54	
	2	-1.54	1.32	-0.22	
	3	-0.22	0.15	-0.06	
	4	-0.06	0.07	0.01	
	5	0.01	0.00	0.01	Converged
0.15	1	0.15	-0.14	0.01	
	2	0.01	0.00	0.01	Converged
0.30	1	0.30	-0.28	0.02	
	2	0.02	-0.01	0.01	
	3	0.01	0.00	0.01	Converged
0.39	1	0.39	-0.36	0.03	
	2	0.03	-0.02	0.01	
	3	0.01	0.00	0.01	Converged
0.80	1	0.80	-0.81	-0.01	
	2	-0.01	0.02	0.01	

	3	0.01	0.00	0.01	Converged
5.00	1	5.00	-4.14	0.86	
	2	0.86	-0.88	-0.02	
	3	-0.02	0.03	0.01	
	4	0.01	0.00	0.01	Converged

Table A.2: Iteration Summary for Estimating Synthetic $h_a = 0.15$cm with Different Initial Guesses on Small-Sized Samples

Initial Guess (h_{a_0})	Iteration (k)	Guess (h_{a_k})	Update (Δh_a)	Result ($h_{a_{k+1}}$)	Comment
-3.70	1	-3.70	2.22	-1.48	
	2	-1.48	1.36	-0.11	
	3	-0.11	0.25	0.14	
	4	0.14	0.01	0.15	
	5	0.15	0.00	0.15	Converged
0.01	1	0.01	0.14	0.15	
	2	0.15	0.00	0.15	Converged
0.30	1	0.30	-0.15	0.15	
	2	0.15	0.00	0.15	Converged
0.39	1	0.39	-0.23	0.16	
	2	0.39	-0.23	0.16	
	3	0.15	0.00	0.15	Converged
0.80	1	0.80	-0.67	0.13	
	2	0.13	0.02	0.15	
	3	0.15	0.00	0.15	Converged
5.00	1	5.00	-4.03	0.97	
	2	0.97	-0.86	0.11	
	3	0.11	0.04	0.15	
	4	0.15	0.00	0.15	Converged

Table A.3: Iteration Summary for Estimating Synthetic $h_a = 0.30$cm with Different Initial Guesses on Small-Sized Samples

Initial Guess (h_{a_0})	Iteration (k)	Guess (h_{a_k})	Update (Δh_a)	Result ($h_{a_{k+1}}$)	Comment

-3.70	1	-3.70	2.28	-1.42	
	2	-1.42	1.43	0.01	
	3	0.01	0.28	0.29	
	4	0.29	0.01	0.30	
	5	0.30	0.00	0.30	Converged
0.01	1	0.01	0.28	0.29	
	2	0.29	0.01	0.30	
	3	0.30	0.00	0.30	Converged
0.15	1	0.15	0.15	0.30	
	2	0.30	0.00	0.30	Converged
0.39	1	0.39	-0.09	0.30	
	2	0.30	0.00	0.30	Converged
0.80	1	0.80	-0.52	0.28	
	2	0.28	0.02	0.30	
	3	0.30	0.00	0.30	Converged
5.00	1	5.00	-3.91	1.09	
	2	1.09	-0.86	0.23	
	3	0.23	0.07	0.30	
	4	0.30	0.00	0.30	Converged

Table A.4: Iteration Summary for Estimating Synthetic $h_a = 0.39$cm with Different Initial Guesses on Small-Sized Samples

Initial Guess (h_{a_0})	Iteration (k)	Guess (h_{a_k})	Update (Δh_a)	Result ($h_{a_{k+1}}$)	Comment
-3.70	1	-3.70	2.31	-1.39	
	2	-1.39	1.48	0.09	
	3	0.09	0.30	0.39	
	4	0.39	0.00	0.39	Converged
0.01	1	0.01	0.37	0.38	
	2	0.38	0.01	0.39	
	3	0.39	0.00	0.39	Converged
0.15	1	0.15	0.24	0.39	
	2	0.39	0.00	0.39	Converged
0.30	1	0.30	0.09	0.39	
	2	0.39	0.00	0.39	Converged

0.80	1	0.80	-0.42	0.38	
	2	0.38	0.01	0.39	
	3	0.39	0.00	0.39	Converged
5.00	1	5.00	-3.83	1.17	
	2	1.17	-0.85	0.32	
	2	0.32	0.07	0.39	
	3	0.39	0.00	0.39	Converged

Δa

Table A.5: Iteration Summary for Estimating Synthetic $\Delta a = 0.10$ with Different Initial Guesses on Small-Sized Samples

Initial Guess (Δa_0)	Iteration (k)	Guess (Δa_k)	$\Delta(\Delta a)$	Result (Δa_{k+1})	Comment
0.04	1	0.04	0.38	0.42	
	2	0.42	-0.18	0.24	
	3	0.24	-0.09	0.15	
	4	0.15	-0.03	0.12	
	5	0.12	-0.02	0.10	
	6	0.10	0.00	0.10	Converged
0.09	1	0.09	0.01	0.10	
	2	0.10	0.00	0.10	Converged
0.11	1	0.11	-0.01	0.10	
	2	0.10	0.00	0.10	Converged
0.20	1	0.20	-0.06	0.14	
	2	0.14	-0.03	0.11	
	3	0.11	-0.01	0.10	
	4	0.10	0.00	0.10	
	5	0.10	0.00	0.10	Converged
0.35	1	0.35	-0.14	0.21	
	2	0.21	-0.07	0.14	
	3	0.14	-0.03	0.12	
	4	0.12	-0.01	0.10	
	5	0.10	0.00	0.10	
	6	0.10	0.00	0.10	Converged
0.50	1	0.50	-0.18	0.32	
	2	0.32	-0.12	0.20	

	3	0.20	-0.06	0.14	
	4	0.14	-0.03	0.11	
	5	0.11	-0.01	0.10	
	6	0.10	0.00	0.10	Converged
0.93	1	0.93	-0.40	0.53	
	2	0.53	-0.17	0.35	
	3	0.35	-0.14	0.22	
	4	0.22	-0.07	0.14	
	5	0.14	-0.03	0.12	
	6	0.12	-0.01	0.10	
	8	0.10	0.00	0.10	Converged

Table A.6: Iteration Summary for Estimating Synthetic $\Delta a = 0.20$ with Different Initial Guesses on Small-Sized Samples

Initial Guess (Δa_0)	Iteration (k)	Guess (Δa_k)	$\Delta(\Delta a)$	Result (Δa_{k+1})	Comment
0.08	1	0.08	0.68	0.76	
	2	0.76	-0.30	0.46	
	3	0.46	-0.16	0.30	
	4	0.30	-0.08	0.22	
	5	0.22	-0.02	0.20	
	6	0.20	0.00	0.20	Converged
0.10	1	0.10	0.33	0.43	
	2	0.43	-0.15	0.28	
	3	0.28	-0.07	0.21	
	4	0.21	-0.01	0.20	
	5	0.20	0.00	0.20	Converged
0.35	1	0.35	-0.11	0.24	
	2	0.24	-0.04	0.20	
	3	0.20	0.00	0.20	
	4	0.20	0.00	0.20	Converged
0.50	1	0.50	-0.17	0.33	
	2	0.33	-0.10	0.24	
	3	0.24	-0.03	0.20	
	4	0.20	0.00	0.20	
	5	0.20	0.00	0.20	Converged

0.93	1	0.93	-0.39	0.54	
	2	0.54	-0.18	0.36	
	3	0.36	-0.11	0.25	
	4	0.25	-0.04	0.20	
	5	0.20	0.00	0.20	
	6	0.20	0.00	0.20	Converged

Table A.7: Iteration Summary for Estimating Synthetic $\Delta a = 0.35$ with Different Initial Guesses on Small-Sized Samples

Initial Guess (Δa_0)	Iteration (k)	Guess (Δa_k)	$\Delta(\Delta a)$	Result (Δa_{k+1})	Comment
0.11	1	0.11	0.81	0.92	
	2	0.92	-0.35	0.57	
	3	0.57	-0.14	0.43	
	4	0.43	-0.06	0.37	
	5	0.37	-0.01	0.35	
	6	0.35	0.00	0.35	Converged
0.20	1	0.20	0.16	0.36	
	2	0.36	-0.01	0.35	
	3	0.35	0.00	0.35	Converged
0.50	1	0.50	-0.10	0.40	
	2	0.40	-0.04	0.36	
	3	0.36	-0.01	0.35	
	4	0.35	0.00	0.35	Converged
0.93	1	0.93	-0.35	0.58	
	2	0.58	-0.14	0.44	
	3	0.44	-0.07	0.37	
	4	0.37	-0.02	0.35	
	5	0.35	0.00	0.35	Converged

Table A.8: Iteration Summary for Estimating Synthetic $\Delta a = 0.50$ with Different Initial Guesses on Small-Sized Samples

Initial Guess (Δa_0)	Iteration (k)	Guess (Δa_k)	$\Delta(\Delta a)$	Result (Δa_{k+1})	Comment
0.14	1	0.14	0.67	0.81	

	2	0.81	-0.23	0.58	
	3	0.58	-0.07	0.52	
	4	0.52	-0.01	0.50	
	5	0.50	0.00	0.50	Converged
0.20	1	0.20	0.34	0.54	
	2	0.54	-0.04	0.50	
	3	0.50	0.00	0.50	Converged
0.35	1	0.35	0.14	0.49	
	2	0.49	0.01	0.50	
	3	0.50	0.00	0.50	Converged
0.93	1	0.93	-0.29	0.64	
	2	0.64	-0.10	0.53	
	3	0.53	-0.03	0.50	
	4	0.50	0.00	0.50	Converged

$E_{\mathrm{f,T}}$

Table A.9: Iteration Summary for Estimating Synthetic $E_{\mathrm{f,T}} = 500\,\mathrm{N/mm^2}$ with Different Initial Guesses on Small-Sized Samples

Initial Guess ($E_{f,T}$)	Iteration (k)	Guess ($E_{f,T,k}$)	$\Delta E_{\mathrm{f,T}}$	Result ($E_{f,T,k+1}$)	Comment
1	1	1	499	500	
	2	500	0	500	Converged
7500	1	7500	-7174	326	
	2	326	174	500	
	3	500	0	500	Converged
21000	1	21000	-20802	198	
	2	198	302	500	
	3	500	0	500	Converged
23000	1	23000	-22971	29	
	2	29	471	500	
	3	500	0	500	Converged
30000	1	30000	-31555	-1555	Negative value of the update step
	2	-1555	—	—	Model failed at this guess

Table A.10: Iteration Summary for Estimating Synthetic $E_{\mathrm{f,T}} = 7\,500\,\mathrm{N/mm^2}$ with Different Initial Guesses on Small-Sized Samples

Initial Guess ($E_{f,T}$)	Iteration (k)	Guess ($E_{f,T,k}$)	$\Delta E_{\mathrm{f,T}}$	Result ($E_{f,T,k+1}$)	Comment
1	1	1	7218	7219	
	2	7219	281	7500	
	3	7500	0	7500	Converged
500	1	500	6728	7228	
	2	7228	272	7500	
	3	7500	0	7500	Converged
21000	1	21000	-13548	7452	
	2	7452	48	7500	
	3	7500	0	7500	Converged
30000	1	30000	-23773	6227	
	2	6227	1235	7462	
	3	7462	38	7500	
	4	7500	0	7500	Converged
75000	1	75000	-74985	15	
	2	15	7204	7219	
	3	7219	281	7501	
	4	7501	-1	7500	
80000	1	80000	-82438	-2438	Negative value of the update step
	2	-2438	—	—	Model failed at this guess

Table A.11: Iteration Summary for Estimating Synthetic $E_{\mathrm{f,T}} = 10\,000\,\mathrm{N/mm^2}$ with Different Initial Guesses on Small-Sized Samples

Initial Guess ($E_{f,T}$)	Iteration (k)	Guess ($E_{f,T,k}$)	$\Delta E_{\mathrm{f,T}}$	Result ($E_{f,T,k+1}$)	Comment
1	1	1	9496	9497	
	2	9497	506	10002	
	3	10002	-2	10000	
	4	10000	0	10000	Converged
7500	1	7500	2472	9972	
	2	9972	28	10000	

Table A.11: Iteration Summary for Estimating Synthetic $E_{\mathrm{f,T}} = 10\,000\,\mathrm{N/mm^2}$ with Different Initial Guesses on Small-Sized Samples

Initial Guess ($E_{f,T}$)	Iteration (k)	Guess ($E_{f,T,k}$)	$\Delta E_{\mathrm{f,T}}$	Result ($E_{f,T,k+1}$)	Comment
	3	10000	0	10000	Converged
21000	1	21000	-11071	9929	
	2	9929	71	10000	
	3	10000	0	10000	Converged
30000	1	30000	-21125	8875	
	2	8875	1092	9967	
	3	9967	33	10000	
	4	10000	0	10000	Converged
81000	1	81000	-80431	569	
	2	569	8941	9511	
	3	9511	492	10002	
	4	10002	-2	10000	
	5	10000	0	10000	Converged

Table A.12: Combined Iteration Summary for Estimating Synthetic $E_{\mathrm{f,T}} = 21\,000\,\mathrm{N/mm^2}$ with Different Initial Guesses on Small-Sized Samples

Initial Guess ($E_{f,T}$)	Iteration (k)	Guess ($E_{f,T,k}$)	$\Delta E_{\mathrm{f,T}}$	Result ($E_{f,T,k+1}$)	Comment
1	1	1	19596	19597	
	2	19597	1397	20994	
	3	20994	6	21000	
	4	21000	0	21000	Converged
7500	1	7500	13320	20820	
	2	20820	180	21000	
	3	21000	0	21000	Converged
10000	1	10000	11055	21055	
	2	21055	-55	21000	
	3	21000	0	21000	Converged
30000	1	30000	-9340	20660	
	2	20660	336	20996	
	3	20996	4	21000	

	4	21000	0	21000	Converged
210500	1	210500	-201607	8893	
	2	8893	12235	21128	
	3	21128	-128	21000	
	4	21000	0	21000	Converged

Table A.13: Combined Iteration Summary for Estimating Synthetic $E_{\mathrm{f,T}} = 30\,000\,\mathrm{N/mm^2}$ with Different Initial Guesses on Small-Sized Samples

Initial Guess ($E_{f,T}$)	Iteration (k)	Guess ($E_{f,T,k}$)	$\Delta E_{\mathrm{f,T}}$	Result ($E_{f,T,k+1}$)	Comment
1	1	1	27594	27595	
	2	27595	1235	7462	
	3	7462	2387	29982	
	4	29982	18	30000	
	5	30000	0	30000	Converged
500	1	500	27132	27632	
	2	27632	2350	29982	
	3	29982	18	30000	
	4	30000	0	30000	Converged
7500	1	7500	21819	29319	
	2	27632	677	29996	
	3	29996	4	30000	
	4	30000	0	30000	Converged
21000	1	21000	8739	29739	
	2	29739	257	29996	
	3	29996	4	30000	
	4	30000	0	30000	Converged
35000	1	35000	-5074	29925	
	2	29925	75	30000	
	3	30000	0	30000	Converged
210500	1	210500	-190152	20348	
	2	20348	9262	29611	
	3	29611	386	29996	
	4	29996	4	30000	
	5	30000	0	30000	Converged

f_c^{max}

Table A.14: Iteration Summary for Estimating Synthetic $f_c^{max} = 0.40$kN with Different Initial Guesses on Small-Sized Samples

Initial Guess (f_c^{max})	Iteration (k)	Guess ${f_c^{max}}_k$	Δf_c^{max}	Result ${f_c^{max}}_{k+1}$	Comment
0.00	1.00	0.00	0.60	0.60	
	2.00	0.60	-0.18	0.43	
	3.00	0.43	-0.02	0.40	
	4.00	0.40	0.00	0.40	Converged
0.30	1.00	0.30	0.10	0.40	
	2.00	0.40	0.00	0.40	Converged
0.60	1.00	0.60	-0.17	0.43	
	2.00	0.43	-0.02	0.40	
	3.00	0.40	0.00	0.40	Converged
0.80	1.00	0.80	-0.34	0.46	
	2.00	0.46	-0.06	0.40	
	3.00	0.40	0.00	0.40	Converged
1.50	1.00	1.50	-0.86	0.64	
	2.00	0.64	-0.21	0.43	
	3.00	0.43	-0.03	0.40	
	4.00	0.40	0.00	0.40	Converged
3.00	1.00	3.00	-2.87	0.13	
	2.00	0.13	0.27	0.41	
	3.00	0.41	-0.01	0.40	
	4.00	0.40	0.00	0.40	Converged

Table A.15: Iteration Summary for Estimating Synthetic $f_c^{max} = 0.60$kN with Different Initial Guesses on Small-Sized Samples

Initial Guess (f_c^{max})	Iteration (k)	Guess ${f_c^{max}}_k$	Δf_c^{max}	Result ${f_c^{max}}_{k+1}$	Comment
0.01	1.00	0.01	0.72	0.73	
	2.00	0.73	-0.12	0.61	
	3.00	0.61	-0.01	0.60	
	4.00	0.60	0.00	0.60	Converged

0.40	1.00	0.40	0.20	0.60	
	2.00	0.60	0.00	0.60	Converged
0.80	1.00	0.80	-0.18	0.62	
	2.00	0.62	-0.02	0.60	
	3.00	0.60	0.00	0.60	Converged
	4.00	0.60	0.00	0.60	Converged
1.50	1.00	1.50	-0.75	0.75	
	2.00	0.75	-0.14	0.61	
	3.00	0.61	-0.01	0.60	
	4.00	0.60	0.00	0.60	Converged
4.90	1.00	4.90	-4.84	0.06	
	2.00	0.06	0.53	0.59	
	3.00	0.59	0.01	0.60	
	4.00	0.60	0.00	0.60	Converged

Table A.16: Iteration Summary for Estimating Synthetic $f_c^{max} = 0.80$kN with Different Initial Guesses on Small-Sized Samples

Initial Guess (f_c^{max})	Iteration (k)	Guess ${f_c^{max}}_k$	Δf_c^{max}	Result ${f_c^{max}}_{k+1}$	Comment
0.01	1.00	0.01	0.72	0.73	
	2.00	0.73	0.07	0.80	
	3.00	0.80	0.00	0.80	Converged
0.40	1.00	0.40	0.42	0.82	
	2.00	0.82	-0.02	0.80	
	3.00	0.80	0.00	0.80	Converged
0.60	1.00	0.60	0.21	0.81	
	2.00	0.81	-0.01	0.80	
	3.00	0.80	0.00	0.80	Converged
1.50	1.00	1.50	-0.62	0.88	
	2.00	0.88	-0.08	0.80	
	3.00	0.80	0.00	0.80	Converged
5.00	1.00	5.00	-4.99	0.01	
	2.00	0.01	0.74	0.76	
	3.00	0.76	0.04	0.80	
	4.00	0.80	0.00	0.80	Converged

Table A.17: Iteration Summary for Estimating Synthetic $f_c^{max} = 1.50$kN with Different Initial Guesses on Small-Sized Samples

Initial Guess (f_c^{max})	Iteration (k)	Guess ${f_c^{max}}_k$	Δf_c^{max}	Result ${f_c^{max}}_{k+1}$	Comment
0.00	1.00	0.00	0.60	0.60	
	2.00	0.60	0.87	1.47	
	3.00	1.47	0.03	1.50	
	4.00	1.50	0.00	1.50	Converged
0.40	1.00	0.40	1.09	1.49	
	2.00	1.49	0.01	1.50	
	3.00	1.50	0.00	1.50	Converged
0.60	1.00	0.60	0.87	1.47	
	2.00	1.47	0.03	1.50	
	3.00	1.50	0.00	1.50	Converged
1.25	1.00	1.25	0.25	1.50	
	2.00	1.50	0.00	1.50	Converged
2.00	1.00	2.00	-0.50	1.50	
	2.00	1.50	0.00	1.50	Converged
3.90	1.00	3.90	-3.81	0.09	
	2.00	0.09	0.92	1.01	
	3.00	1.01	0.48	1.49	
	4.00	1.49	0.01	1.50	
	5.00	1.50	0.00	1.50	Converged

Table A.18: Iteration Summary for Estimating Synthetic $f_c^{max} = 2.00$kN with Different Initial Guesses on Small-Sized Samples

Initial Guess (f_c^{max})	Iteration (k)	Guess ${f_c^{max}}_k$	Δf_c^{max}	Result ${f_c^{max}}_{k+1}$	Comment
0.00	1.00	0.00	0.60	0.60	
	2.00	0.60	1.30	1.90	
	3.00	1.90	0.10	2.00	
	4.00	2.00	0.00	2.00	Converged
0.40	1.00	0.40	1.50	1.90	
	2.00	1.90	0.10	2.00	
	3.00	2.00	0.00	2.00	Converged

0.60	1.00	0.60	1.30	1.90	
	2.00	1.90	0.10	2.00	
	3.00	2.00	0.00	2.00	Converged
0.80	1.00	0.80	1.12	1.92	
	2.00	1.92	0.08	2.00	
	3.00	2.00	0.00	2.00	Converged
1.50	1.00	1.50	0.48	1.98	
	2.00	1.98	0.02	2.00	
	3.00	2.00	0.00	2.00	Converged
4.00	1.00	4.00	-3.11	0.89	
	2.00	0.89	1.07	1.96	
	3.00	1.96	0.04	2.00	
	4.00	2.00	0.00	2.00	Converged

Medium-sized samples

h_a

Table A.19: Iteration Summary for Estimating Synthetic $h_a = 0.10$cm with Different Initial Guesses on Medium-Sized Samples

Initial Guess (h_{a_0})	Iteration (k)	Guess (h_{a_k})	Update (Δh_a)	Result ($h_{a_{k+1}}$)	Comment
-2.50	1	-2.50	0.07	-1.28	
	2	-1.28	0.10	-0.28	
	3	-0.28	0.30	0.02	
	4	0.02	0.03	0.05	
	5	0.05	0.00	0.05	Converged
0.05	1	0.05	0.05	0.10	
	2	0.10	0.00	0.10	Converged
0.35	1	0.35	-0.26	0.09	
	2	0.09	0.01	0.10	
	3	0.10	0.00	0.10	Converged
0.50	1	0.50	-0.43	0.07	
	2	0.07	0.03	0.10	
	3	0.10	0.00	0.10	Converged
0.800	1	0.80	-0.74	0.06	
	2	0.06	0.04	0.10	

	3	0.10	0.000	0.10	Converged
2.50	1	2.50	-2.74	-0.24	
	2	-0.24	0.29	0.05	
	3	0.05	0.05	0.10	
	4	0.10	0.00	0.10	Converged
3.40	1	3.40	-0.20	3.20	
	2	3.20	-3.21	-0.01	
	3	-0.01	0.11	0.10	
	4	0.10	0.00	0.10	Converged
8.00	1	8.00	0.36	8.36	
	2	8.36	0.34	8.70	
	3	8.70	0.43	9.13	
	4	9.13	—	—	Model failed at this guess

Table A.20: Iteration Summary for Estimating Synthetic $h_a = 0.35$cm with Different Initial Guesses on Medium-Sized Samples

Initial Guess (h_{a_0})	Iteration (k)	Guess (h_{a_k})	Update (Δh_a)	Result ($h_{a_{k+1}}$)	Comment
-2.50	1	-2.50	1.30	-1.20	
	2	-2.50	1.10	-0.10	
	3	-0.10	0.43	0.33	
	4	0.33	0.02	0.35	
	5	0.35	0.00	0.35	Converged
-2.00	1	-2.00	1.06	-0.94	
	2	-0.94	0.27	0.34	
	3	0.34	0.01	0.35	
	4	0.35	0.00	0.35	Converged
0.05	1	0.05	0.29	0.34	
	2	0.34	0.01	0.35	
	3	0.35	0.00	0.35	Converged
0.10	1	0.10	0.24	0.34	
	2	0.34	0.01	0.35	
	3	0.35	0.00	0.35	Converged
0.50	1	0.50	-0.16	0.34	
	2	0.34	0.01	0.35	

	3	0.35	0.00	0.35	Converged
0.65	1	0.65	-0.31	0.34	
	2	0.34	0.01	0.35	
	3	0.35	0.00	0.35	Converged
0.80	1	0.80	-0.46	0.34	
	2	0.34	0.01	0.35	
	3	0.35	0.00	0.35	Converged
3.40	1	3.40	-0.25	3.14	
	2	3.14	-2.78	0.35	
	3	0.35	0.00	0.35	Converged
8.00	1	8.00	0.19	8.19	
	2	8.19	0.15	8.34	
	3	8.34	0.20	8.54	
	4	8.54	0.13	8.67	
	5	8.67	0.30	8.97	
	6	8.97	—	—	Model failed at this guess

Table A.21: Iteration Summary for Estimating Synthetic $h_a = 0.5$cm with Different Initial Guesses on Medium-Sized Samples

Initial Guess (h_{a_0})	Iteration (k)	Guess (h_{a_k})	Update (Δh_a)	Result ($h_{a_{k+1}}$)	Comment
-2.50	1	-2.50	1.35	-1.15	
	2	-1.15	1.10	-0.05	
	3	-0.05	0.53	0.48	
	4	0.48	0.02	0.50	
	5	0.50	0.00	0.50	Converged
0.050	1	0.050	0.426	0.476	
	2	0.476	0.024	0.500	
	3	0.500	0.000	0.500	Converged
0.100	1	0.10	0.32	0.47	
	2	0.47	0.03	0.50	
	3	0.50	0.00	0.50	Converged
0.200	1	0.20	0.27	0.47	
	2	0.47	0.03	0.50	
	3	0.50	0.00	0.50	Converged

0.65	1	0.65	-0.57	0.50	
	2	0.50	0.00	0.50	Converged
0.80	1	0.80	-0.30	0.50	
	2	0.50	0.00	0.50	Converged
3.40	1	3.40	-0.30	3.10	
	2	3.10	-2.57	0.52	
	3	0.52	-0.02	0.50	
	4	0.50	0.00	0.50	Converged

Table A.22: Iteration Summary for Estimating Synthetic $h_a = 0.65$cm with Different Initial Guesses on Medium-Sized Samples

Initial Guess (h_{a_0})	Iteration (k)	Guess (h_{a_k})	Update (Δh_a)	Result ($h_{a_{k+1}}$)	Comment
-2.50	1	-2.50	1.38	-1.11	
	2	-1.11	1.30	0.19	
	3	0.19	0.41	0.60	
	4	0.60	0.05	0.65	
	5	0.65	0.00	0.65	Converged
0.05	1	0.05	0.55	0.60	
	2	0.60	0.05	0.65	
	3	0.65	0.00	0.65	Converged
0.10	1	0.10	0.49	0.59	
	2	0.59	0.06	0.65	
	3	0.65	0.00	0.65	Converged
0.35	1	0.35	0.28	0.63	
	2	0.62	0.02	0.65	
	3	0.65	0.00	0.65	Converged
0.50	1	0.50	0.15	0.65	
	2	0.65	0.00	0.65	Converged
0.80	1	0.80	-0.15	0.65	
	2	0.65	0.00	0.65	Converged
3.40	1	3.40	-0.33	3.07	
	2	3.07	-2.37	0.70	
	3	0.70	-0.05	0.65	
	4	0.65	0.00	0.65	Converged

Δa

Table A.23: Iteration Summary for Estimating Synthetic $\Delta a = 0.10$ with Different Initial Guesses on Medium-Sized Samples

Initial Guess (Δa_0)	Iteration (k)	Guess (Δa_k)	$\Delta(\Delta a)$	Result (Δa_{k+1})	Comment
0.03	1	0.03	0.91	0.94	
	2	0.94	-0.47	0.47	
	3	0.47	-0.20	0.27	
	4	0.27	-0.07	0.20	
	5	0.20	-0.05	0.15	
	6	0.15	-0.03	0.12	
	7	0.12	-0.01	0.11	
	8	0.11	-0.01	0.10	
	9	0.10	0.00	0.10	Converged
0.05	1	0.05	0.19	0.25	
	2	0.25	-0.06	0.19	
	3	0.19	-0.04	0.14	
	4	0.14	-0.03	0.12	
	5	0.12	-0.01	0.10	
	6	0.10	0.00	0.10	
	7	0.10	0.00	0.10	Converged
0.20	1	0.20	-0.05	0.15	
	2	0.15	-0.03	0.12	
	3	0.12	-0.02	0.11	
	4	0.11	-0.01	0.10	
	5	0.10	0.00	0.10	Converged
0.50	1	0.50	-0.22	0.28	
	2	0.28	-0.07	0.21	
	3	0.21	-0.05	0.16	
	4	0.16	-0.03	0.13	
	5	0.13	-0.02	0.11	
	6	0.11	-0.01	0.10	
	7	0.10	0.00	0.10	Converged
1.30	1	1.30	-0.67	0.63	
	2	0.63	-0.30	0.33	
	3	0.33	-0.08	0.25	
	4	0.25	-0.06	0.19	

	5	0.19	-0.04	0.15	
	6	0.15	-0.03	0.12	
	7	0.12	-0.01	0.10	
	8	0.10	0.00	0.10	
	9	0.10	0.00	0.10	Converged
	1	2.10	-1.02	1.08	
	2	1.08	-0.54	0.54	
	3	0.54	-0.25	0.29	
	4	0.29	-0.07	0.22	
2.10	5	0.22	-0.05	0.17	
	6	0.17	-0.04	0.13	
	7	0.13	-0.02	0.11	
	8	0.11	-0.01	0.10	
	9	0.10	0.00	0.10	Converged

Table A.24: Iteration Summary for Estimating Synthetic $\Delta a = 0.20$ with Different Initial Guesses on Medium-Sized Samples

Initial Guess (Δa_0)	Iteration (k)	Guess (Δa_k)	$\Delta(\Delta a)$	Result (Δa_{k+1})	Comment
0.05	1	0.05	3.18	3.23	Low guess led to overshoot
	2	3.23	—	—	Forward model failed
0.06	1	0.06	1.83	1.89	
	2	1.89	-1.03	0.86	
	3	0.86	-0.40	0.46	
	4	0.46	-0.19	0.27	
	5	0.27	-0.05	0.22	
	6	0.22	-0.02	0.20	
	7	0.20	-0.00	0.20	
	8	0.20	0.00	0.20	Converged
0.07	1	0.07	1.15	1.22	
	2	1.22	-0.53	0.68	
	3	0.68	-0.32	0.36	
	4	0.36	-0.11	0.25	
	5	0.25	-0.04	0.21	
	6	0.21	-0.01	0.20	
	7	0.20	-0.00	0.20	
	8	0.20	0.00	0.20	Converged

0.10	1	0.10	0.37	0.47	
	2	0.47	-0.19	0.28	
	3	0.28	-0.05	0.23	
	4	0.23	-0.02	0.21	
	5	0.21	-0.01	0.20	
	6	0.20	0.00	0.20	Converged
0.15	1	0.15	0.08	0.23	
	2	0.23	-0.03	0.21	
	3	0.21	-0.01	0.20	
	4	0.20	0.00	0.20	Converged
0.25	1	0.25	-0.04	0.21	
	2	0.21	-0.01	0.20	
	3	0.20	-0.00	0.20	
	4	0.20	0.00	0.20	Converged
0.30	1	0.30	-0.06	0.24	
	2	0.24	-0.03	0.21	
	3	0.21	-0.01	0.20	
	4	0.20	-0.00	0.20	
	5	0.20	0.00	0.20	Converged
0.50	1	0.50	-0.22	0.28	
	2	0.28	-0.05	0.23	
	3	0.23	-0.02	0.21	
	4	0.21	-0.01	0.20	
	5	0.20	0.00	0.20	Converged
0.70	1	0.70	-0.31	0.39	
	2	0.39	-0.13	0.25	
	3	0.25	-0.04	0.22	
	4	0.22	-0.01	0.20	
	5	0.20	-0.00	0.20	
	6	0.20	0.00	0.20	Converged
1.00	1	1.00	-0.48	0.52	
	2	0.52	-0.23	0.29	
	3	0.29	-0.06	0.24	
	4	0.24	-0.03	0.21	
	5	0.21	-0.01	0.20	
	6	0.20	0.00	0.20	Converged
1.50	1	1.50	-0.72	0.78	
	2	0.78	-0.36	0.42	

	3	0.42	-0.16	0.27	
	4	0.27	-0.05	0.22	
	5	0.22	-0.02	0.20	
	6	0.20	-0.00	0.20	
	7	0.20	0.00	0.20	Converged
>3.00	—	—	—	—	Computation failed

Table A.25: Iteration Summary for Estimating Synthetic $\Delta a = 0.35$ with Different Initial Guesses on Medium-Sized Samples

Initial Guess (Δa_0)	Iteration (k)	Guess (Δa_k)	$\Delta(\Delta a)$	Result (Δa_{k+1})	Comment
0.10	1	0.10	3.72	3.82	Large initial update, overshot
	2	3.82	—	—	Forward model failed
0.13	1	0.13	1.67	1.80	
	2	1.80	-0.89	0.91	
	3	0.91	-0.40	0.51	
	4	0.51	-0.14	0.37	
	5	0.37	-0.02	0.35	
	6	0.35	0.00	0.35	Converged
0.15	1	0.15	1.07	1.22	
	2	1.22	-0.54	0.68	
	3	0.68	-0.26	0.42	
	4	0.42	-0.07	0.35	
	5	0.35	-0.00	0.35	
	6	0.35	0.00	0.35	Converged
0.20	1	0.20	0.42	0.62	
	2	0.62	-0.22	0.40	
	3	0.40	-0.05	0.35	
	4	0.35	0.00	0.35	Converged
0.25	1	0.25	0.18	0.43	
	2	0.43	-0.07	0.35	
	3	0.35	-0.00	0.35	
	4	0.35	0.00	0.35	Converged
0.30	1	0.30	0.06	0.36	
	2	0.36	-0.02	0.35	
	3	0.35	0.00	0.35	

	4	0.35	0.00	0.35	Converged
0.40	1	0.40	-0.05	0.35	
	2	0.35	0.00	0.35	
	3	0.35	0.00	0.35	Converged
2.10	1	2.10	-1.00	1.10	
	2	1.10	-0.51	0.59	
	3	0.59	-0.20	0.39	
	4	0.39	-0.04	0.35	
	5	0.35	0.00	0.35	Converged

Table A.26: Iteration Summary for Estimating Synthetic $\Delta a = 0.5$ with Different Initial Guesses

Initial Guess (ΔA_0)	Iteration (k)	Guess (δA_k)	$\Delta(\Delta A)$	Result (ΔA_{k+1})	Comment
0.10	1	0.10	8.44	8.54	Large initial step
	2	8.54	—	—	Forward model failed
0.17	1	0.17	1.82	1.98	
	2	1.98	-0.91	1.07	
	3	1.07	-0.42	0.53	
	4	0.53	-0.03	0.50	
	5	0.50	0.00	0.50	Converged
0.20	1	0.20	1.01	1.21	
	2	1.21	-0.45	0.76	
	3	0.76	-0.21	0.55	
	4	0.55	-0.05	0.50	
	5	0.50	-0.00	0.50	
	6	0.50	0.00	0.50	Converged
0.30	1	0.30	0.24	0.54	
	2	0.54	-0.04	0.50	
	3	0.50	-0.00	0.50	
	4	0.50	0.00	0.50	Converged
0.40	1	0.40	0.10	0.50	
	2	0.50	-0.00	0.50	
	3	0.50	0.00	0.50	Converged
0.45	1	0.45	0.05	0.50	
	2	0.50	-0.00	0.50	

	3	0.50	0.00	0.50	Converged
0.55	1	0.55	-0.05	0.50	
	2	0.50	-0.00	0.50	
	3	0.50	0.00	0.50	Converged
0.60	1	0.60	-0.09	0.51	
	2	0.51	-0.01	0.50	
	3	0.50	0.00	0.50	Converged
0.70	1	0.70	-0.16	0.54	
	2	0.54	-0.04	0.50	
	3	0.50	-0.00	0.50	
	4	0.50	0.00	0.50	Converged
0.80	1	0.80	-0.24	0.56	
	2	0.56	-0.06	0.50	
	3	0.50	-0.00	0.50	
	4	0.50	0.00	0.50	Converged
0.90	1	0.90	-0.31	0.59	
	2	0.59	-0.09	0.51	
	3	0.51	-0.01	0.50	
	4	0.50	0.00	0.50	Converged
1.10	1	1.10	-0.43	0.67	
	2	0.67	-0.15	0.52	
	3	0.52	-0.02	0.50	
	4	0.50	-0.00	0.50	
	5	0.50	0.00	0.50	Converged
1.20	1	1.20	-0.45	0.75	
	2	0.75	-0.21	0.55	
	3	0.55	-0.05	0.50	
	4	0.50	-0.00	0.50	
	5	0.50	0.00	0.50	Converged
1.30	1	1.30	-0.51	0.79	
	2	0.79	-0.23	0.56	
	3	0.56	-0.05	0.50	
	4	0.50	-0.00	0.50	
	5	0.50	0.00	0.50	Converged
2.10	1	2.10	-0.96	1.13	
	2	1.13	-0.44	0.69	
	3	0.69	-0.16	0.53	

	4	0.53	-0.03	0.50	
	5	0.50	0.00	0.50	Converged

$E_{\mathrm{f,T}}$

Table A.27: Iteration Summary for Estimating Synthetic $E_{\mathrm{f,T}} = 500\,\mathrm{N/mm^2}$ with Different Initial Guesses on Medium-Sized Samples

Initial Guess ($E_{f,T}$)	Iteration (k)	Guess ($E_{f,T,k}$)	$\Delta E_{\mathrm{f,T}}$	Result ($E_{f,T,k+1}$)	Comment
1	1	1	496	497	
	2	497	3	500	
	3	500	0	500	Converged
250	1	250	248	498	
	2	498	2	500	
	3	500	0	500	Converged
7500	1	7500	-7213	287	
	2	287	211	498	
	3	498	2	500	
	4	500	0	500	Converged
16000	1	16000	-15747	253	
	2	253	246	498	
	3	498	2	500	
	4	500	0	500	Converged
21000	1	21000	-23577	-2577	Negative value of the update step
	2	-2577	—	—	Model failed at this guess

Table A.28: Iteration Summary for Estimating Synthetic $E_{\mathrm{f,T}} = 7\,500\,\mathrm{N/mm^2}$ with Different Initial Guesses on Medium-Sized Samples

Initial Guess ($E_{f,T}$)	Iteration (k)	Guess ($E_{f,T,k}$)	$\Delta E_{\mathrm{f,T}}$	Result ($E_{f,T,k+1}$)	Comment
1	1	1	6209	6210	
	2	6210	1300	7510	
	3	7510	-10	7500	
	4	7500	0	7500	Converged
7000	1	7000	505	7505	

Table A.28 – Continued

Initial Guess (δA_0)	Iteration (k)	Guess (δA_k)	$\Delta(\delta A)$	Result (δA_{k+1})	Comment
	2	7505	-5	7500	
	3	7500	0	7500	Converged
21000	1	21000	-14805	6195	
	2	6195	1314	7509	
	3	7509	-9	7500	
	4	7500	0	7500	Converged
44500	1	44500	-43771	729	
	2	729	5655	6385	
	3	6385	1126	7511	
	4	7511	-11	7500	
	5	7500	0	7500	Converged
45000	1	45000	-45490	-490	Negative value of the update step
	2	-490	—	—	Model failed at this guess

Table A.29: Iteration Summary for Estimating Synthetic $E_{\mathrm{f,T}} = 10\,000\,\mathrm{N/mm^2}$ with Different Initial Guesses on Medium-Sized Samples

Initial Guess ($E_{f,T}$)	Iteration (k)	Guess ($E_{f,T,k}$)	$\Delta E_{\mathrm{f,T}}$	Result ($E_{f,T,k+1}$)	Comment
1	1	1	7959	7960	
	2	7960	2006	9966	
	3	9966	34	10000	
	4	10000	0	10000	Converged
500	1	500	7669	8169	
	2	8169	1802	9971	
	3	9971	29	10000	
	4	10000	0	10000	Converged
7500	1	7500	2460	9960	
	2	9960	40	10000	
	3	10000	0	10000	Converged
21000	1	21000	-12082	8918	
	2	8918	1106	10024	
	3	10024	-24	10000	

	4	10000	0	10000	Converged
50000	1	50000	-49687	313	
	2	313	7663	7977	
	3	7977	1989	9966	
	4	9966	34	10000	
	5	10000	0	10000	Converged
55000	1	55000	-58247	-3247	Negative value of the update step
	2	-3247	—	—	Model failed at this guess

Table A.30: Iteration Summary for Estimating Synthetic $E_{\mathrm{f,T}} = 21\,000\,\mathrm{N/mm^2}$ with Different Initial Guesses on Medium-Sized Samples

Initial Guess ($E_{f,T}$)	Iteration (k)	Guess ($E_{f,T,k}$)	$\Delta E_{\mathrm{f,T}}$	Result ($E_{f,T,k+1}$)	Comment
1	1	1	15766	15767	
	2	15767	4782	20549	
	3	20549	441	20990	
	4	20990	10	21000	
	5	21000	0	21000	Converged
15000	1	15000	5568	20568	
	2	20568	422	20990	
	3	20990	10	21000	
	4	21000	0	21000	Converged
20000	1	20000	976	20976	
	2	20568	14	21000	
	3	21000	0	21000	Converged
25000	1	25000	-4025	20975	
	2	20975	25	21000	
	3	21000	0	21000	Converged
40000	1	40000	-19812	20188	
	2	20188	789	20977	
	3	20977	23	20977	
	4	21000	0	21000	Converged
85000	1	85000	-83019	1981	
	2	1981	15568	17548	
	3	17548	3283	20831	
	4	20831	160	20991	

Table A.30: Iteration Summary for Estimating Synthetic $E_{\mathrm{f,T}} = 21\,000\,\mathrm{N/mm^2}$ with Different Initial Guesses on Medium-Sized Samples

Initial Guess ($E_{f,T}$)	Iteration (k)	Guess ($E_{f,T,k}$)	$\Delta E_{\mathrm{f,T}}$	Result ($E_{f,T,k+1}$)	Comment
	5	20991	9	21000	
	6	21000	0	21000	Converged
350000	1	350000	-382940	-32940	Negative value of the update step
	2	-32940	—	—	Model failed at this guess

Table A.31: Iteration Summary for Estimating Synthetic $E_{\mathrm{f,T}} = 30\,000\,\mathrm{N/mm^2}$ with Different Initial Guesses on Medium-Sized Samples

Initial Guess ($E_{f,T}$)	Iteration (k)	Guess ($E_{f,T,k}$)	$\Delta E_{\mathrm{f,T}}$	Result ($E_{f,T,k+1}$)	Comment
1	1	1	20885	20885	
	2	20885	8202	29087	
	3	29087	905	29992	
	4	29992	8	30000	
	5	10000	0	10000	Converged
7500	1	7500	18761	26261	
	2	26261	3720	29981	
	3	29981	19	30000	
	4	10000	0	10000	Converged
10000	1	10000	16678	26678	
	2	26261	3320	30008	
	3	30008	-8	30000	
	4	10000	0	10000	Converged
21000	1	21000	8092	29092	
	2	29092	900	29992	
	3	29992	8	30000	
	4	30000	0	30000	Converged
40000	1	40000	-10401	29599	
	2	29599	401	30000	
	3	29992	401	30000	
	4	30000	0	30000	Converged
147500	1	147500	-145264	2236	

	2	2236	21175	23411	
	3	23411	6171	29582	
	4	29582	418	30000	
	5	30000	0	30000	Converged
350000	1	350000	-371416	-21416	Negative value of the update step
	2	-21416	—	—	Model failed at this guess

f_c^{max}

Table A.32: Iteration Summary for Estimating Synthetic $f_c^{max} = 1.50$kN with Different Initial Guesses on Medium-Sized Samples

Initial Guess (f_c^{max})	Iteration (k)	Guess $f_c^{max}{}_k$	Δf_c^{max}	Result $f_c^{max}{}_{k+1}$	Comment
0.00	1.00	0.00	2.36	2.36	
	2.00	2.36	-0.81	1.54	
	3.00	1.54	-0.04	1.50	
	4.00	1.50	0.00	1.50	Converged
2.00	1.00	2.00	-0.47	1.53	
	2.00	1.53	-0.03	1.50	
	3.00	1.50	0.00	1.50	Converged
3.00	1.00	3.00	-1.39	1.61	
	2.00	1.61	-0.11	1.50	
	3.00	1.50	0.00	1.50	Converged
4.50	1.00	4.50	-3.32	1.18	
	2.00	1.18	0.32	1.51	
	3.00	1.51	-0.01	1.50	
	4.00	1.50	0.00	1.50	Converged
5.70	1.00	5.70	-5.54	0.16	
	2.00	0.16	0.95	1.11	
	3.00	1.11	0.40	1.51	
	4.00	1.51	-0.01	1.50	
	5.00	1.50	0.00	1.50	Converged

Table A.33: Iteration Summary for Estimating Synthetic $f_c^{max} = 2.00$kN with Different Initial Guesses on Medium-Sized Samples

Initial Guess (f_c^{max})	Iteration (k)	Guess ${f_c^{max}}_k$	Δf_c^{max}	Result ${f_c^{max}}_{k+1}$	Comment
0.00	1.00	0.00	2.36	2.36	
	2.00	2.36	-0.35	2.00	
	3.00	2.00	0.00	2.00	Converged
1.50	1.00	1.50	0.50	2.00	
	2.00	2.00	0.00	2.00	Converged
2.25	1.00	2.25	-0.25	2.00	
	2.00	2.00	0.00	2.00	Converged
3.00	1.00	3.00	-0.96	2.04	
	2.00	2.04	-0.04	2.00	
	3.00	2.00	0.00	2.00	Converged
4.00	1.00	4.00	-2.04	1.96	
	2.00	1.96	0.04	2.00	
	3.00	2.00	0.00	2.00	Converged
6.00	1.00	6.00	-5.84	0.16	
	2.00	0.16	1.07	1.23	
	3.00	1.23	0.81	2.04	
	4.00	2.04	-0.04	2.00	
	5.00	2.00	0.00	2.00	Converged

Table A.34: Iteration Summary for Estimating Synthetic $f_c^{max} = 3.00$kN with Different Initial Guesses on Medium-Sized Samples

Initial Guess (f_c^{max})	Iteration (k)	Guess ${f_c^{max}}_k$	Δf_c^{max}	Result ${f_c^{max}}_{k+1}$	Comment
0.00	1.00	0.00	2.36	2.36	
	2.00	2.36	0.63	2.99	
	3.00	2.99	0.01	3.00	
	4.00	3.00	0.00	3.00	Converged
1.50	1.00	1.50	1.45	2.95	
	2.00	2.95	0.05	3.00	
	3.00	3.00	0.00	3.00	Converged
2.00	1.00	2.00	0.95	2.95	

	2.00	2.95	0.05	3.00	
	3.00	3.00	0.00	3.00	Converged
3.25	1.00	3.25	-0.25	3.00	
	2.00	3.00	0.00	3.00	Converged
4.50	1.00	4.50	-1.73	2.77	
	2.00	2.77	0.23	3.00	
	3.00	3.00	0.00	3.00	Converged
7.50	1.00	7.50	-7.48	0.02	
	2.00	0.02	5.35	5.37	
	3.00	5.37	-2.98	2.39	
	4.00	2.39	0.59	2.98	
	5.00	2.98	0.02	3.00	
	6.00	3.00	0.00	3.00	Converged

Table A.35: Iteration Summary for Estimating Synthetic $f_c^{max} = 4.00$kN with Different Initial Guesses on Medium-Sized Samples

Initial Guess (f_c^{max})	Iteration (k)	Guess $f_c^{max}{}_k$	Δf_c^{max}	Result $f_c^{max}{}_{k+1}$	Comment
0.00	1.00	0.00	2.36	2.36	
	2.00	2.36	1.91	4.27	
	3.00	4.27	0.22	4.49	
	4.00	4.49	0.01	4.50	
	5.00	4.50	0.00	4.50	Converged
1.50	1.00	1.50	2.59	4.09	
	2.00	4.09	0.38	4.47	
	3.00	4.47	0.03	4.50	
	4.00	4.50	0.00	4.50	Converged
2.00	1.00	2.00	2.16	4.16	
	2.00	4.16	0.32	4.48	
	3.00	4.48	0.02	4.50	
	4.00	4.50	0.00	4.50	Converged
3.00	1.00	3.00	1.36	4.36	
	2.00	4.36	0.14	4.50	
	3.00	4.50	0.00	4.50	Converged
5.00	1.00	5.00	-0.52	4.48	
	2.00	4.48	0.02	4.50	

	3.00	4.50	0.00	4.50	Converged
9.70	1.00	9.70	-9.67	0.03	
	2.00	0.03	7.34	7.38	
	3.00	7.38	-3.95	3.43	
	4.00	3.43	0.96	4.39	
	5.00	4.39	0.11	4.50	
	6.00	4.50	0.00	4.50	Converged

Large-sized samples

h_a

Table A.36: Iteration Summary for Estimating Synthetic $h_a = 0.05$cm with Different Initial Guesses on Large-Sized Samples

Initial Guess (h_{a_0})	Iteration (k)	Guess (h_{a_k})	Update (Δh_a)	Result ($h_{a_{k+1}}$)	Comment
-1.70	1	-1.70	1.37	-0.33	
	2	-0.33	0.16	-0.16	
	3	-0.16	0.21	0.05	
	4	0.05	0.00	0.05	Converged
0.01	1	0.01	0.04	0.05	
	2	0.05	0.00	0.05	Converged
0.2	1	0.2	-0.15	0.05	
	2	0.05	0.00	0.05	Converged
0.50	1	0.50	-0.34	0.16	
	2	0.16	-0.11	0.05	
	3	0.05	0.00	0.05	Converged
0.80	1	0.80	-0.78	0.02	
	2	0.02	-0.15	0.05	
	3	0.05	0.00	0.05	Converged
0.95	1	0.95	-0.96	-0.01	
	2	-0.01	0.06	0.05	
	3	0.05	0.00	0.05	Converged
1.50	1	1.50	-1.62	-0.12	
	2	-0.12	0.17	0.05	
	3	0.05	0.00	0.05	Converged
2.40	1	2.40	-0.14	2.26	

	2	2.26	-1.18	1.08	
	3	1.08	-1.07	0.00	
	4	0.00	0.05	0.05	
	5	0.05	0.00	0.05	Converged

Table A.37: Iteration Summary for Estimating Synthetic $h_a = 0.5$cm with Different Initial Guesses on Large-Sized Samples

Initial Guess (h_{a_0})	Iteration (k)	Guess (h_{a_k})	Update (Δh_a)	Result ($h_{a_{k+1}}$)	Comment
-1.70	1	-1.70	1.68	-0.02	
	2	-0.02	0.49	0.47	
	3	0.47	0.03	0.50	
	4	0.50	0.00	0.50	Converged
0.05	1	0.05	0.45	0.50	
	2	0.50	0.00	0.50	Converged
0.80	1	0.80	-0.30	0.50	
	2	0.50	0.00	0.50	Converged
0.95	1	0.95	-0.46	0.49	
	2	0.49	0.01	0.50	
	3	0.50	0.00	0.50	Converged
1.50	1	1.50	-1.07	0.43	
	2	0.43	0.06	0.49	
	3	0.49	0.01	0.50	
	4	0.50	0.00	0.50	Converged
2.40	1	2.40	-0.24	2.16	
	2	2.16	-1.76	0.40	
	3	0.40	0.10	0.50	
	4	0.50	0.00	0.50	Converged

Table A.38: Iteration Summary for Estimating Synthetic $h_a = 0.8$cm with Different Initial Guesses on Large-Sized Samples

Initial Guess (h_{a_0})	Iteration (k)	Guess (h_{a_k})	Update (Δh_a)	Result ($h_{a_{k+1}}$)	Comment
	1	-1.70	1.87	0.17	
-1.70					

	2	0.17	0.59	0.76	
	3	0.76	0.04	0.80	
	4	0.80	0.00	0.80	Converged
	1	0.05	0.71	0.76	
0.05	2	0.76	0.04	0.80	
	3	0.80	0.00	0.80	Converged
	1	0.50	0.21	0.71	
0.50	2	0.71	0.09	0.80	
	3	0.80	0.00	0.80	Converged
0.95	1	0.95	-0.15	0.80	
	2	0.80	0.00	0.80	Converged
	1	2.00	-1.26	0.74	
2.00	2	0.74	0.06	0.80	
	3	0.80	0.00	0.80	Converged
	1	2.40	-0.27	2.13	
2.40	2	2.13	-1.39	0.74	
	3	0.74	0.06	0.80	
	4	0.80	0.00	0.80	Converged

Table A.39: Iteration Summary for Estimating Synthetic $h_a = 0.95$cm with Different Initial Guesses on Large-Sized Samples

Initial Guess (h_{a_0})	Iteration (k)	Guess (h_{a_k})	Update (Δh_a)	Result ($h_{a_{k+1}}$)	Comment
	1	-1.70	1.95	0.25	
-1.70	2	0.25	0.50	0.75	
	3	0.75	0.20	0.95	
	4	0.95	0.00	0.95	Converged
	1	0.05	0.84	0.89	
0.05	2	0.89	0.06	0.95	
	3	0.95	0.00	0.95	Converged
	1	0.50	0.30	0.80	
0.50	2	0.80	0.14	0.94	
	3	0.94	0.01	0.95	
	4	0.95	0.00	0.95	Converged
	1	0.80	0.14	0.94	
0.80					

	2	0.94	0.01	0.95	
	3	0.95	0.00	0.95	Converged
1.50	1	1.50	-0.59	0.91	
	2	0.91	0.04	0.95	
	3	0.95	0.00	0.95	Converged
2.00	1	2.00	-1.09	0.91	
	2	0.91	0.04	0.95	
	3	0.95	0.00	0.95	Converged
2.40	1	2.40	-0.28	2.12	
	2	2.12	-1.22	0.90	
	3	0.90	0.05	0.95	
	4	0.95	0.00	0.95	Converged

Δa

Table A.40: Iteration Summary for Estimating Synthetic $\Delta a = 0.10$ with Different Initial Guesses on Large-Sized Samples

Initial Guess (Δa_0)	Iteration (k)	Guess (Δa_k)	$\Delta(\Delta a)$	Result (Δa_{k+1})	Comment
0.03	1	0.03	0.91	0.94	
	2	0.94	-0.46	0.48	
	3	0.48	-0.23	0.25	
	4	0.25	-0.06	0.19	
	5	0.19	-0.04	0.15	
	6	0.15	-0.03	0.12	
	7	0.12	-0.02	0.10	
	8	0.10	0.00	0.10	Converged
0.20	1	0.20	-0.05	0.15	
	2	0.15	-0.03	0.12	
	3	0.12	-0.02	0.10	
	4	0.10	0.00	0.10	Converged
0.35	1	0.35	-0.13	0.12	
	2	0.12	-0.02	0.10	
	3	0.10	0.00	0.10	Converged
0.50	1	0.50	-0.24	0.26	
	2	0.26	-0.06	0.19	
	3	0.19	-0.05	0.15	

	4	0.15	-0.03	0.12	
	5	0.12	-0.02	0.10	
	6	0.10	0.00	0.10	Converged
2.50	1	2.50	-1.33	1.17	
	2	1.17	-0.59	0.58	
	3	0.58	-0.29	0.29	
	4	0.29	-0.07	0.22	
	5	0.22	-0.05	0.17	
	6	0.17	-0.04	0.13	
	7	0.13	-0.03	0.10	
	8	0.10	0.00	0.10	Converged

Table A.41: Iteration Summary for Estimating Synthetic $\Delta a = 0.20$ with Different Initial Guesses on Large-Sized Samples

Initial Guess (Δa_0)	Iteration (k)	Guess (Δa_k)	$\Delta(\Delta a)$	Result (Δa_{k+1})	Comment
0.06	1	0.06	1.83	1.89	
	2	1.89	-1.00	0.89	
	3	0.89	-0.17	0.72	
	4	0.72	-0.34	0.38	
	5	0.38	-0.06	0.32	
	6	0.32	-0.08	0.24	
	7	0.24	-0.03	0.21	
	8	0.21	-0.01	0.20	
	9	0.20	0.00	0.20	Converged
0.10	1	0.10	0.37	0.47	
	2	0.47	-0.21	0.26	
	3	0.26	-0.04	0.22	
	4	0.26	-0.02	0.20	
	5	0.20	0.00	0.20	Converged
0.35	1	0.35	-0.11	0.24	
	2	0.24	-0.03	0.21	
	3	0.21	-0.01	0.20	
	4	0.20	0.00	0.20	Converged
0.50	1	0.50	-0.23	0.27	
	2	0.27	-0.05	0.22	
	3	0.22	-0.02	0.20	

	4	0.20	0.00	0.20	Converged
2.50	1	2.50	-1.32	1.18	
	2	1.18	-0.59	1.18	
	3	1.18	-0.59	0.58	
	4	0.58	-0.28	0.30	
	5	0.30	-0.07	0.23	
	6	0.23	-0.02	0.21	
	7	0.21	-0.01	0.20	
	8	0.20	0.00	0.20	Converged

Table A.42: Iteration Summary for Estimating Synthetic $\Delta a = 0.35$ with Different Initial Guesses on Large-Sized Samples

Initial Guess (Δa_0)	Iteration (k)	Guess (Δa_k)	$\Delta(\Delta a)$	Result (Δa_{k+1})	Comment
0.11	1	0.11	2.26	2.37	
	2	2.37	-1.22	1.15	
	3	1.15	-0.54	0.61	
	4	0.61	-0.22	0.39	
	5	0.39	-0.02	0.37	
	6	0.37	-0.02	0.35	
	7	0.35	0.00	0.35	Converged
0.20	1	0.20	0.33	0.53	
	2	0.53	-0.16	0.37	
	3	0.37	-0.02	0.35	
	4	0.35	0.00	0.35	Converged
0.50	1	0.50	-0.14	0.36	
	2	0.36	-0.01	0.35	
	3	0.35	0.00	0.35	Converged
2.50	1	2.50	-1.30	1.20	
	2	1.20	-0.21	0.99	
	3	0.99	-0.44	0.55	
	4	0.55	-0.17	0.37	
	5	0.37	-0.02	0.35	
	6	0.35	0.00	0.35	Converged

Table A.43: Iteration Summary for Estimating Synthetic $\Delta a = 0.50$ with Different Initial Guesses on Large-Sized Samples

Initial Guess (Δa_0)	Iteration (k)	Guess (Δa_k)	$\Delta(\Delta a)$	Result (Δa_{k+1})	Comment
0.15	1	0.15	2.02	2.17	
	2	2.17	-1.06	1.11	
	3	1.11	-0.45	0.66	
	4	0.66	-0.14	0.52	
	5	0.52	-0.02	0.50	
	6	0.50	0.00	0.50	Converged
0.20	1	0.20	0.82	1.02	
	2	1.02	-0.39	0.63	
	3	0.63	-0.12	0.51	
	4	0.51	-0.01	0.50	
	5	0.50	0.00	0.50	Converged
0.35	1	0.35	0.17	0.52	
	2	0.52	-0.02	0.50	
	3	0.50	0.00	0.50	Converged
2.50	1	2.50	-1.27	1.23	
	2	1.23	-0.54	0.69	
	3	0.69	-0.16	0.53	
	4	0.53	-0.03	0.50	
	5	0.50	0.00	0.50	Converged

$E_{\mathrm{f,T}}$

Table A.44: Combined Iteration Summary for Estimating $E_{\mathrm{f,T}} = 500\,\mathrm{N/mm^2}$ with different initial guesses

Initial Guess ($E_{f,T}$)	Iteration (k)	Guess ($E_{f,T,k}$)	$\Delta E_{\mathrm{f,T}}$	Result ($E_{f,T,k+1}$)	Comment

Table A.44 – Continued

Initial Guess (δA_0)	Iteration (k)	Guess (δA_k)	$\Delta(\delta A)$	Result (δA_{k+1})	Comment
1	1	1	527	528	
	2	528	-28	500	
	3	500	0	500	Converged

250	1	250	95	345	
	2	345	155	500	
	3	500	0	500	Converged
1000	1	1000	-497	503	
	2	503	-3	500	
	3	500	0	500	Converged
2500	1	2500	-2119	381	
	2	381	119	500	
	3	500	0	500	Converged
4800	1	4800	-1480	3320	
	2	3320	-3003	317	
	3	317	184	501	
	4	501	-1	500	
	5	500	0	500	Converged
7500	1	7500	-7808	-308	
	2	-308	—	—	Model failed at this guess

Table A.45: Combined Iteration Summary for Estimating $E_{\mathrm{f,T}} = 7\,500\,\mathrm{N/mm^2}$ with different initial guesses

Initial Guess ($E_{f,T}$)	Iteration (k)	Guess ($E_{f,T,k}$)	$\Delta E_{\mathrm{f,T}}$	Result ($E_{f,T,k+1}$)	Comment
1	1	1	6791	6792	
	2	6792	707	7499	
	3	7499	1	7500	
	4	7500	0	7500	Converged
500	1	500	6279	6779	
	2	6779	720	7499	
	3	7499	1	7500	
	4	7500	0	7500	Converged
10000	1	10000	-2494	7506	
	2	7506	-6	7500	
	3	7500	0	7500	Converged
21000	1	21000	-14883	6117	
	2	6117	1340	7457	
	3	7457	43	7500	

Table A.45 – Continued

Initial Guess (δA_0)	Iteration (k)	Guess (δA_k)	$\Delta(\delta A)$	Result (δA_{k+1})	Comment
	4	7500	0	7500	Converged
30000	1	30000	-27506	2494	
	2	2494	4655	7149	
	3	7149	351	7500	
	4	7500	0	7500	Converged
60500	1	60500	-59312	1188	
	2	1188	1871	3059	
	3	3059	1210	4269	
	4	4269	3170	7439	
	5	7439	61	7500	
	6	7500	0	7500	Converged
150000	1	150000	9920	159920	
	2	159920	16604	176526	
	2	176526	—	—	Model failed at this guess

Table A.46: Combined Iteration Summary for Estimating $E_{\mathrm{f,T}} = 10\,000\,\mathrm{N/mm^2}$ with different initial guesses

Initial Guess ($E_{f,T}$)	Iteration (k)	Guess ($E_{f,T,k}$)	$\Delta E_{\mathrm{f,T}}$	Result ($E_{f,T,k+1}$)	Comment
1	1	1	8738	8738	
	2	8738	1243	9981	
	3	9981	19	10000	
	4	10000	0	10000	Converged
500	1	500	8218	8718	
	2	8718	1263	9981	
	3	9981	19	10000	
	4	10000	0	10000	Converged
7500	1	7500	2393	9893	
	2	9893	107	10000	
	3	10000	0	10000	Converged
21000	1	21000	-11872	9128	
	2	9128	872	10000	

Table A.46 – Continued

Initial Guess (δA_0)	Iteration (k)	Guess (δA_k)	$\Delta(\delta A)$	Result (δA_{k+1})	Comment
	3	10000	0	10000	Converged
30000	1	30000	-23880	6120	
	2	6120	3700	9820	
	3	9820	180	10000	
	4	10000	0	10000	Converged
64500	1	64500	-62948	1552	
	2	1552	7297	8849	
	3	8849	1133	9982	
	4	9982	18	10000	
	5	10000	0	10000	Converged
150000	1	150000	6580	156580	
	2	156580	—	—	Model failed at this guess

Table A.47: Combined Iteration Summary for Estimating $E_{\mathrm{f,T}} = 21\,000\,\mathrm{N/mm^2}$ with different initial guesses

Initial Guess ($E_{f,T}$)	Iteration (k)	Guess ($E_{f,T,k}$)	$\Delta E_{\mathrm{f,T}}$	Result ($E_{f,T,k+1}$)	Comment
1	1	1	17528	17529	
	2	17529	3594	21123	
	3	21123	-123	21000	
	4	21000	0	21000	Converged
500	1	500	17048	17548	
	2	17548	3575	21123	
	3	21123	-123	21000	
	4	21000	0	21000	Converged
7500	1	7500	12523	20023	
	2	20023	803	20826	
	3	20826	175	21001	
	4	21001	-1	21000	
	5	21000	0	21000	Converged
10000	1	10000	10100	20100	
	2	20100	725	20825	

Table A.47 – Continued

Initial Guess (δA_0)	Iteration (k)	Guess (δA_k)	$\Delta(\delta A)$	Result (δA_{k+1})	Comment
	3	20825	175	21001	
	4	21001	-1	21001	
	5	21000	0	21000	Converged
30000	1	30000	-9036	20964	
	2	20964	725	20825	
	3	20825	36	21000	
	4	21000	0	21000	Converged
73000	1	73000	-1508	71492	
	2	71492	-9494	61998	
	3	61998	-44920	17077	
	4	17077	2607	19684	
	5	19684	1330	21014	
	6	21014	-14	21000	
	7	21000	0	21000	Converged
300000	1	300000	4405	304405	
	2	304405	5053	309458	Consistent updating in the wrong directio
	3	309458	—	—	Model failed at this guess

Table A.48: Combined Iteration Summary for Estimating $E_{\mathrm{f,T}} = 30\,000\,\mathrm{N/mm^2}$ with different initial guesses

Initial Guess ($E_{f,T}$)	Iteration (k)	Guess ($E_{f,T,k}$)	$\Delta E_{\mathrm{f,T}}$	Result ($E_{f,T,k+1}$)	Comment
1	1	1	8738	8738	
	2	8738	1243	9981	
	3	9981	19	10000	
	4	10000	0	10000	Converged
500	1	500	21375	21875	
	2	21875	7726	29601	
	3	29601	386	29987	
	4	29987	13	30000	
	5	30000	0	30000	Converged
21000	1	21000	8344	29344	
	2	29344	642	29986	

	3	29986	14	30000	
	4	30000	0	30000	Converged
92000	1	92000	-7347	84653	
	2	84653	-5953	78700	
	3	78700	-8281	70420	
	4	70420	-12505	57915	
	5	57915	-28600	29315	
	6	29315	706	30021	
	7	30021	-21	30000	
	8	30000	0	30000	Converged
50000	1	50000	-19721	30279	
	2	30279	-279	30000	
	3	30000	0	30000	Converged

f_c^{max}

Table A.49: Iteration Summary for Estimating Synthetic $f_c^{max} = 1.00$kN with Different Initial Guesses on Large-Sized Samples

Initial Guess (f_c^{max})	Iteration (k)	Guess ${f_c^{max}}_k$	Δf_c^{max}	Result ${f_c^{max}}_{k+1}$	Comment
0.01	1.00	0.01	0.62	0.62	
	2.00	0.62	0.39	1.01	
	3.00	1.01	-0.01	1.00	
	4.00	1.00	0.00	1.00	Converged
0.50	1.00	0.50	0.51	1.01	
	2.00	1.01	-0.01	1.00	
	4.00	1.00	0.00	1.00	Converged
2.00	1.00	2.00	-0.85	1.15	
	2.00	1.15	-0.14	1.01	
	3.00	1.01	-0.01	1.00	
	4.00	1.00	0.00	1.00	Converged
3.00	1.00	3.00	-1.56	1.44	
	2.00	1.44	-0.38	1.06	
	3.00	1.06	-0.06	1.00	
	4.00	1.00	0.00	1.00	Converged
4.50	1.00	4.50	-2.73	1.77	
	2.00	1.77	-0.65	1.11	

	3.00	1.11	-0.11	1.00	
	4.00	1.00	0.00	1.00	Converged
8.10	1.00	8.10	-8.09	0.01	
	2.00	0.01	0.28	0.30	
	3.00	0.30	0.77	1.07	
	4.00	1.07	-0.07	1.00	
	5.00	1.00	0.00	1.00	Converged

Table A.50: Iteration Summary for Estimating Synthetic $f_c^{max} = 2.00$kN with Different Initial Guesses on Large-Sized Samples

Initial Guess (f_c^{max})	Iteration (k)	Guess ${f_c^{max}}_k$	Δf_c^{max}	Result ${f_c^{max}}_{k+1}$	Comment
0.01	1.00	0.01	3.92	3.92	
	2.00	3.92	-1.65	2.27	
	3.00	2.27	-0.26	2.01	
	4.00	2.01	-0.01	2.00	
1.00	1.00	1.00	1.06	2.06	
	2.00	2.06	-0.06	2.00	
	3.00	2.00	0.00	2.00	Converged
1.50	1.00	1.50	0.50	2.00	
	2.00	2.00	0.00	2.00	Converged
3.00	1.00	3.00	-0.89	2.11	
	2.00	2.11	-0.10	2.00	
	3.00	2.00	0.00	2.00	Converged
4.50	1.00	4.50	-2.20	2.30	
	2.00	2.30	-0.29	2.01	
	3.00	2.01	-0.01	2.00	
	4.00	2.00	0.00	2.00	Converged
8.40	1.00	8.40	-8.24	0.16	
	2.00	0.16	1.40	1.56	
	3.00	1.56	0.43	1.99	
	4.00	1.99	0.01	2.00	

Table A.51: Iteration Summary for Estimating Synthetic $f_c^{max} = 3.00$kN with Different Initial Guesses on Large-Sized Samples

Initial Guess (f_c^{max})	Iteration (k)	Guess ${f_c^{max}}_k$	Δf_c^{max}	Result ${f_c^{max}}_{k+1}$	Comment
	1.00	0.01	8.76	8.77	
	2.00	8.77	-8.47	0.30	
0.01	3.00	0.30	2.42	2.72	
	4.00	2.72	0.29	3.00	
	5.00	3.00	0.00	3.00	Converged
	1.00	1.00	2.11	3.11	
1.00	2.00	3.11	-0.11	3.00	
	3.00	3.00	0.00	3.00	Converged
	1.00	2.00	1.02	3.02	
2.00	2.00	3.02	-0.02	3.00	
	3.00	3.00	0.00	3.00	Converged
	1.00	2.50	0.51	3.01	
2.50	2.00	3.01	-0.01	3.00	
	3.00	3.00	0.00	3.00	Converged
	1.00	4.50	-1.44	3.06	
4.50	2.00	3.06	-0.06	3.00	
	3.00	3.00	0.00	3.00	Converged
	1.00	9.00	-8.91	0.09	
	2.00	0.09	0.98	1.07	
9.00	3.00	1.07	2.11	3.17	
	4.00	3.17	-0.17	3.00	
	5.00	3.00	0.00	3.00	Converged

Table A.52: Iteration Summary for Estimating Synthetic $f_c^{max} = 4.50$kN with Different Initial Guesses on Large-Sized Samples

Initial Guess (f_c^{max})	Iteration (k)	Guess ${f_c^{max}}_k$	Δf_c^{max}	Result ${f_c^{max}}_{k+1}$	Comment
	1.00	0.01	8.54	8.55	
	2.00	8.55	-5.60	2.96	
0.01	3.00	2.96	1.54	4.49	
	4.00	4.49	0.01	4.50	

	5.00	4.50	0.00	4.50	Converged
1.00	1.00	1.00	3.53	4.53	
	2.00	4.53	-0.03	4.50	
	3.00	4.50	0.00	4.50	Converged
2.00	1.00	2.00	2.55	4.55	
	2.00	4.55	-0.05	4.50	
	3.00	4.50	0.00	4.50	Converged
3.00	1.00	3.00	1.50	4.50	
	2.00	4.50	0.00	4.50	Converged
5.00	1.00	5.00	-0.49	4.51	
	2.00	4.51	-0.01	4.50	
	3.00	4.50	0.00	4.50	Converged
10.70	1.00	10.70	-10.52	0.18	
	2.00	0.18	2.40	2.58	
	3.00	2.58	1.96	4.54	
	4.00	4.54	-0.04	4.50	
	5.00	4.50	0.00	4.50	Converged

Bibliography

[1] ASTM C1116/C1116M-10a. Standard specification for fiber-reinforced concrete, 2015.

[2] F. Minelli and G.A. Plizzari. On the effectiveness of steel fibers as shear reinforcement. Structural Journal, 110:379–390, 2013.

[3] Z. Deng. Utilisation of steel fibres to reinforce waste glass concrete: Alkali–silica reaction, engineering properties, and 3d mesoscale modelling. Case Studies in Construction Materials, 17:e01686, 2022.

[4] Á. Mena-Alonso, D. C. González, J. Mínguez, and M. A. Vicente. Mechanical behavior of high-strength steel fiber-reinforced concrete. In Longbiao Li, editor, Fiber-Reinforced Composites, chapter 4. IntechOpen, 2024. doi: 10.5772/intechopen.1004302. URL `https://doi.org/10.5772/intechopen.1004302`.

[5] Z. Deng and Z. Deng. Short-term improvement of ductile geopolymer composites exposed to magnesium sulfate: Mechanical properties, sorptivity, and mechanisms. Construction and Building Materials, 408:133648, 2023.

[6] Z. Deng, S. Zhang, and Z. Deng. Pva fiber-reinforced geopolymer mortar made with hybrid recycled aggregates: Toward thermal insulation, lightweight and improved durability. Journal of Cleaner Production, 426:139200, 2023.

[7] A.M. Brandt. Fibre reinforced cement-based (frc) composites after over 40 years of development in building and civil engineering. Composite Structures, 86:3–9, 2008.

[8] W. Shao, Y. Wang, and D. Shi. Corrosion-fatigue life prediction of reinforced concrete square piles in marine environments. Engineering Failure Analysis, 138:106324, 2022.

[9] R. Basan, T. Marohnić, and Ž. Božić. Application of material fatigue parameters estimation in analysis of rolling-sliding contact fatigue of gears. Procedia Structural Integrity, 46:62–67, 2023.

[10] B. Nečemer, Ž. Božić, and S. Glodež. Fatigue resistance of the auxetic honeycombs. Procedia Structural Integrity, 46:68–73, 2023.

[11] I. Kožar, T. Sulovsky, M. Plovanić, and Ž. Božić. Verification of a displacement model for three-point bending test. Procedia Structural Integrity, 46:143–148, 2023.

[12] X. Guan et al. A stochastic multiscale model for predicting mechanical properties of fiber reinforced concrete. International Journal of Solids and Structures, 56–57:280–289, 2015.

[13] I. Kožar, N. Torić Malić, D. Simonetti, and Ž. Božić. Stochastic properties of bond-slip parameters at fibre pull-out. Engineering Failure Analysis, 111: 104478, 2020.

[14] I. Kožar, N. Bede, S. Mrakovčić, and Ž. Božić. Layered model of crack growth in concrete beams in bending. Procedia Structural Integrity, 31:134–139, 2021.

[15] T. Rukavina, A. Ibrahimbegovic, and I. Kožar. Fiber-reinforced brittle material fracture models capable of capturing a complete set of failure modes including fiber pull-out. Computer Methods in Applied Mechanics and Engineering, 355:157–192, 2019.

[16] F. Minelli and G. A. Plizzari. On the effectiveness of steel fibers as shear reinforcement. ACI Structural Journal.

[17] Cement Concrete & Aggregates Australia (CCAA). Guide to Concrete Construction - Part II. Constituents of Concrete.

[18] Y. He. Testing and modelling of the mechanical properties of fibre-matrix interfacial transition zone. Master thesis, TU Delft - Civil Engineering and Geosciences, 2024.

[19] Z. F. Akbulut, T. A. Tawfik, P. Smarzewski, and S. Guler. Advancing hybrid fiber-reinforced concrete: Performance, crack resistance mechanism, and future innovations. Buildings, 15(8), 2025. ISSN 2075-5309. doi: 10.3390/buildings15081247. URL https://www.mdpi.com/2075-5309/15/8/1247.

[20] V. C. Li. Postcrack scaling relations for fiber reinforced cementitious composites. Journal of Materials in Civil Engineering, 4(1).

[21] P.S. Mangat and M.Motamedi Azari. Influence of steel fibre reinforcement on the fracture behaviour of concrete in compression. International Journal of Cement Composites and Lightweight Concrete, 6(4):219–232, 1984. ISSN 0262-5075. doi: https://doi.org/10.1016/0262-5075(84)90017-4. URL https://www.sciencedirect.com/science/article/pii/0262507584900174.

[22] G. Plizzari and S. Mindess. Fiber-reinforced concrete. In Concrete: Microstructure, Properties, and Materials.

[23] P. Hájek and C. Fiala. Savings in primary material use through optimized rc and frc structures in building construction. In Proceedings of the International Conference on Sustainable Building 2007 (SB07 HK - Sustainable Building 2007), iiSBE 2007.

[24] S. Aidarov, A. Nadaždi, E. Pugach, N. Tošić, and A. de la Fuente. Cost-oriented analysis of fibre reinforced concrete column-supported flat slabs construction. Journal of Building Engineering, 51:104205, 2022. ISSN 2352-7102. doi: https://doi.org/10.1016/j.jobe.2022.104205. URL https://www.sciencedirect.com/science/article/pii/S2352710222002182.

[25] A. Shapira and L. C. Bank. Constructability and economics of frp reinforcement cages for concrete beams. Journal of Composites for Construction, 1 (3).

[26] A. de la Fuente, L. Liao, S. H. P. Cavalaro, and A. Aguado. Fibre reinforced precast concrete segments: design and applications. In World Tunnelling Congress: Tunnels for a Better Life (WTC 2014), Iguassu Falls, Brazil, May 2014.

[27] A. M. Brandt. Fibre reinforced cement-based (frc) composites after over 40 years of development in building and civil engineering. Composite Structures, 86(1):3–9, 2008. doi: 10.1016/j.compstruct.2008.03.006.

[28] S. Cangiano, R. Cucitore, and G. Plizzari. Sulla caratterizzazione del comportamento flessionale post-picco di calcestruzzi rinforzati con fibre di acciaio. 2008.

[29] S. Anders and M. Schovenberg. Performance of steel fiber reinforced concrete – comparability of tests according to dafstb-guideline "stahlfaserbeton" and en 14651. Acta Polytechnica.

[30] A. Machida and K. Maruyam. Design code development for fibre-reinforced polymer structures and repairs. Progress in Structural Engineering and Materials, 4(2):149–160, April/June 2002.

[31] E. Bernard and G. G. Xu. Influence of fibre count on variability in post-crack performance of fibre reinforced concrete. Materials and Structures, 50(3).

[32] J. A. O. Barros and S. Foster. Fibres as shear reinforcement in RC beams: an overview on assessment of material properties and design approaches, pages 111–120. fib - International Federation for Structural Concrete, October 2020.

[33] P. Visintin. Simulating the mechanics of ultra-high performance fibre reinforced concrete for rapid low cost material development and analysis. Final report, The University of Adelaide, December 2017. URL https://apps.dtic.mil/sti/tr/pdf/AD1056982.pdf.

[34] A. Carpinteri, G. Ferro, and G. Ventura. The Influence of Fibers on the Structural Response of Reinforced Concrete Beams, pages 41–50. Springer Netherlands, January 2002.

[35] Á. Picazo, M. G. Alberti, J. C. Gálvez, A. Enfedaque, and A. C. Vega. The size effect on flexural fracture of polyolefin fibre-reinforced concrete. Applied Sciences, 9(9), 2019. ISSN 2076-3417. doi: 10.3390/app9091762. URL https://www.mdpi.com/2076-3417/9/9/1762.

[36] A. Jansson, I. Lofgren, K. Lundgren, and K. Gylltoft. Bond of reinforcement in self-compacting steel-fibre-reinforced concrete. Magazine of Concrete Research, 64(7):617–630, 2012. doi: 10.1680/macr.11.00091.

[37] I. Kožar, N. Torić Malić, D. Simonetti, and Ž. Smolčić. Bond-slip parameter estimation in fiber reinforced concrete at failure using inverse stochastic model. Engineering Failure Analysis, 104:84–95, 2019.

[38] J. J. Timothy, T. Iskhakov, Y. Zhan, and G. Meschke. A multiscale model for high performance frc. In V. Mechtcherine, . Slowik, and P. Kabele, editors, Strain-Hardening Cement-Based Composites, pages 97–105, Dordrecht, 2018. Springer Netherlands. ISBN 978-94-024-1194-2.

[39] G. Ruiz, C. Andrade, R. C. Yu, and X. X. Zhang. A multiscale oriented concept for the analyses of steel fiber reinforced concrete materials and structures. 2012. URL https://api.semanticscholar.org/CorpusID:201720296.

[40] V. M. C. F. Cunha. Steel fibre reinforced self-compacting concrete (from micromechanics to composite behavior). 2010. URL https://api.semanticscholar.org/CorpusID:135207821.

[41] M. Khan, M. Cao, and M. Ali. Cracking behaviour and constitutive modelling of hybrid fibre reinforced concrete. Journal of Building Engineering, 30:101272, 2020. ISSN 2352-7102. doi: https://doi.org/10.1016/j.jobe.2020.101272. URL https://www.sciencedirect.com/science/article/pii/S2352710219323356.

[42] Y. Zhan and G. Meschke. Multilevel computational model for failure analysis of steel-fiber–reinforced concrete structures. Journal of Engineering Mechanics, 142(11), 2016. doi: 10.1061/(ASCE)EM.1943-7889.0001154.

[43] Y. Huang, J. Huang, W. Zhang, and X. h. Liu. Experimental and numerical study of hooked-end steel fiber-reinforced concrete based on the meso- and macro-models. Composite Structures, 2023. URL https://api.semanticscholar.org/CorpusID:256581741.

[44] R. Blaheta, I. Georgiev, K. Georgiev, O. Jakl, R. Kohut, S. Margenov, and J. Starý. High performance computing applications. Cybernetics and Information Technologies, 17(5):5–16, December 2017. doi: 10.1515/cait-2017-0050. Special Issue With Selected Papers From The Workshop "Two Years Avitohol: Advanced High Performance Computing Applications 2017".

[45] V. Buljak, T. Oesch, and G. Bruno. Simulating fiber-reinforced concrete mechanical performance using ct-based fiber orientation data. Materials, 12(5).

[46] I. Kožar, N. Malić, and T. Rukavina. Inverse model for pullout determination of steel fibers. Coupled Systems Mechanics, 7(2):197–209, 2018.

[47] C.A. Nonato Da Silva, J. Ciambella, J.A.O. Barros, T.D. dos Santos Valente, and I.G. Costa. A multiscale model for optimizing the flexural capacity of frc structural elements. Composites Part B: Engineering, 200: 108325, 2020. ISSN 1359-8368. doi: https://doi.org/10.1016/j.compositesb.2020.108325. URL https://www.sciencedirect.com/science/article/pii/S1359836820333746.

[48] D.-Y. Yoo, S.-T. Kang, N. Banthia, and Y.-S. Yoon. Nonlinear finite element analysis of ultra-high-performance fiber-reinforced concrete beams. International Journal of Damage Mechanics, 26(5):735–757, 2015. doi: 10.1177/1056789515612559.

[49] S. Marfia and E. Sacco. Micromechanical analysis of fibre reinforced concrete. In Proceedings of the 12th International Conference on Composite Materials, ICCM-12, Parigi.

[50] M. Ďubek, P. Makýš, S. Ďubek, and M. Petro. The evaluation of the content of fibers in steel fiber reinforced structures and image analysis. Journal of Civil Engineering and Management, 24(3):Article 3, 2018. doi: 10.3846/jcem.2018.1642.

[51] J. Lu, J. Liu, H. Yang, X. Wan, J. Gao, J. Zhang, and P. Li. Experimental investigation on the mechanical properties and pore structure deterioration of fiber-reinforced concrete in different freeze-thaw media. Construction and Building Materials, 350:128887, 2022. ISSN 0950-0618. doi: https://doi.org/10.1016/j.conbuildmat.2022.128887. URL https://www.sciencedirect.com/science/article/pii/S0950061822025430.

[52] F. L. de Oliveira. Design-oriented constitutive model for steel fiber reinforced concrete. PhD thesis, Universitat Politècnica de Catalunya, Barcelona, March 2010. Doctoral Thesis; Directed by: Antonio Aguado de Cea and Climent Molins Borrell.

[53] S. Kalinčević. Ispitivanje homogenosti raspodjele vlakana u mikroarmiranom betonu primjenom računalne tomografije, 2016. URL https://urn.nsk.hr/urn:nbn:hr:157:730997. Info:eu-repo/semantics/masterThesis, University of Rijeka, Faculty of Civil Engineering in Rijeka.

[54] S. G. Advani and C. L. Tucker III. The use of tensors to describe and predict fiber orientation in short fiber composites. Journal of Rheology, 31(8):751–784, 1987. doi: 10.1122/1.549945.

[55] V. Gudžulić, T.S. Dang, and G. Meschke. Computational modeling of fiber flow during casting of fresh concrete. Computational Mechanics, 63(4):1111–1129, 2019. doi: 10.1007/s00466-018-1639-9.

[56] J. Reinold, V. Gudžulić, and G. Meschke. Computational modeling of fiber orientation during 3d-concrete-printing. Computational Mechanics, 71(6):1205–1225, 2023. doi: 10.1007/s00466-023-02304-z.

[57] H.-C. Tseng, R.-Y. Chang, and C.-H. Hsu. Comparison of recent fiber orientation models in injection molding simulation of fiber-reinforced composites. Journal of Thermoplastic Composite Materials, 33(1):35–52, 2020. doi: 10.1177/0892705718804599.

[58] S. K. Kugler, A. Kech, C. Cruz, and T. Osswald. Fiber orientation predictions—a review of existing models. Journal of Composites Science, 4(2), 2020. ISSN 2504-477X. doi: 10.3390/jcs4020069. URL https://www.mdpi.com/2504-477X/4/2/69.

[59] V. Marcos-Meson, A. Solgaard, G. Fischer, C. Edvardsen, and A. Michel. Pull-out behaviour of hooked-end steel fibres in cracked concrete exposed to wet-dry cycles of chlorides and carbon dioxide – mechanical performance. Construction and Building Materials, 240:117764, 2020. ISSN 0950-0618. doi: https://doi.org/10.1016/j.conbuildmat.2019.117764. URL https://www.sciencedirect.com/science/article/pii/S0950061819332179.

[60] P. D. Nieuwoudt and W. P. Boshoff. Time-dependent pull-out behaviour of hooked-end steel fibres in concrete. Cement and Concrete Composites, 79:133–147, 2017. ISSN 0958-9465. doi: https://doi.org/10.1016/j.cemconcomp.2017.02.006. URL https://www.sciencedirect.com/science/article/pii/S0958946517301580.

[61] I. Kožar, N. Bede Odorčić, A. Bogdanić, and S. Mrakovčić. Data driven inverse stochastic models for fiber reinforced concrete. Coupled Systems Mechanics, 10:509–520, 2021.

[62] P. Robins, S. Austin, and P. Jones. Pull-out behaviour of hooked steel fibres. Materials and Structures.

[63] M. Alhassan, N. Betoush, N. Al-Huthaifi, and A. Al Dalou. Estimation of the fracture parameters of macro fiber-reinforced concrete based on nonlinear elastic fracture mechanics simulations. Results in Engineering, 15:100539, 2022. doi: 10.1016/j.rineng.2022.100539.

[64] M. A. Mujalli, S. Dirar, E. Mushtaha, A. Hussien, and A. Maksoud. Evaluation of the tensile characteristics and bond behaviour of steel fibre-reinforced concrete: An overview. Fibers, 10(12), 2022. ISSN 2079-6439. doi: 10.3390/fib10120104. URL https://www.mdpi.com/2079-6439/10/12/104.

[65] J. Xiao, X. Long, M. Ye, H. Jiang, L. Liu, F. Mo, D. Deng, and Z. Huang. Bond-slip law between steel bar and different cement-based materials considering anchorage position function. Frontiers in Materials, 8, 2021. doi: 10.3389/fmats.2021.801452.

[66] P. Croce, P. Formichi, and F. Landi. Experimental assessment and numerical modeling of the bond-slip correlation for steel rebars in r.c. members. Materials (Basel), 15(3):951, 2022. doi: 10.3390/ma15030951.

[67] Ž. Smolčić and J. Ožbolt. Meso scale model for fiber-reinforced-concrete: Effective bond-slip relationship of fibers. Proceedings of works (Faculty of Civil Engineering, University of Rijeka), 17:197–212, 2014. doi: 10.32762/zr.

[68] K.-C. Kim, I.-H. Yang, and C. Joh. Effects of single and hybrid steel fiber lengths and fiber contents on the mechanical properties of high-strength fiber-reinforced concrete. Advances in Civil Engineering, 2018(1):7826156, 2018. doi: https://doi.org/10.1155/2018/7826156. URL https://onlinelibrary.wiley.com/doi/abs/10.1155/2018/7826156.

[69] R. Wang, N. Tian, J. Liu, R. Jin, G. Liang, Y. Li, J. Hu, H. Zhou, Y. Jia, and Y. Liu. Evaluation of dynamic mechanical properties of steel-fiber-reinforced concrete subjected to freeze–thaw cycles. Buildings, 14(9):2880, 2024. doi: 10.3390/buildings14092880.

[70] M. Parise. Constitutive modelling of fibre reinforced concrete. PhD thesis, Universita' Degli Studi di Padova, 2014.

[71] D.-Y. Yoo, J. Je, H.-J. Choi, and P. Sukontasukkul. Influence of embedment length on the pullout behavior of steel fibers from ultra-high-performance concrete. Materials Letters, 276:128233, 2020. ISSN 0167-577X. doi: https://doi.org/10.1016/j.matlet.2020.128233. URL https://www.sciencedirect.com/science/article/pii/S0167577X20309381.

[72] S. Abdallah and D.W.A. Rees. Comparisons between pull-out behaviour of various hooked-end fibres in normal-high strength concretes. International Journal of Concrete Structures and Materials, 13:27, 2019. doi: 10.1186/s40069-019-0337-0.

[73] W. j. Meng, H. x. Liu, G. j. Liu, X. q. Kong, and X. z. Wang.

[74] W. W. Sampson. Modelling Stochastic Fibrous Materials with Mathematica®. Springer Science & Business Media, 2008.

[75] M. Kunieda, H. Ogura, N. Ueda, and H. Nakamura. Tensile fracture process of strain hardening cementitious composites by means of three-dimensional meso-scale analysis. Cement and Concrete Composites, 33(9):956–965, 2011. doi: 10.1016/j.cemconcomp.2011.05.010.

[76] A. Caggiano, D. S. Schicchi, G. Etse, and E. Martinelli. Meso-scale modeling of hybrid industrial/recycled steel fiber-reinforced concrete. In Eccomas Proceedia, pages 2353–2362, 2016. doi: 10.7712/100016.1965.9036.

[77] Ž. Smolčić and J. Ožbolt. Meso scale model for fiber-reinforced-concrete: Microplane based approach. Computers and Concrete, 19:375–385, 2017. URL https://api.semanticscholar.org/CorpusID:136439740.

[78] T. Soetens, S. Matthys, L. Taerwe, and A. Van Gysel. Basis of a Finite-Element Simulation Tool to Predict the Flexural Behavior of SFRC Prisms, pages 91–98. Springer Netherlands, Dordrecht, 2012. ISBN 978-94-007-2436-5. doi: 10.1007/978-94-007-2436-5_12. URL https://doi.org/10.1007/978-94-007-2436-5_12.

[79] Z. Zhang, X. Zhu, Y. Zhang, and R. Gong. Experimental and numerical investigation on flexural and fracture performance of steel fiber reinforced shotcrete. Construction and Building Materials, 2021. URL https://api.semanticscholar.org/CorpusID:244693168.

[80] A. Pros, Pedro Díez, and Climent Molins. Modeling steel fiber reinforced concrete: Numerical immersed boundary approach and a phenomenological mesomodel for concrete-fiber interaction. International Journal for Numerical Methods in Engineering, 90:65–86, 04 2012. doi: 10.1002/nme.3312.

[81] M. Congro, D. Roehl, and C. Mejia. Mesoscale computational modeling of the mechanical behavior of cement composite materials. Composite Structures, 257:113137, 2021. ISSN 0263-8223. doi: https://doi.org/10.1016/j.compstruct.2020.113137. URL https://www.sciencedirect.com/science/article/pii/S0263822320330634.

[82] A. H. A. Al-Ahmed, A. Al-Rumaithi, A. A. Allawi, and A. El-Zohairy. Mesoscale analysis of fiber-reinforced concrete beams. Engineering Structures, 2022. URL https://api.semanticscholar.org/CorpusID:250257502.

[83] J. Wu, H. Zou, N. He, H. Xu, Z. Wang, and X. Rui. Experimental and numerical analysis of flexural properties and mesoscopic failure mechanism of single-shell lining concrete. Buildings, 14(9), 2024. ISSN 2075-5309. doi: 10.3390/buildings14092620. URL https://www.mdpi.com/2075-5309/14/9/2620.

[84] V.M.C.F. Cunha, J. A.O. Barros, and J.M. Sena-Cruz. A finite element model with discrete embedded elements for fibre reinforced composites. Computers & Structures, 94-95:22–33, 2012. ISSN 0045-7949. doi: https://doi.org/10.1016/j.compstruc.2011.12.005. URL https://www.sciencedirect.com/science/article/pii/S0045794911003038.

[85] J. Kang, K. Kim, Y. M. Lim, and J. E. Bolander. Modeling of fiber-reinforced cement composites: Discrete representation of fiber pullout. International Journal of Solids and Structures, 51(10):1970–1979, 2014. ISSN 0020-7683. doi: https://doi.org/10.1016/j.ijsolstr.2014.02.006. URL https://www.sciencedirect.com/science/article/pii/S0020768314000547.

[86] Y. Li, X. Ruan, M. Akiyama, M. Zhang, J. Xin, and S. Lim. Modelling method of fibre distribution in steel fibre reinforced concrete based on x-ray image recognition. Composites Part B: Engineering, 223:109124, 2021. ISSN 1359-8368. doi: https://doi.org/10.1016/j.compositesb.2021.109124. URL https://www.sciencedirect.com/science/article/pii/S1359836821005084.

[87] G.S. Watson. Equatorial distributions on a sphere. Biometrika, 52(1–2):193–201, 1965.

[88] W. Huang, B. Huang, A. Pan, Q. Chen, Q. Huang, R. Xu, Y. Yang, and F. Xue. Numerical statistics-based research on the spatial distribution of cylindrical fiber in ideal simulated fiber reinforced concrete matrix. Construction and Building Materials, 379:131209, 2023. ISSN 0950-0618. doi: https://doi.org/10.1016/j.conbuildmat.2023.131209. URL https://www.sciencedirect.com/science/article/pii/S0950061823009224.

[89] P. Soroushian and C.-D. Lee. Distribution and orientation of fibers in steel fiber reinforced concrete. ACI Materials Journal, 87(5):433 – 439, 1990. URL https://www.scopus.com/inward/record.uri?eid=2-s2.0-0025488934&partnerID=40&md5=7f98d5de668a1567eac388fdec99b8d0. Cited by: 283.

[90] P. Stroeven. Stereology of concrete reinforced with short steel fibres. HERON, 31 (2), 1986, 31, 01 1985.

[91] I. Kožar, N. T. Malić, S. Mrakovčić, and D. Simonetti. Parameter estimation in fiber reinforced concrete. In Proceedings of the International Conference on Sustainable Materials, Systems and Structures (SMSS2019) Novel Methods for Characterization of Materials and Structures, pages 75–81, Pariz, 2019. RILEM Publications SARL.

[92] I. Kožar, T. Sulovsky, and M. Plovanić. A simple model for inverse estimation from three-point bending tests. Procedia Structural Integrity, 47:185–189, 2023.

[93] F. Laranjeira, S. Grünewald, and J. Walraven. Characterization of the orientation profile of steel fiber reinforced concrete. Materials and Structures, 44 (6).

[94] M.G. Alberti, A. Enfedaque, and J.C. Gálvez. On the prediction of the orientation factor and fibre distribution of steel and macro-synthetic fibres for fibre-reinforced concrete. Cement and Concrete Composites, 77: 29–48, 2017. ISSN 0958-9465. doi: https://doi.org/10.1016/j.cemconcomp.2016.11.008. URL https://www.sciencedirect.com/science/article/pii/S0958946516307569.

[95] ASTM International. Standard test method for flexural performance of fiber-reinforced concrete (using beam with third-point loading), 2012.

[96] F. Medeghini, G. Tiberti, J. Guhathakurta, S. Simon, G. A. Plizzari, and P. Mark. Fiber orientation and orientation factors in steel fiber-reinforced concrete beams with hybrid fibers: A critical review. Structural Concrete, 26 (1):481–500, 2025. doi: https://doi.org/10.1002/suco.202400461. URL https://onlinelibrary.wiley.com/doi/abs/10.1002/suco.202400461.

[97] M.G. Alberti, A. Enfedaque, and J.C. Gálvez. A review on the assessment and prediction of the orientation and distribution of fibres for concrete. Composites Part B: Engineering, 151:274–290, 2018. ISSN 1359-8368. doi: https://doi.org/10.1016/j.compositesb.2018.05.040. URL https://www.sciencedirect.com/science/article/pii/S1359836817344001.

[98] T. Sulovsky and I. Kožar. Predictive numerical model for simulation of fiber-reinforced concrete beams in bending and inverse parametric analysis. Engineering Failure Analysis, 165:108818, 2024. doi: https://doi.org/10.1016/j.engfailanal.2024.108818.

[99] Hrvatski zavod za norme. Concrete – part 9: Additional rules for self-compacting concrete (scc) (en 206-9:2010), 2010.

[100] Hrvatski zavod za norme. Testing fresh concrete – part 2: Slump-test (en 12350-2:2019), 2019.

[101] Hrvatski zavod za norme. Testing fresh concrete – part 4: Degree of compactability (en 12350-4:2019), 2019.

[102] Hrvatski zavod za norme. Testing fresh concrete – part 3: Vebe test (en 12350-3:2019), 2019.

[103] Hrvatski zavod za norme. Testing fresh concrete – part 5: Flow table test (en 12350-5:2019), 2019.

[104] Hrvatski zavod za norme. Testing fresh concrete – part 10: Self-compacting concrete – l-box test (en 12350-10:2010), 2010.

[105] KrampeHarex GmbH & Co. KG. Data sheet | fibres—wire fibre, hooked ends, 2019. Data sheet.

[106] Hrvatski zavod za norme. Metalni materijali – umjeravanje i provjeravanje statičkih jednoosnih ispitnih uređaja – 1. dio: Ispitni uređaji za zatezanje/kompresiju – umjeravanje i provjeravanje sustava za mjerenje sile (iso 7500-1:2018; en iso 7500-1:2018), 2018.

[107] Hrvatski zavod za norme. Testing concrete in structures – part 1: Cored specimens – taking; examining and testing in compression (en 12504-1:2019), 2019.

[108] Hrvatski zavod za norme. Testing hardened concrete – part 5: Flexural strength of test specimens (en 12390-5:2019), 2019.

[109] M. Grbac. Nelinearni proračun gredice armirane vlaknima, 2016. URL https://urn.nsk.hr/urn:nbn:hr:157:633930. Info:eu-repo/semantics/masterThesis, University of Rijeka, Faculty of Civil Engineering in Rijeka.

[110] Hrvatski zavod za norme. Ispitivanje očvrsnuloga betona – 2. dio: Izrada i njega ispitnih uzoraka za ispitivanja čvrstoće (en 12390-2:2019), 2019.

[111] Hrvatski zavod za norme. Vlakna za beton – 1. dio: Čelična vlakna – definicije, specifikacije i sukladnost (en 14889-1:2006), 2007.

[112] G. Wu and H. Wang. Numerical simulation of steel fiber pull-out process based on cohesive zone model and unified phase-field theory. Sustainability, 15(5): 4015, 2023. doi: 10.3390/su15054015.

[113] I. Kožar, N. Bede, S. Mrakovčić, and Ž. Božić. Verification of a fracture model for fiber reinforced concrete beams in bending. Engineering Failure Analysis, 138:106378, 2022.

[114] R.C. Aster, B. Borchers, and C.H. Thurber. Parameter Estimation and Inverse Problems. Elsevier, 2018.

[115] Marine Data Science. How to normalize the rmse. `https://www.marinedatascience.co/blog/2019/01/07/normalizing-the-rmse/`, January 2019. Accessed: 2024-10-19.

[116] L. Giménez Rodríguez. Aquacrop model evaluation in maize under different water availabilities in the western of uruguay. 9:103–117, 07 2019.

[117] M. Yaman, M. Elaty, and M. Taman. Predicting the ingredients of self compacting concrete using artificial neural network. Alexandria Engineering Journal, 56, 04 2017. doi: 10.1016/j.aej.2017.04.007.

[118] D.N. Moriasi, J.G. Arnold, M.W. Van Liew, R.L. Bingner, R.D. Harmel, and T.L. Veith. Model evaluation guidelines for systematic quantification of accuracy in watershed simulation. American Society of Agricultural and Biological Engineers, 50:885–900, 2007.